From Positive to Negative Ions, Studies Based on Rydberg Spectroscopy

Felix Engel

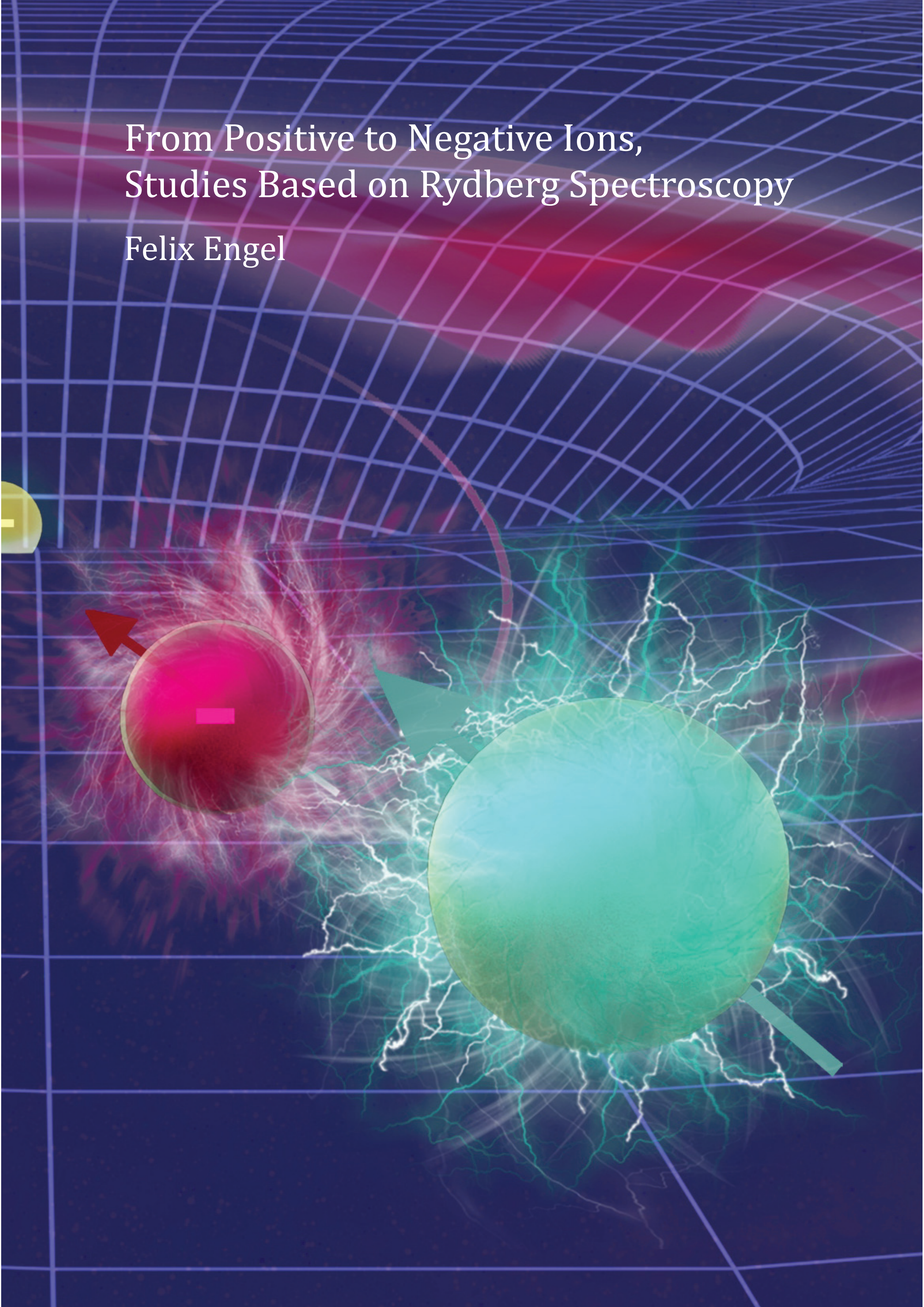

From Positive to Negative Ions, Studies Based on Rydberg Spectroscopy

Von der Fakultät Mathematik und Physik der Universität Stuttgart
zur Erlangung der Würde eines Doktors der Naturwissenschaften
(Dr. rer. nat.) genehmigte Abhandlung.

vorgelegt von

Felix Engel

aus Schwäbisch Hall

Hauptberichter:	Prof. Dr. Tilman Pfau
Mitberichter:	Prof. Dr. Peter Michler
Prüfungsvorsitzende:	Prof. Dr. Maria Daghofer
Tag der mündlichen Prüfung:	18. September 2020

5. Physikalisches Institut
Universität Stuttgart
2020

List of publications

[S1] F. Engel, T. Dieterle, T. Schmid, C. Tomschitz, C. Veit, N. Zuber, R. Löw, T. Pfau, and F. Meinert. "Observation of Rydberg Blockade Induced by a Single Ion". Physical Review Letters **121** (2018), 193401. arXiv: `1809.00993` (cit. on pp. 10, 16, 56, 180).

[S2] F. Engel, T. Dieterle, F. Hummel, C. Fey, P. Schmelcher, R. Löw, T. Pfau, and F. Meinert. "Precision Spectroscopy of Negative-Ion Resonances in Ultralong-Range Rydberg Molecules". Physical Review Letters **123** (2019), 073003. arXiv: `1904.08372` (cit. on pp. 11, 16, 17, 41, 48, 49, 119, 145, 182).

[S3] F. Engel, T. Dieterle, S. K. Tiwari, S. Wüster, M. Wagner, C. Fey, R. Schmidt, R. Löw, F. Meinert, and T. Pfau. "In preparation". 2020 (cit. on pp. 149, 158).

[S4] K. S. Kleinbach, F. Engel, T. Dieterle, R. Löw, T. Pfau, and F. Meinert. "Ionic Impurity in a Bose-Einstein Condensate at Submicrokelvin Temperatures". Physical Review Letters **120** (2018), 193401. arXiv: `1802.08587` (cit. on pp. 11, 16, 39).

[S5] K. S. Kleinbach, F. Meinert, F. Engel, W. J. Kwon, R. Löw, T. Pfau, and G. Raithel. "Photoassociation of Trilobite Rydberg Molecules via Resonant Spin-Orbit Coupling". Physical Review Letters **118** (2017), 223001. arXiv: `1703.01096` (cit. on pp. 11, 16, 39, 117).

[S6] M. Schlagmüller, T. C. Liebisch, H. Nguyen, G. Lochead, F. Engel, F. Böttcher, K. M. Westphal, K. S. Kleinbach, R. Löw, S. Hofferberth, T. Pfau, J. Pérez-Ríos, and C. H. Greene. "Probing an Electron Scattering Resonance using Rydberg Molecules within a Dense and Ultracold Gas". Physical Review Letters **116** (2016), 53001. arXiv: `1510.07003` (cit. on pp. 11, 16, 39, 52, 53, 103, 117).

[S7] M. Schlagmüller, T. C. Liebisch, F. Engel, K. S. Kleinbach, F. Böttcher, U. Hermann, K. M. Westphal, A. Gaj, R. Löw, S. Hofferberth, T. Pfau, J. Pérez-Ríos, and C. H. Greene. "Ultracold Chemical Reactions of a Single Rydberg Atom in a Dense Gas". Physical Review X **6** (2016), 031020. arXiv: `1605.04883` (cit. on pp. 11, 16, 39, 97, 101, 117, 152, 160).

[S8] T. C. Liebisch et al. "Controlling Rydberg atom excitations in dense background gases". Journal of Physics B: Atomic, Molecular and Optical Physics **49** (2016), 182001. arXiv: `1607.01325` (cit. on pp. 11, 16, 53).

Contents

Zusammenfassung

Die Quantenmechanik bildet die Grundlage für viele Bereiche der modernen Physik. Die Beschreibung von Materie und Licht wird im kleinsten Detail von der Quantentheorie erfasst. Insbesondere werden Prozesse auf atomarer Ebene mit bemerkenswerter Genauigkeit und Zuverlässigkeit wiedergegeben. Auf dem Maßstab von Atomen verhalten sich die Dinge typischerweise überhaupt nicht so wie etwas das wir mit Erfahrungen aus dem täglichen Leben in Verbindung bringen können. Die Quantennatur atomarer Objekte (z.B. Elektronen, Protonen, Neutronen, Photonen, usw.) wird häufig mit dem Begriff „Teilchenwelle“ bzw. „Wellenteilchen“ assoziiert. Der Grund für die (mehr oder weniger zutreffende) Bezeichnung ist, dass alle diese Objekte Eigenschaften von beiden besitzen, die eines Teilchens, da wir einzelne Klicks auf einem Detektor erfassen können, und die einer Welle, da wir die Interferenz zwischen Objekten durch mehrmaliges Wiederholen von Experimenten sichtbar machen können.

Zu Beginn des 20. Jahrhunderts sorgte eine immer mehr wachsende Anzahl an Experimenten auf atomarer Ebene, welche bereits Hinweise zu dem Verhalten kleinster Teilchen lieferten, für eine zunehmende Verwirrung der noch großteils klassisch denkenden Gesellschaft. Schließlich gelang es Schrödinger, Heisenberg und Born um 1926/27 eine konsistente Beschreibung des Verhaltens der Materie auf kleinstem Maßstab zu formulieren, mit der die Verwirrung größtenteils aufglöst wurde. Die Theorie bildet die Grundlage der heute bekannten Quantenmechanik.[9]

Einer der grundlegendsten Unterschiede zwischen der Beschreibung der klassischen und der Quantenmechanik besteht darin, dass wir in der klassischen Mechanik das Ergebnis einer Messung anhand der Anfangsbedingungen (deterministisch) bestimmen. In der Quantenmechanik hingegen müssen wir den Determinismus aufgeben und akzeptieren, dass wir lediglich eine Chance ein Messergebnis zu erhalten vorhersagen können. Bei der Anwendung der Quantentheorie erkennen wir, dass unser vom klassischen Standpunkt aus idealisiertes Verständnis der Natur eingeschränkt wird, was in manchen Situationen schwierig zu akzeptieren sein kann. Auf diese Weise jedoch können wir quantenmechanische Phänomene beschreiben, die aus klassischer Sicht nicht zu verstehen sind. In der Quantentheorie ergibt sich die Wahrscheinlichkeit des Auftretens eines Ereignisses aus der Wellenfunktion, die das quantenmechanische System beschreibt.

In dieser Hinsicht sind Rydberg-Atome faszinierende Objekte mit für Atome übertriebenen Eigenschaften und Größen, was sie zu perfekten Kandidaten für die Untersuchung quantenmechanischer Phänomene auf „klassischem Maßstab“ macht. Manchmal kann das Ergebnis dieser Studien sehr überraschend sein, und in diesem Fall ist zu Beginn oft nicht klar, ob das beobachtete Phänomen quantenmechanischer oder klassischer Natur ist. Diese Studien sind meist die aufregendsten, da wir unser Wissen über die Natur wie wir sie verstehen erweitern können, indem wir die Grenzen der klassischen und der quantenmechanischen Beschreibung austesten.

Diese Arbeit berichtet über Studien von positiven und negativen Ionen basierend auf Rydberg-Spektroskopie. Die Experimente werden in einem ultrakalten Gas aus Rubidium-87-Atomen durchgeführt. Im Bereich der kalten und ultrakalten Atome ist die Bewegung der Gasatome auf der Zeit- und Längenskala (Mikrometer pro Mikrosekunde) von typischen Rydberg-Experimenten eingefroren.

In den vergangenen Jahren haben sich ultrakalte Rydberg-Atome als vielseitige Plattform für die Quantensimulation von langreichweitig-wechselwirkenden Vielkörpersystemen [10–12], für die Erzeugung nichtklassischer photonischer Zustände [13, 14] und für die Verarbeitung von Quanteninformationen [15–17], erwiesen. Ein zentraler Aspekt für zukünftige Vorhaben in diesen Bereichen ist das Phänomen der Rydberg-Blockade [18–20]. Das Blockadephänomen beruht auf der starken Wechselwirkung der Rydberg-Atome, welche die Unterdrückung der gleichzeitigen Anregung von zwei oder mehr Atomen in Rydberg-Zustände innerhalb eines bestimmten Blockadevolumens zur Folge hat. Die Rydberg-Rydberg Blockade in einem kalten und dichten Atomensemble wurde erstmals 2004 experimentell beobachtet [21, 22] und 2009 für ein Paar einzelner Atome demonstriert [23].

Ein ähnliches Konzept existiert für Hybridsysteme aus Ionen und Rydberg-Atomen. In diesem Fall führen starke Wechselwirkungen zwischen einem einzelnen Ion und Rydberg-Atomen zu ladungsinduzierten Blockadephänomenen, die über makroskopische Entfernungen wirken. Die ioneninduzierte Rydberg-Blockade wurde zur Anwendung für den Quanteninformationstransfer zwischen ionischen und atomaren Quantensystemen vorgeschlagen [24]. Die experimentelle Beobachtung des Blockademechanismus ist jedoch bisher ausgeblieben. Der Grund hierfür liegt darin, dass in traditionellen Hybridsystemen die durch Ionenfallen induzierte Linienverschiebung in den Rydberg-Zuständen die Beobachtung von Wechselwirkungseffekten erschwert [25]. Dennoch wurde erst kürzlich in einer Studie zum Ladungstransfer in einem solchen Hybridsystem über erste Hinweise auf ioneninduzierte Linienverschiebungen berichtet [26]. Darüber hinaus wurden Ionen-Rydberg-Atom-Wechselwirkungen in Atomstrahlexperimenten untersucht [27] und in jüngster Zeit wurde gezeigt, dass die Ionen-Rydberg-Atom-Wechselwirkung quantenoptische Anwendungen, die auf Dämpfen bei Raumtemperatur basieren, beeinflussen [28].

Im Rahmen dieser Arbeit wird ein alternativer Ansatz zur Realisierung eines Ionen-Rydberg-Atomsystems erarbeitet. Hierfür wird ein einzelnes Ion in einem ultrakalten Gas aus Rubidium-Atomen erzeugt. Das Vorhandensein des Ions wird überprüft, indem das Valenzelektron eines einzelnen Gasatoms in den Rydberg-Zustand angeregt wird. Eine hohe räumliche Kontrolle über das Ion und die Rydberg-Anregung wird durch einen eng fokussierten Photoionisations- und Anregungslaser erreicht. Die Ionen-Rydberg-Atom-Wechselwirkung wird mittels einer ioneninduzierten Rydberg-Anregungsblockade untersucht und der Blockademechanismus wird dazu eingesetzt, ein einzelnes Ion als empfindliche Sonde für kleine elektrische Felder zu verwenden. Das Ergebnis dieser Studien wurde in Ref. [S1] veröffentlicht. Zusätzlich werden Experimente mit einem einzelnen Ion in einem Bose-Einstein Kondensat durchgeführt und erste Blockademessungen des Ions im Kondensat vorgestellt.

Studien über Wechselwirkungen zwischen Rydberg-Atomen und neutralen Atomen reichen zurück bis in das späte 19. Jahrhundert. Im Jahr 1879 kategorisierten Liveing und Dewar die spektrale Linienformen von Natrium in scharfe und diffuse Linien [29]. Heute wissen wir, dass diese diffuse Linien in Natrium den d-Zuständen entsprechen. Da d-Zustände in Natrium energetisch nahe der entarteten wasserstoffartigen Zuständen liegen, weisen diese im Spektrum eher eine Druckverbreiterung auf [27]. Die Verbreiterung der Emissionslinie folgt aus der Wechselwirkung des Rydberg-Atoms mit den umgebenden Atomen. Im Jahr 1934 berichteten Amaldi und Segré (Ref. [30]) für Experimente mit hohem Hintergrundgasdruck über wechselwirkungsinduzierte Linienverschiebungen und Verbreiterungen der Rydberg-Serie in Natrium für Hauptquantenzahlen im Bereich von $n = 30$. Sie erwarteten, dass das Puffergas die Rydberg-Serie unterbrechen würde, da das Rydberg-Atom für die experimentellen Bedingungen 10.000 Moleküle des Hintergrundgases enthalten müsste. Im selben Jahr führte Enrico Fermi das heutzutage bekannte Fermi-Pseudopotential [31] für die Streuung des Rydberg-Elektrons an Atomen ein, um diese Ergebnisse zu erklären und ebnete damit den Weg für immer mehr faszinierende Perspektiven der Rydberg-Atom-Wechselwirkungen. Diese erstrecken sich über den Bereich von einzelnen oder wenigen Atomen, welche mit dem Rydberg-Atom interagieren [S2, S5, 32–45], bis hin zu unzähligen neutralen Atomen die sich in dem Rydberg-Elektronenorbit aufhalten [S4, S6–S8, 38, 46, 47]. Dies ist lediglich eine unvollständige Liste an experimentellen Studien, die sich mit der Untersuchung von Rydberg-Atom-Wechselwirkungen in dem vergangenen Jahrzehnt befasst haben.

In dieser Arbeit werden ultralangreichweitige Rydberg-Moleküle verwendet, um Resonanzen im Rubidium-Anion zu untersuchen. Ultralangreichweitige Rydberg-Moleküle (ULRMs) können sich bilden, wenn sich ein oder mehrere neutrale Atome innerhalb der Rydberg-Elektronenwellenfunktion aufhalten. Die neutralen Atome sind durch attraktive Elektron-Atom-Streuwechselwirkungen innerhalb des Elektronenorbits gebunden und bilden lokal ein negatives Ion. Die resultierenden gebundenen Molekülzustände sind hochempfindlich gegenüber der Streuwechselwirkung und ermöglichen daher einen detaillierten Einblick in die zugrundeliegenden Anionenzustände nahe der Elektronenablösungsgrenze. Zu diesem Zweck wird die ULRM-Spektroskopie in einer kombinierten experimentellen und theoretischen Studie auf ein bislang unerreichtes quantitatives Maß an Präzision angehoben. Hierbei werden die ultralangreichweitigen Rydberg-Moleküle als ein ultrasensitives Werkzeug zur Untersuchung der quasi-gebundenen Negativionenresonanzen der Rubidiumanion eingesetzt. Das Ergebnis dieser Studien wurde in Ref. [S2] veröffentlicht.

Im letzten Teil dieser Arbeit wird das Ergebnis einer experimentellen Untersuchung eines lokalen Atomverlusts in einem Bose-Einstein Kondensat vorgestellt, der durch ein einzelnes Rydberg-Atom induziert wird. Die ersten Experimente sind ursprünglich der optischen Abbildung einer Elektronenwellenfunktion eines Rydberg-Atoms gewidmet. Für das Wellenfunktionsbildgebungsverfahren wird das Rydberg-Atom im Zentrum eines Bose-Einstein Kondensats präpariert. Die Elektron-Atom-Wechselwirkung führt zur Aufprägung einer Phase auf der Kondensatwellenfunktion, die in erster Ordnung proportional zum absoluten Quadrat der Elektronenwellenfunktion ist. Aufgrund des Gradienten der eingeprägten Phase, fließen die Kondensatatome in Bereiche mit hoher Elektronendichte. Der Atomfluss setzt sich fort, auch wenn das Rydberg-Atom nicht mehr vorhanden ist. Im Gegensatz zur erwarteten Dichtezunahme aufgrund der attraktiven Elektron-Atom-Wechselwirkung, wird experimentell eine lokale Abnahme der Kondensatdichte im Bereich der Rydberg-Anregung beobachtet. Das beobachtete lokale Atomverlustmerkmal wird für ein einzelnes Rydberg-Atom und mehrere nachfolgende Rydberg-Anregungen sowie für unterschiedliche Atomdichten charakterisiert. Darüber hinaus wird der experimentell beobachtete Verlust mit numerischen Simulationen abgeglichen, bei denen das Ausmaß der Änderung der Kondensatdichte im Anregungsbereich des Rydberg-Atoms weitgehend unterschätzt wird.

1

Introduction

General introduction Quantum mechanics forms the basis for many areas of modern physics. The theory of quantum mechanics comprises a description of matter and light in every detail. In particular, the behavior of processes on the atomic scale is accurately described with remarkable reliability. On the very small scale of atoms, things usually don't behave at all like something we've experience from our daily life. The quantum nature of atomic objects (electrons, protons, neutrons, photons, et cetera) is often associated with the term "wave particle". The reason for this (more or less accurate) term is that all of these objects have properties of both a particle, as we can detect single clicks on a detector, and a wave, as interference effects can be made visible by repeating experiments many times.

At the beginning of the 20th century, the results of a gradually increasing number of experiments on the atomic and small-scale, which already gave some clues as to how small things behave, led to increasing confusion in the largely classical-thinking physical society. Around 1926/27, Schrödinger, Heisenberg, and Born succeeded in formulating a consistent description of the behavior of matter on a small scale, which largely resolved the confusion. The theory forms the basis of quantum mechanics known today.[9]

One of the most important differences between the description of classical and quantum mechanics is that in classical mechanics we predict the outcome of a measurement based on the initial conditions (deterministically). Meanwhile, we give up determinism for quantum mechanics and are content with the fact that we can only predict the odds of a measurement result. When applying quantum theory, we recognize that we have to withdraw our ideal understanding of nature from the classic point of view, which sometimes can be difficult to accept. In this way, however, we can describe quantum mechanical phenomena that are impossible to understand by classic means. In quantum theory, the probability of the occurrence of an event results from the wavefunction that describes the quantum mechanical system.

In this regard, Rydberg atoms are intriguing objects that feature exaggerated properties and sizes, making them a perfect platform for studying quantum mechanical phenomena on a "classical scale". Sometimes the outcome of these studies can be very surprising, and in this case, it is often not clear at the beginning whether the observed phenomenon is of quantum mechanical or classical nature. These studies are the most exciting ones since we can extend our knowledge of nature by testing the boundaries between the classical and the quantum world.

This thesis reports on studies of positive and negative ions based on Rydberg spectroscopy. The experiments are carried out in an ultracold gas of rubidium-87 atoms. In the cold and ultracold regime, the motion of atoms is usually frozen out on the time and length scale (micrometer per microsecond) of typical Rydberg experiments.

In recent years, ultracold Rydberg atoms have proven to be a versatile platform for quantum simulation of long-range interacting many-body systems [10–12], for nonclassical photonic state generation [13, 14], and for quantum information processing [15–17]. A central aspect for many proposals in these fields is the phenomenon of the Rydberg blockade [18–20]. The blockade phenomenon originates from strong interactions between Rydberg atoms, which lead to the suppression of simultaneous excitation of two or more atoms into Rydberg states within a certain blockade volume. The Rydberg-Rydberg blockade in a cold and dense atomic ensemble was first observed experimentally in 2004 (ref. [21, 22]) and has been demonstrated for two individual atoms in 2009 by Urban *et al.* [23].

A similar concept applies to hybrid systems of ions and Rydberg atoms. In this case, strong interactions between a single ion and Rydberg atoms lead to charge-induced blockade phenomena mediated over macroscopic distances. The ion-induced Rydberg blockade has been proposed as a useful tool for quantum information transfer between ionic and atomic quantum systems [24]. However, experimental observation of the blockade mechanism has so far remained elusive. The reason for this is that in traditional hybrid settings, the ion-trap induced lineshift on the Rydberg states complicates the observation of interaction effects [25]. Recently, first indications of ion-induced lineshifts have been reported in a study of charge transfer in a hybrid setting [26]. Besides that, ion-Rydberg atom interactions have been explored in atom-beam experiments [27] and more recently have been demonstrated to influence quantum optics applications based on room temperature vapors [28].

In the context of this thesis, an alternative approach to the realization of an ion-Rydberg atom hybrid system is elaborated. A single ion is generated in an ultracold gas of rubidium-87 atoms. The ion is probed by exciting the valence electron of a single atom from the gas into the Rydberg state. High spatial control over the ion and the Rydberg excitation is achieved by a tightly focused photoionization and excitation laser. The ion-Rydberg atom interaction is examined by means of an ion-induced Rydberg excitation blockade and the blockade mechanism is employed to utilize a single ion as a sensitive probe for small electric fields. The outcome of these studies is published in ref. [S1]. In addition, experiments of a single ion placed in a Bose-Einstein condensate are presented and blockade measurements of the single ion in the condensate are carried out.

Studies of Rydberg atoms interacting with neutral atoms go back to the late 19th century. In 1879 Liveing and Dewar categorized the spectral line shape of sodium into sharp and diffuse lines [29]. Today we know that the lines associated with d-states in sodium are the diffuse ones as they are more likely to suffer from pressure broadening [27], meaning that the interaction with the surrounding atoms leads to a broadened emission line. In 1934 Amaldi and Segré (ref. [30]) reported on interaction induced line shifts and broadening of the Rydberg series of sodium for principal quantum numbers around $n = 30$ due to high background buffer gas pressure. They expected that the buffer gas would destroy the Rydberg series since the Rydberg atom must contain 10,000 molecules of the background gas for the experimental conditions. Within the same year, Enrico Fermi introduced the nowadays well-known Fermi pseudopotential [31] for Rydberg electron-atom scattering to explain these findings, paving the way for evermore fascinating perspectives of Rydberg-neutral atom interactions; ranging from a single or few atoms interacting with the Rydberg atom [S2, S5, 32–45] to many atoms within the Rydberg electron orbit [S4, S6–S8, 38, 46, 47]. This is just an incomplete list of experiments dedicated to the study of Rydberg-neutral atom interactions.

In this thesis, ultralong-range Rydberg molecules are utilized to study negative-ion resonances in the rubidium-anion. Ultralong-range Rydberg molecules (ULRMs) can form when one or several neutral atoms reside within the Rydberg electron wavefunction. The neutral atoms are bound within the electron orbit by attractive electron-atom scattering interactions, forming locally a negative ion compound.

The resulting molecular bound states are highly sensitive to the scattering interactions and therefore allow detailed insight into the underlying near-threshold anion states. For this purpose, ULRM-spectroscopy is elevated to a so-far unequaled quantitative level of precision, in a combined experimental and theoretical effort, devising ultralong-range Rydberg molecules as an ultrasensitive tool for studying the quasi-bound negative-ion resonances of the rubidium-anion. The outcome of these studies has been published in [S2].

In the last part of this thesis, the outcome of an experimental study of a local atom loss in the Bose-Einstein condensate induced by a single Rydberg atom is presented. The first experiments were originally intended to optically image the electron wavefunction of a Rydberg atom. For the wavefunction imaging method, the Rydberg atom is immersed in a Bose-Einstein condensate. The electron-atom interaction leads to a phase imprint on the condensate wavefunction which is to first order proportional to the absolute square of the electron wavefunction. Due to the gradient of the imparted phase, the condensate atoms flow towards regions of high electron density. The atomic flow continues even when the Rydberg atom is no longer present. Contrary to the expected density increase, due to the attractive electron-atom interaction, a local decrease of the condensate density is experimentally observed in the region of the Rydberg excitation.

2

Theory and background

This thesis studies interactions of Rydberg atoms with neutral atoms and with single ions. While for the studies of Rydberg atom-neutral interaction the case of one, few or even many atoms interacting with a single Rydberg electron is investigated, for the ion-Rydberg atom system mostly binary interaction is studied. The purpose of this chapter is to introduce here relevant experimental work and to build a theoretical foundation for the studies following in the main part of the thesis.

2.1 Rydberg atoms

Rydberg atoms are atoms with at least one valence electron in a highly excited electronic state. In comparison to atoms in the electronic ground-state, they show exaggerated properties such as huge size and very large polarizability. A fundamental and detailed description of Rydberg atoms and their properties can be found in numerous atomic physics textbooks like [27, 48–51].

In this section, we briefly discuss the most important properties of Rydberg alkali-metal atoms, such as the energy levels, the wavefunction, and the polarizability of the Rydberg state. To begin with, a historical introduction to Rydberg atoms is given and the Rydberg energy levels including the quantum defect for alkali-metal atoms are introduced. Following this, an overview of the here most relevant properties and their scaling laws are presented, and the electron wavefunction is introduced and discussed. In the last part of this section, we consider Rydberg atoms in external electric fields. In particular, we calculate the energy level shifts induced on the Rydberg states for a static electric field and introduce the interaction between Rydberg atoms and ions.

2.1.1 Rydberg energy levels and wavefunction

Energy levels of alkali Rydberg atoms. Rydberg atoms made their first historical appearance at the end of the 19th century. In 1885 Johann Jakob Balmer formulated a mathematical expression to describe the measured absorption spectra of the converging line series in hydrogen, which later became known as the Balmer series [52]. After, Johannes Rydberg generalized the formula found by Balmer to all levels of alkali-metal atoms in terms of wavenumbers of the line series observed.

$$\nu_\ell = \nu_{\infty\ell} - \frac{R_\infty}{(n-\delta_\ell)^2} \tag{2.1}$$

Here $\nu_{\infty\ell}$ denotes the limit of each line series and δ_ℓ the quantum defect for alkali-metal atoms, while n corresponds to the principal quantum number. ℓ is historically termed with s, p and d describing the line series as sharp, principal and diffuse respectively. The introduced constant R_∞, nowadays known as the Rydberg constant, can be used to describe not only the wavenumbers for transitions of different series, but also transitions of different atoms.[27]

It was with the phenomenologically motivated model for hydrogen by Niels Bohr in 1913 that the principal quantum number n and the angular momentum ℓ were given a physical meaning [53]. Bohr considered the electron on circular orbits moving around the core, with a circle length of n-multiple of the de-Broglie wavelength $n\lambda_\mathrm{D} = 2\pi r$, leading to a constant angular momentum L of the electron. Further, he assumed the electron being held on stable orbits in the electrostatic field of the core, that means the Coulomb force acting on the electron is equal to the centripetal force holding the electron captured. Assuming this and using the de-Broglie wavelength $\lambda_\mathrm{D} = h/p$, the electron orbit radius immediately ensues as:

$$r_n = \frac{n^2}{Z}\frac{4\pi\epsilon_0\hbar^2}{m_\mathrm{e}e^2}, \tag{2.2}$$

with the electron mass m_e, the elementary charge e, the core charge Z ($Z = 1$ for hydrogen), the dielectric constant ϵ_0 and $\hbar$ being the Planck constant h divided by 2π. From this, Bohr derived the electron energy levels in hydrogen.

$$E_n = -R_y\frac{Z^2}{n^2} \tag{2.3}$$

Here n is the principal quantum number and R_y is the Rydberg energy, which is related with the Rydberg constant via $R_y = hcR_\infty$. From equation 2.2 and 2.3 we find that the binding energies of the electron are discrete ($n = 1, 2, 3, \dots$) and decrease with n^{-2} as the energy levels converge to the ionization threshold, while the size of the atom rapidly increases with n^2. Consequently, these highly excited atoms can reach for atomic scales abnormal sizes but on the downside are much more loosely bound by the ionic core.

With this, the Bohr-model gives an intuitive n-scaling not only for the binding energy ($\sim n^{-2}$) but also for the Rydberg electron orbit size ($\sim n^{2}$) and additionally connects the Rydberg constant (cf. equation 2.1) with fundamental constants.

$$R_y = \frac{m_\mathrm{e} e^4}{8\epsilon_0^2 h^2} \approx 13.6\,\mathrm{eV} \tag{2.4}$$

Note that in (Hartree) atomic units the hartree energy E_h is twice the Rydberg energy, and thus in atomic units equation 2.3 with $Z = 1$ reads: $E_n = -\frac{1}{2n^2}$.

In 1916, the electron-shell model of Bohr was extended by Sommerfeld [54], who introduced two additional quantum numbers ℓ and m_ℓ. He proposed to lift the restriction of electrons moving in circles to allow elliptical electron orbits. For this, he considered the electron motion in spherical coordinates and derived a quantized quantity for each degree-of-freedom, which led to the azimuthal (or orbital) quantum number ℓ (with $\ell = 0, 1, 2, \ldots n-1$), describing the angular momentum of the electron, and the magnetic quantum number m_ℓ (with $m_\ell = -\ell, -(\ell-1), \ldots (\ell-1), \ell$) defining the orientation of the angular momentum in space. With that, he found that the electrons with the same n but different ℓ and m_ℓ have the same binding energy. The electron energy levels of the same principal quantum number are degenerate.

In 1922 Otto Stern and Walther Gerlach proved experimentally the existence of the spatial quantization by sending a beam of silver atoms through a strong gradient magnetic field, which deflected the atom beam before hitting the detector screen. The outcome was rather surprising since with previous experiments suggesting an angular momentum of $\ell = 1$, and based on the Bohr-Sommerfeld model, Stern and Gerlach expected a splitting into $2\ell + 1 = 3$ lines. However, in the experiment they clearly observed two lines. The middle line of straight flying atoms was missing. The reason for this is that in silver atoms only the $5s$ electron contributes to the total magnetic moment of the atom and thus only the line for $m_\ell = 0$ appears which, however, is split into two lines due to the non-zero magnetic moment of the electron spin. The findings of Stern and Gerlach already indicated the presence of a half-integer angular momentum of the electron. It was later with the introduction of the electron spin S and the corresponding magnetic quantum number m_S that the experiment was correctly interpreted.

The spin of an electron $\vec{S}$ is connected with a magnetic moment $\vec{\mu}_S$ and couples with the orbital angular momentum $\vec{L}$. The total angular momentum $\vec{J} = \vec{L} + \vec{S}$ best describes the resulting coupled system, where the total angular momentum quantum number J can take integer or half-integer values between $|L - S|$ and $|L + S|$. The spin-orbit coupling lifts the degeneracy in each n-manifold for energy levels assigned with a different quantum number J.

Semi-classically, the spin-orbit coupling can be understood by considering the ionic core from the resting frame of the electron. In this frame, the ion moves around the electron inducing a magnetic field $\vec{B}_L$, which interacts with the electrons magnetic moment $\vec{\mu}_S$. The resulting spin-orbit interaction is given as:

$$H_{LS} = -\vec{B}_L \cdot \vec{\mu}_S = \frac{a}{\hbar^2} \vec{L} \cdot \vec{S}, \tag{2.5}$$

with the coupling constant a. Introducing the electron spin and the spin-orbit coupling was an important step towards the explanation of the spectroscopically measured fine structure.

In a similar fashion one can treat the coupling between the nuclear spin $\vec{I}$ and the total electron angular momentum $\vec{J}$, which leads to a new total angular momentum $\vec{F} = \vec{I} + \vec{J}$. Again, the corresponding quantum number F can take integer of half-integer values of $|J - I| < F < |J + I|$. In first order the energy shift of the electron levels is given by:

$$\Delta E_{\mathrm{HFS}} = A_{\mathrm{HFS}} \, \vec{I} \cdot \vec{J} = \frac{A_{\mathrm{HFS}}}{2} \left[F(F+1) - I(I+1) - J(J+1) \right], \tag{2.6}$$

with the hyperfine structure constant A_{HFS} [55]. Note that the coupling constant decreases rapidly with increasing n, as the electron overlap with the nucleus quickly abates. Generally, the IJ-coupling is neglected for highly excited electronic states and thus a Rydberg state is usually described by the four quantum numbers n, L, J and m_J, including the LS-coupling.

In contrast to hydrogen, alkali-metal atoms have several inner-bound electrons, which shield the charged nucleus. Considering Rydberg states with large angular momentum such as circular Bohr orbitals, the electron never comes close to the shielded atom core and, like in hydrogen, interacts with a point-like singly charged core. For low-angular momentum states, however, the electron orbitals are highly elliptical, and as a result can penetrate and polarize the screened core. In this case, the polarizability of the cloud of inner-bound electrons leads to a depression of the energies below the hydrogen levels. Additionally, when close to the core, the electron is exposed to the now unshielded charges Z of the nucleus and consequently is more tightly bound (see also equation 2.3), resulting in an increased binding energy.[27, 56]

In total, the energy levels of alkali-metal atoms for high-L states are degenerate, like in hydrogen, while for low L the energy levels are depressed. Their energy levels E_{nLJ} are given by:

$$E_{nLJ} = -R_y \frac{Z^2}{(n - \delta_{nLJ})^2}, \tag{2.7}$$

with the quantum defect δ_{nLJ}, which additionally includes the spin-orbit coupling [56]. Note that the quantum defect was already empirically included in the Rydberg formula introduced by Johannes Rydberg (cf. equation 2.1). The quantum defects are accurately described by the empiric Rydberg-Ritz formula.

$$\delta_{nLJ} = \delta_0 + \frac{\delta_2}{(n - \delta_0)^2} + \frac{\delta_4}{(n - \delta_0)^4} + \frac{\delta_6}{(n - \delta_0)^6} + \cdots \tag{2.8}$$

Throughout this thesis, the Rydberg-Ritz formula is employed to estimate the quantum defect up to the second term (δ_2). The corresponding Rydberg-Ritz

State	n_0	δ_0	δ_2
$S_{1/2}$	13	3.131 180 7(8)	0.1787(2)
$P_{1/2}$	20	2.654 884 9(10)	0.2900(6)
$P_{3/2}$	20	2.641 673 7(10)	0.2950(7)
$D_{3/2}$	11	1.348 094 8(11)	−0.6054(4)
$D_{5/2}$	11	1.346 462 2(11)	−0.5940(4)
$F_{5/2}$	9	0.016 519 2(9)	−0.085(9)
$F_{7/2}$	9	0.016 543 7(7)	−0.086(7)

Table 2.1: Rubidium Rydberg-Ritz parameters up to the second term (δ_2), taken from [57–59]. n_0 denotes the lowest principal quantum number for which the energy levels are calculated using the Rydberg-Ritz parameters.

parameters δ_0 and δ_2 for rubidium are listed in table 2.1 and can be found in [57–59]. Here, n_0 denotes the lowest principal quantum number for which the energy levels are calculated using equation 2.7 and 2.8.

For high angular momentum states (typically $L > 3$) the quantum defect becomes negligible and the hydrogen solution can be used. In this case, the energy levels are determined from the Dirac theory [48, 51]. A sufficiently accurate result can be achieved by expanding the resulting energies in powers of (Za) [48] (with a being the fine-structure constant and Z the core charge) and by further, including the core polarization by adding the energy shift caused by the static dipole core polarizability α_c [27, 56]. With this, the resulting energy levels of the high angular momentum states up to the second-order in (Za) are given by:

$$E_{nLJ} \simeq -R_y \frac{Z^2}{n^2}\left[1 - \frac{(Za)^2}{n^2}\left(\frac{3}{4} - \frac{n}{J+1/2}\right)\right] - \frac{3\alpha_c}{4n^3L^5}. \tag{2.9}$$

The leading term recovers the Bohr-like Rydberg energy levels, while the following term gives the first relativistic correction proportional to $(Za)^2$ [51].

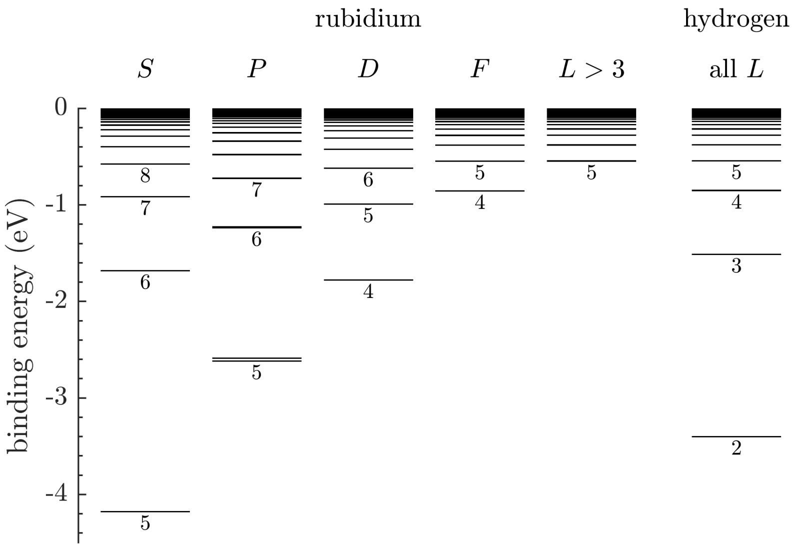

Fig. 2.1: Energy level diagram for rubidium and hydrogen. Numbers below the levels indicate the principal quantum number n. The values are obtained from equation 2.3 or 2.7 and 2.9 or taken from [55, 59–61]

Figure 2.1 illustrates the calculated energy levels of rubidium and hydrogen. For rubidium, the binding energies are either obtained from equation 2.7 and 2.9 for low and high ($L > 3$) angular momentum, using the reduced Rydberg constant R_y for rubidium [58, 59] and the in table 2.1 listed quantum defects, or taken from [55, 57–61]. For hydrogen, the Bohr-like energy levels are calculated from equation 2.3. In comparison, the quantum defect shifted energy levels ($L \leq 3$) of rubidium converge towards the hydrogen energies with increasing angular momentum L. For $L > 3$ the energy difference to the hydrogen-like states becomes imperceptibly small. Note that the fine structure splitting in rubidium is much smaller than the energy range plotted in figure 2.1 and thus is hardly visible.

Property	n-scaling	Rb($5S_{1/2}$)	$nS_{1/2}$ for $n = 30 \dots 130$
Binding energy	$(n^\star)^{-2}$	4.18 eV	18.8 … 0.8 meV
Energy spacing of adjacent n states	$(n^\star)^{-3}$	604 THz	321 … 3 GHz
Classical ionization field	$(n^\star)^{-4}$	30 MV/cm	616 … 1.2 V/cm
Orbital radius	$(n^\star)^{2}$	2.98 Å	76 nm … 1.7 µm
Radiative lifetime	$(n^\star)^{3}$	26.2 ns	13 µs … 1 ms
Polarizability	n^7	$-79.6\,\frac{\text{mHz}}{(\text{V/cm})^2}$	$-1.4 \dots -4 \times 10^4\,\frac{\text{MHz}}{(\text{V/cm})^2}$

Table 2.2: Scaling laws of selected properties for rubidium atoms in the $nS_{1/2}$ Rydberg state taken from [27, 62, 63]. The corresponding values for the range of principal quantum numbers ($n = 30 - 130$) investigated in this work are shown in the fourth column.

Scaling with the principal quantum number n. Despite its shortcomings, the Bohr-model contains many properties of Rydberg atoms and offers quick access to the scaling with the principal quantum number for many characteristic parameters. Some of the most useful scaling laws for Rydberg atoms are listed in table 2.2. For many properties it is practical to introduce an effective principal quantum number $n^\star$, which includes the quantum defect δ_{nLJ}. Motivated by equation 2.7 one finds $n^\star = n - \delta_{nLJ}$. The depict properties show in several ways that Rydberg atoms differ fundamentally from atoms in their ground state.[27] For example, the ground-state electron is more than 200 times deeper bound than the electron in the $30S$ state, while the size of the Rydberg atom is over 200 times larger. Because of its size, the Rydberg electron is more loosely bound and consequently easier to ionize. While for $n = 30$ an ionization voltage of about 600 V/cm is required, for $n = 130$ a few V/cm are sufficient to ionize the Rydberg electron. With increasing size of the Rydberg atom, the electron cloud becomes much easier to polarize, leading to relatively large energy shifts in external electric fields for the spherical symmetric nS Rydberg state. While many of the properties can be deduced from the semi-classical perspective of Bohr, for some, the quantum mechanical treatment of the Rydberg electron is essential.

Rydberg electron wavefunction of alkali-metal atoms. Next, to describe Rydberg atoms quantitatively we need to introduce the electron wavefunction. In the framework of quantum mechanics, the electron wavefunction allows for calculations of many properties, in particular, dipole moments and transition matrix elements, energy shifts in external electric fields and many more.

To introduce the wavefunction for alkali-metal atoms, it is educative to start with the hydrogen atom and bring in corrections later, accounting for the non-hydrogenic atom core and the spin-orbit coupling. For the treatment of the hydrogen wavefunction, we follow the standard introduction in the literature as it can be found in many textbooks, for example in [48–50].

First, let us start with the well-known stationary Schrödinger equation. The Hamilton operator H consists of a kinetic H_{kin} and potential term H_{pot}. With the spherical symmetric Coulomb potential of the hydrogen core acting on the electron, we get the following expression (equation 2.10).

$$\begin{aligned} H\Psi(\vec{r}) &= \left(H_{\text{kin}} + H_{\text{pot}}\right)\Psi(\vec{r}) \\ &= \left(-\frac{\hbar^2}{2\mu}\nabla^2 - \frac{Zq^2}{r}\right)\Psi(\vec{r}) = E\Psi(\vec{r}) \end{aligned} \tag{2.10}$$

Here, E is the eigenenergy for the relative motion of the electron and the nucleus, $-e$ and $+eZ$ are the electron charge and the core charge respectively, where we used $q^2 = e^2/(4\pi\epsilon_0)$ and the reduced mass $\mu = m_e M/(m_e + M)$ with the electron mass m_e and the nuclear mass M.

For the spherical symmetric Coulomb potential, it is advisable to use spherical coordinates. In these, the second derivative ∇^2 reads:

$$\nabla^2 = \frac{1}{r^2}\frac{\partial}{\partial r}\left(r^2\frac{\partial}{\partial r}\right) - \frac{1}{\hbar^2 r^2}L^2(\theta,\phi),$$

where we introduced the angular momentum operator $\vec{L}$. Inserting this in equation 2.10 one finds that L^2 acts only on the angular part (θ,ϕ) but not on the radial part (r) of the eigenfunctions and consequently, $\Psi(r,\theta,\phi)$ also have to be an eigenfunction to L^2 (and also L_z for completeness). This can also be seen by the fact that H, L^2 and L_z all commute. With this, the variables in equation 2.10 separate with $\Psi(r,\theta,\phi) = \mathcal{R}(r)Y_{lm}(\theta,\phi)$. Here, $Y_{lm}(\theta,\phi)$ are the well-known Laplace's spherical harmonics which are the eigenfunctions of L_z and L^2.

$$\begin{aligned} L_z Y_{lm}(\theta,\phi) &= m\hbar Y_{lm}(\theta,\phi) \\ L^2 Y_{lm}(\theta,\phi) &= \hbar^2 l(l+1) Y_{lm}(\theta,\phi) \end{aligned}$$

With this, the stationary Schrödinger equation for the radial part $\mathcal{R}(r)$ of the wavefunction is given by:

$$-\frac{\hbar^2}{2\mu}\frac{1}{r^2}\frac{d}{dr}\left(r^2\frac{d}{dr}\right)\mathcal{R}(r) + \left[-\frac{Zq^2}{r} + \frac{\hbar^2}{2\mu}\frac{l(l+1)}{r^2}\right]\mathcal{R}(r) = E\mathcal{R}(r), \qquad (2.11)$$

where the first term corresponds to a radial kinetic energy and the second to the radial potential, consisting of the Coulomb potential and a centrifugal term. For the hydrogen atom, we recover the Bohr-like energy levels $E = -R_y\frac{Z^2}{n^2}$, neglecting the prior discussed spin-orbit coupling, and an analytic solution for the eigenfunctions $\mathcal{R}_{n,l}(r)$ for the quantum numbers n and l, proportional to the generalized Laguerre polynomial $L_{n-l-1}^{(2l+1)}$ [50].

For alkali-metal atoms, the same reasoning from above applies with the exception that one has to adept the outlined method for taking into account the inner electrons of the alkali core. Essentially, for electron wavefunctions penetrating the core, a modified potential acts on the electron. It turns out that it is sufficient to adept the radial Schrödinger equation 2.11 by replacing the Coulomb potential with the modified potential V_{mod}, while the angular wavefunction is still described by the spherical harmonics [64].

$$V_{\text{mod}}(r) = -\frac{q^2 Z_{\text{eff}}(r)}{r} + V_{\text{pol}}(r) + V_{\text{so}}(r) \tag{2.12}$$

The first term equals the Coulomb potential with an effective charge Z_{eff} taking into account the enhanced Coulomb interaction for small electron-core distances, in particular, when the valence electron penetrates the cloud of inner-bound electrons. An expression for the effective charge is given in [64]:

$$Z_{\text{eff}}(r) = 1 + (Z-1)e^{-a_1 r} - r(a_3 + a_4 r)e^{-a_2 r}, \tag{2.13}$$

where the model parameters a_1, a_2, a_3 and a_4 depend on the angular momentum of the valence electron. The second term in equation 2.12 represents the core polarization, which originates from the inner electrons polarizability. The core polarization potential can be approximated by:

$$V_{\text{pol}} = -\frac{\alpha_c}{2r^4}\left(1 - e^{(r/r_c)^6}\right), \tag{2.14}$$

where α_c is the static dipole polarizability of the positively charged ion core and r_c is a short range cut-off parameter.[64] With the last term we also include the potential resulting from spin-orbit coupling (taken from [51]) in the modified potential V_{mod}.

$$V_{\text{so}}(r) = \frac{Zq^2}{2m_e^2c^2}\frac{\hbar^2}{2r^3}\big[j(j+1) - l(l+1) - s(s+1)\big] \tag{2.15}$$

Here, for the spin-orbit coupling we neglect the energy shifts due to core penetration, assuming a point-like charge $Z = 1$. Note that only for the hydrogen atom an exact solution for the radial Schrödinger equation exists. For alkali-metal atoms

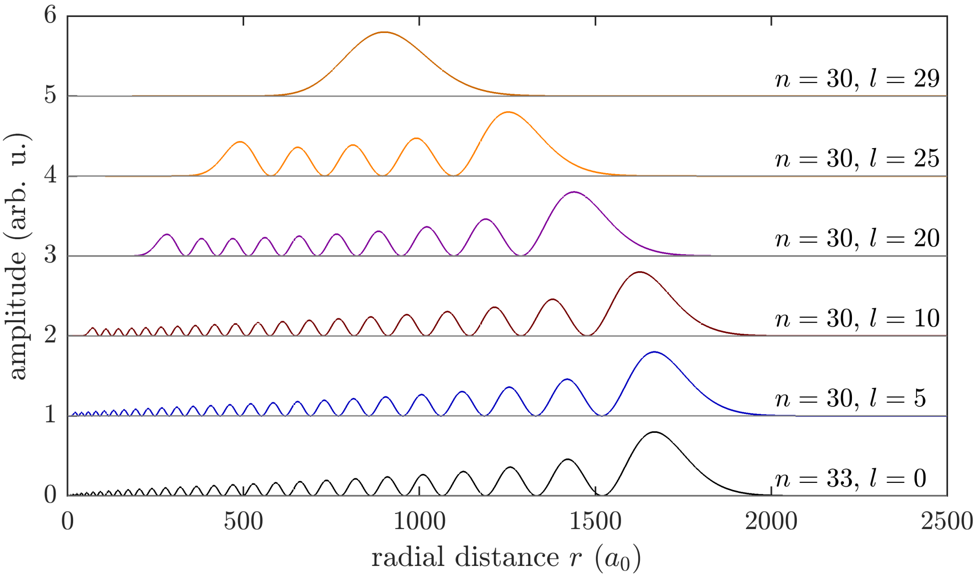

Fig. 2.2: Calculated radial Rydberg wavefunction for different angular momentum l in rubidium. The amplitude $\sim |\Psi|^2 r^2$ is plotted over the radial distance r. For better visibility the curves are each offset by 1. For comparison, in the case of $l = 0$, the wavefunction is shown for a principal quantum number of $n = 33$ instead of $n = 30$.

one has to fall back on numerical approximation methods. One of the methods for solving the radial Schrödinger equation for alkali-metal atoms is the Numerov method [27].

Exemplary, in figure 2.2 the calculated radial Rydberg wavefunction for rubidium-87 is shown for different angular momentum l and $n = 30$ ($n = 33$ for $l = 0$). From the figure above, we can deduce that for decreasing l the number of nodes increases by one. Consequently, the maximum number of nodes of the wavefunction is given by $n - 1 - l$, like in hydrogen. Further, with increasing angular momentum, the outermost lobe shifts to a smaller radial distance r, as, classically, the electron orbit transitions from a highly elliptical to a circular trajectory. For the maximum $l = n - 1$ only one lobe of the radial wavefunction remains, which position naturally coincides with the Rydberg atom size predicted by Bohr. In contrast, for $l = 0$

the outermost lobe is equal to twice the radius of the circular orbits given by the Bohr-model. Classically speaking, in this case, the electron moves back and forth in the core potential on an infinitesimal thin ellipse, where the outermost turning point of the electron is approximately equal to the position of the last lobe of the electron wavefunction. More precisely, since the kinetic energy of the wavefunction is given by the derivative (cf. equation 2.10) the classical outermost turning point coincides with the outermost inflection point of the wavefunction.

The fact that the low angular momentum states are lowered energetically due to the quantum defect is reflected in the electron wavefunction by the fact that the outermost turning point is shifted towards smaller distances. This can be seen in particular when comparing the blue and the black curve in figure 2.2, for which the outermost lobe almost coincides. The black curve corresponds to the wavefunction for the low angular momentum S-state, while the blue curve represents the wavefunction for higher l, for which the quantum defect is negligible. Next, let us recall that the quantum defect for the nS Rydberg state in rubidium is $\delta_0 = 3.13\ldots \simeq 3$. Now, it comes naturally that the outermost turning point of the electron coincides for the two wavefunctions, as the difference in the principal quantum number of both is equal to three.

2.1.2 Rydberg atoms in external electric fields

In this section, we discuss the influence of external electric fields on Rydberg atoms. In contrast to ground state atoms, where the valence electron is deeply bound, Rydberg atoms exhibit an enormous sensitivity to electric fields increasing with principal quantum number n.

In the following, first we introduce the interaction Hamilton and calculate the electric field induced energy shift on Rydberg states. Following this, we briefly discuss the situation of a Rydberg atom in the Coulomb field of an ion.

The unperturbed Hamilton H_0 for an atom is given by equation 2.10. For an atom placed in a static electric field we can define an interaction Hamilton $H_{\mathcal{E}}$.

$$H_{\mathcal{E}} = -e\vec{\mathcal{E}} \cdot \vec{x} = -\vec{d} \cdot \vec{\mathcal{E}} \tag{2.16}$$

Here, $\vec{d}$ is the dipole operator and $\vec{\mathcal{E}}$ the external electric field, with the field strength $\mathcal{E}$. The order of magnitude of electric fields in atoms is given by $E_{\mathrm{H}}/ea_0 \simeq 10 \times 10^{10}\,\mathrm{V/m}$, with the electron charge e and the typical atomic length scale a_0 (Bohr radius) and energy scale E_{H} (hartree energy). For that reason, in the case of ground-state atoms, the external electric field can be treated as a small perturbation to the Hamilton H_0 for the field strengths typically achievable in atomic physics laboratories [50]. However, for highly excited Rydberg atoms this is not necessarily the case. In practice, one usually needs to use a full diagonalization method with a truncated basis set to solve for the eigenenergies and the eigenstates of the total Hamilton operator $H = H_0 + H_{\mathcal{E}}$ [65].

For the hydrogen atom one can use parabolic coordinates to solve the problem analytically. In this case, the Hamiltonian H is diagonal for the so-called parabolic states, for which n, m, and the parabolic quantum numbers n_1 and n_2 are good quantum numbers. To the first order, the energy levels shift linearly with the applied electric field $\mathcal{E}$, while the energy shift itself is proportional to the quantum numbers n and k, where k is associated with n_1 and n_2 via $k = n_1 - n_2$. Note that n_1 and n_2 are related to n and $|m|$ via $n = n_1 + n_2 + |m| + 1$.

$$E = -R_y\frac{1}{n^2} + \frac{3ea_0}{2}\mathcal{E}kn \tag{2.17}$$

In contrast, for alkali-metal atoms, states with the same quantum number m and different n can interact, as the electron wavefunction penetrates the non-hydrogenic ionic core. As a result, the Hamiltonian does not diagonalize in the parabolic

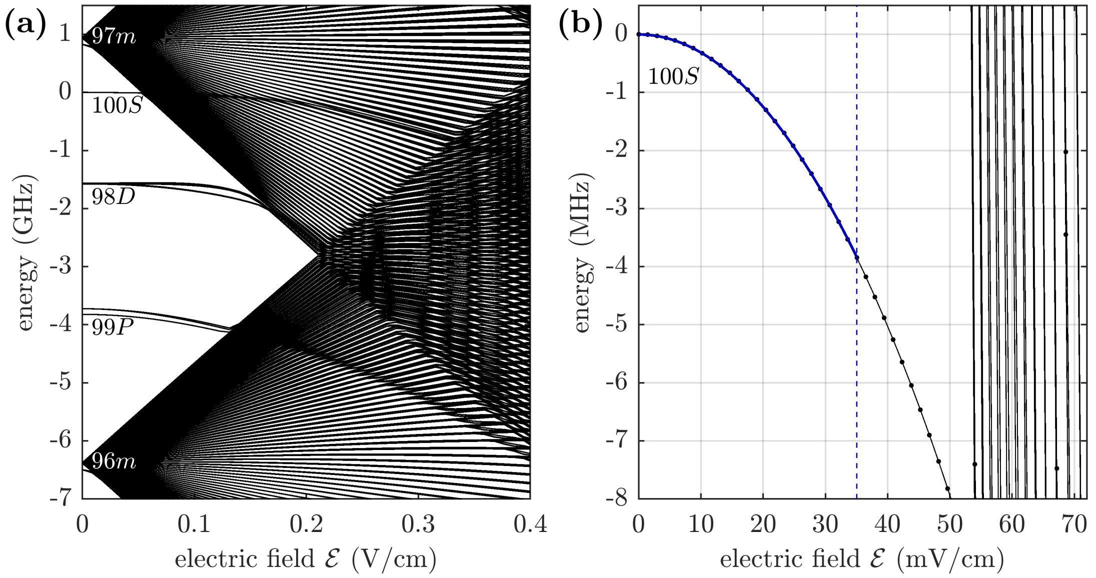

Fig. 2.3: Calculated energy shifts for different static electric fields $\mathcal{E}$. (a) shows an overview of the energy levels in the vicinity of the 100S Rydberg state. (b) depicts the quadratic energy shift of the 100S state. Blue solid line represents a quadratic fit up to a maximum field indicated by a vertical dashed line. For zero electric field, the states are labeled via the principal quantum number n and the angular momentum S P and D for low l. For high l the states are degenerate at a zero electric field and collectively assigned as hydrogenic manifold m of the corresponding n.

basis [65]. Therefore, instead of the parabolic basis, one usually uses the spherical representation $|n, l, m\rangle$ to calculate the energy shifts.

Now, armed with the electron wavefunctions which we introduced in the previous section 2.1.1, we are able to calculate the energy level coupling $\left\langle\vec{d}\cdot\vec{\mathcal{E}}\right\rangle_\psi$ and the resulting energy level shift (Stark shift).

$$\left\langle\vec{d}\cdot\vec{\mathcal{E}}\right\rangle_\psi = \left\langle\psi_{nLJm_J}\middle|\vec{d}\cdot\vec{\mathcal{E}}\middle|\psi_{n'L'J'm'_J}\right\rangle \tag{2.18}$$

In figure 2.3 the resulting energies in the vicinity of the 100S Rydberg state are presented for different static electric fields $\mathcal{E}$. On the left, the energy levels between the $n = 97$ and $n = 96$ manifolds are shown. The energy levels of the low angular momentum states ($l < 3$) are energetically lowered with respect to the corresponding n-manifold due to the quantum defect. For high angular momentum states, the energy level shifts linear like in hydrogen, up to the field where the hydrogenic manifolds of two different principal quantum numbers n cross. As mentioned earlier, in alkali-metal atoms states with the same quantum number m of different n can interact due to the quantum defect, and as a result, the corresponding energy levels reveal an avoided crossing which appears for an electric field of $\mathcal{E} \simeq 0.2\,\mathrm{V/cm}$ for the presented case. Note that in the literature the crossing point between two neighboring n-manifolds is usually referred to as the Inglis-Teller limit.

On the right in figure 2.3, the energy shift of the $100S$ Rydberg state is depicted for smaller electric fields. The quadratic behavior of the S-state arises from the polarizability of the electron wavefunction and can be understood as the interaction between an induced dipole moment and the external electric field.

In the case of small electric fields, when the energy spacing to neighboring states is large, one can treat the problem perturbatively. Explicitly, when applying perturbation theory to the energetically well-isolated low angular momentum states, one finds for the first non-vanishing term (in second-order) the following energy shift for the S-state:

$$\Delta E(\mathcal{E}) = -\frac{\alpha}{2}\mathcal{E}_z^2 \tag{2.19}$$

where α corresponds to the polarizability of the S-state and $\mathcal{E}$ is the electric field strength, which we assumed to be in the z-direction defining the quantization axis. Further, the perturbation theory yields an expression for the polarizability.

$$\alpha = -2e^2 \sum_{k \neq k'}^{\infty} \frac{|\langle k|z|k'\rangle|^2}{E_k - E_{k'}} \tag{2.20}$$

Here, k and k' are the collective indices for (n, L, J, m_J) and (n', L', J', m_J'), respectively. Note that, when evaluating the expression above for the Rydberg

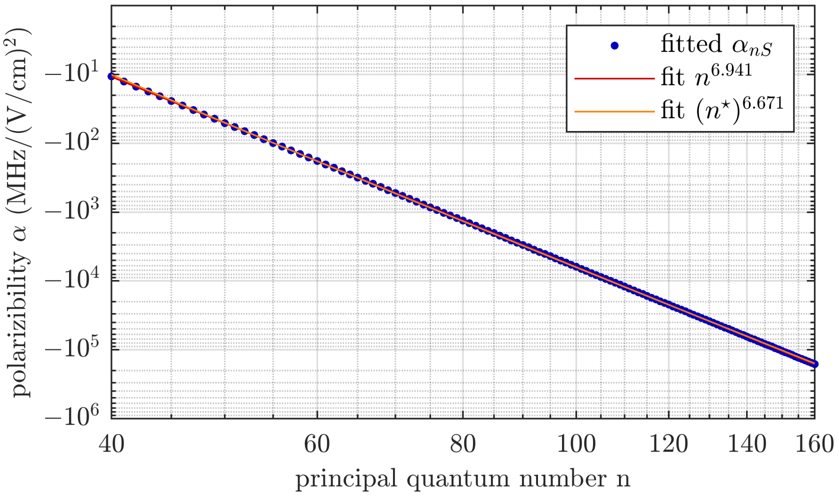

Fig. 2.4: Polarizability of the nS Rydberg state obtained from quadratic fits to the energy level shifts for asymptotic small electric fields. The data is fitted with a power law for the (effective) principal quantum number n $(n^{\star})$. n^x: $x = 6.941(2)$ $(n^{\star})^x$: $x = 6.671(8)$

electron wavefunction, one can derive the prior mentioned scaling with the principal quantum number of the polarizability. The spacing between the manifolds scales with n^{-3} and the dipole moment $\left\langle \psi_{nLJm_J} \middle| z \middle| \psi_{n'L'J'm'_J} \right\rangle$ with n^2, which in total yields the scaling n^7 for α_{nS} [27].

Regarding the polarizability of the nS Rydberg state used in this work (chapter 3), we do not simply rely on the n-scaling with the principal quantum number, but instead deduce α_{nS} from calculated energy shifts for the limit of small electric fields. As an example, figure 2.3b shows a fit (blue solid line) of the energies for the quadratically shifting $100S$ Rydberg state. The vertical (blue dashed) line indicates an electric field cutoff, for which the electric field is low enough that the $100S$ state is still well described by equation 2.19.

Figure 2.4 shows the determined S-state polarizability α_{nS} over a large range of principal quantum numbers n. The obtained α_{nS} are fitted via $\sim n^x$ and $\sim (n^{\star})^x$, where we find a quite significant deviation from the n^7 scaling when using the effective principal quantum number $n^\star$. To point this out let us exercise a small example. When applying the $(n^\star)^7$ scaling to determine the polarizability for a $100S$ state based on α_{nS} for $n = 40$ we get a ratio of $\left(\frac{n^\star(100)}{n^\star(40)}\right)^7 / \left(\frac{n^\star(100)}{n^\star(40)}\right)^{6.671} \simeq 1.34$ between the estimated and the actually fitted polarizability.

Finally, let us turn to the situation where the external electric field is given by the Coulomb potential of an ion near the Rydberg atom. Without loss of generality, any arbitrary electric field can be decomposed into multipole fields. In particular, for the Coulomb interaction one finds in second-order perturbation theory the adiabatic polarization potential:

$$V_{\mathrm{pol}}(R) = -e^2 \sum_{k=1}^{\infty} \frac{\alpha^{(k)}}{2R^{2k+2}}, \tag{2.21}$$

with the elementary charge e, the multipole polarizability $\alpha^{(k)}$ of order k and ion-Rydberg atom distance R.[66]

In the case of a S-state Rydberg atom interacting with a S-state ion, the multipole expansion can be approximated by:

$$V_{\mathrm{pol}}(R) \approx -\frac{C_4}{R^4} - \frac{C_6}{R^6} + \cdots \approx -\frac{C_4}{R^4}, \tag{2.22}$$

where we identify the C-coefficients with the polarizabilities $\alpha^{(k)}$. For sufficiently large ion-Rydberg atom distances, when the ion is far away from the Rydberg atom ($R \gg n^2 a_0$), the leading contribution to V_{pol} is usually contained by the long-range polarization potential $\sim 1/R^4$ [67].

At last, let us consider the physical meaning of the approximated polarization potential $V_{\mathrm{pol}}(R) = C_4/R^4$. The C_4-term in equation 2.22 can be interpreted as follows: The charge of the ion induces an electric dipole moment ($\vec{p} = \alpha_{nS}\vec{E}$) in the atom. The induced dipole moment in turn, interacts with the electric field of the ion $\vec{E}$. When considering the interaction energy $U_{\mathrm{ind}} = -\frac{1}{2}\alpha|\vec{E}|^2$ between the induced dipole moment $\vec{p}$ and the electric field $\vec{E}$, we get the following expression

$$-C_4/R^4 = -\frac{\alpha_{nS}}{2}\left|\vec{E}\left(\vec{R}\right)\right|^2 = -\frac{\alpha_{nS}}{2}\left(\frac{e}{4\pi\epsilon_0}\right)^2\frac{1}{R^4}, \tag{2.23}$$

from which we further identify the relation $\alpha_{nS} = 2(4\pi\epsilon_0)^2 C_4$.

2.2 Ultralong-range Rydberg molecules

Rydberg atoms exhibit a remarkably long-range interaction among each other. The strong interaction between the Rydberg states can lead to the formation of diatomic molecules which consist of two Rydberg atoms. The binding results from the interplay of long-range attractive and short-range repulsive forces induced by the Rydberg pair-state potential. This, in turn, results in deep potential wells, which can support a ladder of vibrational molecular states. Such exotic molecules are called Rydberg macrodimers as their bond-length reaches the micrometer scale. These types of Rydberg molecules were first predicted by Boisseau *et al.* [68] and observed for the first time by Overstreet *et al.* [69] via ion-recoil spectroscopy. More recently, macrodimers have been directly measured spectroscopically [70] in an optically trapped ensemble of atoms and in a quantum gas microscope experiment [71] in an optical lattice.

A second type of exotic molecules associated with highly excited Rydberg states are ultralong-range Rydberg molecules (ULRM). In contrast to macrodimers, these molecules form when a ground-state atom resides within the Rydberg electron orbital. Large interaction energies can arise from low-energy electron-atom scattering between the ground-state atom and the Rydberg electron, which potentially leads to molecular bound states for a negative electron-atom s-wave scattering length. In this case, the Rydberg electron binds the ground-state atom in a well-confined location, defined by potential minima associated with the oscillating radial Rydberg electron wavefunction. Typically, these types of molecules yield bond lengths of several thousand Bohr radii (set by the size of the electron orbit), as close to the classical turning point the electron probability is the largest and consequently the ground-state atom is attracted the most (for s-wave scattering) to the outermost well of the potential. ULRM were first predicted by Greene *et al.* [72] in 2000. In their publication, the authors classified two types of ULRMs, polar and non-polar molecules. For the non-polar molecules, the molecular bound states are associated with the quantum defect states of the Rydberg atom and the ground-state atom is bound at a distance close to the classical outermost turning point of the Rydberg electron. In contrast, the polar ULRM (also called trilobite molecule) are associated with the hydrogen-like degenerate manifolds. In these molecules, the ground-state atom is bound in a comparatively deep potential well formed from a mixture of high angular momentum states (with opposite parity [72, 73]) detaching from the hydrogenic manifold.

Shortly after, Hamilton *et al.* [74] predicted yet another type of polar ULRMs (also called butterfly molecules), which arise from the presence of a p-wave shape resonance (e.g. found in all alkali-metal atoms) in electron-atom scattering. The first type of ULRMs (non-polar) were observed for the first time by Bendkowsky *et al.* [32] via two-color photo-association (S-state Rydberg molecule), which triggered intensive studies of ULRMs in various experimental realizations [S4–S7, 33–46]. The second type of ULRMs (polar) were observed by Booth *et al.* [40] (trilobite ULRM) in an ensemble of ultracold Cs atoms, while the p-wave dominated butterfly molecules were first realized by Niederprüm *et al.* [44] in Bose-Einstein condensate of ^{87}Rb atoms.

More recently, the interest in the field of ULRMs shifted from qualitative studies towards a more quantitative and detailed description of the molecular bound states. A renewed interest in including spin effects, in particular the hyperfine interaction in the ground-state atom and spin-orbit coupling effects between the

Rydberg atom and the ground-state atom, has been shown recently [75–77].

In this section, a brief overview of the description of ULRMs of the non-polar type is given with the aim to build a theoretical foundation for the presented work outlined in the main body (chapter 4) of this thesis. First, we discuss the Rydberg electron-neutral atom interaction in the context of electron-atom scattering. Importantly, we include the spin-orbit interaction between the scattering angular momentum and the total electron spin, leading to three p-wave scattering phase shifts, which differ due to the non-zero spin-orbit coupling. Second, exemplarily, the resulting scattering potentials are then used to calculate the Born-Oppenheimer potential energy curves and the molecular bound state of a ULRM dimer which is radially confined in the outermost well of the Rydberg electron.

2.2.1 Electron-neutral atom interaction in ULRM

In ultralong-range Rydberg molecules, the molecular bound states are supported by interaction energies originating from the Rydberg electron scattering off a neutral atom. In this case, the electron-atom interaction can be described by an effective potential V_L including the polarizability of the atom (see also equation 2.22) and a centrifugal term for the relative angular momentum of the scattering partners:

$$V_L(r) = -\frac{\alpha_{\mathrm{gs}}}{2r^4} + \frac{\hbar^2}{2\mu}\frac{L(L+1)}{r^2} \tag{2.24}$$

Here, α_{gs} is the polarizability of the ground-state atom, r the electron ground-state atom distance, μ the reduced mass, and L the scattering angular momentum. The short-range interactions are included via an inner hard-wall at a variable distance r_0. Due to the low kinetic energy of the Rydberg electron for large enough Rydberg core-electron distances (typically distances larger than a few hundred Bohr radii) only s- and p-wave scattering ($L = 0$ and $L = 1$) has to be taken into account [78]. Note that p-wave scattering has to be included due to the presence of a ^3P shape resonance for low-energy electron scattering with alkali-metal atoms [79, 80].

Additionally, one has to take into account relativistic electron-electron interactions between the (quasi)free Rydberg electron and the valence electron of the ground-state atom. Treating this to its full extent quickly reaches a high level of complexity. However, it turns out that in the case of alkali-metal atoms, relativistic effects can be neglected for low-energy scattering, except for the mutual spin-orbit coupling between the valence electron of the ground-state atom and the incident scattering electron [81].

In state-of-the-art calculations, the electron-atom system is described by a model potential of two active electrons in an effective core potential. The problem is then solved by applying relativistic R-matrix scattering theory [81–83]. These calculations are mainly performed in the context of heavy alkali-metal negative ions. In particular, *ab initio* phase shift calculations for the scattering of a low-energy electron off alkali-metal atoms (Rb, Cs, Fr) were carried out by Bahrim *et al.* [80, 84], revealing the presence of excited bound states for resonant electron-atom p-wave scattering. The exact treatment via relativistic R-matrix scattering theory is beyond the scope of this thesis but can be looked up in literature [85].

In the context of Rydberg atoms, a different approach has been employed by Khuskivadze *et al.* [78]. In their phase shift calculations, the electron-neutral atom interaction is modeled via a pseudopotential, which reproduces the phase shifts from Dirac R-matrix calculations and the resulting binding energies of the corresponding negative ion system.

In the context of this thesis (investigation of negative ion resonances in ULRM see [S2] and chapter 4), yet another more simple approach is used. In addition to the electron-atom interaction V_L (see equation 2.24), for p-wave scattering, we add the standard spin-orbit coupling term given by equation 2.25 and then use the inner hard-wall position r_0 to fine tune the outcome of the scattering calculations.

$$V_{LS}(r) = \frac{dV_L(r)/dr}{2m_e c^2 r} \left\langle \vec{L} \cdot \vec{S} \right\rangle = \frac{dV_L(r)/dr}{2m_e c^2 r} \frac{\hbar}{2} \left[J(J+1) - 4 \right]. \tag{2.25}$$

Here, m_e is the electron mass, c is the speed of light, $\vec{S}$ is the total spin ($S = 1$) of the valence electron and the Rydberg electron, $\vec{L}$ is the angular momentum ($L = 1$ for p-wave scattering) of the scattering partners, and J is the quantum number associated with the resulting total angular momentum $\vec{J} = \vec{L} + \vec{S}$ ($J \in \{0, 1, 2\}$).

With the interaction terms (equation 2.24 and 2.25) set up, solving the radial Schrödinger equation for a range of momenta k yields the (triplet) s- and p-wave scattering phase shifts $\delta_s^T(k)$ and $\delta_{p,J}^T(k)$, respectively. The corresponding scattering length (scattering volume) $a_{s/p,J}^T(k)$ are connected to the calculated phase shifts by:

$$a_s^T(k) = -\frac{\tan(\delta_s^T(k))}{k} \tag{2.26}$$

$$a_{p,J}^T(k) = -\frac{\tan(\delta_{p,J}^T(k))}{k^3}. \tag{2.27}$$

Note that the scattering parameter a_p is often referred to as a scattering volume since a_p has the dimension of a length cubed. Thus, in literature a_p is denoted regularly as a_p^3, which is not to be confused with the here introduced nomenclature of triplet scattering ($a_{s/p,J}^T$). Here, we will not bother with the exact distinction between scattering length and scattering volume as it is not of essential importance and out of convenience call both, a_s and a_p a scattering length or parameter.

In order to verify the model potential introduced above, the s- and p-wave phase shifts from [78, 79, 84] (for comparison see also appendix B.1) have been reproduced by adjusting the inner hard-wall position r_0 for each scattering channel [86]. Furthermore, it has been found that the functional k-dependence of the phase shifts is insensitive to the precise value of α_{gs}, i.e. for small variations of α_{gs} a slightly different hard-wall position can be found to reproduce the same shifts.

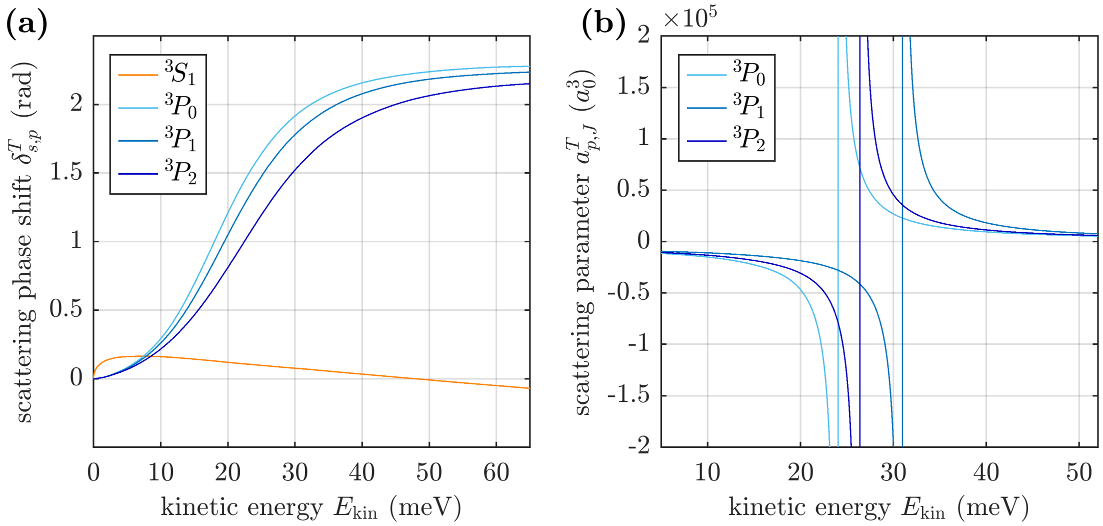

Fig. 2.5: k-dependent e^--Rb scattering phase shifts $\delta^T_{s/p,J}(k)$ and scattering lengths (volume) $a^T_{s/p,J}(k)$. In (a) the calculated triplet s- and p-wave scattering phase shifts [78, 84] are shown for different kinetic energies $E_{\mathrm{kin}} = \hbar^2 k^2/2m_e$. (b) shows the corresponding p-wave scattering parameter $\delta^T_{p,J}(k)$ obtained from the phase shifts in (a) via equation 2.27.

In figure 2.5, the calculated triplet phase shifts for e^--Rb scattering [78, 84] and the resulting scattering lengths are shown for kinetic energies in the meV regime. Let us first have a look at $a^T_{p,J}$. Mathematically, the scattering length diverges for a phase shift of $\delta = \pi/2$. However, an infinitely large scattering length is unphysical, and naturally, the scattering length is limited, e.g., due to uncertainties in the kinetic energy of the scattering event. Nonetheless, the divergence of the scattering length, as it is apparent for all three p-wave scattering channels, strongly indicates the presence of a scattering resonance. In fact, each p-wave channel (^3P_J, $J \in \{0, 1, 2\}$) exhibits a shape-resonance, which can be associated with the corresponding Rb$^-$ (^3P_J) negative ion resonance, where the resonance position can be defined as the inflection point of $\delta^T_{p,J}(k)$ [80]. Note that one can assign a resonance position E_r and a resonance width Γ_r to the characteristic form of the scattering length in figure 2.5(b) [85]. By doing so, $\tau = \hbar/\Gamma_r$ can be interpreted as the lifetime of a metastable state, with energy E_r, which is temporarily formed by the scattering partners.

Armed with the scattering length which describes the electron-atom scattering in Rydberg atoms, we can define the well-known Fermi pseudopotential for s-wave scattering. Historically, it was Enrico Fermi [31] who first realized that the low-energy scattering of the Rydberg electron with perturber atoms in its wavefunction can be described effectively by a short-range elastic scattering interaction. To this day, Fermi's model of an effective pseudopotential had much success in determining the electron-atom scattering length for low-energy scattering of many species [87]. Moreover, his model of short-range scattering interaction sets up the foundation on which the state-of-the-art description of ultralong-range Rydberg molecules is built. Following the approach of Fermi, the form of zero-energy s-wave scattering of the Rydberg electron scattering off a neutral atom in its electron orbit, is given by:

$$V_s(\vec{r},\vec{R}) = \frac{2\pi\hbar^2}{m_e} a_s(k)\delta^{(3)}(\vec{r}-\vec{R}), \tag{2.28}$$

including the contact interaction of the Rydberg electron with a neutral atom via the (three-dimensional) Dirac delta function $\delta^{(3)}$ and the k-dependent s-wave scattering length $a_s(k)$. Here, $\vec{r}$ is the electronic coordinate of the Rydberg electron in the core potential, while the vector $\vec{R}$ connects the Rydberg core with the nucleus of the neutral atom. The delta-function contact interaction formalism has been extended by Omont [88] to higher scattering angular momenta in an analytic form. He derived the following p-wave scattering potential:

$$V_p(\vec{r},\vec{R}) = \frac{6\pi\hbar^2}{m_e} a_p(k)\delta^{(3)}(\vec{r}-\vec{R})\overleftarrow{\nabla}\cdot\overrightarrow{\nabla}, \tag{2.29}$$

with the scattering volume $a_p(k)$. Note that for reasons of simplicity the prior introduced nomenclature of (singlet) triplet scattering is omitted in the definition of the scattering potentials above.

2.2.2 Born-Oppenheimer potential energy curves

In the previous section, the electron-atom interaction for a Rydberg electron scattering with a neutral atom has been introduced, and based on the concept of contact interaction, the scattering potentials for s- and p-wave scattering were defined (see equation 2.28 and 2.29). The purpose of this section is to convey a basic understanding of how the Born-Oppenheimer potential energy curves (PECs) resulting from the low-energy Rydberg electron-neutral atom scattering are calculated. Exemplary, the PEC for $n = 35$ is employed to determine the molecular bound state of an ultralong-range S-state Rydberg molecule.

When applying the Born-Oppenheimer approximation, namely that the nuclear motion of the Rydberg atom and the neutral atom can be separated from the electronic motion of the Rydberg atom, solving the stationary Schrödinger equation yields the potential energy curves (PECs) for the electronic degrees of freedom. With the interaction potential for s- and p-wave scattering defined in equation 2.28 and 2.29, we have all important ingredients to construct the electronic Hamilton H for calculating the PECs, which are employed later on to calculate the molecular bound states:

$$H = H_{\mathrm{Ryd}} + H_{\mathrm{G}} + H_{\mathrm{B}} + V. \tag{2.30}$$

Here, H_{Ryd} describes the Rydberg electron dynamics at position $\vec{r}$ in the ionic core potential of the Rydberg atom, which is placed at the coordinate origin. The Rydberg electron possesses an angular momentum $\vec{l}$ and spin $\vec{s}_1$, which couple to a total angular momentum $\vec{j} = \vec{l} + \vec{s}_1$. The energy eigenvalues E_{nlj} of H_{Ryd} are given by equation 2.7. $H_{\mathrm{G}} = A\,\vec{I} \cdot \vec{s}_2$ corresponds to the hyperfine interaction in the ground-state atom, where the spin $\vec{s}_2$ of the valence electron couples with the nuclear spin $\vec{I}$ to the angular momentum $\vec{F} = \vec{I} + \vec{s}_2$. The coupling strength for the ground-state of ^{87}Rb is given by the hyperfine constant $A = h \cdot 3.417\,\mathrm{GHz}$

(see section 2.1). With $H_\mathrm{B} = \frac{e}{m_e}\vec{B} \cdot (\vec{s}_1 + \vec{s}_2 + \vec{l}/2)$, the Zeeman coupling of the electronic angular momenta with an external magnetic field is included. Finally, V represents the interaction between the Rydberg electron and the ground-state atom. The interaction depends on the total electron spin $\vec{S} = \vec{s}_1 + \vec{s}_2$ and the relative orbital angular momentum $\vec{L}$ of the scattering partners (see also section 2.2.1). For the interaction potential V, one can employ a generalized form of the Fermi pseudopotential given by [75] (in atomic units):

$$V = \sum_\beta \frac{(2L+1)^2}{2} a^{T/S}_{s/p,J}(k) \frac{\delta(X)}{X^{2(L+1)}} \left|\beta\right\rangle \left\langle\beta\right| , \tag{2.31}$$

for singlet ($S = 0$) and triplet ($S = 1$) interaction in the s-wave ($L = 0$) and p-wave ($L = 1$) scattering channel. Here, $X = |\vec{r} - \vec{R}|$ denotes the distance between the Rydberg electron and the ground-state atom and $\beta = \{(LS)JM_J\}$ is a multi index, while $\left|\beta\right\rangle \left\langle\beta\right|$ represents the projector onto the different interaction channels $\left|\beta\right\rangle = \left|(LS)JM_J\right\rangle$. The quantum number J (M_J) corresponds to the total angular momentum $\vec{J} = \vec{L} + \vec{S}$ (and the corresponding magnetic quantum number M_J) of the two electrons in the reference frame of the ground-state atom. Note that the commutator of the interaction potential V with H_R, H_G or H_B is non-zero. However, for a zero magnetic field, the projection of the total angular momentum onto the internuclear axis $\Omega = m_l + m_1 + m_2 + m_I$ turns out to be a good quantum number to discriminate the PECs [75, 76], which we will use later on.

Next, we turn to the calculation of the Born-Oppenheimer PECs. For this, let us first recall that the nuclear motion is frozen out in the Born-Oppenheimer approximation, which allows us to solve the stationary radial Schrödinger equation for different internuclear distances R between the Rydberg core and the ground-state atom independently. For each R, the local kinetic energy of the Rydberg electron scattering off the static ground-state atom can be determined by the kinetic energy gain $E_\mathrm{kin} = \frac{\hbar^2 k^2}{2m_e}$ of the Rydberg electron moving towards the ionic Rydberg core, which leads to the semi-classical relation for the wave number

$k(R) = \sqrt{\frac{2m_e}{\hbar^2}\left(\frac{e^2}{4\pi\epsilon_0 R} - E_{nlj}\right)}$, where E_{nlj} is the binding energy of the atomic Rydberg state of interest.

In this thesis, there are two different approaches used for calculating the PECs, namely, a truncated diagonalization method, which uses a finite basis set of the system Hamiltonian, and the Green's function approach. While the latter intrinsically yields converging results, which include all Rydberg levels [78], the former, in contrast, allows one to include all relevant spin degrees of freedom [37, 75, 89], but suffers from uncertainties that result from the size of the basis set chosen [90].

With the potential energies set up for different internuclear distances, the radial vibrational bound states can be calculated. For this, the PECs are plugged into the Schrödinger equation, which is then solved numerically by applying the Numerov method in a similar fashion as it is done for calculations of the Rydberg wavefunction (cf. 2.1.1). In figure 2.6 the calculated potential energies for different internuclear distances R for both the truncated diagonalization method and the Green's function approach, are shown for energies close to the $35S_{1/2}$ Rydberg state. The oscillatory potential energy curve mimics the Rydberg electron density distribution, which, given the attractive electron-atom interaction, allows for bound molecular states; especially close to the outermost turning point of the Rydberg electron, where the electron density is the largest. As a result of the strong radial confinement, the motion of the ground-state atom is determined by the deep wells of the PEC, which support discrete vibrational dimer states. An exemplary molecular bound state (lowest lying vibrational state) is depicted for the outermost well which is centered around $R = 1900\,\mathrm{a}_0$. In this case, the attractive s-wave scattering interaction between the $35S_{1/2}$ Rydberg electron and ground-state atom dominates allowing for the formation of a spherically symmetric so-called S-state Rydberg molecule. Later on (in chapter 4), we will see that the

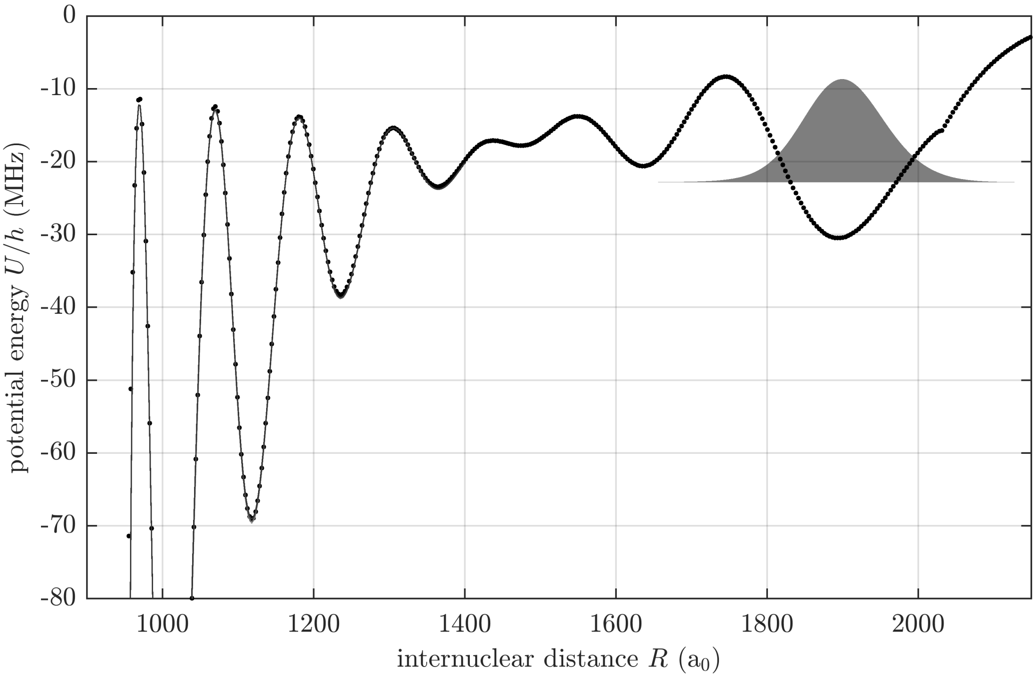

Fig. 2.6: Potential energy curve resulting from e$^-$-Rb scattering for zero magnetic field in the vicinity of the $35S_{1/2}$ Rydberg state. The asymptotic zero potential energy is set to the binding energy of the Rydberg electron. Black dots represent the outcome of the Green's function calculus, while the gray lines show the results from the truncated diagonalization. Exemplarily, a molecular bound state is depicted, indicated by the gray shaded area at $R = 1900\,\mathrm{a}_0$. The vibrational wavefunction is offset by its binding energy.

spherical symmetry for Rydberg molecules that are located closer to the Rydberg core, where p-wave scattering dominates, is broken due to the non-zero spin-orbit coupling between the total electron spin $\vec{S}$ and the scattering angular momentum $\vec{L}$, which mixes the different scattering channels [77].

For the truncated diagonalization calculations the fitted s- and p-wave phase shifts from [S2] are employed, while for the Green's function calculus the J-averaged phase shifts from [S2] (see also [84]) are used for the p-wave. The basis set used for the diagonalization method can be tested against the Green's function calculations by switching off the LS-coupling term (equation 2.25). An optimal match between the two methods has been found for taking into account in total four manifolds of the electronic Rydberg state, two below and above ($n-5$ to $n-2$) the $nS_{1/2}$ Rydberg state of interest. Moreover, the total angular momenta j is considered completely, while the projection m_j is truncated for $|m_j| > 3/2$ as for these states the interaction with the ground-state atom can be neglected. The complete basis set $|F, m_F\rangle$ of the ground-state atom is taken into account.[S2] More details about the calculations can be found in [75–77] and in the supplement material of [S2].

2.3 Rydberg atoms in a Bose-Einstein condensate

This section gives a brief introduction to Rydberg atoms immersed in an ultracold and highly dense gas, here a Bose-Einstein condensate (BEC). First, we will discuss the interaction between a single Rydberg atom and many neutral atoms, stemming from the condensate. For this, we review the most important experimental and theoretical work carried out in this field. Afterwards, with regard to the ion creation and probing in a BEC (section 3.6), involving the Rydberg excitation in the condensate, exemplarily, an experimentally obtained Rydberg excitation spectrum in a BEC is presented and discussed.

As introduced earlier in section 2.2.1, the low-energy Rydberg electron can scatter off neutral atoms in its orbital wavefunction. In the case of one or even multiple neutrals, the attractive scattering can lead to the formation of Rydberg molecules, in which the atoms are bound inside the Rydberg wavefunction (see section 2.2.2).

In the case of many neutral atoms, the strong scattering induced interaction results in line shifts and broadening of the Rydberg energy levels. This was already observed in 1934 by E. Amaldi and E. Segré [30] for principal quantum numbers around $n = 30$ and high buffer gas densities at pressures reaching up to one atmosphere, for which on average more than 10,000 atoms are inside the Rydberg orbit. Within the same year, Enrico Fermi introduced the nowadays well-known Fermi pseudopotential [31] (see also section 2.2.1) to explain the findings of Amaldi and Segré.

To describe the Rydberg electron interacting with many neutral atoms, first let us recall the Fermi pseudopotential (cf. equation 2.28), which describes the short-range interaction of a neutral ground-state atom at a distance R from the ionic Rydberg core with the quasifree Rydberg electron at distance r:

$$V_{\mathrm{pseudo}}(\vec{r}, \vec{R}) = \frac{2\pi\hbar^2 a_{\mathrm{s}}}{m_{\mathrm{e}}} \delta^{(3)}(\vec{r} - \vec{R}) \tag{2.32}$$

Here $\delta^{(3)}$ is the Dirac delta function in three dimensions, which represents the short-range contact interaction between the Rydberg electron and the neutral ground-state atoms. When neglecting the k-dependence, the contribution of higher partial waves, and the internal spin structure, then the interaction strength is given by the expression for V_{pseudo}, which is characterized solely by the s-wave scattering length a_{s}. This is certainly true for large internuclear distances, where the electron momentum is low and s-wave scattering dominates. An evaluation of equation 2.32, given the Rydberg electron wavefunction $\Psi(r)$, leads to a mean field potential

$$V_{\mathrm{mean}}(R) = \frac{2\pi\hbar^2 a_{\mathrm{s}}}{m_{\mathrm{e}}} \left|\Psi(R)\right|^2 . \tag{2.33}$$

The resulting potential is proportional to the scattering length a_{s} and the electron density distribution $|\Psi(R)|^2$ of the Rydberg wavefunction at the position of the neutral atom R.

Finally, considering many neutral atoms inside the Rydberg orbit, Fermi used this expression to formulate a density-dependent mean field energy shift $\Delta E(\rho)$

by summing up the energy shifts given by equation 2.33 of each atom inside the Rydberg orbit, in order to explain the line shifts observed by Amaldi and Segré.

$$\Delta E(\rho) = \frac{2\pi\hbar^2 a_\mathrm{s}}{m_\mathrm{e}}\rho \tag{2.34}$$

It turns out that this definition of the mean field energy shift holds in the regime of ultracold temperatures for sufficiently high densities. Balewski *et al.* (ref. [46]) experimentally observed a mean field shift given by equation 2.34 for a single Rydberg atom excited inside a Bose-Einstein condensate.

In a work of Gaj *et al.* (ref. [38]) the transition from a few to many neutral atoms inside the Rydberg orbit is demonstrated. It directly corresponds to a step from spectroscopically resolvable molecular bound states, essentially supported by the mean field potential V_mean of equation 2.33, to the mean density shift $\Delta E(\rho)$ given by equation 2.34 with an additional broadening caused by the randomness of the spatial distribution of the many neutral atoms. Gaj *et al.* showed a series of spectra ranging from $n = 51$ up to $n = 111$ for a BEC density of $3 \times 10^{12}\,\mathrm{atoms/cm^3}$. For low principal quantum numbers n, on average one or even less atoms are inside the electron orbit and strong molecular lines are observed when detuning the excitation laser from the bare Rydberg state by the binding energy of the photo-associated Rydberg molecule. The separated lines can be associated with one (dimer), two (trimer), three (tetramer) and so on neutral atoms bound by the quasifree Rydberg electron. For increasing n, the number of atoms inside increases rapidly, since the Rydberg orbit grows with n^2. In turn, the potential depth of the scattering induced electron-atom potential decreases, since the integrated electron density distribution is conserved by the norm of the wavefunction. Consequently, for increasing n the observed molecular lines shift closer to the bare Rydberg state and become broader and more equally in height with more perturbing atoms inside the electron orbit. Eventually, a single broad spectroscopic feature emerges, shifted by the mean density shift equal to the expression given by equation 2.34.

Beyond the above presented mean field energy shift, a more detailed consideration of the electron-neutral atom interaction additionally revealed the importance of a p-wave shape resonance in rubidium (ref. [79]) and allowed Schlagmüller *et al.* (ref. [S6]) for an accurate modeling of the experimentally obtained Rydberg excitation spectra in a BEC, by means of a classical statistical model of the spectral line shape. Moreover, a more rich theoretical description by a functional determinant approach (ref. [91]) including the many-body Rydberg electron-neutral atom molecular states, shows a remarkable agreement with the experimental results of Camargo *et al.* (ref. [47]) and validates the classical statistical approach of Schlagmüller *et al.* (ref. [S6]) even for on average only a few tens of atoms randomly distributed in the Rydberg orbit. In the following (figure 2.7) a typical experimental spectrum of a single Rydberg atom excited in a Bose-Einstein condensate is shown. The excitation laser is detuned from the atomic resonance of the bare Rydberg state and for each Rydberg detuning δ a Rydberg signal N_R is obtained by electric field ionization of the prior excited Rydberg electron and detection of the remaining ion on a microchannel plate detector. The spectrum can be separated into three different regions of detuning. Due to the high density in the BEC, even for a detuning much larger than the excitation bandwidth (here $\Gamma = 450\,\mathrm{kHz}$), a Rydberg atom is successfully excited. In this case, the scattering induced interaction between the Rydberg electron and the neutral atoms inside its orbit compensates for the energy difference of the Rydberg detuning δ. Since the interaction potential is mostly negative ($a_\mathrm{s} < 0$) with respect to the atomic resonance ($\delta = 0$), adding more atoms into the electron wavefunction increases the resulting mean field shift towards red detuning ($\delta < 0$). Consequently, for large red detunings (region 1) a Rydberg excitation is favored in the center of the BEC, where the density is the highest. When decreasing the red detuning (region 2), the mean field shift in the BEC center is larger than δ and an excitation

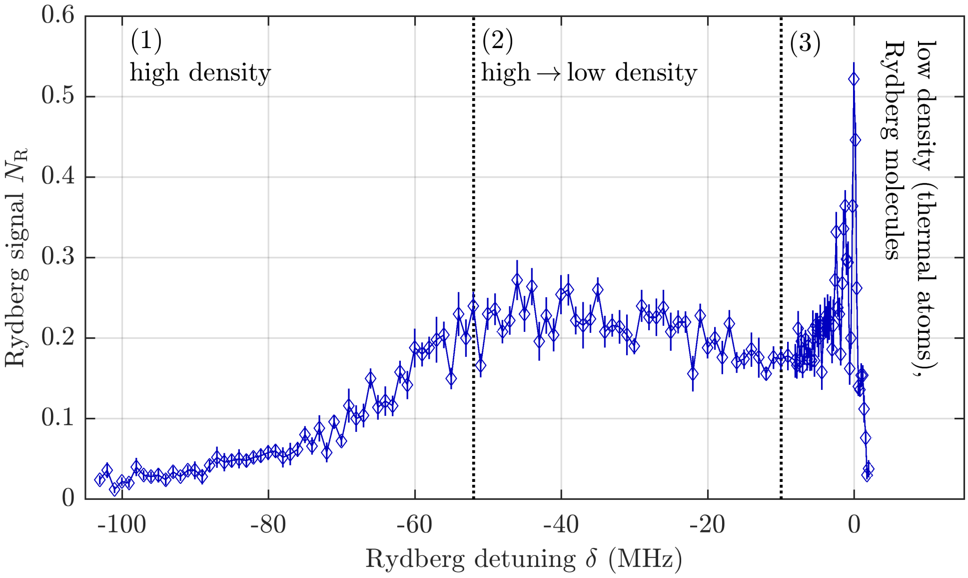

Fig. 2.7: $53S$ Rydberg excitation spectrum in a BEC (ref. [S6]). The Rydberg signal N_R is shown as a function of the Rydberg detuning δ. The atomic resonance of the Rydberg excitation is set to zero detuning. Vertical dotted lines separate the spectrum in three different regions of addressed densities. (1) For large red detuning the Rydberg atom is excited in a high density region. (2) For less red detuning, lower density regions are addressed. (3) Close to the atomic resonance shallow bound molecular states are observed.

is preferred in a region with less atoms inside the Rydberg orbit. The density dependence of the Rydberg excitation probability is a direct consequence of the mean field energy shift given in equation 2.34, which allows for a detuning to density mapping [S8, 91]. As a consequence, for a certain Rydberg detuning ($\delta < 0$) a Rydberg excitation is favored in a narrow shell of similar density inside the BEC [S8]. For small red detunings $\delta > -10\,\mathrm{MHz}$ (region 3) sharp peaks of molecular bound states become prominent in the spectrum of figure 2.7. In this case, ultralong-range Rydberg molecules are predominantly photo-associated in the very low-density region, mostly in the thermal atom cloud around the BEC, where only a few atoms are located within the Rydberg electron wavefunction.

3

Ion-induced Rydberg blockade

In recent years, ultracold Rydberg atoms have been proven to provide a versatile platform for quantum simulation of long-range interacting many-body systems [10–12], for nonclassical photonic state generation [13, 14], and for quantum information processing [15–17]. In particular, the Rydberg blockade phenomenon is a central aspect for many proposals in these fields [18–20]. The blockade phenomenon results from strong Rydberg-Rydberg interactions, which suppress the simultaneous excitation of two or more atoms into Rydberg states within a certain blockade volume. The Rydberg-Rydberg blockade in a cold and dense atomic ensemble has been first observed experimentally in 2004 (ref. [21, 22]) and has been demonstrated for two individual atoms (ref. [23]) in 2009.

In hybrid systems of ions and Rydberg atoms, a similar concept applies. Strong interactions between a single ion and Rydberg atoms potentially lead to charge-induced blockade phenomena mediated over macroscopic distances, which have been proposed as a tool for quantum information transfer between ionic and atomic quantum systems [24]. The experimental observation of such a blockade mechanism, however, remained so far elusive. In traditional hybrid settings, which typically consist of a radio-frequency (rf) ion trap and Rydberg states excited in an ensemble of trapped neutral atoms, the ion-trap induced lineshift on the Rydberg states complicates the observation of interaction effects [25]. First indications of ion-induced lineshifts have been reported in a study of charge transfer in a hybrid setting [26]. The ion-Rydberg atom interaction has been investigated in the context of atom-beam experiments [27] and more recently has been shown to affect quantum optics applications based on room temperature vapors [28].

In this chapter studies of ion-Rydberg atom interactions are presented. In particular measurements on an ion-induced Rydberg blockade are carried out. Parts of this work has been published in [S1].

First, the creation of a single ion in an ultracold ensemble of rubidium-87 atoms is presented in section 3.1. The low energy ion is efficiently created by employing a novel V-type photo-ionization scheme [S1, 92, 93]. The ionization scheme incorporates a Rydberg state to ensure the creation of a single ion at a time, utilizing the Rydberg blockade mechanism [19]. A Photo-ionization efficiency of up to 75 % is reached. The efficiency is predominantly limited by the photo-ionization rate of the $6P_{3/2}$ state, which is given by the photo-ionization cross-section and the laser field intensity of the ionization laser [94], that in general, can be overcome by higher laser intensity.

In section 3.2, an experimental measurement strategy is presented, including the aforementioned V-type photo-ionization scheme, a subsequent Rydberg excitation, and a tailored electric field pulse sequence, with which interactions between a single ion and a Rydberg atom are demonstrated by means of an ion-induced Rydberg excitation blockade. Note, these ion-Rydberg atom interactions were demonstrated for the first time in this work (ref. [S1]). Only shortly after, indications of strong interactions between ions and Rydberg atoms were observed (ref. [26]) in a hybrid system consisting of a single rf-trapped ion overlapped with a cold atomic cloud.

Following that, measurements of the ion-induced Rydberg excitation blockade for different interaction strengths and ion-Rydberg atom distances are carried out in section 3.3. The ion's motion is precisely controlled by tunable external electric fields, while the creation center of the Rydberg atom is well localized. This allows for probing ion-atom interactions between a single ion and a Rydberg atom, mediated over tens of micrometer distances. The tailored electric field pulses are designed for field ionization of Rydberg atoms and the separation of the ion signal, stemming from the field ionized and the photo-ionized Rydberg atoms, on the detector. With this, we are able to directly measure the suppressed on-resonance Rydberg excitation probability in the presence of the Coulomb field the ion. By post-selection on the ion signal of the photo-ionized Rydberg atom, the contrast of the blockade measurements is increased by a substantial amount.

Furthermore, the ion-induced blockade mechanism is utilized to use a single ion as a sensitive probe for electric fields (section 3.4). For this, the blockade measurement sensitivity is enhanced by increasing the ion-atom interaction strength, allowing for a stray field compensation down to a level of 100 μV/cm. Moreover, a remarkable precise control of electric fields is demonstrated on the micrometer scale.

Additionally, characterization measurements on the V-type photo-ionization scheme in an ultracold and dense ensemble are presented (section 3.6.1) and finally, the ion-induced Rydberg blockade mechanism is employed (section 3.6.3) to trace the motion of the ion when pulled through the ultracold and dense sample of atoms in a Bose-Einstein condensate.

3.1 Single Ion creation

In order to probe Rydberg atom-ion interactions, first a single initially slow ion is created. For this purpose, out of an ultracold sample of rubidium-87 atoms the

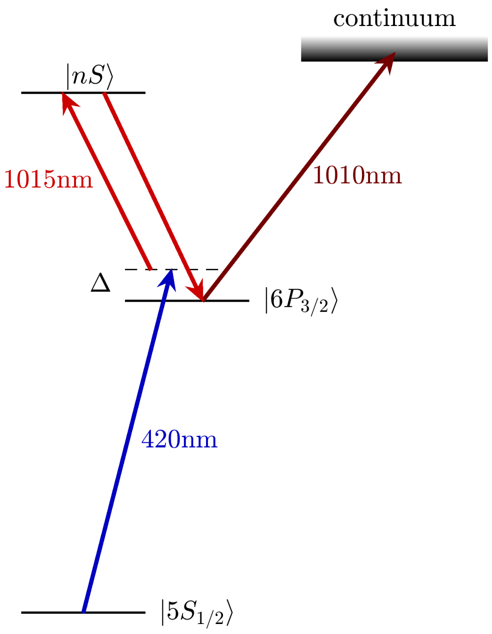

Fig. 3.1: All-optical V-type photo-ionization scheme incorporating the intermediate state $6P_{3/2}$ and the nS Rydberg state. The Rydberg state is addressed via a two-photon excitation scheme (420 nm and 1015 nm) and subsequently deexcited via a resonant 1015 nm laser and coupled to the continuum by 1010 nm laser light, involving the intermediate state $6P_{3/2}$.

valence electron of a single atom is elevated to a highly excited Rydberg state and subsequently ripped off from its ionic core, leaving a single Rb^+ ion behind. The Rydberg atom is ionized by applying an all-optical V-type photo-ionization scheme (ref. [92]). A schematic of the used ionization scheme is depicted in figure 3.1.

Applying this specific ionization scheme, which is outlined in the following paragraph, serves a threefold purpose. First, by incorporating the nS Rydberg state multiple creations of Rydberg atoms and thus subsequently photo-ionized ions is heavily suppressed through Rydberg-Rydberg interaction. Consequently, for a small enough excitation volume the preparation of a single photo-ionized ion is ensured through the Rydberg excitation blockade. Second, the kinetic energy transfer onto the initially ultracold atom corresponds to the total photon recoil energy of the photo-ionization scheme, which is kept very low by using counterpropagating (co-propagating) beam paths for the Rydberg excitation (photo-ionization). In an ideal situation, the ionization excess energy of the ion is then only given by the energy difference between the intermediate $|nS\rangle$ Rydberg state and the continuum limit. Eventually, the ions initial position overlaps with the excitation center of Rydberg atoms and thus eases the preparation for probing the Rydberg atom-ion interaction.

In the experiments the $\left|5S_{1/2}, F=2, m_F=2\right\rangle$ ground state is coupled to a excited state via a two-photon excitation scheme, involving 420 nm and 1015 nm laser light, for the lower (σ^+) and upper (σ^-) transition respectively, addressing the $m_J = +1/2$ Zeeman substate of nS Rydberg state. The $6P_{3/2}$ state population of the intermediate state is kept low by employing a large detuning of $\Delta = +160\,\mathrm{MHz}$. The Rydberg population is measured by detecting single ions on a microchannel plate (MCP) detector, stemming from electric field ionized Rydberg atoms. A Rydberg signal N_R is obtained by averaging the number of electric field ionized Rydberg atoms detected on the MCP for many realizations of the performed experiments. For the Rydberg excitation, the laser powers are adjusted to reach a Rydberg signal of $N_\mathrm{R} = 0.3$, which by including the detection efficiency of the MCP corresponds to a mean number of 0.5 Rydberg atoms per experiment [95]. Statistics is gained by repeating experiments within one atom sample up to 500 times and averaging over typically 10-20 thermal atom cloud realizations. The experiments are performed with a spin polarized ($F = m_F = +2$) atom sample prepared in a crossed optical dipole trap, cf. section A.2, with typical atom temperatures and atom numbers of $T_\mathrm{therm} = 1\,\mu\mathrm{K}$ and $N_\mathrm{therm} = 1.2 \times 10^5$. For the V-type photo-ionization (cf. figure 3.1), after a successful Rydberg excitation the Rydberg atom is resonantly deexcited to the $6P_{3/2}$ state by employing a laser pulse of circular polarized light driving σ^- transitions. Subsequently, an infrared 1010 nm laser with the same circular polarization, photo-ionizes the prior excited Rydberg atom by coupling the $6P_{3/2}$ state to the continuum. The photo-ionization laser is locked to a wavelength of 1010.2 nm, resulting in a total ionization excess energy of about 25 GHz, which is determined by the energy difference between the ionization laser and the continuum relative to the $6P_{3/2}$ state. The time-resolved detection of ions on the MCP allows for separate evaluation of electric field ionized and photo-ionized ions.

3.1.1 Deexcitation

In order to demonstrate the deexcitation involved in the photo-ionization scheme, Rabi oscillations between the $|51S, m_J = +1/2\rangle$ Rydberg state and the intermediate state $6P_{3/2}$ are measured. For this, a single Rydberg atom is excited and afterwards coupled back to the $6P_{3/2}$ state via the resonant deexcitation laser. In the following (figure 3.2) the Rydberg signal N_R is shown as a function of the pulse length, while the power of the deexcitation laser ($P_\mathrm{de} = 0.5\,\mathrm{mW}$) is kept constant. In absence of deexcitation laser light, the mean Rydberg signal is set to $N_\mathrm{R} = 0.3$. The blue data points correspond to the measured Rydberg signal, while the red curve serves as a guide to the eye based on a calculated Rabi frequency of $\Omega_\mathrm{de} = 28\,\mathrm{MHz}$ using an estimated beam waist of about $7\,\mu$m. For a short pulse duration, especially for $t \leq 60\,\mathrm{ns}$, the limited rise time of the acousto-optic modulator used for switching the laser light on and off becomes comparable to the pulse length, thus the pulse area, defined as the coupling strength (here the Rabi frequency Ω_de) times the pulse length, does only change linear with the pulse length for sufficiently long laser pulses. For a long pulse duration the Rydberg signal N_R does not drop to zero, indicating a non-fully blockaded atom ensemble for the $51S$ Rydberg state. Indeed for the Rydberg excitation bandwidth ($\approx 2\,\mathrm{MHz}$),

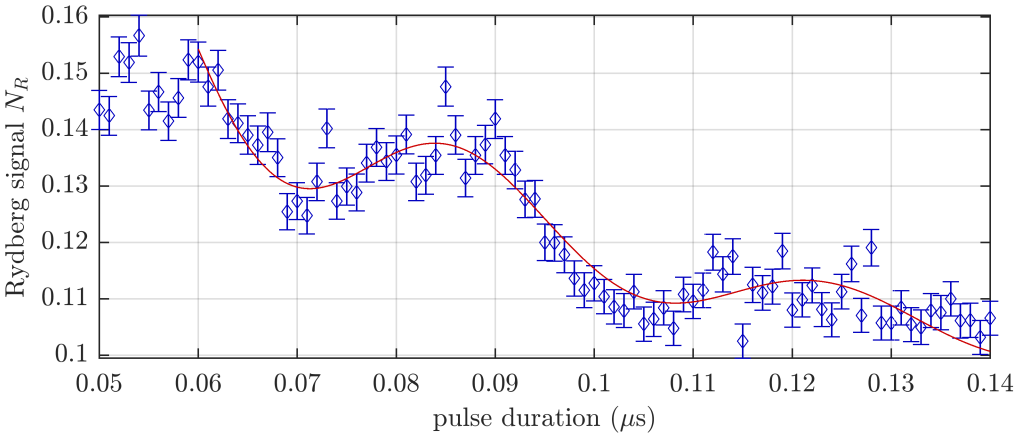

Fig. 3.2: Measurement of resonant single-photon Rabi oscillations between $|51S, m_J = +1/2\rangle$ Rydberg state and $6P_{3/2}$ state, driven by the deexcitation laser. The deexcitation pulse length is varied between 50 ns and 140 ns. Blue diamonds represent the measured data points, with error bars corresponding to the standard deviation, while the red line is a guide to the eye based on a calculated Rabi frequency of $\Omega_{\mathrm{de}} = 28\,\mathrm{MHz}$. The mean Rydberg signal in absence of the deexcitation laser pulse is set to $N_{\mathrm{R}} = 0.3$ by adjusting the Rydberg excitation laser powers.

given by the Fourier width of a 500 ns square pulse for a non-power broadened transition, the Rydberg blockade of about 5 μm is on the same order as the cloud radius along the direction of the infrared Rydberg excitation laser (1015 nm) beam path (see chapter A.2). Additionally to the limited rise time of the laser pulse, which considerably diminishes the oscillation contrast, the comparatively short lifetime of the $6P_{3/2}$ state of $\tau = 112\,\mathrm{ns}$ [96], rapidly damps the Rabi oscillations. Nonetheless, the experimental data show about two full Rabi cycles, ranging from about 60 ns to 140 ns. Furthermore and most importantly, the Rydberg signal decreases by more than 50 % from $N_{\mathrm{R}} = 0.3$ to $N_{\mathrm{R}} \leq 0.15$ within 60 ns exposure time of the deexcitation laser, demonstrating a successful deexcitation of Rydberg atoms. Note that the lifetime of the $51S$ Rydberg state amounts several tens of microseconds and thus can be neglected [62].

3.1.2 Photo-ionization efficiency

In the following the V-type photo-ionization of a single $51S$ Rydberg atom is presented and the corresponding photo-ionization efficiency is measured. After the preparation of a single Rydberg atom, the excited atom is deexcited to the $6P_{3/2}$ state, following the first branch of the V-type ionization scheme, cf. figure 3.1. The Rydberg electron is then photo-ionized by coupling an infrared laser, with a wavelength of $\lambda = 1010.28\,\mathrm{nm}$[1], which reaches above the ionization threshold, and with this completing the ionization protocol; following the second branch in figure 3.1 to the continuum. In order to overcome the low deexcitation efficiency owing to the short lifetime of the $6P_{3/2}$ state, the ionization laser pulse is kept short and is applied immediately after the Rydberg atom is excited. Furthermore, the Rydberg atom is simultaneously exposed to the photo-ionization and deexcitation laser. Additionally, the beam paths of the photo-ionization laser and the deexcitation laser are overlapped and co-propagating, passing through a high numerical aperture lens (NA = 0.55). Both laser beams are focused down onto the atomic cloud, reaching a beam waist of about $1.8\,\mu\mathrm{m}$ for the photo-ionization laser and a beam waist of roughly $7\,\mu\mathrm{m}$ for the deexcitation laser. This allows for relatively high light intensities with the laser powers available in the experiment, especially for the photo-ionization laser. Thus, high ionization efficiencies are reached employing short but intense laser pulses. For the efficiency measurement, subsequent to a Rydberg excitation pulse of 500 ns, the deexcitation and photo-ionization laser illuminate the prior excited Rydberg atom for 200 ns, photo-detaching the Rydberg electron from its ionic core. The deexcitation power is set to 5 mW, while the photo-ionization laser power is varied between 0 mW and

---

[1] The ionization threshold for the $6P_{3/2}$ state is estimated by using the ionization energy of the $|5S_{1/2}, F = 1\rangle$ state [59], the hyperfine splitting of the $5S_{1/2}$ ground state [97], and the energy level of the $6P_{3/2}$ state [61], neglecting the hyperfine splitting of the excited state.

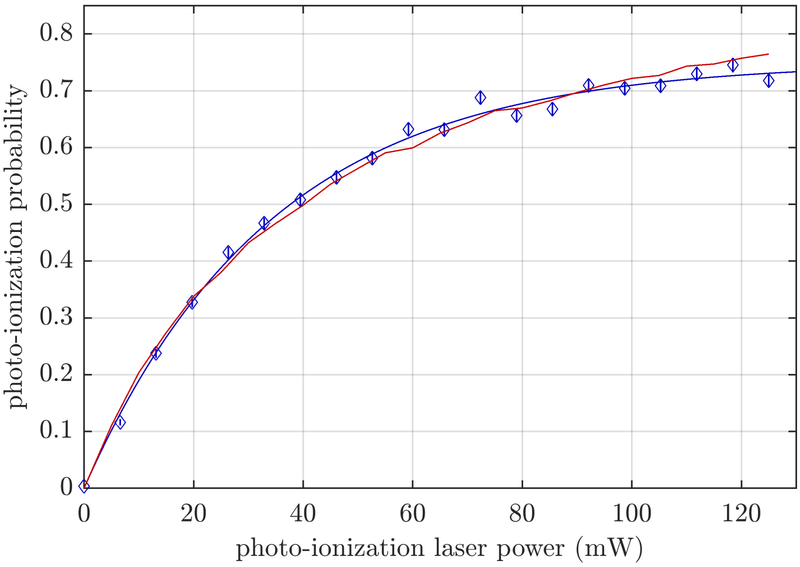

Fig. 3.3: Photo-ionization efficiency of the V-type photo-ionization scheme, incorporating the $|51S, m_J = +1/2\rangle$ Rydberg state and the $6P_{3/2}$ state, for different photo-ionization laser powers of up to 125 mW and a deexcitation power of 5 mW. The experimentally obtained ionization probability is shown by blue diamonds (standard deviations, indicated by error bars, are smaller than the symbols), while the blue curve corresponds to an exponential fit. The red line is the theoretical prediction of a time-dependent four-level system (see text). The deexcitation and photo-ionization laser are simultaneously pulsed into the atom sample for 200 ns, photo-ionizing the prior excited Rydberg atom.

125 mW. Figure 3.3 shows the photo-ionization efficiency measured for different powers of the ionization laser. The blue data points represent the experimentally obtained photo-ionization probability fitted by an exponential curve (blue), which saturates at higher laser powers to an ionization efficiency of 75 %. From an independent measurement the Rydberg signal is obtained as $N_{\mathrm{R}} = 0.3012(50)$, allowing to deduce the photo-ionization probability shown in figure 3.3. Owing to the tight focus of the photo-ionization and deexcitation laser an efficiency of up to 70 % is reached for a laser power ≥ 90 mW.

For the experimental parameters listed above, simulations of the time-dependent energy level distribution for the photo-ionization process have been performed. The calculations are carried out, solving the Liouville-von Neumann equation for the states primarily involved in the ionization scheme. Starting from the populated $51S$ Rydberg state, a resonant laser couples the excited state with the intermediate $6P_{3/2}$ state, which represents the deexcitation process. From the intermediate state two possible decay channels are introduced. The first one is a laser induced loss channel to an artificial state with infinite lifetime, modeling the photo-ionization process to the continuum. The second channel is a rapid decay from the intermediate state to the ground state. For the performed calculations a photo-ionization cross section of $\sigma_{\mathrm{PI}} = 15 \times 10^{-22}\,\mathrm{m}^2$ [98] and a decay rate of $\Gamma_{\mathrm{decay}} = 1/\tau = 8.93\,\mathrm{MHz}$ for the intermediate $6P_{3/2}$ state ($\tau = 112\,\mathrm{ns}$ ref. [96]), are applied. In the context of this work, a more detailed description of the time-dependent four-level evolution modeling for the photo-ionization process is outlined in [99]. Based on this, a theoretical photo-ionization efficiency of up to $90\,\%$ is predicted for an ionization laser power of $90\,\mathrm{mW}$. The photo-ionization probability is ultimately limited due to the decay from the intermediate state to the ground state, and in general can be overcome by applying shorter and more intense laser pulses for deexcitation and photo-ionization. The calculated efficiency exceeds the experimentally obtained ionization probability by about $20\,\%$.

For the theoretical description so far, neither the extension of the laser beams nor of the atom sample are taken into account, assuming a point-like excitation volume. Furthermore, the differential ac stark shift between the intermediate $6P_{3/2}$ state and the Rydberg state, resulting from the high photo-ionization laser intensities, is expected to be on the order of several tens of MHz [99] and thus need to be taken into account as well.

In order to include the finite size of the excitation volume, a Monte Carlo sampling for both, the spatial laser intensities and atom density distribution, is performed, which yields a photo-ionization probability of 0.8 for the aforementioned mentioned experimental parameters. Additionally introducing an ac stark shift, an ionization efficiency curve (cf. red curve of figure 3.3) matching the measured data is obtained from the simulations. The ac stark shift calculations performed in [99] suggest a differential shift of 58 MHz. However, for a shift of 35 MHz a much better agreement with the experimentally obtained data is found. A conceivable reason for the apparent discrepancy between the simulations matching the experimental data and the findings of [99], is the break-down of the four-level picture due to an off-resonant coupling to different hyperfine substates of the intermediate $6P_{3/2}$ state. A comparison of the simulated efficiencies for the two different ac stark shifts is shown in section A.1. For a further investigation, the ac stark shift can be measured by e.g. varying the intermediate detuning of the $6P_{3/2}$ state, maximizing the ionization efficiency.

The achieved photo-ionization probability of 75 % is already quite remarkable and allows for a detailed investigation of the ion-Rydberg atom interaction by means of the aforementioned ion-induced Rydberg excitation blockade.

3.2 Ion motion and ion-induced Rydberg excitation blockade

So far the preparation of single ions in an ensemble of ultracold rubidium-87 atoms is presented. The prepared ions are created by employing the V-type photo-ionization scheme presented in the previous section 3.1.

This section reviews the ion-Rydberg atom interactions and introduces the concept of an ion-induced Rydberg excitation blockade. Following that, measurements of the ion-induced Rydberg excitation blockade are carried out and the results are discussed. For demonstrating the excitation blockade, a measurement technique is presented that has been specifically adapted for probing the ion-Rydberg atom interaction, involving the V-type photo-ionization scheme and a subsequent probe Rydberg excitation. Exemplarily, the excitation blockade is measured in a time-resolved manner, allowing to draw conclusions on the ion trajectory. The time-dependent Rydberg signal is modeled employing an interaction energy shift of the Rydberg levels based on the pair interaction potential. Furthermore, the contrast of the obtained Rydberg signal is greatly increased by post-selecting on the signal of the photo-ionized ions on the detector.

First, consider an ion in its electronic ground state and a highly excited Rydberg atom separated by a distance R. Due to the polarizability of the Rydberg atom, in the presence of an ion the Rydberg energy levels are shifted as a consequence of the ion-induced stark effect. The pair interaction between ion and Rydberg atom can be described asymptotically by the long-range polarizability potential for sufficiently large internuclear distances where the Coulomb field of the ion is abated well below the Inglis-Teller limit [100].

As introduced in section 2.1.2 the polarization potential for a pair of an ion and a Rydberg atom can be described by

$$V(R) = -C_4/R^4. \tag{3.1}$$

The ion-Rydberg atom interaction strength is defined by the state-dependent Rydberg atom polarizability $\alpha_{\mathrm{Ryd}} = 2\left(4\pi\epsilon_0/e\right)^2 C_4$ (cf. equation 2.23), which scales strongly with the principal quantum number n. In the case of a nS Rydberg state, the polarizability approximately scales with n^7 (see section 2.1.2). For the principal quantum numbers investigated in the context of the ion-induced Rydberg blockade measurements ($n > 50$), the large polarizability of the Rydberg atom leads to sizable interactions of several MHz over a distance of tens of micrometer.

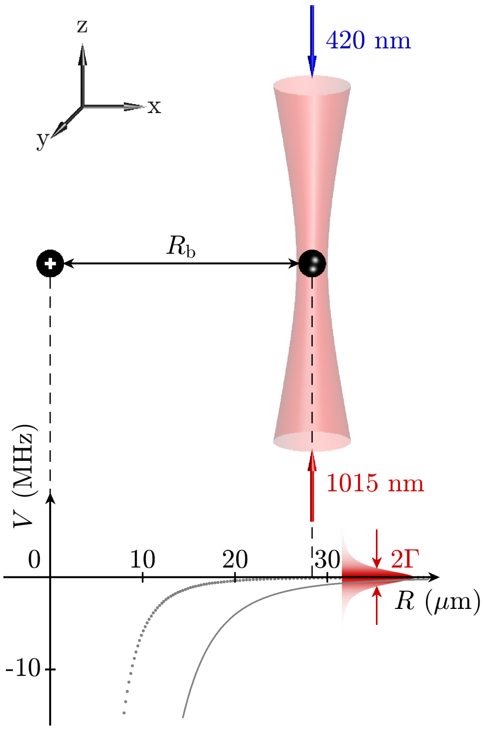

Fig. 3.4: Illustration of measurement method for probing single ions by means of an ion-induced Rydberg excitation blockade. (Top) Rydberg excitation probes a single ion at distance R. Rydberg excitation beams counterpropagating. The tightly focused 1015 nm beam confines along z-direction, while 420 nm beam much larger and illuminates everything. (Bottom) Pair-interaction potential $V(R)$ of a single ion and Rydberg atom separated by distance R for $n = 71$ (dotted) and $n = 100$ (line). The Rydberg excitation bandwidth Γ is indicated with a shaded red curve.

Figure 3.4 illustrates the measurement method for probing the ion-Rydberg atom interactions by means of an ion-induced excitation blockade. A single Rydberg excitation is probed in the presence of a beforehand photo-ionized ion at distance R. With an ion nearby a laser excitation attempt into a certain Rydberg state may be affected due to the ion-Rydberg atom interactions. More precise, an excitation suppression sets in for a pair interaction strength larger than the excitation bandwidth Γ, which occurs at a certain distance between ion and

Rydberg atom. In analogy to the Rydberg-Rydberg blockade mechanism, this defines a blockade sphere enclosing the ion, with a radial extension of

$$R_\mathrm{b} = \left(C_4/\Gamma\right)^{1/4}. \tag{3.2}$$

In the lower half of figure 3.4 the pair interaction potential for $n = 71$ (dotted) and $n = 100$ (line) are depicted. The energy level shifts depend upon the distance between ion and Rydberg atom, for smaller internuclear distances huge energy shifts are revealed. The excitation bandwidth $\Gamma = 1.09(1)\,\mathrm{MHz}$ is indicated by a shaded red curve. In the case of $n = 100$, we can obtain a blockade radius of about $28\,\mu\mathrm{m}$ (indicated by a vertical dashed line) by comparing the ion-induced energy shift with the excitation bandwidth Γ.

In the upper half of figure 3.4, a single Rydberg atom is successfully excited in the presence of a distant ion. On the right hand side the tightly focused 1015 nm excitation laser beam path for the upper transition is illustrated. The 1015 nm laser beam passes through a lens with high numerical aperture and is focused down to a beam waist of $1.8\,\mu\mathrm{m}$. The counterpropagating 420 nm laser homogeneously illuminates the entire atom cloud. Combined with the strongly compressed atom sample along the excitation beam path, see chapter A.2, a high spatial control over the created Rydberg atoms is achieved. In the experiment, the same lasers are used for both Rydberg excitations, the one involved in the photo-ionization scheme and the other used for probing the ion-Rydberg atom interactions, utilizing the precise control for positioning and for probing the ion. For probing the interactions, not only an accurate spatial control of the initial positioning for both ion and Rydberg atom is indispensable, but also the motion of the ion has to be precisely controlled, which places high demands on the electric field control. For the measurements performed, Stark spectroscopy [101] at a principal quantum number of $n = 133$ allows for a stray electric field compensation on the level of $\sim 1\,\mathrm{mV/cm}$.

Figure 3.5 shows a sketch of the relevant section of the experimental measurement

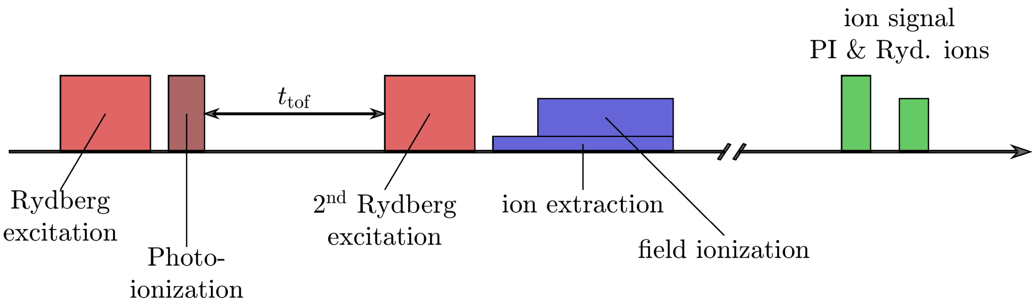

Fig. 3.5: Experimental measurement sequence starting with a first Rydberg excitation pulse, which is immediately followed by a photo-ionization pulse. After a variable time-of-flight of the created ion, a second (probe) Rydberg excitation pulse is applied. Subsequently, an ion extraction electric field is used to pre-accelerate the photo-ionized ions before a larger field pulse electric field ionizes the still present Rydberg atoms, which stem from the first or second Rydberg excitation attempt. The ions are guided to the MCP and a time-resolved ion-signal is recorded. The experimental sequence is repeated 500 times within one thermal atom cloud.

sequence. The experimental setup and atom sample preparation starting from cooling hot atoms in a magneto-optical trap is outlined in [102].

After an ultracold sample of atoms is prepared, the actual measurement is initiated by the creation of an ultracold ion. The ion is generated by the V-type photo-ionization scheme described in section 3.1. Briefly summarized, a single Rydberg atom is excited (cf. first red pulse in figure 3.5) from an ultracold ensemble of rubidium-87 atoms. Immediately afterwards, the Rydberg atom is photo-ionized by ripping off the Rydberg electron from its ionic core using a strong infrared photo-ionization laser pulse, which leaves a single ion, the prior Rydberg core, behind. Following the ion preparation, after a certain time t_{tof}, a probe Rydberg excitation takes place. Eventually, a small ion-extraction electric field is applied to pre-accelerate the prior photo-ionized ion, before a large electric field ionization pulse ionizes present Rydberg atoms. In a final step, both the photo-ionized ion and the electric field ionized ion are guided towards a microchannel plate (MCP) detector and the number of ions and their corresponding arrival times at the detector are recorded for many realizations of the experiment. As a result of the pre-acceleration, the arrival time on the detector is different for photo-ionized and electric field ionized ions, indicated by the two green bars in figure 3.5, allowing for separate evaluation of the ion signals stemming from photo-ionized ions and Rydberg atoms. The experiment is performed 500 times within a single atom cloud of typically $N_{\text{therm}} = 1.2 \times 10^5$ thermal atoms with a temperature of $T_{\text{therm}} = 1\,\mu\text{K}$. In order to gain statistics the ion signal is averaged over 20-30 atom cloud realizations.

During the time-of-flight t_{tof}, the ions trajectory is dictated by external electric fields. As mentioned before (see section 3.1), the photo-ionization laser is locked to a wavelength of 1010.2 nm, which gives rise to a total ionization excess energy of about 25 GHz, determined by the energy difference between the ionization laser and the continuum relative to the $6P_{3/2}$ state. The kinetic excess energy of the photo-ionized Rydberg atom is distributed between the detached electron and the remaining ion. Due to momentum conservation, the kinetic energy carried away by the prior Rydberg electron is over five orders of magnitude higher than the excess energy transfer on the ion. Essentially, the ionization excess energy ratio between the photo-ionized ion and the detached electron is given by the inverse mass ratio of the Rb^+ and the electron. The resulting kinetic excess energy of the photo-ionized Rb^+ ion is below $10\,\mu\text{K}$ or 0.86 neV. Thus, for typical residual stray electric fields present in the experiment ($\sim$1 mV/cm), the motion of the initially ultracold ion is dominated rather by external electric fields than the photo-ionization excess energy. Note that the total photon recoil caused by the

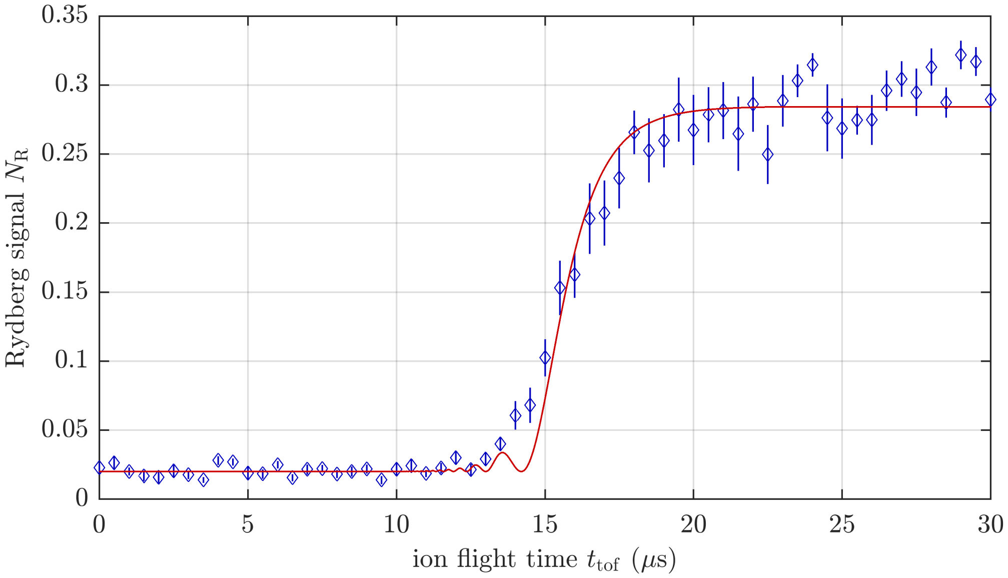

Fig. 3.6: Conditioned measurement of the ion-induced Rydberg blockade, probed with a 90S Rydberg state. In blue experimentally obtained Rydberg signal over the free evolution time-of-flight of the ion. In red the simulation of a two-level system with ground state and excited Rydberg state including the excitation bandwidth and the distance dependent ion-Rydberg atom interaction.

Rydberg excitation lasers is several orders of magnitudes smaller than the ion excess energy and thus can be neglected for the presented experimental findings.

In figure 3.6 an exemplary measurement of the ion-induced Rydberg excitation blockade is presented. In the line with the above introduced measurement protocol, after a single ion preparation, a probe excitation of a single atom into the 90S Rydberg state is performed in the presence of the close-by ion. A photo-ionization is achieved with an ionization laser pulse of 200 ns and a laser power of 210(5) mW. The probe Rydberg excitation is performed via a two-photon transition from the 5S ground state into the 90S Rydberg state, involving a 420 nm and 1015 nm laser, driving σ^+ and σ^- transitions respectively, in order to address the $m_J = +1/2$ Zeeman substate of the Rydberg atom. For both, the Rydberg excitation involved in the photo-ionization and for probing the ion-Rydberg atom interactions, a 500 ns excitation pulse with the same laser parameters is applied (see also section 3.1). The total electric field pulse sequence for ionization and acceleration is 20 microseconds long. The pulse sequence starts with the pre-acceleration pulse with an electric field strength of $E_{\mathrm{ext}} = 1.5\,\mathrm{V/cm}$. After 5 microseconds, additionally, the Rydberg ionization field is switched on ($E_{\mathrm{ioni}} = 115\,\mathrm{V/cm}$). Within the total pulse length of $20\,\mu\mathrm{s}$ the created ions reach the MCP detector. The obtained Rydberg signal N_R of the probe Rydberg excitation is conditioned on the presence of a photo-ionized ion.

First consider the experimentally obtained data, represented by the blue diamonds in figure 3.6. For a short time-of-flight of the ion, the probe Rydberg excitation is strongly suppressed due to the strong ion-Rydberg atom interaction at close internuclear distances. Thus, the energy levels of the addressed $90S$ Rydberg state are stark shifted out of resonance from the two-photon excitation. Explicitly, the energy shift on the $90S$ Rydberg state is greater than the two-photon excitation bandwidth. The excitation bandwidth is independently determined by measuring the spectral width of the bare $90S$ Rydberg state for the aforementioned excitation laser parameters, resulting in an excitation bandwidth of $\Gamma = 1.09(1)\,\mathrm{MHz}$, which is essentially given by the Fourier width of the excitation laser pulse. In figure 3.6 a strong suppression is evident for $t_{\mathrm{tof}} \lesssim 13\,\mu\mathrm{s}$. In this case the Rydberg signal N_{R} has dropped below 0.03.

For longer times ($t_{\mathrm{tof}} > 13\,\mu\mathrm{s}$) a sharp increase is apparent, and in total the Rydberg signal resembles an almost step-like function depending on the flight time of the ion. The signal reaches a plateau of $N_R = 0.3$ for later times-of-flight, which corresponds to a signal height of the bare Rydberg excitation. In this case, the ion-induced energy shift is much smaller than the Rydberg excitation bandwidth, and the probe Rydberg atom can be excited in an undisturbed manner. Thus, the ion trajectories for $t \geq 20\,\mu$s surpass a distance for which the pair interaction energy shift on the $90S$ Rydberg state can be neglected.

In accordance to the step-like behavior, it seems reasonable to define a critical time $t_{\mathrm{B}} \approx 16\,\mu$s at the center of the step function, for which the Rydberg signal N_{R} reaches 50% of its maximum signal height. In this case, the ion-induced energy shift on the $90S$ Rydberg state is approximately equal to the excitation bandwidth, which is in accordance to the blockade radius definition given in equation 3.2. Assuming the ion being exposed to a homogeneous electric field of about 1.5 mV/cm, which is on the order of the stray fields present in the experiment, the ion travels a distance of about $21\,\mu$m in $16\,\mu$s. In fact, we will see later on that this matches the predicted blockade radius for $n = 90$ quite nicely.

Next consider the red curve depicted in figure 3.6. In order to model the experimentally obtained data, the Liouville-von Neumann equation for a two-level system, here the ground state and the excited Rydberg state, is applied to obtain the Rydberg excitation dynamic including the ion-Rydberg atom interactions. Steady state calculations are carried out including the ion-Rydberg atom interaction for different internuclear distances, which yields the excitation dynamics for different ion-Rydberg atom separations. For this, an effective detuning, given by the distance dependent pair interaction potential as defined in equation 3.1 is applied, using the experimentally determined polarizability $\alpha_{90S} = 0.3\,\mathrm{MHz/(V/m)^2}$ of the $90S$ Rydberg state. In the calculations, the Rydberg excitation strength ($\Omega = 2\pi \times 0.43\,\mathrm{MHz}$) has been adjusted to match the Rydberg signal height of the experimentally obtained data for long ion flight times, corresponding to a bare Rydberg excitation with the ion-Rydberg atom interaction being negligible. Additionally, the calculated results are offset by 0.02 to account for the finite size of the excitation volume, which is defined through the spatial atom density and excitation laser intensity distribution. Ensuing that, the obtained excitation probabilities for different separations are mapped onto the ion time-of-flight assuming an accelerated motion caused by a constant homogeneous electric field. For the simulated Rydberg signal shown in figure 3.6 a constant electric field of 1.7 mV/cm has been used. Note that for the discussed modeling, both the stray electric field and the ion motion is neglected in the Rydberg excitation process, which is valid for the small stray electric fields present.

For the experimentally obtained data, presented above and in the following section 3.3, the Rydberg signal is conditioned on detecting ions stemming from photo-ionization. Owing to the pre-acceleration electric field pulse, the photo-ionized ions and the ions stemming from Rydberg atoms arrive at the detector for different arrival times. Thus, allowing conditioned measurement on detected photo-ionized ions.

In the following (figure 3.7) the time-resolved ion counts of the above presented ion-Rydberg blockade measurement of the $90S$ Rydberg state is depicted. After the probe Rydberg excitation, an elaborated electric field pulse sequence (cf. experimental sequence in figure 3.5) is applied to separate the ion counts, stemming from photo-ionization and electric field ionized Rydberg atoms, on the microchannel plate detector. Due to the ion extraction electric field, the ions originated by photo-ionization arrive at later times $t \gtrsim 10.1\,\mu$s. The count signal at earlier arrival times $t = 9.8\,\mu$s corresponds to the electric field ionized Rydberg atoms. At first this might seem odd. However, on a closer examination of the applied electric field sequence, guiding the ions towards the MCP detector, and the finite distance of the electric field plates[1], it becomes apparent that the electric field ionized ions overtake the pre-accelerated ions before reaching the detector. The reason for this is a shorter exposure time, of photo-ionized ions, to the strong

---

[1] Currently used second generation electric field compensation box [102, 103]

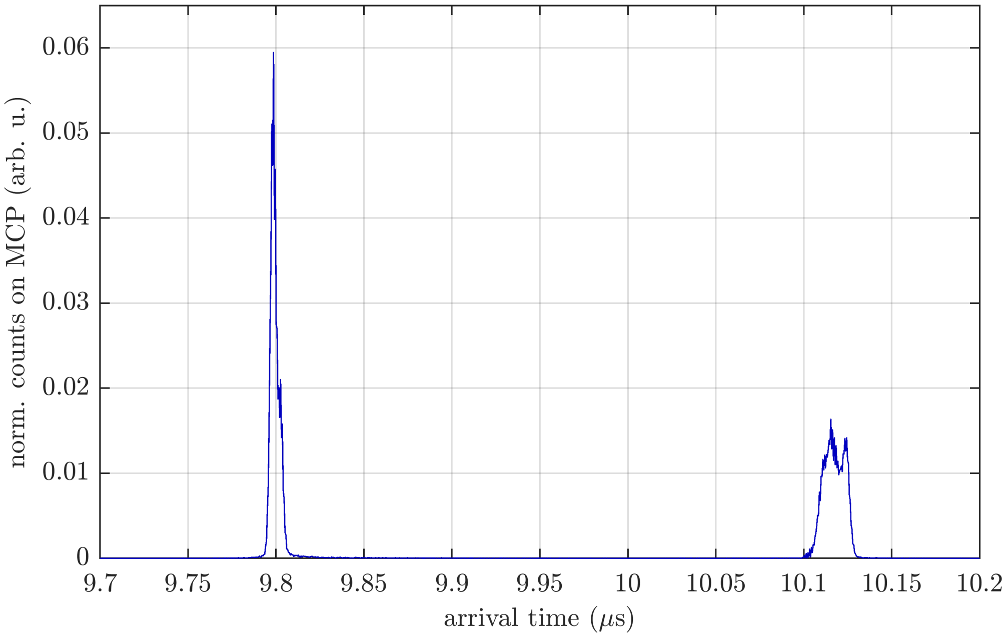

Fig. 3.7: Time-resolved ion counts, recorded by the microchannel plate detector, for the ion-induced Rydberg blockade measurement of the $90S$ Rydberg state shown in figure 3.6. The first peak, at an arrival time of $9.8\,\mu$s, corresponds to the ions stemming from electric field ionized Rydberg atoms. Ions produced by photo-ionization arrive the detector after about $10.1\,\mu$s.

electric field ionization pulse, which aims to field ionize the prior excited Rydberg atom and accelerate the produced ions towards the detector. The allocation of the ion count signal in figure 3.7 to ions stemming from electric field ionized Rydberg atoms and to photo-ionized atoms has been experimentally verified.

The Rydberg signal contrast for the blockade measurements is enormously increased by post-selection on the presence of an ion stemming from photo-ionization. In comparison, for the previously presented blockade measurement, the unconditioned total Rydberg signal and the conditioned Rydberg signal N_{R} is shown in figure 3.8.

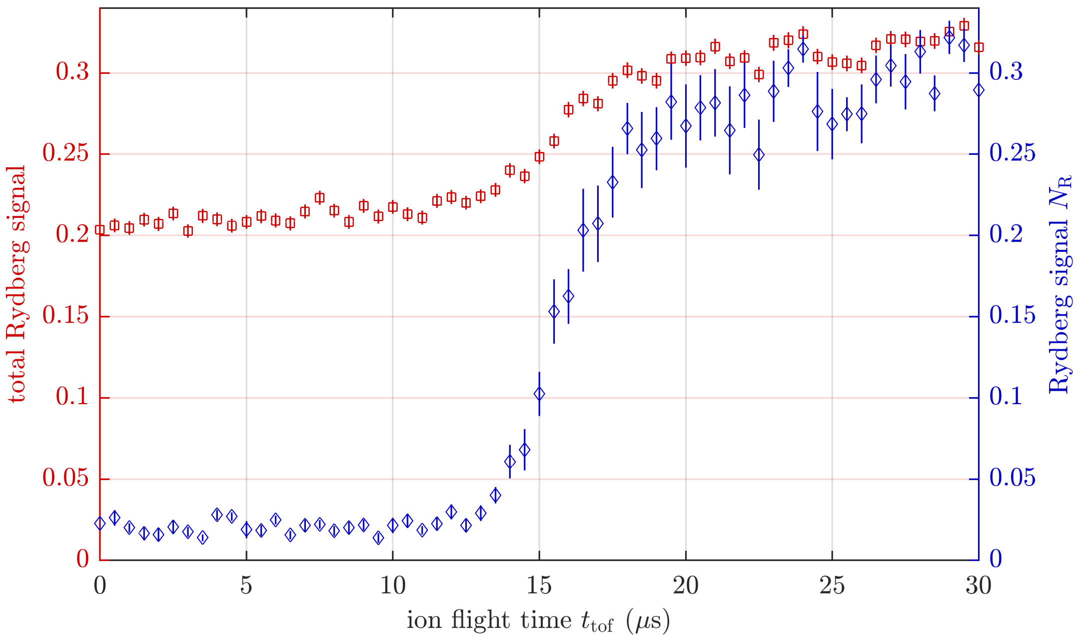

Fig. 3.8: Unconditioned total Rydberg signal and conditioned Rydberg signal N_R, for the 90S Rydberg blockade measurement presented in figure 3.6. In red, the total Rydberg signal without post-selection on detected ions stemming from photo-ionization is shown. In contrast, the blue data represent the post-selected or conditioned Rydberg signal.

By post-selecting on detected photo-ionized ions, the measurement is to a certain degree disentangled from the limited deexcitation and photo-ionization efficiencies, which is of particular importance. Since, deexcitation and photo-ionization not only depend on the laser powers but also on the Rydberg state involved in the ionization scheme. For technical reasons the same Rydberg state is used for both, photo-ionization and ion probing. Thus, by applying post-selection, the contrast, and comparability of the ion-Rydberg blockade measurements for different principal quantum numbers n, is increased. The blockade contrast for the total Rydberg signal presented in red in figure 3.8 is about 30%, while for the post-selected Rydberg signal N_R the contrast almost reaches 100%.

3.3 Ion-induced Rydberg blockade measurements

In the previous section, the pair interaction of a single ion and a single Rydberg atom, and the measurement technique for probing ion-Rydberg atom interactions was introduced. To demonstrate the ion-Rydberg atom interactions, the performed measurements of an ion-induced excitation blockade for the $90S$ Rydberg state were presented. For the demonstrated excitation blockade, a high contrast between suppressed and non-suppressed Rydberg excitations was revealed by post-selecting on detected photo-ionized ions. However, the blockade measurements so far, strongly depend on the stray electric fields present in the experiment.

In this section, the measurement method of the previous section is modified in order to minimize the importance of the stray electric fields, allowing a quantitative measurement of the ion-induced Rydberg excitation blockade. To perform this, an external electric field is applied, which dominates over the weak stray electric fields. With this, not only the field strength is defined during the measurements but also the electric field direction, which enables precise control of the ion motion down to the level of the stray electric field compensation.

In order to suppress the stray electric fields, which are evident in the blockade measurement presented in the previous section, a strong external electric field is applied to control the ion motion during the time-of-flight. In fact, instead of changing the flight time (cf. figure 3.5), the external electric field is scanned for a constant time-of-flight of the ion. For the measurement, the same ion preparation as presented in section 3.1, and the same measurement method as outlined in section 3.2, is used. Additionally, during a time-of-flight of $7\,\mu$s, the ion is exposed to an external electric field E_x. The measurements are performed for different electric fields, ranging from $-11.5\,\mathrm{mV/cm}$ to $11.5\,\mathrm{mV/cm}$. Figure 3.9 shows the blockade measurements for a range of principal quantum numbers ($51 \leq n \leq 100$).

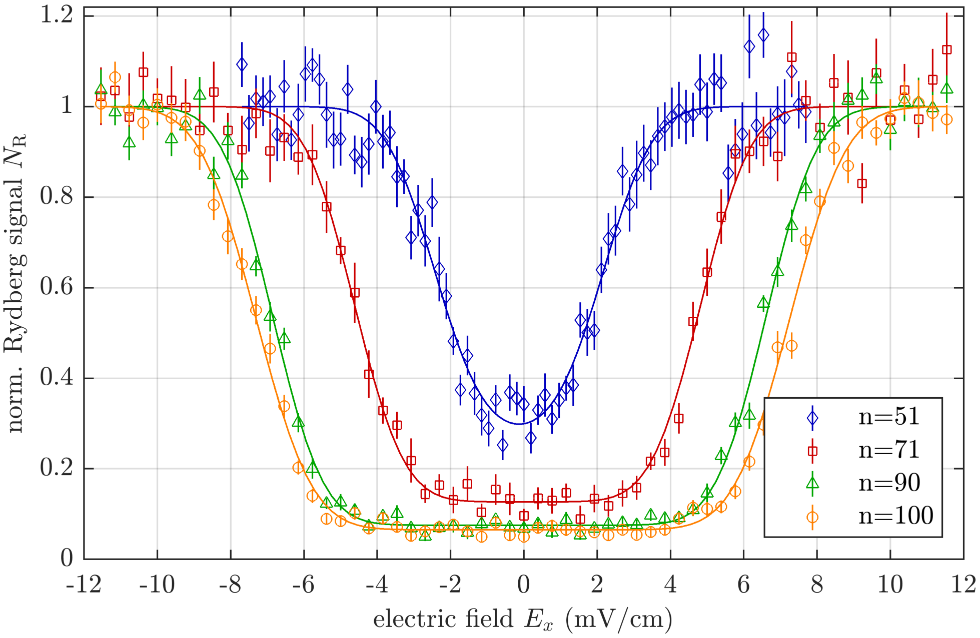

Fig. 3.9: Ion-induced Rydberg blockade measurement for different external electric fields E_x and a time-of-flight of $7\,\mu$s. For principal quantum numbers ranging from $n = 51$ (blue) over $n = 71$ (red), and $n = 90$ (green) up to $n = 100$ (yellow). The mean Rydberg signal N_R is normalized to the value obtained in the absence of the ion. Solid lines represent error-function fits to the data to extract the blockade radii. Error bars correspond to one standard deviation obtained from averaging over typically 20 atom cloud realizations.

For better comparison between the measurements of different principal quantum numbers, the Rydberg signal of the bare Rydberg excitation is used to normalize the signal to a maximum equals to one. In the limit of large electric fields, the Rydberg signal N_R settles to a constant value. In this case, the ion traveled further than the blockade radius within its time-of-flight of $7\,\mu$s, as on average the initial position of the ion is equal to the excitation volume of the probe Rydberg excitation (cf. section 3.2). In contrast, for smaller electric fields $|E_x|$, an excitation blockade is evident since in this case the Rydberg signal significantly drops. As expected, the suppression window visible in figure 3.9 becomes broader for larger

n, since increasing the principal quantum number increases the polarizability and consequently the blockade radius R_{b}. Additionally, with increasing blockade radius the finite size of the Rydberg excitation volume becomes more and more like a point-like excitation, when compared to the large blockade sphere, and thus loses on relevance, resulting in an increased suppression contrast. For example, at $E_x = 0$ the measured Rydberg signal drops virtually to zero for higher principal quantum numbers ($n = 90, 100$), while for $n = 51$ the signal reaches only down to about 30% of the bare Rydberg signal height.

In order to determine the blockade radius R_{b} from the measured Rydberg signal shown in figure 3.9, for each set of data an error-function fit of the form $\propto \operatorname{erf}\left((E_x - E^\star)/w\right)$ is applied to both, the positive and the negative flank. From the fitting procedure the center position $E^\star$ of the observed edge of the normalized Rydberg signal is obtained for each principal quantum number. The resulting fit functions are represented by the solid lines in figure 3.9, and given the accelerated motion of the ion in the electric field $E^\star$, are directly related to the blockade radius via $R_{\mathrm{b}} = eE^\star t_{\mathrm{tof}}^2/(2m)$, where m corresponds to the mass of an ^{87}Rb atom.

It should be noted that the ion flight time of $t_{\mathrm{tof}} = 7\,\mu\mathrm{s}$ is well conceived. On the one hand, the time-of-flight is chosen short enough to ensure that the expected $E^\star$ for the examined principal quantum numbers is larger than the residual stray electrical fields that are present during the experiments. On the other hand, t_{tof} is chosen long enough to ensure that the ion exceeds the blockade radius for the maximum value of the applied electric fields $|E_x|$, while the E_x induced energy stark shift on the nS Rydberg state is small compared to the Rydberg excitation bandwidth, ensuring an unperturbed probe excitation in the absence of the ion. Explicitly, for $n = 100$ the Rydberg line is shifted by $\sim 300\,\mathrm{kHz}$ for an electric field of $10\,\mathrm{mV/cm}$, which is small compared to the full excitation bandwidth $2\Gamma = 2.18(2)\,\mathrm{MHz}$.

In order to verify the extracted blockade radii from the measurements presented in figure 3.9, the time evolution of the state population for the system at hand is calculated and the blockade radius is determined applying the same fitting procedure as for the experimentally obtained data. For this, the time-dependent Liouville-von Neumann equation (3.3), including the ion-Rydberg atom pair interaction (see equation 3.4), is solved for different external electric fields.

$$\frac{\partial \rho}{\partial t} = \frac{i}{\hbar}\left[\rho, H\right] \tag{3.3}$$

$$H = \hbar \begin{pmatrix} 0 & \Omega/2 \\ \Omega/2 & \Delta + V(R)/\hbar \end{pmatrix} \tag{3.4}$$

Here Ω is the Rabi frequency and Δ the detuning from the interaction free Rydberg energy level. The two level system consists of the $\left|5S_{1/2}, F = 2, m_F = 2\right\rangle$ ground state and the excited nS Rydberg state. The pair interaction introduced in equation 3.1 is included by $V(R)$ and acts as an additional effective detuning from the excited state. For $\Delta = 0$ and large internuclear distances, for which the ion-Rydberg atom interaction becomes negligible ($V(R) \ll \hbar\Omega$), the ground state is resonantly coupled to the excited state. In contrast, and as mentioned in the previous section 3.2, for sufficiently large ion-Rydberg atom interactions ($V(R) \gg \Omega\hbar$), the addressed nS Rydberg energy level is shifted out of resonance, which gives rise to an ion-induced Rydberg excitation blockade. Furthermore, the interaction potential implicitly depends on the ion motion $V(R) = V(R(t, E))$ and thus on the ion flight time and the applied external electric field, which dictates the ion trajectory during the time-of-flight.

Figure 3.10 shows the calculated $90S$ Rydberg state population for different external electric fields. For each electric field the system is solved for the ion time-of-flight $t_{\text{tof}} = 7\,\mu$s used in the experiments. The excitation pulse length is set

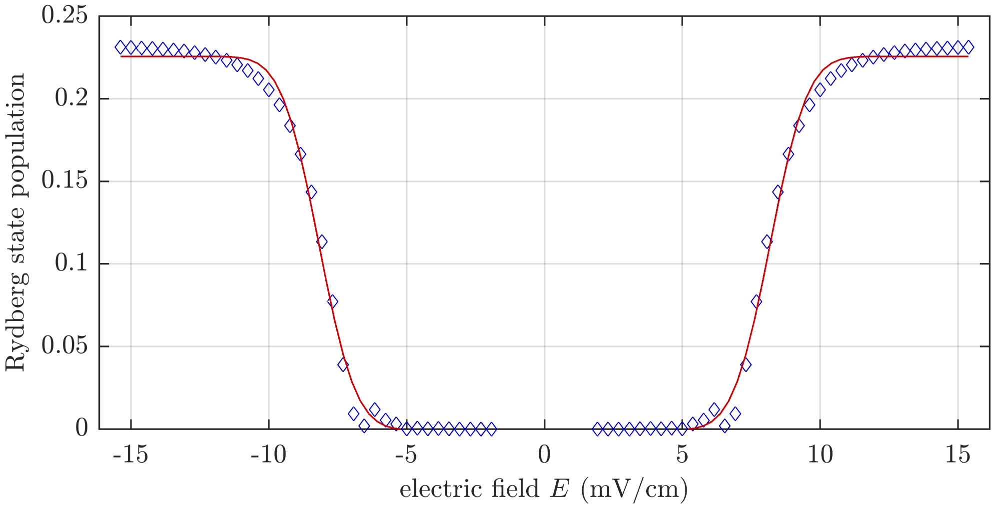

Fig. 3.10: Calculated $90S$ Rydberg state population of a probe Rydberg atom excited in the presence of an ion for different external electric fields E_x and an ion time-of-flight of $7\,\mu$s. The excitation pulse length is set to $0.4\,\mu$s to match the measured excitation bandwidth and a two-photon Rabi frequency of $\Omega = 2\pi \times 0.4\,$MHz is used.

to reflect the experimentally determined excitation bandwidth of $\Gamma = 1.09(1)$ MHz. A two-photon Rabi frequency of $\Omega = 2\pi \times 0.4\,$MHz is chosen to match the Rydberg signal height N_R of the experimentally obtained data. The red line corresponds to a symmetrized error-function fit of the same type, which is used to obtain $E^\star$ from the measured data shown in figure 3.9. From the fitting of the simulated Rydberg population, an electric field of $E^\star = 21.31\,$mV/cm is extracted, yielding a blockade radius of $R_\mathrm{b} = eE^\star t_\mathrm{tof}^2/(2m) = 23.6\,\mu$m. The theoretical blockade radius calculated via equation 3.2, using the polarizability $\alpha_{90S} = 0.3\,\mathrm{MHz}/(\mathrm{V/m})^2$ of the $90S$ Rydberg state, delivers a blockade radius of $R_\mathrm{b,theo} = 23.7\,\mu$m. In comparison, the theoretical blockade radius deviates by less than 0.5%, validating the blockade radii extracted via the error-function fit. For the examined principal quantum numbers, the above outlined comparison is carried out and a similar good agreement is found between the theoretical and the extracted blockade radii of the simulated state population, verifying the method used for extracting the blockade radius from the signal form of the measured data shown in figure 3.9.

The extracted blockade radii R_b from figure 3.9 are depicted as blue symbols in figure 3.11 for different principal quantum numbers. The error bars combine the effects of the two dominant sources of experimental uncertainties. These are, the finite pulse length of both, photo-ionization and Rydberg excitation and the residual stray electric fields present during the experiments. For small n, especially for $n = 51$, the relatively low extraction field $E^\star$ becomes comparable to the stray electric fields present in the experiments and a seemingly smaller $E^\star$ is extracted from the Rydberg signal, which, consequently, leads to an underestimation of the blockade radius. In fact, a blockade measurement for an electric field along the y-direction revealed a stray field of about $E_y \leq 1.5\,\mathrm{mV/cm}$. In contrast, for increasing principal quantum number this effect rapidly abates and the finite pulse length of photo-ionization ($0.2\,\mu\mathrm{s}$) and Rydberg excitation ($0.5\,\mu\mathrm{s}$) dominates, thereby the error is mainly given by the statistical uncertainty of the ion time-of-flight ($\pm 0.35\,\mu\mathrm{s}$).

The experimentally obtained blockade radii are compared to the theoretical prediction of equation 3.2 (cf. solid line in figure 3.11), which depends on the polarizability α_{nS} and the excitation bandwidth Γ. For the calculation of the theoretical value of R_b, the polarizability has been extracted from performed stark map calculations (see section 2.1.2), while for Γ an experimentally determined excitation bandwidth $\Gamma = 1.09(1)\,\mathrm{MHz}$ is used. For small n the measured R_b is captured by the theory and as expected the blockade expands for increasing principal quantum numbers. However, the measurement unveils a systematic suppression towards smaller R_b for increasing n. On closer examination, it becomes clear that the observed deviation can be traced back to the external electric field E_x present during the experiments. While the E_x induced energy level shift on the

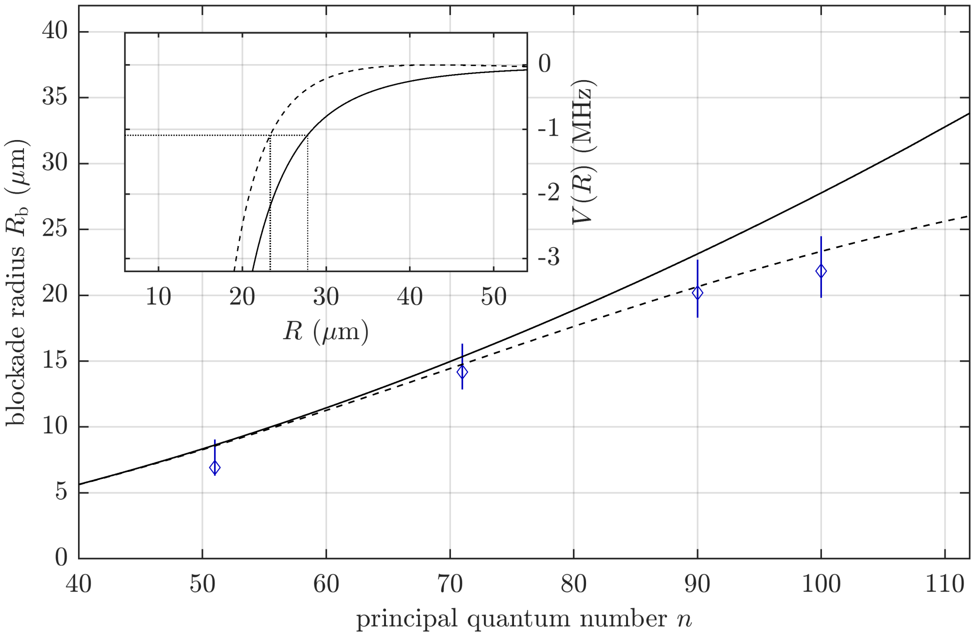

Fig. 3.11: Theoretical and measured Blockade radii for different principal quantum numbers. The diamonds represent the extracted blockade radius R_b from the measurements presented in figure 3.9 for different n. The solid line and the dashed line show the theoretical prediction of the field free and the non-field free case, respectively. The inset displays $V(R)$ for zero electric field (solid line) and for the applied electric field $E^\star$ (dashed line) for $n = 100$ ($E^\star = 7.3\,\mathrm{mV/cm}$). Dotted lines demonstrate the difference of R_b for a bandwidth $\Gamma = 1.09(1)\,\mathrm{MHz}$.

Rydberg state is negligible in the absence of the ion, the situation differs drastic when the ion is present. In that case, the external electric fields significantly effect the extension of the blockade sphere surrounding the ion, revealing a suppression of the blockade radius, which is most prominent for high principal quantum numbers.

In order to understand this, first recall that the pair interaction $V(R)$ originates from the energy shift of a Rydberg atom in the Coulomb field of an ion E_ion. In particular, for $n = 100$ and an ion-Rydberg atom distance equal to the blockade radius, the electric field of the ion at the position of the Rydberg atom reaches values on the order of the external electric field E_x applied ($E_{\text{ion}}(R_{\text{b}}) = 18\,\text{mV/cm}$). Furthermore, since the ion trajectory is determined by the external electric field, the field vectors of E_x and E_{ion} always point in the opposite direction. Consequently, E_x lowers the Coulomb field at the position of the probe Rydberg excitation, and thus effectively diminishes the blockade sphere surrounding the ion. This is illustrated in the inset of figure 3.11, where for $n = 100$ the modified in-field potential $V_{\text{mod}}(R)$ (dashed line) and the field free potential $V(R)$ (solid line) is depicted. The modified pair interaction, which includes the sum of the field of the ion $E_{\text{ion}}(R) = e/(4\pi\epsilon_0 R^2)$ and the external electric field E_x reads as

$$V_{\text{mod}}(R) = -\alpha_{nS} \frac{\left(E_{\text{ion}}(R) - |E_x|\right)^2}{2}. \tag{3.5}$$

The minus sign in front of $|E_x|$ accounts for the opposite directions of the external and the ion-induced electric field at the position of the Rydberg atom. In analogy to the previously introduced R_{b} (cf. equation 3.2), the in-field modified blockade radius $R_{\text{b}}^{\text{mod}}$ is obtained by equating the pair interaction $V_{\text{mod}}(R)$ with the excitation bandwidth Γ.

$$R_{\text{b}}^{\text{mod}} = \left(\frac{e\alpha_{nS}}{4\pi\epsilon_0 (|E_x|\alpha_{nS} + \sqrt{2\alpha_{nS}\Gamma})} \right)^{1/2} \tag{3.6}$$

The experimentally obtained in-field blockade radii displayed in figure 3.11 are measured in an external electric field of $E_x = E^\star$. The measured $E^\star$ in turn, is related to the modified blockade radius $R_{\text{b}}^{\text{mod}}$ via equation 3.6. Consequently, both the in-field blockade radius $R_{\text{b}}^{\text{mod}}$ and the corresponding electric field $E^\star$ must be determined in a consistent manner for a purely theoretical prediction. For this, $E^\star$ and $R_{\text{b}}^{\text{mod}}$ are calculated in an iterative and self-consistent way.

In the following we acquire the theoretical in-field blockade radii step-by-step. For a given principal quantum number n, first the blockade radius $R_{\text{b}}^{(1)}$ for the field free case given by equation 3.2 (or by equation 3.6 with $E_x = 0$) is calculated. Next, from the ion trajectory the electric field $E^{(1)}$ (equation 3.7) is determined and plugged into equation 3.8, which yields the modified blockade radius $R_\mathrm{b}^{(2)}$ for an electric field $E^{(1)}$.

$$E^{(i)} = 2mR_\mathrm{b}^{(i)}/(et_\mathrm{tof}^2) \tag{3.7}$$

$$R_\mathrm{b}^{(\mathrm{i+1})} = \left(\frac{e\alpha_{nS}}{4\pi\epsilon_0(|E^{(i)}|\alpha_{nS} + \sqrt{2\alpha_{nS}\Gamma})}\right)^{1/2} \tag{3.8}$$

Subsequently, the resulting blockade radius is used to determine the electric field needed to displace the ion by $R_\mathrm{b}^{(2)}$ during the time-of-flight t_tof. Now, the blockade radius $R_\mathrm{b}^{(i)}$ and the electric field $E^{(i)}$ is calculated iteratively. After a few iterations, the procedure converges to self-consistent values for the electric field $E^\star$ and the modified blockade radius $R_\mathrm{b}^\mathrm{mod}$. In figure 3.11, the resulting $R_\mathrm{b}^\mathrm{mod}$ (dashed line) are compared with the experimentally obtained blockade radii and an overall good agreement between theoretically and experimentally determined blockade radii is observed. Note that this procedure is also tested against the state population simulations presented in figure 3.10 by introducing the modified pair interactions $V_\mathrm{mod}(R)$ from equation 3.5. An exemplary comparison between the measured and the simulated Rydberg signal is presented in figure 3.12 for $n = 90$. The visible deviations at the positive and negative flank of the signal are well covered by the estimated statistical uncertainty (green shaded area) of the time-of-flight of the ion (see also error bars in figure 3.11).

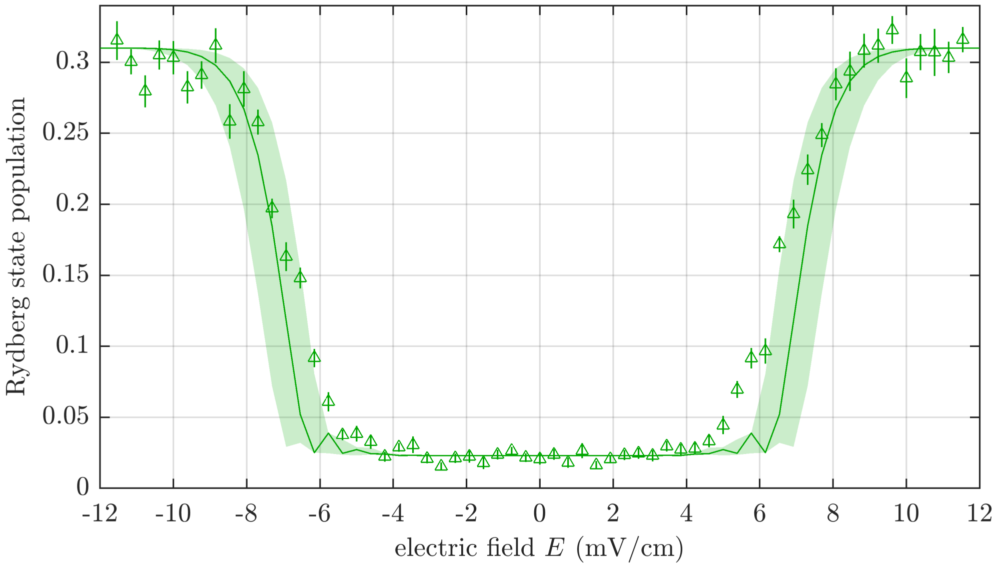

Fig. 3.12: Calculated (solid line) and measured (symbols) $90S$ Rydberg state population of a probe Rydberg atom excited in the presence of an ion as a function of the electric field E_x and an ion time-of-flight of $7\,\mu$s. The shaded region represents the statistical uncertainty of t_{tof} ($\pm 0.35\,\mu$s). For the simulations, an excitation pulse length of $0.4\,\mu$s is used to match the measured excitation bandwidth and a two-photon Rabi frequency of $\Omega = 2\pi \times 0.45\,$MHz to match the signal height from the experiment. Furthermore, the simulated data is offset by 0.02 to match the experimental data. This accounts for the finite excitation volume.

3.4 Single atom electric field probe

In the previous sections 3.2 and 3.3, the pair interaction between a single ion and a Rydberg atom was investigated by means of an ion-induced Rydberg excitation blockade. External electric fields are used to precisely control the ion's motion, allowing for an accurate measurement of the extension of the excitation blockaded region around the ion.

This section examines the potential of the ion-induced blockade measurement technique as a sensitive single atom electric field probe. In contrast to the previous blockade radius measurements, for which the experimental sequence was specifically tailored to minimize the effect of stray electric fields, here, the experimental parameters are adapted to determine the direction and strength of the stray electric field present in the experiment. For this purpose, a more sensitive excitation blockade measurement, for different electric fields, is carried out in all three spatial directions.

In order to increase the sensitivity of the blockade measurement, the ion time-of-flight is extended, and consequently, smaller electric fields are required to draw the ion out of the blockade region. Additionally, the measurements are performed with a highly excited ($n = 100$) Rydberg state, to minimize finite size effects of the excitation volume. This allows for a more accurate electric field measurement. In figure 3.13 the electric field probe measurements for all three spatial directions and an ion time-of-flight of $t_{\mathrm{tof}} = 34\,\mu\mathrm{s}$ are presented. The top row shows the Rydberg signal N_{R} for different applied electric fields E_i along the $i = \{x, y, z\}$ directions. The blockade features are quantified via a Gaussian fit to the Rydberg signal. In comparison to the blockade radius measurements from section 3.3, the observed blockade features reveal greatly reduced widths ($\lesssim 2\,\mathrm{mV/cm}$) around the center of the zero electric field. For the prolonged ion flight time $t_{\mathrm{tof}} = 34\,\mu\mathrm{s}$ and the theoretical blockade radius $R_{\mathrm{b}} = 27.8\,\mu\mathrm{m}$ for the $100S$ Rydberg state, the expected value of the half width half maximum is given as: $E^{\star} = 2m/(et_{\mathrm{tof}}^2)R_{\mathrm{b}} = 0.43\,\mathrm{mV/cm}$. While the feature width for the field scan along the z-direction matches the predicted value of $2E^{\star}$, the widths for the E_x and E_y scan deviate significantly. The difference of the widths along the x- and y-direction can be attributed to a residual electric field gradient in the xy-plane. To verify this, stark spectroscopy is performed on the $133S$ Rydberg state for different positions of the tightly focused 1015 nm excitation beam. The resulting spectra for $\pm 40\,\mu\mathrm{m}$ shift in x- and y-direction each, reveal a Rydberg line shift of

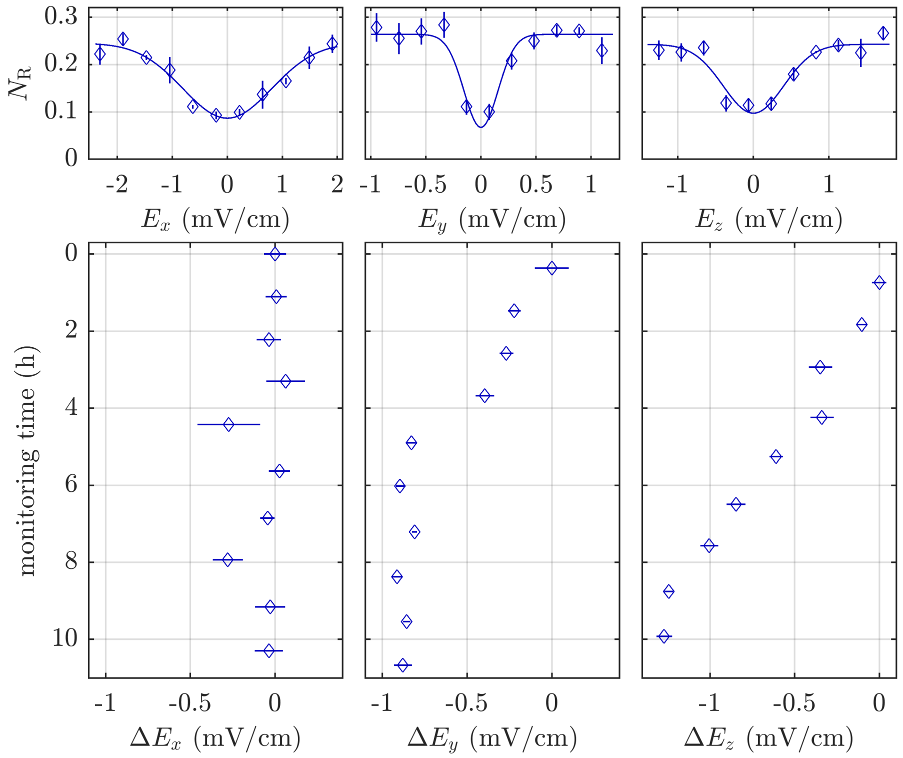

Fig. 3.13: Single ion electric field probe measurement. In the top row, the Rydberg signal N_R is shown for different applied electric fields E_i in all spatial directions $i = \{x, y, z\}$ for $n = 100$ and an ion flight time of $t_\mathrm{tof} = 34\,\mu$s. Solid lines result from Gaussian fits to the data. The center position of the ion-induced blockade feature yields the residual stray field along respective spatial component. Error bars indicate one standard deviation, which results from averaging over typically four realizations. The bottom row shows the temporal drift ΔE_i of the electric field in all three spatial directions. The drift is obtained from the difference of the fitted centers of the data shown in the top row. The error bars represent the 1σ confidence bound of the corresponding fit result.

the S-state corresponding to an electric field difference of about $1\,\mathrm{mV/cm}$ over a distance of $10\,\mu$m, which gives rise to an electric field gradient of $0.01\,\mu\mathrm{V}/\mu\mathrm{m}^2$ present in the experiment. As can be seen from the experimentally obtained data, the relatively small gradient has a significant influence on the ion trajectory for the small, homogeneous electric fields applied.

Contrary to the previous evaluation of the blockade feature in section 3.3, instead of the blockade width, which yields the blockade radius, the center position is extracted in order to obtain the zero electric field present in the experiment. In turn, the extracted zero fields allows one to precisely monitor and compensate for temporal changes of the residual stray electric fields. In the bottom row of figure 3.13, the relative center positions of the fitted Rydberg signals for all three spatial directions are shown for a series of measurements taken over the course of more than 10 hours. The error bars represent the 1σ confidence bound of the corresponding fit results, which indicates electric stray field monitoring at the level of $\lesssim 100\,\mu\mathrm{V/cm}$. Note that, the here presented level of electric field control in principle allows for detection of the excess energy transferred onto the ion during the photo-ionization process (cf. section 3.1) if the residual electric field gradients are thoroughly compensated.

In conclusion, the presented measurements demonstrate that the produced, photo-ionized ion can be used as a sensitive electric field probe, which is read out via a subsequent Rydberg excitation. Owing the spatially localized ion creation and probe Rydberg excitation, electric fields are measured with high spatial resolution on the micrometer scale. The achieved accuracy of the measured electric field significantly exceeds the level of stray field compensation typically used on the experimental apparatus ($\sim 1-2\,\mathrm{mV/cm}$ for Rydberg stark spectroscopy of $160S$ state). Furthermore, the obtained data reflect the fact that in the experiment the ion is additionally exposed to a small electric field gradient, which affects the resulting ion trajectory. In principle, even higher sensitivities can be achieved by the presented measurement method for longer ion flight times. Note that, the electric field sensitivity of the measurements presented above is limited by slowly drifting stray electric fields during the data acquisition, which takes about 20 minutes for each data set shown in the top row of figure 3.13.

3.5 Ion-Rydberg and Rydberg-Rydberg atom blockade

So far, the strong long-range interaction between a single ion and a single Rydberg atom is studied in the context of ultracold gases. For this, an ion-induced Rydberg excitation blockade was introduced in section 3.2 in analogy to the Rydberg blockade between two excited atoms, which was originally proposed in a parallel work of D. Jaksch *et al.* and M. D. Lukin *et al.* (ref. [18] and [19]). In conclusion to the previous sections 3.2 and 3.3, the investigated ion-induced Rydberg excitation blockade is compared with the well known and widely used Rydberg blockade [12, 13, 18–20, 104–106], which originates from strong Rydberg-Rydberg interaction. In the following, the excitation blockade of a Rydberg atom in the presence of either a single ion (Rb^+) or a Rydberg atom (Rb^*) is compared for the case of $^{87}\mathrm{Rb}$. For this, the blockade radius is derived by equating the Rydberg excitation bandwidth Γ with the interaction for both, the ion-Rydberg atom pair ($\mathrm{Rb}^+ + \mathrm{Rb}^*$) and a pair of Rydberg atoms ($\mathrm{Rb}^* + \mathrm{Rb}^*$). First, consider that for relatively large internuclear distances R (typically on the micrometer scale) the pair interaction for both cases can be described by the leading term of the second-order perturbation theory [24, 62]. In this case, the interaction between an ion in the ground state and an atom in the nS Rydberg state is given by the asymptotic polarization potential $V_{C_4}(R) = -C_4/R^4$ (cf. section 2.1.2), while in turn for a pair of two nS Rydberg atoms the van-der-Waals interaction $V_{C_6}(R) = -C_6/R^6$ dominates [62].

Consequently, the blockade radii for the ion-Rydberg atom (see also equation 3.2) and the Rydberg-Rydberg atom pair interaction are defined as follows.

$$R_{\mathrm{Ion-Ryd}} = (C_4/\Gamma)^{1/4} \tag{3.9}$$

$$R_{\mathrm{Ryd-Ryd}} = (C_6/\Gamma)^{1/6} \tag{3.10}$$

The C_4 coefficient is related to the Rydberg atom polarizability via $\alpha_{nS} = 2\left(4\pi\epsilon_0/e\right)^2 C_4$, which can be extracted from stark map calculations (cf. sec-

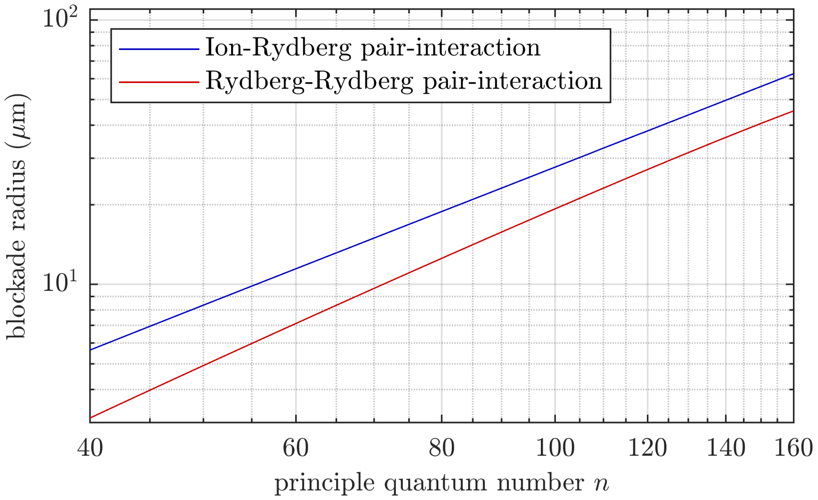

Fig. 3.14: Comparison of the nS Rydberg excitation blockade for ion-induced pair interaction ($\mathrm{Rb}^* + \mathrm{Rb}^+$) and induced dipole-dipole pair interaction ($\mathrm{Rb}^* + \mathrm{Rb}^*$). The interaction strength is given by the C_4 and C_6 coefficient for the ion-induced and the dipole-dipole induced blockade, respectively. For different n, the C_4 coefficient is extracted from stark map calculations. C_6 coefficients are determined via equation 3.11. In both cases, the excitation bandwidth is set to the experimentally obtained value of $\Gamma = 1.09(1)\,\mathrm{MHz}$.

tion 2.1.2). For the C_6 coefficient, a n-dependent fit of the energy shifts of two Rydberg atoms interacting via induced dipole-dipole interaction (van-der-Waals interaction) can be utilized. A fit-model of the C_6 coefficient was derived by Singer *et al.* [107]. The corresponding expression for two atoms in the nS Rydberg state is given (in atomic units) by:

$$C_6 = n^{11}(11.97 - 0.8486n + 3.385 \times 10^{-3} n^2). \tag{3.11}$$

Figure 3.14 shows the calculated excitation blockade radius for a nS Rydberg atom interacting with an ion (blue) and with second nS Rydberg atom (red), over a large range ($40 \leq n \leq 160$) of principal quantum numbers n.

In comparison, the calculated blockade radii presented in figure 3.14 exhibit an overall larger excitation blockade for the ion-Rydberg atom interaction. For the principal quantum numbers examined, the ion-Rydberg blockade radii exceed the Rydberg-Rydberg blockade radii by almost a factor of 2, while a similar scaling with n is observed for both, the ion-Rydberg atom and the Rydberg-Rydberg atom interaction. The almost identical n-scaling of the two blockade radii comes with no surprise and can be understood easily.

For this, let us recall the scaling of the interaction strength by n for both interacting pairs, the ion-Rydberg atom pair $C_4 \propto \alpha_{nS} \propto n^7$ and the pair of two Rydberg atoms $C_6 \propto n^{11}$. Although the n-scaling of the polarizability $\left(n^7\right)$ and the van-der-Waals interaction strength $\left(n^{11}\right)$ is different, the blockade radius for both cases (given by equation 3.9 and 3.10) finally yield a similar n-dependence.

$$R_{\mathrm{Ion-Ryd}} \propto n^{1.75}$$

$$R_{\mathrm{Ryd-Ryd}} \propto n^{1.83}$$

In conclusion, by comparing the here studied ion-induced Rydberg excitation blockade with the well-known excitation blockade of two interacting Rydberg atoms, a similar n-dependence and extension of the blockaded region is found. Although, the polarization potential is relatively short-ranged compared to the long-range van-der-Waals interaction, it turns out that for the energy and length scales investigated the blockade sphere of the explored pair interactions result in an blockade radius of similar size over a large range of principal quantum numbers. Note that when exceeding the energy range of a few MHz, e.g. by employing an excitation bandwidth or a Rydberg detuning on the order of several tens of MHz, the difference between the short-range polarization potential and the long-range van-der-Waals interaction becomes unambiguous.

Despite the fact, that the ion-induced Rydberg and the Rydberg-Rydberg blockade exhibit a similar spatial extension for the here investigated energy and length scale, which is also commonly used in the context of Rydberg atoms in the field of atomic physics, employing a system combining ions and Rydberg atoms is of particular interest. Such a hybrid ion-atom system enables one to bridge the field of trapped ions and the field of (ultra-)cold neutral atoms, allowing for utilization of the advantages of both: The versatility of neutral atoms and the precise control of the ion preparation and measurement, which is proposed to be of great use in the field of quantum information processing and quantum simulation [20, 24, 108]. In particular, the hybrid system consisting of trapped ions and ultracold fermions has been proposed to emulate solid-state physics (ref. [108]) as it features analogies close to natural solid-state systems. Furthermore, on the one hand, ion-Rydberg atom interactions might be used for generating entanglement between Rydberg atoms and the ion motion or the internal state of an ion [24], or, on the other hand, to modify ion-atom collisions (ref. [109]), control ion-atom chemistry (ref. [110]) or influence ionic transport by hopping conductivity (ref. [111]).

3.6 Measurements in a dense ensemble

Up to now, the binary interaction between a single ion and a Rydberg atom has been studied on a single particle level. By means of an ion-induced Rydberg excitation blockade, and in analogy to the Rydberg-Rydberg blockade, an ion-Rydberg blockade radius was introduced and the ion trajectory was probed in an external electric field (section 3.2 and 3.3). Furthermore, based on the pair interaction, spatially resolved electric field measurements have been performed (section 3.4).

This section discusses the potential application of the ion creation and probing technique discussed above to study the ion motion in an ultracold and dense gas. In particular, the excitation blockade might be used to probe the ion trajectory and draw conclusions on the ion-neutral atom collisions during the ion time-of-flight. For this, an ultracold ion is embedded in a Bose-Einstein condensate and the ion-induced Rydberg excitation blockade mechanism is employed to probe the ion's position in time, with the ultimate goal of tracing the ion transport in a BEC [111]. In contrast to ion-atom hybrid systems, which are commonly used to study ion-atom interactions [112], here, no ion trap is needed and additionally, the blockade measurement technique enables one to trace the ion motion on the micrometer scale. At this point, it should be mentioned that yet another approach for studying ion-atom collisions, which is initiated by photo-detaching the Rydberg electron of an ultralong-range Rydberg molecule, has been proposed by Schmid *et al.* [92, 93]. The main purpose of this section is to present the status of an ongoing investigation, with the focus on the emerging challenges, when employing the ion creation and probing technique in a BEC where many-body effects become important.

The section is structured as follows. In the first part, characterization measurements for the ion creation inside a BEC are presented. In particular, the results on the photo-ionization efficiency and the prior Rydberg deexcitation probability are discussed. In the second part, the above defined ion-induced Rydberg blockade is considered for many neutral atoms interacting with the probe Rydberg atom, following that first blockade measurements in the condensate are presented, and finally classical trajectory simulations including ion-atom collisions are performed to model the measured probe Rydberg signal.

First of all, contrary to the previous measurements in this chapter, here a large, elongated, cigar-shaped BEC is used for the purpose of future ion transport measurements. For these, typically, an electric field is applied to induce an ion motion along the field axis. As a consequence of the 20 times higher density, frequent Langevin collisions with the neutral gas atoms are expected to cause a diffusive drift of the ion. In order to reach a drift regime, many ion-neutral atom collisions have to take place before the ion leaves the atom sample. Consequently, for the experiments, the large, magnetically trapped, cigar-shaped BEC is used rather than the smaller, pancake-like, optically trapped condensate (cf. section A.3 and A.2). In addition, a larger condensate allows for more subsequent Rydberg excitations per atom sample and thus provides more statistics compared to the BEC in the optical trap.

In the experimental setup, the diameters of a BEC with typical $N_{\mathrm{BEC}} = 1 \times 10^6$ ^{87}Rb atoms condensed in the magnetic trap are: $d_{\mathrm{TF}} = \{10\,\mu\mathrm{m}, 120\,\mu\mathrm{m}, 10\,\mu\mathrm{m}\}$, where d_{TF} is twice the Thomas-Fermi radius along the spatial directions $\{x, y, z\}$. This means, for the level of achieved stray electric field compensation of about 0.1 mV/cm and an ion prepared in the center of the BEC, when neglecting ion-atom collisions, the ion stays in the atom sample for at least $30\,\mu$s. With this in mind, a rough estimate of the ion-neutral atom scattering rate $\Gamma_{\mathrm{sc}} = n\sigma_{\mathrm{L}}v = 2\pi n\sqrt{2C_4/\mu} = 1.1\,\mu\mathrm{s}^{-1}$ suggests that in the experiment multiple collisions might actually occur before the ion reaches the edge of the BEC. For the here determined scattering rate Γ_{sc}, a BEC peak density $\hat{\rho}_{\mathrm{BEC}} = 4.5 \times 10^{14}\,\mathrm{atoms/cm^3}$, the reduced mass μ of the colliding ^{87}Rb atom and ion, the ^{87}Rb ground state polarizability $\alpha_0 = 318.8(14)\mathrm{a.u.}$ [113], where α_0 is related to C_4 via $\alpha_0 = 2(4\pi\epsilon_0/e)^2 C_4$, and the Langevin cross section $\sigma_{\mathrm{L}} = 2\pi\sqrt{C_4/E_{\mathrm{c}}}$, with the collision energy E_{c} [114], are used.

Before the measurements of the photo-ionization efficiency and the ion-induced Rydberg excitation blockade for an ion in a Bose-Einstein condensate are presented, it is important to reflect that for the earlier introduced concept of creating (section 3.1) and probing (section 3.2) a single ion, the interaction between Rydberg and neutral atoms is neglected due to the low density of the cold but dilute thermal atom sample used for the experiments.

The situation changes drastically, when considering the relatively high density in a BEC. For the peak density in the experiment ($4.5 \times 10^{14}\,\mathrm{atoms/cm^3}$), the mean nearest neighbor distance between neutral atoms of the condensate is about 80 nm ($1500\,\mathrm{a_0}$), which is much smaller than the extension of the Rydberg electron for the principal quantum numbers investigated in the context of this work. In fact, a Rydberg atom ($100S$) placed in the BEC center engulfs about 2000 condensed atoms in its spherical Rydberg electron orbit, which extends over a radius of $1\,\mu$m.

3.6.1 Photo-ionization in a BEC

As introduced in the background section 2.3, for a Rydberg atom excited in a BEC, a mean field energy shift proportional to the local density of the neutral ground-state atoms inside the Rydberg electron orbit is apparent. It is intriguing to utilize this density shift to initialize a scattering event of the photo-ionized ion with the surrounding ultracold atoms in a high density region of the condensate.

For this, the V-type photo-ionization scheme presented in section 3.1 is applied to create a single ultracold ion in the BEC. In the first step of the ionization scheme a Rydberg atom is excited and the positioning of the later ionized ion is approximately equal to the initial Rydberg position. By utilizing the electron-atom scattering, for a large red detuning from the atomic resonance, the ion can be positioned in the center of the BEC. However, for a Rydberg atom excited in an environment of such high densities, the probability for chemical reactions is high. In fact, in a work of Schlagmüller *et al.* (ref. [S7]) state-changing collisions induced by Rydberg electron-neutral atom scattering in the vicinity of the ionic Rydberg core have been observed on the microsecond timescale.

For the experiments a magnetically trapped BEC (cf. section A.3) of $N_{\mathrm{BEC}} =$ 900k condensed atoms and a thermal fraction of about 25% is used. In the following, the experimentally obtained photo-ionization probability for an ion in the BEC is shown. For the ion creation, the $71S$ Rydberg state is used and a Rydberg detuning of $\delta = -40\,\mathrm{MHz}$ is applied in order to initialize the V-type ionization process by exciting a Rydberg atom in a region with a density of about $4 \times 10^{14}\,\mathrm{atoms/cm^3}$, which corresponds to the center region of the BEC. In contrast to the ionization scheme introduced in section 3.1, for the photo-ionization efficiency measurements in the BEC, the Rydberg excitation and deexcitation pulses are overlapped, in order to compensate for the relatively short collisional lifetime ($\tau < 1\,\mu\mathrm{s}$ cf. ref. [S7]) of the excited $71S$ Rydberg state.

In figure 3.15 the photo-ionization efficiency for an ion created close to the BEC center is shown. The ionization probability reaches a maximum just below 10% for an ionization laser power of about 45 mW. In comparison to the earlier reported efficiencies in an optically trapped thermal atom cloud (cf. section 3.1.2), the here measured maximum value is about 8-10 times lower.

However, when taking into account the offset magnetic field direction and the laser polarization, it becomes clear that in the case of the optical trap, where the circular polarized deexcitation laser propagates along the magnetic field axis,

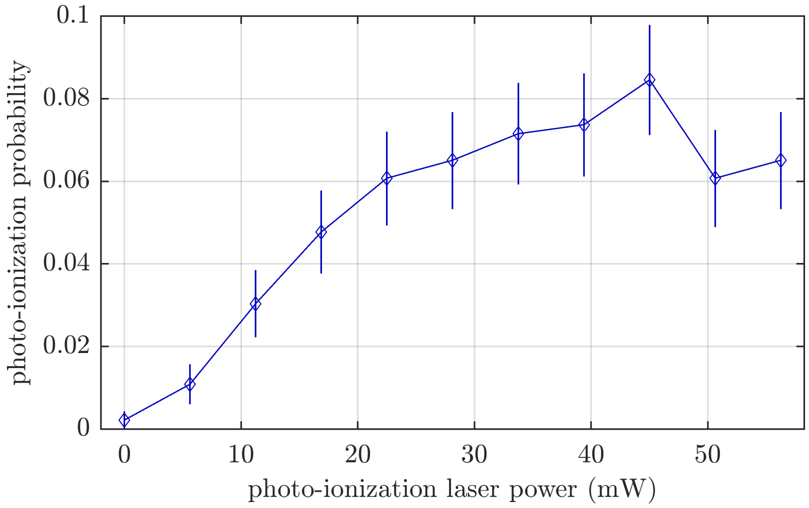

Fig. 3.15: Photo-ionization efficiency for different photo-ionization laser powers in a BEC. The ionization scheme (cf. section 3.1) involves the $71S$ Rydberg state, and a Rydberg detuning of $\delta = -40\,\mathrm{MHz}$ is used to prepare the ion in the center of the BEC. For the photo-ionization, the Rydberg excitation and deexcitation pulses are overlapped.

only a σ^- transition is driven. While in the case of the magnetic trap the linear polarized deexcitation laser is perpendicular to the offset B-field, and thus couples at max with 50% laser power. In fact, the measured photo-ionization probability, when using a magnetically trapped thermal atom cloud, yields an efficiency of 30% for an ionization laser power of 100 mW, while in the optical trap about 70% efficiency is reached for the same power.

Furthermore, the ionization probability drops for higher powers of the photo-ionization laser. At first this seems contradictory, however, considering the relatively high intensity ($I_{\mathrm{peak}} \sim 8\,\mathrm{mW}/\mu\mathrm{m}^2$ for 45 mW) of the tightly focused laser beam, it becomes obvious that the ionization laser induces an optical dipole potential, which attracts neutral atoms inside the laser focus. Indeed, for a laser power of e.g. 50 mW the depth $\hat{U}_{\mathrm{dip}}$ of the dipole potential (cf. ref. [115]) induced by the ionization laser is: $\hat{U}_{\mathrm{dip}} = -h \times 36\,\mathrm{MHz}$, which leads to a time averaged potential depth of $-h \times 28\,\mathrm{kHz}$ for the ionization laser pulse duration 400 ns and the repetition rate 2 kHz used in the experiment.

In comparison, the resulting laser induced average potential depth is on the order of the chemical potential $\mu = h \times 3.6\,\mathrm{kHz}$ of the BEC. The neutral atoms move towards the laser focus position, which leads to a sizable density increase given enough time and eventually results in three-body atom loss. In turn, the three-body atom loss leads to a heating of the BEC. In the experiment, significant atom loss is evident for 500 repetitions of Rydberg excitation and subsequent photo-ionization over a time of 250 ms. In consequence, for the evaluation of the experimentally obtained data, typically only the first 50 or 100 shots are used, for which the atom loss is low. Nonetheless, for the aforementioned ionization pulse duration, repetition rate and only 100 experimental realizations within one atom cloud, the ionization probability drops by about 10-20% for ionization laser powers $\gtrsim 45\,\mathrm{mW}$, as is visible in figure 3.15. The reduced efficiency can be traced back to a decrease of the Rydberg excitation probability for increasing photo-ionization laser power, which has been experimentally confirmed by blocking the deexcitation laser and measuring the Rydberg signal N_R for different photo-ionization laser powers.

In order to conclude the results of the experimentally obtained photo-ionization efficiency in the BEC, a series of characterization measurements for the deexcitation of the $71S$ Rydberg state are performed. For this the typical photo-ionization scheme as introduced in section 3.1 is applied, but in comparison to the above presented measurements, the photo-ionization power is set to zero and the deexcitation laser pulse is applied after the Rydberg excitation. The deexcitation efficiency is directly related to the Rydberg state population after the deexcitation laser pulse. The Rydberg signal N_R is normalized to the signal height in absence of the deexcitation laser. In the following, the Rydberg state population after a

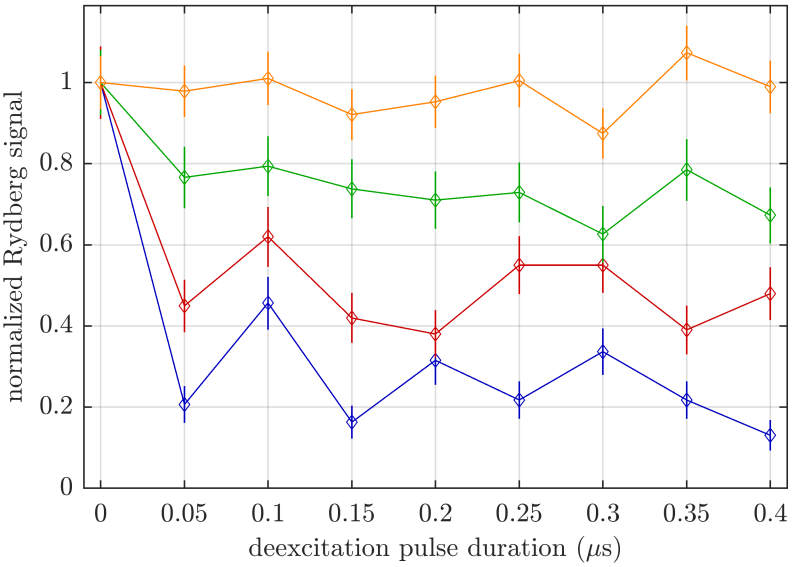

Fig. 3.16: Density-dependent Rydberg deexcitation measurement for a $71S$ Rydberg state excited in a BEC. The Rydberg signal N_R is normalized to one for a deexcitation pulse duration of zero. The different curves represent the deexcitation probability for different Rydberg detunings δ. From bottom to top, $\delta = \{0\,\mathrm{MHz}, -5\,\mathrm{MHz}, -32\,\mathrm{MHz}, -40\,\mathrm{MHz}\}$.

deexcitation attempt, for a Rydberg atom embedded in the BEC, is presented for different Rydberg detunings δ and different interaction times of the Rydberg atom with the surrounding neutral atoms of the condensate.

Figure 3.16 shows the results of the deexcitation measurements for a Rydberg detuning varying between 0 MHz and −40 MHz, which corresponds to a Rydberg excitation in a density region ranging from the dilute thermal atom cloud around the BEC for $\delta \approx 0\,\mathrm{MHz}$ ($\rho \approx 1.6 \times 10^{13}\,\mathrm{atoms/cm^3}$) to the peak density for $\delta \approx -40\,\mathrm{MHz}$ ($\rho \approx 4 \times 10^{14}\,\mathrm{atoms/cm^3}$) of the condensate. For small detunings, the Rydberg population rapidly decreases already for short deexcitation pulse durations. The Rydberg signal drops to 20% for a deexcitation duration of 50 ns for $\delta = 0\,\mathrm{MHz}$ and to about 50% for $\delta = -5\,\mathrm{MHz}$. In both cases, the Rydberg atom is expected to be excited on the very edge of the condensate, where the density is

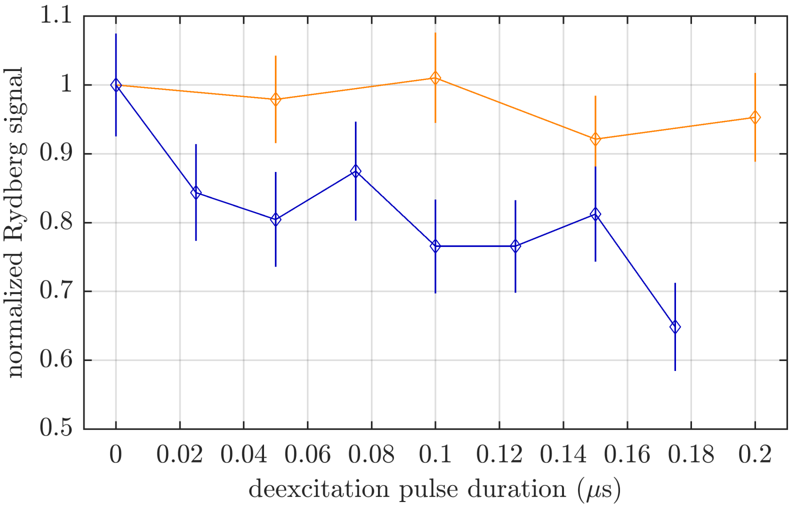

Fig. 3.17: Fast deexcitation measurement for a Rydberg detuning of $\delta = -40\,\text{MHz}$ for the $71S$ Rydberg state excited in a BEC. The Rydberg signal N_R is normalized to one for a deexcitation pulse duration of zero. The blue (lower) curve represents the obtained Rydberg signal for a fast Rydberg excitation ($t_\text{exc} = 150\,\text{ns}$) and subsequent deexcitation, while the yellow (upper) data points, which are taken from figure 3.16, correspond to a Rydberg state population after deexcitation for a Rydberg excitation duration of 500 ns.

low. Accordingly, the efficiency is similar to the deexcitation probabilities obtained for a thermal atom cloud in the optical trap (cf. section 3.1.1). Additionally, when increasing the pulse duration, an oscillating Rydberg signal, corresponding to damped Rabi oscillations for the light coupled intermediate $6P_{3/2}$ state with the $71S$ Rydberg state, is evident. However, when exciting a Rydberg atom close to the BEC center (cf. curve for $\delta = -32\,\text{MHz}$ and $\delta = -40\,\text{MHz}$ in figure 3.16) where the density is relatively high and the Rydberg atom interacts with many neutral atoms, the Rydberg state population almost stays constant, indicating that no deexcitation takes place. The microsecond timescale of the observed state-changing collisions (ref. [S7]) of Rydberg atoms excited in the BEC, strongly indicate that the dynamics of the neutral atoms inside the Rydberg orbit prevent the deexcitation process of the Rydberg atom.

To validate this reasoning, a deexcitation measurement for a shorter Rydberg excitation pulse and a Rydberg detuning of $\delta = -40\,\mathrm{MHz}$ is performed. Instead of the 500 ns Rydberg excitation pulse duration, here a pulse length of 150 ns is applied, reducing the total time from Rydberg excitation to deexcitation from $0.6\,\mu\mathrm{s}$ down to $0.25\,\mu\mathrm{s}$. As is apparent from figure 3.17, the measured Rydberg signal for a faster Rydberg excitation yields an overall lower Rydberg population. Consequently, for an overall faster photo-ionization pulse sequence higher ion creation efficiencies are achievable.

3.6.2 Ion-induced Rydberg blockade in a BEC

In the previous 3.6.1, the photo-ionization of a Rydberg atom immersed in a BEC was discussed. When considering the high densities in a condensate and accordingly a large number of atoms interacting with the Rydberg electron, it turns out that by choosing a large Rydberg detuning δ, a Rydberg excitation in a region of higher densities is provoked (see also section 2.3). However, the interaction of the Rydberg electron with the neutral atoms also prevents an efficient photo-ionization. Nonetheless, an ion creation and probing in the center of the condensate is still desirable for studies on ion-atom interactions, even for low ionization efficiencies. This section discusses the ion-induced Rydberg blockade in a dense ensemble, displays the occurring complications accompanied by a probe Rydberg excitation including the electron-atom interaction, and presents a way of treating these. In the following, the experiments are performed in a magnetically trapped BEC (cf. section A.3) of $N_{\mathrm{BEC}} = 900\mathrm{k}$ condensed atoms and $N_{\mathrm{thermal}} = 300\mathrm{k}$ uncondensed thermal atoms with a temperature of $T < 200\,\mathrm{nK}$.

First, consider a Rydberg excitation in the condensate. In figure 3.18 an experimentally obtained Rydberg spectrum of the $71S$ state is shown, for an excitation in the BEC (blue data) and the thermal cloud (red data) surrounding

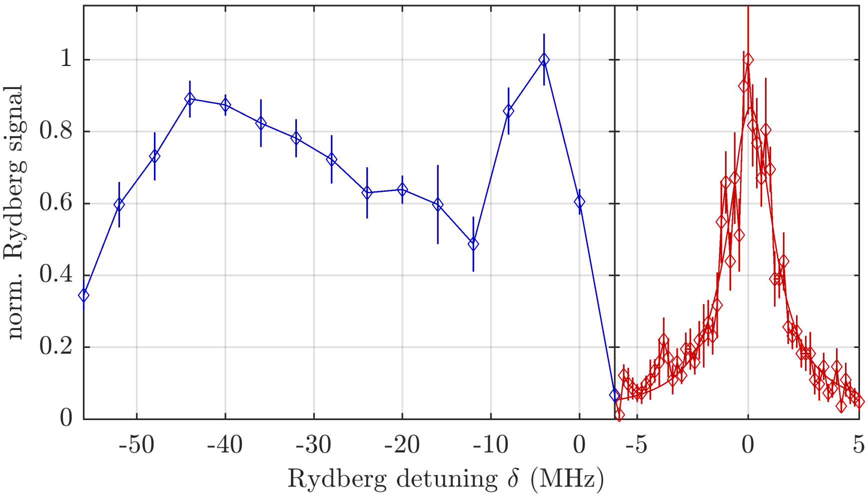

Fig. 3.18: $71S$ Rydberg spectrum for an excitation in the BEC and in the thermal part of the condensate. For better comparison the Rydberg signal N_R of both spectra are normalized to their respective maximum value. Left panel (blue curve): Rydberg spectrum in the BEC, the excitation laser is focused onto the BEC center. Right panel (red curve): Rydberg spectrum in the thermal cloud around the BEC, the excitation laser focus is displaced in x-direction by $8\,\mu$m.

the condensate. In contrast to the spectrum in the condensate, for the spectrum in the thermal part, the tightly focused excitation laser is displaced from the BEC center by $8\,\mu$m in x-direction, illuminating the thermal cloud next to the short axis of the cigar-shaped condensate, but not the BEC. Given the high density, the strong Rydberg electron-atom interaction leads to a large mean field energy shift and broadening (cf. section 2.3) of several tens of MHz, while for an excitation in the thermal part of the condensate the spectral line shape is essentially defined by the Fourier transform of the Rydberg excitation pulse.

Next, consider the ion-Rydberg atom interaction, which is given by the asymptotic Rydberg atom polarization potential $V(R) = -C_4/R^4$ (see section 3.2), and the mean field energy shift ΔE of equation 2.34. In a classical picture (ref. [S6]), the neutral atoms are distributed inside the Rydberg orbit according to the local

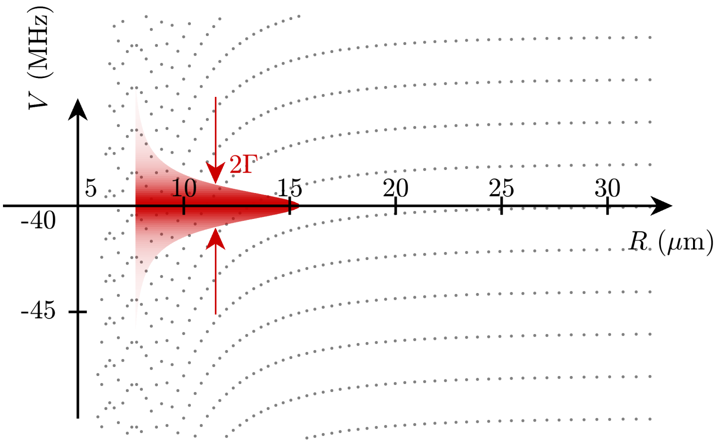

Fig. 3.19: Schematic illustration of the ion-Rydberg atom interaction in the BEC for the $71S$ Rydberg state and a Rydberg detuning of $\delta = -40\,\mathrm{MHz}$. The Rydberg atom-ion interaction (dotted) is shown for asymptotic energies ranging from $-50\,\mathrm{MHz}$ to $0\,\mathrm{MHz}$ for different internuclear distances R. The total excitation bandwidth of $2\Gamma = 2.2\,\mathrm{MHz}$ is indicated by a red shaded curve.

density distribution, leading to the aforementioned Rydberg electron-neutral atom interaction induced energy shift. This energy shift is essentially offset by the ion-Rydberg atom interaction for a Rydberg excitation in the presence of an ion. As a consequence, when addressing the high density region in the BEC, using a negative Rydberg detuning, the ion-induced Rydberg energy level shift can be compensated by the electron-atom interaction. This situation is illustrated for the $71S$ Rydberg state in figure 3.19, where the ion-Rydberg atom interaction over the internuclear distance R is depicted for asymptotic energies ranging from $-50\,\mathrm{MHz}$ to $0\,\mathrm{MHz}$ emulating different mean density shifts $\Delta E(\rho)$. For a distance $R \lesssim 6\,\mu\mathrm{m}$, the ion-induced energy shift is larger than $45\,\mathrm{MHz}$ and thus covers already a major fraction of the density broadened spectrum. When considering a negative Rydberg detuning, it becomes obvious that the excitation blockade radius defined in section 3.2 is not valid for a probe Rydberg excitation in the center of the condensate.

For a negative Rydberg detuning of e.g. $\delta = -40\,\mathrm{MHz}$, indicated by the shaded red curve in figure 3.19, a whole band of density shifted Rydberg energy levels crosses the excitation bandwidth at an internuclear distance $R \gtrsim 6\,\mu\mathrm{m}$, allowing a probe Rydberg excitation for an ion-Rydberg atom distance much smaller than the measured blockade radius in the thermal atom sample (cf. section 3.3). Overall, due to the low photo-ionization efficiency and the strongly reduced ion-Rydberg blockade radius, an alternative approach for studying ion-atom interactions in a condensate, using the in section 3.1 and 3.2 outlined approach of ion creation and probing, is realized in the following. Note that in the simplified picture illustrated in figure 3.19, by offsetting the ion-induced interaction with the mean field energy shift ΔE, one neglects that for different density shifts different regions in the BEC are addressed (cf. detuning to density mapping in section 2.3). This approximation is valid since the relatively large ion-induced energy shifts exceed the maximum mean field density shift for ion-Rydberg atom distances larger than the radial extension of the condensate.

3.6.3 Probing ion motion inside a BEC

Instead of utilizing the density shift to place the ion and probe Rydberg atom in the center of the BEC, the ion creation and the probe excitation are both located in the dilute thermal atom cloud surrounding the condensate. For this, the tightly focused photo-ionization and the infrared excitation laser focus are displaced in x-direction by $8\,\mu\mathrm{m}$ from the center of the BEC. With a dilute atom sample, the photo-ionization efficiency reaches a value of 20-30%, which is more than twice the efficiency reached in the condensate center. Furthermore, for the ion probe excitation in the thermal part, the mean field energy shift is small compared to the total excitation bandwidth $2\Gamma = 2.5(3)\,\mathrm{MHz}$. The excitation bandwidth is determined by a Lorentz function fit to the thermal spectrum shown in figure 3.18.

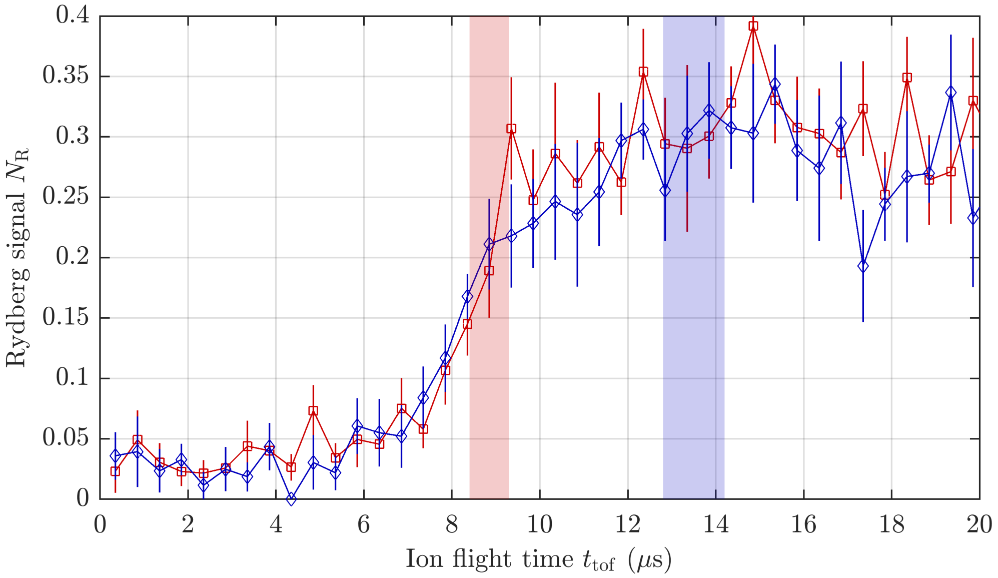

Fig. 3.20: Ion-induced Rydberg excitation blockade measurement next to the condensate for the $100S$ Rydberg state. Photo-ionization and probe Rydberg excitation laser focus are displaced from the BEC center in x-direction by $8\,\mu$m. In blue (red), the probe Rydberg excitation signal N_{R} for $E_x = +5\,\mathrm{mV/cm}$ ($E_x = -5\,\mathrm{mV/cm}$), dragging the ion through (away from) the condensate, over the ion flight time t_{tof}, is shown. The shaded regions indicate the resulting t_{tof} including a stray field of up to $1\,\mathrm{mV/cm}$ in the direction of E_x and a constant average drift velocity $\bar{v}_{\mathrm{drift}}$ inside the condensate (see text).

Figure 3.20 shows the ion-induced Rydberg blockade measurement for the ion creation and probing next to the condensate. The experimentally obtained probe Rydberg excitation signal N_{R} is shown for an ion guiding electric field of $E_x = +5\,\mathrm{mV/cm}$ (blue data) and $E_x = -5\,\mathrm{mV/cm}$ (red data), accelerating the ion towards the BEC and away, respectively. The in-field blockade radius for the $100S$ Rydberg state is given by equation 3.6. For the applied electric field $|E_x| = 5\,\mathrm{mV/cm}$, the measured Rydberg excitation bandwidth $\Gamma = 1.25(15)\,\mathrm{MHz}$ and a polarizability of $\alpha_{100S} = 0.63\,\mathrm{MHz/(V/m)^2}$, extracted from performed stark map calculations (cf. section 2.1.2) yields a blockade radius of $R_{\mathrm{b}} = 24\,\mu$m. In analogy to the evaluation of the probe Rydberg signal in section

3.2, and given the accelerated motion of the ion, the edge center $t^\star$ of the rising Rydberg signal N_R is expected at an ion time-of-flight of $t_\mathrm{tof} = \sqrt{2R_\mathrm{b}/(|E_x|e/m)} = 9.3\,\mu\mathrm{s}$. The experimentally obtained probe signal N_R, however, shows a sharp edge around $t_\mathrm{tof} = 8.4\,\mu\mathrm{s}$. When considering the thermal cloud expansion and the level of stray electric field control during the experiments, the seemingly apparent discrepancy can be explained for the non-collisional case (red data). Assuming a maximum initial distance between the ion and the probe Rydberg atom of $10\,\mu\mathrm{m}$ perpendicular to the ion trajectory (displacement along z-direction), which corresponds to the $1/e$-diameter of the thermal atom cloud along the excitation beam axis, and an uncertainty along the ion trajectory of $\pm 1.8\,\mu\mathrm{m}$, taking into account the excitation laser focus, this alone results in an uncertainty of $1.1\,\mu\mathrm{s}$. When additionally considering the Rydberg excitation (500 ns) and photo-ionization pulse duration (200 ns) a width of about $\Delta t_\mathrm{tof} = 1.8\,\mu\mathrm{s}$ for the Rydberg signal edge is expected. Furthermore, as mentioned before (see section 3.2), the stray electric field compensation level of the stark spectroscopy used in the experiment is $\lesssim 1\,\mathrm{mV/cm}$. Moreover, stray field drifts on the same order are observed over the course of a few hours (cf. section 3.4). When assuming an additional electric field of $1\,\mathrm{mV/cm}$ present during the experiment, the edge center of the Rydberg signal is expected at $t_\mathrm{tof} = 8.4\,\mu\mathrm{s}$ (cf. red shaded region in figure 3.20), matching the experimentally obtained data ($E_x = -5\,\mathrm{mV/cm}$) for pulling the ion away from the condensate.

So far the case of an unperturbed trajectory of the prior photo-ionized ion has been discussed. In contrast, for an ion dragged through the BEC, when collisions between the ion and the atoms of the condensate become important, the trajectory of the field guided ion is strongly perturbed. This, in turn, is expected to be reflected in the probe Rydberg signal, since, in the case of many collisions the ion is slowed down in the condensate and consequently leaves the ion-induced blockade volume for later times-of-flight in comparison to an ion which trajectory is only weakly perturbed. The experimentally obtained data for dragging the ion through the short axis of the BEC, with an electric field of $E_x = +5\,\mathrm{mV/cm}$ (cf. blue data set in figure 3.20), shows only a minor difference to the data for which the ion was moved away from the condensate ($E_x = -5\,\mathrm{mV/cm}$).

Apparently, for the situation realized in the experiment, either only a small amount of Langevin (spiraling) ion-atom collisions occur or the ion trajectory is additionally affected in a so far non-contemplated manner. In order to investigate this further, first, consider the Langevin ion-atom collisions. By definition, a spiraling collision results in a large scattering angle (ref. [114]) in the relative frame of the collision partners, deflecting the incoming particle by angles up to 180°. In the laboratory reference frame, due to momentum conservation, scattering into large angles translates into a significant momentum transfer from the moving ion onto a quasi-stationary neutral atom. In this picture, the ion motion is slowed down inexorably when enough spiraling collisions take place.

When an external electric field is applied, the accelerated motion of the ion is interrupted for each spiraling collision and the current ion velocity is reduced. Considering many collisions, an average drift of the ion, whose velocity is closely related to the scattering rate Γ_{sc} can be defined as:

$$\vec{v}_{\mathrm{drift}} = \frac{e}{m}\tau\vec{E} \tag{3.12}$$

The drift velocity points in the electric field direction and is multiplied by the elementary charge e divided by the effective mass m, which in the present system is equal to the ion mass, and the inverse scattering rate $\tau = 1/\Gamma_{\mathrm{sc}}$. For modeling the ion motion in the presence of an external electric field, as a first estimate, one might try to utilize the drift velocity defined above (deduced from the well-known Drude model), which is regularly used in solid-state physics with great success.

In a simplified model, a mean density $\bar{\rho}$ is determined by averaging the condensate density distribution along the x- and z-direction over the extension of the BEC, taking into account the different density regions, which the ion probes when dragged through the condensate by the external electric field E_x, while assuming uniformly distributed ion creation positions along the excitation beam path (z-axis).

The resulting average density of $\bar{\rho} = 1.7 \times 10^{14}\,\mathrm{atoms/cm^3}$, leads to a mean scattering rate of $\bar{\Gamma}_{\mathrm{sc}} = 0.4\,\mu\mathrm{s}^{-1}$ (cf. section introduction 3.6), which in turn yields a mean drift velocity of $\bar{v}_{\mathrm{drift}} = 1.4\,\mathrm{m/s}$ for an external electric field of $E_x = 5\,\mathrm{mV/cm}$. Considering the relatively short extension of the BEC along the electric field axis ($d_{\mathrm{TF}} = 10\,\mu\mathrm{m}$), one might argue that the application of a drift velocity is not suitable, since, for the parameters mentioned above, on average only 3 spiraling collisions occur per ion trajectory. While this is certainly questionable for a single trajectory or the average of only a few experimental realizations, in the case of the presented data, the Rydberg signal is obtained from averaging over several thousand experimental realizations, and thus the ion-atom collisions in the condensate are sampled many times over. Consequently, the definition of a drift velocity for modeling the ion motion within the BEC appears to be reasonable.

For an ion creation center $8\,\mu\mathrm{m}$ displaced in x-direction from the condensate center, as it is the case for the experimental data presented in figure 3.20, an accelerated ion motion outside of the BEC, and a constant velocity equal to the determined average drift velocity $\bar{v}_{\mathrm{drift}} = 1.4\,\mathrm{m/s}$ inside the condensate, on average, the ion exceeds a flight distance equal to the in-field $100S$ ion-Rydberg blockade radius $R_{\mathrm{b}} = 24\,\mu\mathrm{m}$ for a time-of-flight of $t_{\mathrm{tof}} = 14.2\,\mu\mathrm{s}$, and $t_{\mathrm{tof}} = 12.8\,\mu\mathrm{s}$ when including a $1\,\mathrm{mV/cm}$ stray field in the direction of the applied electric field E_x (cf. blue shaded region in figure 3.20). In comparison to the free-flight case, for which an average time-of-flight of $t_{\mathrm{tof}} = 9.3\,\mu\mathrm{s}$ is expected, the simple model outlined above suggests that in the presence of ion-atom collisions inside the condensate, on average, the ion flight time is delayed by about $3\,\mu\mathrm{s}$.

These findings seemingly contradict the experimentally obtained data shown in figure 3.20, where a similar $t^\star$ is found for both cases, for dragging the ion through (blue data) and away (red data) from the condensate. At this point, it should be noted that for the considerations above, the choice of the average density $\bar{\rho}$ strongly influences the result of the average scattering rate and can, therefore, change the resulting drift velocity and consequently the outcome of the above applied simple model drastically. Nonetheless, for the system at hand, for pulling the ion through the condensate, the theoretical contemplation suggests a stronger probe excitation suppression for longer ion times-of-flight. On a closer examination, when comparing the data sets shown in figure 3.20, despite the fact that the probe signals rise at a similar time, the condensate data for $E_x = +5\,\mathrm{mV/cm}$ (blue data) reach a maximum for slightly later ion flight times.

So far, the theoretical treatment takes into account the presence of a stray electric field of up to $1\,\mathrm{mV/cm}$. That, however, does not explain why the probe signal for the condensate data appears to be less affected by ion-atom scattering than expected. One can think of two experimental parameters, which strongly influence the obtained probe Rydberg signal in a manner that ion-atom collisions are seemingly less influential; namely the excitation bandwidth Γ and additional uncompensated electric field gradients. Actually, for an increased excitation bandwidth the ion-induced Rydberg blockade radius is reduced and consequently, the ion leaves the blockaded region for an earlier time-of-flight. However, in this case, the Rydberg signal shape is mostly compressed along the ion flight time axis, but for a large enough blockade radius, the ion-atom collisions are still expected to be evident in the probe signal. In contrast, for a non-zero electric field gradient, the ion experiences a different field strength for an increasing distance from the stray field compensated Rydberg excitation region and thus is primarily either slowed down or additionally accelerated along its trajectory. Especially for the latter, the ion is dragged faster through the condensate and consequently less ion-atom scattering events occur. Furthermore, while the excitation bandwidth is experimentally determined and basically given by the Fourier transform of the Rydberg excitation pulse, the stray electric fields are compensated before and after each measurement but only at the Rydberg excitation position. In a previous measurement (see section 3.4) an electric field gradient of 1 mV/cm over a distance of 10 μm has been determined.

In order to test the influence of a stray electric field gradient on the probe Rydberg signal, semi-classical state population simulations were performed. The results of these calculations are presented in the following. To model the Rydberg signal, first, classical trajectory simulations including the ion-atom scattering by utilizing a stochastic collision approach are carried out. After that, for each resulting ion trajectory, the time-dependent state population (for details see section 3.3) for the probe Rydberg excitation is calculated, from which a mean probe Rydberg state population is obtained for different ion flight times. For the ion trajectory simulations and the state population calculations, the initial ion position and the probe Rydberg atom location are sampled according to the atom density distribution and the intensity profile of the tightly focused excitation laser, respectively. In detail, spiraling ion-atom collisions, for which, in contrast to glancing collisions, the ion trajectory is strongly affected, are included assuming a density-dependent scattering rate for Langevin collisions. In analogy to the approach of Zipkes *et al.* (ref. [114]), the density distribution of the condensate is taken into account by applying a local density collision time sampling method.

In the following the experimentally obtained probe Rydberg signal N_{R} from figure 3.20 are compared with the results of the performed state population simulation using the Monte Carlo sampled ion trajectories including the ion-atom collisions. As a reminder, for the blue data, the ion is dragged through the condensate via an applied external electric field of $E_x = +5\,\mathrm{mV/cm}$, while the red data serves as a reference measurement, for which the ion is pulled away from the BEC by applying the electric field in the opposite direction $E_x = -5\,\mathrm{mV/cm}$. For both data sets the ion is created and probed $8\,\mu\mathrm{m}$ away from the condensate center in x-direction. As previously discussed, for both experimental data sets, N_R systematically rises for earlier flight times, which could be caused by either a stray electric field or an electric field gradient (or both). For a constant electric field offset during both measurements, the sign of the stray electric field in x-direction must be reversed between the two measurements to additionally accelerate the ion motion along the applied field axis. In contrast, a positive constant electric field gradient affects both data sets similar by additionally accelerating the ion for an increasing distance from the field compensated excitation region. Furthermore, the electric fields at the Rydberg excitation position are carefully compensated before, and verified after each measurement, whereas determining an electric field gradient is more involved and thus a gradient compensation is carried out less frequently. In figure 3.21 the experimental data are compared with the simulated Rydberg signal. For the simulations, the experimentally obtained atom number $N = 1 \times 10^6$, and a BEC fraction of 0.8, an excitation laser beam waist of $w_0 = 1.8\,\mu\mathrm{m}$ at the focus position, an excitation bandwidth of $\Gamma = 1.25(15)\,\mathrm{MHz}$, and the in the experiment applied electric fields of $E_x = \pm 5\,\mathrm{mV/cm}$, are used. Additionally, a stray electric field and an electric field gradient along the axis of the applied field E_x are introduced to reproduce the measured Rydberg signal N_R. For reasons of simplicity, the electric field gradient is modeled via a constantly changing electric field offset along the x-axis, with a zero electric field at the excitation laser focus position. Typically, in the experiment, the zero electric field changes on the order of a few mV/cm over a distance of a few tens of micrometers in the vicinity of the

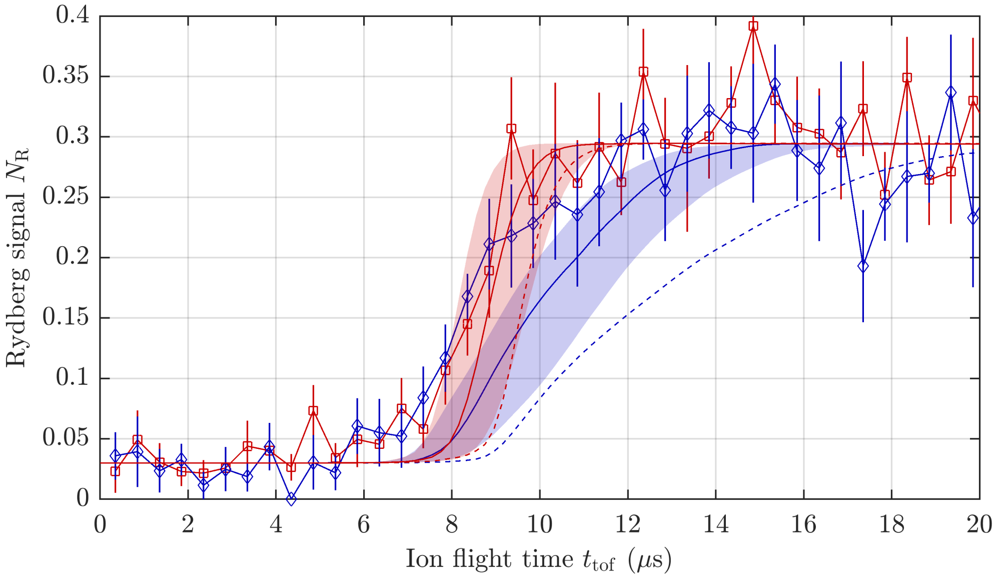

Fig. 3.21: Ion-induced Rydberg excitation blockade measurement next to the condensate for the $100S$ Rydberg state. Photo-ionization and probe Rydberg excitation laser focus are displaced from the BEC center in x-direction by $8\,\mu$m. In blue (red), the probe Rydberg excitation signal N_R for $E_x = +5\,$mV/cm ($-5\,$mV/cm), dragging the ion through (away from) the BEC, over the ion flight time t_{tof}, is shown. Solid (dashed) lines represent the probe Rydberg state population for the performed classical trajectory simulations, including ion-atom collisions, with (without) an electric field gradient, while the shaded regions show the results for the stray electric fields present in the experiment (see text).

Rydberg excitation center. For the simulations presented in figure 3.21, an increase of the applied electric field $|E_x|$ of $5\,$mV/cm over a distance of $10\,\mu$m in x-direction is used. That means, for the simulated ion trajectories, the applied electric field of $E_x = \pm 5\,$mV/cm, acting on the ion, is enhanced by an additional field caused by a field gradient of $\pm 0.5\,\text{mV/cm}\frac{1}{\mu m}$ along the x-axis. Besides that, the simulations include a stray electric field along the x-direction of up to $\pm 1\,$mV/cm, which is represented by the shaded blue (red) region around the data (solid lines) for a zero stray field shown in figure 3.21. The dashed lines represent the simulated state population in absence of any additional stray or gradient electric fields.

First, consider the modeled data including the electric field gradient. While the free-flight data (red) are well reproduced, the simulations for pulling the ion through the BEC deviate for the rising edge of the signal, but model N_R for $t_\mathrm{tof} \gtrsim 10\,\mu$s accurately, when taking into account the stray field compensation level (shaded regions). In contrast to the free-flight data, the simulated data for $E_x = +5\,\mathrm{mV/cm}$ show, in comparison to the data without any additional stray or gradient electric fields (cf. dashed line in figure 3.21), not only a rising edge position of N_R for earlier ion flight times but more importantly, that the characteristic shape is significantly changed. The slowly rising signal for longer ion flight times, which is attributed to a long tail of ions leaving the ion-induced blockade radius delayed as a consequence of collision-induced deceleration of the ion motion, is overall contracted to shorter t_tof. This makes it hard to deduce ion-atom collisions in the presence of uncontrolled additional electric fields, as for increasing gradient and stray electric fields N_R more and more resembles the shape of a non-collisional free-flight ion trajectory with a steep increasing step-like blockade signal. Exemplarily, when regarding the Rydberg signal without stray and gradient electric fields (see blue and red dashed lines in figure 3.21), in comparison, the shaded regions exhibit a relatively small gap. Consequently, in the case of the considered stray and gradient electric fields, the measurement of ion-atom collisions is more involved but in principle feasible.

3.6.4 Conclusions on creating, probing and the ion motion in a BEC

In conclusion to the realization of the creation and probing of a single ultracold ion in a dense and ultracold ensemble, a photo-ionization efficiency of up to 10% has been demonstrated (section 3.6.1). The rather low efficiency could be traced back to an inadequate slow deexcitation, resulting in a low deexcitation efficiency (section 3.6.1). Conclusively, it has been shown that for a faster deexcitation process a higher efficiency is achievable and the ion preparation in a Bose-Einstein condensate (applying the in section 3.1 introduced V-type photo-ionization scheme) is in principle possible, despite the reduced photo-ionization efficiency. However, for probing the ion-atom collisions in the BEC, utilizing the ion-induced Rydberg blockade (cf. section 3.2), it turns out, as discussed in section 3.6.2, that due to the strong Rydberg electron-neutral atom interactions, the blockade radius is heavily diminished for a probe Rydberg excitation in a high-density region and therefore is inappropriate for probing the ion motion inside the BEC. As an alternative, the probe Rydberg excitation is located outside of the condensate, making use of the trapped thermal atoms surrounding the BEC. For technical reasons, the ion creation center is allocated to the same spatial position.

With the setting of creating and probing the ion next to the condensate, the effect of ion-atom collisions is investigated for dragging the ion through the BEC by applying a small external electric field (cf. section 3.6.3). The resulting experimentally obtained probe Rydberg excitation signal revealed at first unexpectedly only a minor dependency on the presence of ion-atom collisions, which, when taking into account the level of electric field control, can be explained by an additional electric field originating from an electric field gradient. For probing the ion-atom collisions for the system at hand, the modeling of the measured probe signal reflected the importance of well-controlled electric fields on a level of 1 mV/cm over a distance of several tens of micrometers. A possible solution for an improved electric field compensation method was already presented in section 3.4, where the ion-induced blockade measurement technique is utilized to determine the zero electric field in the vicinity of the ion trajectory. Beyond that, the width of the probe Rydberg signal for different external applied electric fields also carries information about the electric field gradient present during the experiments. Consequently, the presented field probe method can be extended to efficiently deduce not only the stray electric field but also the electric field gradient probed by the ion along its trajectory, allowing for an improved electric field compensation and thus might path the way for a quantitative study of ion-atom collisions using the prior introduced (cf. section 3.2) ion probing method. In future experiments, the enhanced field compensation allows one to drag the ion along the elongated BEC axis for even smaller electric fields, prolonging the ion-condensate interaction time by a substantial amount. Furthermore, the measurement technique can be refined by initializing the ion-atom scattering in the condensate, while the probe Rydberg excitation is allocated next to the BEC to inhibit the Rydberg electron-neutral atom interaction. In principle, a higher photo-ionization efficiency of a Rydberg atom prepared in the condensate can be achieved for a shorter and stronger deexcitation and photo-ionization pulses. However, already for the photo-ionization laser power settings used for the ionization efficiency measurements in the BEC (cf. section 3.6.1), the atom sample is substantially heated up for 200 subsequent experimental realizations. Consequently, for higher laser intensities the atom sample is heated up for an even lower number of experiments per atom cloud. Alternatively, when creating the ion outside of the condensate, one can apply an elaborate electric field pulse sequence to transport and stop the ion in the BEC center within a few tens of nanoseconds, which is made possible by the high level of electric field control present in the experiment. An overall different but promising approach is to carefully electric field ionize the Rydberg atom in the BEC instead of using the photo-ionization technique. Consequently, more experiments per atom sample are possible and thus more statistics can be gained, as the strong laser pulses for deexcitation and photo-ionization, which are predominantly responsible for the sample heating, are redundant. Very recently, this technique was utilized to study transport properties of an ion immersed in a condensate (ref. [116]).

4

Precision spectroscopy in ultralong-range Rydberg molecules

Ultralong-range Rydberg molecules (ULRM) have been studied extensively in the past decades. Among other things, beyond the studies of the first realized S-state ULRM [32], angular confined molecules build from D-states [39], ULRMs where not only one but several ground-state atoms are bound in the Rydberg electron wavefunction, which shift the Rydberg energy level in an additive [38] or more exotically non-additive [117] way, and moreover, homonuclear Rydberg molecules build from a superposition of opposite-parity eigenstates (the trilobite or the butterfly state), which feature an exotic shape and an exaggerated large permanent electric dipole moment [S5, 34, 40, 44] have been realized. Furthermore, ULRMs bound by internal quantum reflection on a steep potential drop, which originates from a Rydberg electron-Rb p-wave shape resonance have been investigated [33]. Studies on the same shape resonance revealed spectroscopic features in a more dense environment with many ground-state atoms inside the Rydberg electron orbit [S6]. Additionally, the resonance partakes an essential role in ultracold chemical reactions [S7, 43]. Beyond that, the importance of spin coupling between the Rydberg electron and the valence electron of the ground-state atom has been demonstrated [37, 45]. A more detailed introduction of ultralong-range Rydberg molecules is presented in the theory section 2.2.

Recently, the interest in the field of ULRMs has shifted from qualitative studies towards a more quantitative and detailed description of the molecular bound states. A renewed interest in the inclusion of spin effects, in particular the hyperfine interaction in the ground-state atom and spin-orbit coupling effects between the Rydberg atom and the ground-state atom, has been shown recently [75–77]. Spin-orbit interactions between an electron and a neutral atom have been investigated in the context of negative ions. The interactions have been shown to play an important role when it comes to low-energy quantum scattering.

Negative ions are essentially different from neutral atoms and positively charged ions in multiple ways and by themselves are intriguing objects, which have been studied thoroughly throughout the past decades [118, 119]. An anion is usually weakly bound and features only a few or merely one bound state. Apart from the true bound states, negative ions also feature quasi-bound states lying just above the first electron detachment limit. Those states are bound by the centrifugal barrier. With this, anions constitute ideal model systems to investigate electron-electron correlations since, additionally, they feature an amplified sensitivity as a consequence of the inner-shell electrons effectively screening the nucleus [119]. A recent experimental study on the Os^- anion delivered evidence for the presence of opposite-parity excited bound states [120], which led to a revived interest in high-resolution negative-ion spectroscopy [121–123] with the ultimate goal of laser cooling of trapped anions [124, 125]. The fine details of the negative-ion interaction potential define the low-energy quantum scattering between the free electron and the parent atom [84, 126, 127]. In particular, broad scattering resonances for the electron-neutral atom system can occur a few meV above the electron-detachment threshold. Those resonances are a result of the quasi-bound states bound by the centrifugal barrier mentioned above. The underlying details of these negative-ion states, for instance, the effects of the relativistic fine-structure, are difficult to access experimentally due to their short lifetime and very low binding energy [128], or due to optical selection rules for photodetachment studies of the anion ground-state [129].

In this work, studies on negative-ion resonances of Rb^-, devising ultralong-range Rydberg molecules as an ultrasensitive tool, are presented. For this purpose, ULRM-spectroscopy is elevated to a so-far unequaled quantitative level of precision, in a combined experimental and theoretical effort. The outcome of these studies, which have been published in [S2], are presented in the following. Exemplary, the potential of utilizing ULRMs to perform precision spectroscopy of the quasi-bound ^3P_J negative-ion states, is demonstrated. Prior unobserved molecular bound states, that are strongly influenced by resonant electron-atom p-wave scattering, are identified and used to unravel the fine-structure triplet ($J \in \{0, 1, 2\}$) of the Rb^- anion, originated from spin-orbit coupling, which by other means is experimentally challenging to resolve.

In this chapter, at first, the electron-neutral atom scattering is introduced in the context of ULRMs and negative ions in section 4.1. Following this, section 4.2 and 4.3 address the different experimentally observed spectroscopic lines, which are evident in a series of spectra taken for principal quantum numbers ranging from $n = 37$ down to $n = 31$. In particular, in section 4.3, spectra for $n = 31$ reveal a molecular alignment, originating from the spin-orbit interaction of the underlying ^3P_J anion state [77]. Finally, section 4.4 reviews the adapted electron-Rb phase shifts, which, in combination with state-of-the-art calculations, yield the molecular bound-states observed in the experiment and additionally allow for extracting the fine-structure splitting of the ^3P_J above-threshold states of the Rb$^-$ anion on a so-far unmatched experimental precision.

The work presented in this section is acquired in a combined theoretical and experimental effort with the group of P. Schmelcher (Univ. Hamburg). Specifically, I am grateful to C. Fey and F. Hummel for the calculations of phase shifts and potential energy curves.

4.1 Electron-neutral atom scattering on an atomic scale

On an atomic scale, ultralong-range Rydberg molecules (ULRM) provide in a natural way a sensitive and highly versatile microscopic scattering laboratory with electron-atom collision energies in the range of meV [32, 33]. Besides the very low scattering energy provided by the quasifree Rydberg electron, which is inapplicable with free electrons, a high accuracy results from the resonating electron wave bound by the Coulomb potential of the ionic Rydberg core, and the corresponding narrow Rydberg states. With a ground-state atom inside the Rydberg electron orbit, quantum scattering between the Rydberg electron and the ground-state atom occurs, resulting in a phase shift conveyed on the electron wavefunction distinguishable from the unperturbed Rydberg electron via a slightly shifted resonance energy.

Regarding a rubidium anion Rb$^-$, build from a neutral atom and an electron, the compound of a negative ion in the context of Rydberg molecules at first seems out of place, however from a different perspective it becomes clear that they are closely related. In fact, when considering the quasifree Rydberg electron, which binds the neutral atom in its wavefunction, forming an ULRM (cf. section 2.2), from the viewpoint of the bound atom the Rydberg electron scatters off the neutral, potentially forming a negative ion compound.

The purpose of this section is to introduce the electron-atom scattering for both ULRMs and negative ions and to relate them to each other. For this, first recall that for a neutral atom interacting with a charged particle, the atoms ground-state polarizability gives rise to an attractive short-ranged interaction potential. Asymptotically, for large internuclear distances, the interaction is described by the asymptotic polarization potential $V(r) = -C_4/r^4$ (see also section 2.1 and 2.2). In the case of a non-zero angular momentum between the scattering partners, mathematically a repulsive centrifugal potential arises when reducing the dimensionality of the interaction to the radial spacing of the scattering pair. The resulting scattering potential for a charged particle with a neutral atom including the centrifugal term reads:

$$V_L(r) = -\frac{C_4}{r^4} + \frac{\hbar^2}{2\mu}\frac{L(L+1)}{r^2}, \tag{4.1}$$

with the quantum mechanical angular momentum L for the scattering event, the reduced mass μ, and the distance r between the scattering partners.

The situation of a free electron scattering off a neutral atom via the interaction potential $V_L(r)$ for $L = 1$ is depicted in figure 4.1. Here, for the ^{87}Rb ground state polarizability a value of $\alpha_0 = 318.8(14)$a.u. [113] is used, where α_0 is related to C_4 via $\alpha_0 = 2(4\pi\epsilon_0/e)^2 C_4$. The orange horizontal dashed line indicates the kinetic energy E_{kin} of the incoming scattering electron e$^-$. V_L shows a maximum for $L = 1$ of about 43 meV at a Rb-e$^-$ distance of $r \approx 18\,\mathrm{a}_0$. For distances smaller than the maximum value of V_L, above-threshold, transient negative-ion states bound by the centrifugal barrier might exist. In fact, in 2000 Bahrim *et al.* [80, 84] predicted the presence of such a quasi-bound state ^3P_J for the heavy alkali metal anions Rb$^-$, Cs$^-$ and Fr$^-$, which due to spin-orbit coupling between the valence electron spin of the ground-state atom and the incoming electron p-wave results in a fine-structure triplet ($J \in \{0, 1, 2\}$). For the Rb$^-$ negative ion, these quasi-bound fine-structure split states are estimated at 19.21 meV, 20.42 meV and 23.22 meV [84] above the

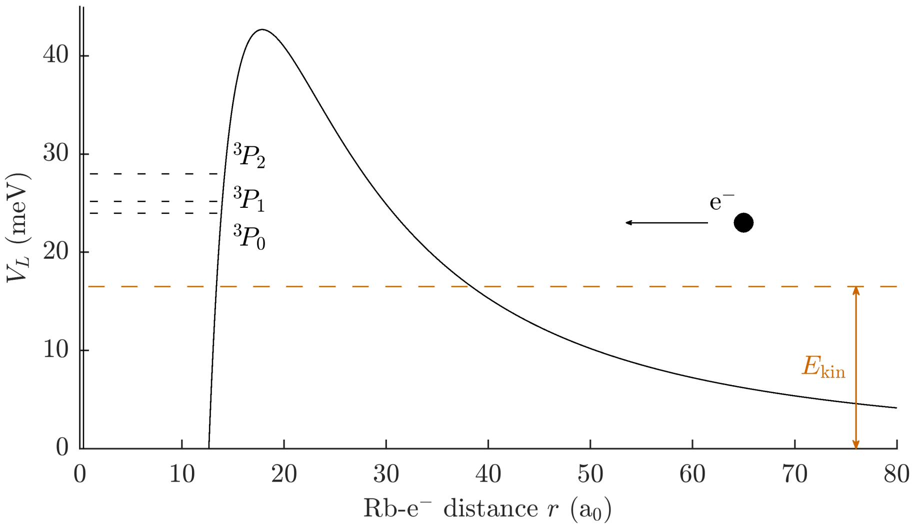

Fig. 4.1: Illustration of electron-atom scattering. The solid line represents the asymptotic electron-atom polarization potential V_L including the centrifugal barrier for $L = 1$ over the Rb-e$^-$ distance r. The orange horizontal dashed line depicts the kinetic energy E_{kin} of the incoming free electron, while the black dashed lines indicate quasi-bound states behind the centrifugal barrier split by the spin-orbit coupling, which are labeled with ^3P_J ($J \in \{0, 1, 2\}$) respectively.

electron detachment limit. In figure 4.1, the energies of these states are indicated by the black horizontal dashed lines left of the centrifugal barrier.

For kinetic energies of the incoming electron close to the binding energy of these states, the electron couples strongly with the ground-state atom, and as a result the electron-atom interaction is drastically enhanced, leading to a significantly enlarged cross-section for p-wave scattering. In this case, a p-wave shape resonance occurs as the potential well formed by V_L temporarily traps the incoming electron before it is released in a p-wave, hence the term p-wave shape resonance. For the Rb$^-$ anion, these states are relatively high in energy compared to the p-wave barrier maximum and thus are relatively short-lived, leading to broad resonance features with widths larger than the fine-structure splitting of the ^3P_J state [80, 84], making the experimental determination of the binding energies challenging.

Next, let us turn to the situation where the scattering electron is hosted by the Rydberg atom. As introduced in the theory section 2.2, the quasifree Rydberg electron scatters off neutral atoms inside the Rydberg electron wavefunction. The predominantly attractive scattering interaction leads to well-localized ultralong-range Rydberg molecules (ULRM). In the following, we introduce the potential energy curves and the resulting molecular dimer states which are of particular interest for the measurements to follow in the next sections.

The Born-Oppenheimer potential energy curves (PECs), which are obtained from Green's function calculations and the truncated diagonalization method (cf. section 2.2.2), resulting from the e^{-}-Rb scattering are shown in figure 4.2 for energies in the vicinity of the $35S$ state. Note, in the following we treat only the experimentally relevant PECs resulting from triplet electron-atom scattering, where the ground-state atom occupies the hyperfine state $F = 2$.

The truncated diagonalization calculations yield in total a set of 6 PECs, which can be discriminated by the projection of the total angular momentum onto the internuclear axis $\Omega = m_F + m_j$ for a zero magnetic field. Here, m_F and m_j are the magnetic quantum numbers of the ground-state atom hyperfine level and the Rydberg electron angular momentum. In the case of zero magnetic field the potential energies are on top of each other for a negligible p-wave contribution. However, when the p-wave scattering becomes relevant, the PECs split up into three pair-wise degenerate potentials. The splitting occurs due to the presence of the three p-wave scattering channels (quantified by the scattering lengths $a^T_{p,J}(k)$ see section 2.2.1) which can be associated with the ^3P_J anion states. Note that the Green's function approach does not include the hyperfine structure splitting of the ^3P state and thus the J-averaged phase shifts (cf. section 2.2.2 or 4.4) are used for the calculations.

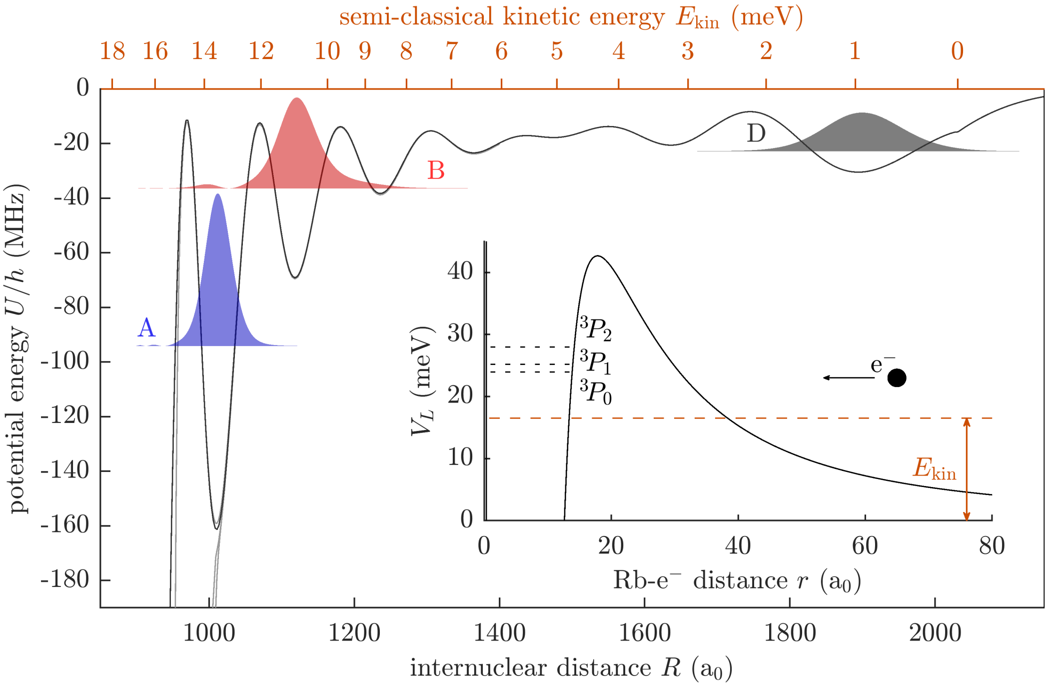

Fig. 4.2: Potential energy curves resulting from e^--Rb scattering for zero magnetic field in the vicinity of the $35S_{1/2}$ Rydberg state obtained by Green's function calculations (black line) and from truncated diagonalization (gray lines). The internuclear distance R is related to E_{kin} (top axis) via equation 4.2. The asymptotic zero potential energy is set to the binding energy of the Rydberg electron. The vibrational ground-states of the molecular dimer A (blue), B (red) and D (gray) are represented by the shaded areas. The molecular wavefunctions are offset by their binding energies. The inset illustrates the e^--Rb scattering for $L = 1$ from the viewpoint of the neutral atom.

The semi-classical kinetic energy (top axis in figure 4.2) of the Rydberg electron at the neutral atom position is related to the internuclear distance R via equation 4.2.

$$E_{\text{kin}} = \frac{-R_y}{(n^\star)^2} - \left(\frac{-e^2}{4\pi\epsilon_0 R}\right) \tag{4.2}$$

Here, R_y is the Rydberg constant and $n^\star$ the effective principal quantum number, which accounts for the quantum defect in Rb (see section 2.1). The inset of figure 4.2 shows the scattering event from the perspective of the neutral atom.

For each R the electron scatters with a different kinetic energy off the neutral atom. At the outermost potential well, the electron orbit reaches its maximum size and the kinetic energy drops to zero at the outermost turning point. In this case, the interaction is dominated by s-wave scattering only, due to the very-low energy scattering. For smaller distances R the scattering kinetic energy increases as the electron gains potential energy in the Coulomb field of the ionic Rydberg core. When E_{kin} becomes comparable with the binding energies of the ^3P_J anion states (cf. inset figure 4.2), the p-wave contribution increases enormously as the incoming electron resonantly couples to the quasi-bound states (see also theory section 2.2). As a result of the resonant p-wave contribution the potential energy curve steeply drops, which is evident in figure 4.2 for distances $R \lesssim 950\,\mathrm{a}_0$ (Green's function calculations and truncated diagonalization with $|\Omega| = 5/2$) and $R \lesssim 1000\,\mathrm{a}_0$ (truncated diagonalization with $|\Omega| = 1/2$ and $|\Omega| = 3/2$).

The deep potential wells of the resulting PECs can support discrete vibrational dimer states (cf. 2.2.2). The lowest vibrational wavefunction of the most important dimer states are depicted in figure 4.2, indicated by the shaded areas. The wavefunctions are offset by their binding energy with respect to the energy of the addressed $35S$ Rydberg state.

As a consequence of the R-dependent kinetic energy, for large internuclear distances the binding energy of the dimer state D is dominated by s-wave scattering, while for smaller distances the molecular states A and B are influenced by the resonant p-wave scattering. In fact, as will become evident in the following sections, the exact position of potential drop is heavily influenced by the exact p-wave shape resonance positions, and as a result, the deeply bound dimer state A is strongly dependent on the binding energy of the ^3P_J anion states. The importance of the exact binding energies of the Rb^- (^3P_J) is already indicated by the results of the truncated diagonalization method shown in figure 4.2. While the potentials associated with $|\Omega| = 1/2$ and $|\Omega| = 3/2$ steeply drop at $R \approx 1000\,\mathrm{a}_0$, the PEC for $|\Omega| = 5/2$ (and also the results from the Green's function calculations) exhibit a potential well around $R = 1000\,\mathrm{a}_0$ which can support molecular bound states.

4.2 Spectroscopy of negative-ion resonances in ULRMs

In this section, we compare the binding energies of ULRMs obtained from experimental spectra with calculated molecular binding energies, with the aim to experimentally prove the presence of the so-far unobserved fine structure of the ^3P_J state of Rb$^-$. For this purpose, the results of an extensive spectroscopic study of the molecular bound states D, A, and B are used to benchmark the theoretically predicted molecular binding energies for a large range of principal quantum numbers ($n = 31, \ldots, 37$). Note that at first the binding energies of the dimer states were computed using the *ab initio* calculated scattering length data from [80, 84], but a rather poor agreement was found. In consequence, own phase shift calculations were performed based on a model potential (see section 2.2.1) for the e$^-$-Rb interaction, which importantly allows us to include the full molecular spin structure; especially, the spin-orbit coupling of the ^3P_J anion state.

In the following, we find an overall very good agreement between theory and experiment for the investigated range of n, when using our adapted s-wave and p-wave scattering phase shifts for determining the molecular bound states. Equally important, we are able to correctly predict a splitting in the molecular line of the dimer state A, which occurs for $n = 31$. In particular, it is found that the observed doublet structure of A results from the existence of the spin-orbit coupling of the underlying (^3P_J) anion state of Rb$^-$. Moreover, in the following section 4.3, the adapted phase shifts are further applied with remarkable success to predict the doublet structure spacing and spectral line shape of the dimer state A.

Before we start with the discussion of the obtained spectroscopic data and the molecular binding energies, it is important to emphasize that our phase shift calculations aim to model the measured energies of the molecular bound states, especially, the binding energy of the deeply bound state A which is expected to be strongly affected by the Rb^- fine structure. Explicitly, the inner hard wall position of the model potential was adjusted to match the outcome of the computed binding energies of the dimer states D, A, and B with the experimentally obtained data. A more detailed description of the fitting procedure, and a comparison of the measured binding energies with the computed bound state energies based on the *ab initio* phase shifts (from refs. [78, 84]) and the calculated energies resulting from our adapted phase shifts, are presented section 4.4. The adapted phase shifts are quantified by the zero-energy s-wave scattering length $a_s^T(0) = -15.2\,\mathrm{a}_0$ and the J-averaged p-wave shape resonance position $E_r^{\mathrm{avg}} = 26.6\,\mathrm{meV}$, which are varied by $a_s^T(0) \pm 0.5\,\mathrm{a}_0$ and $E_r^{\mathrm{avg}} \pm 0.2\,\mathrm{meV}$, respectively, demonstrating the sensitivity of the determined resonance position and s-wave scattering length (cf. section 4.4).

Let us now turn to the s-wave scattering dominated dimer state D. In the following (figure 4.3), the results of an experimentally obtained spectrum of the shallow bound dimer and excited dimer states are presented for $n = 35$. The spectroscopic data are obtained from Rydberg spectroscopy involving electric field ionization and ion detection performed in an ultracold ($1.5\,\mu\mathrm{K}$) sample of about 4.5×10^6 $^{87}\mathrm{Rb}$ atoms. The atoms are prepared in the fully spin-stretched hyperfine state $|F = 2, m_F = 2\rangle$ and are captured in a magnetic quadrupole trap (see section A.3) with a magnetic offset field of typically $B = 2.2\,\mathrm{G}$. The $nS_{1/2}$ Rydberg state is addressed via a two-photon excitation incorporating the intermediate $6P_{3/2}$ state. The intermediate laser detuning is typically set to values between $+80\,\mathrm{MHz}$ and $+400\,\mathrm{MHz}$, while the polarizations of the $420\,\mathrm{nm}$ (lower transition)

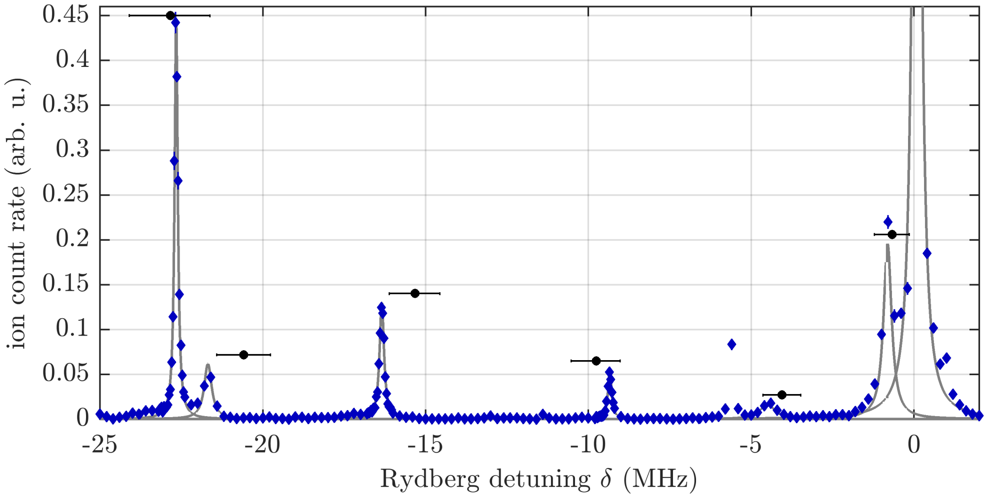

Fig. 4.3: ULRM spectroscopy of excited dimer states D* bound by quantum reflection for $n = 35$. The ion signal is shown as a function of δ. The spectrum spans a detuning ranging from the atomic resonance of the $\left|35S_{1/2}, m_j = 1/2\right\rangle$ Rydberg state at $\delta = 0$ to the dimer state D at $\delta = -22.6\,\mathrm{MHz}$. The solid lines result from a mulitple Lorentzian fit to the data. The peak at $\delta = -5.6\,\mathrm{MHz}$ originates from a weak residual coupling to the atomic resonance of the $\left|35S_{1/2}, m_j = -1/2\right\rangle$ state. The black circles are the molecular states resulting from Green's function calculations using the adapted s- and p-wave phase shifts. The error bars correspond to a variation of the scattering lengths (see text).

and 1020 nm (upper transition) excitation lasers are set to address the $m_j = 1/2$ Zeeman sublevel of the Rydberg state. The formation of the ULRMs is assisted by photo-association via the Rydberg excitation lasers. Individual molecular bound states are addressed by detuning the 1020 nm laser from the atomic Rydberg resonance by the molecular binding energy.

Figure 4.3 shows a Rydberg spectrum in the vicinity of the $35S$ Rydberg state. The blue symbols correspond to the average number of field-ionized ions detected per experiment for a certain Rydberg detuning δ. The gray lines represent Lorentzian fits to the signal peaks. The atomic resonance of the $\left|35S_{1/2}, m_j = 1/2\right\rangle$ state is set to $\delta = 0$. The error bars indicate one standard deviation and are typically smaller than the symbol size. For a detuning δ equal to the binding energy of a molecular bound state an ULRM can form. Similar to the detection of Rydberg atoms, the Rydberg electron that binds the ground-state atom is torn away from the Rydberg core by an external electric field and the remaining ion is detected, leading to an increased ion count rate on the detector. The signal peaks for $\delta < 0$ in figure 4.3 can be associated with molecular bound states, where the binding energy is equal to the detuning δ for which the peak occurs.

With the calculated binding energies, we can identify the signal peak at $\delta = -22.6\,\mathrm{MHz}$ with the dimer D (cf. figure 4.2), which is solely bound by the outermost potential well. For detunings closer to the atomic resonance we find the excited dimers ($\mathrm{D}^\star$) which are bound by quantum reflection on the steep potential drop (ref. [33]) which is caused by the ${}^3P$ shape resonance. The binding energies resulting from our adapted s- and p-wave phase shifts are represented by the black dots in figure 4.3. The error bars result from the above mentioned variation of the zero-energy scattering length $a_s^T(0) \pm 0.5\,\mathrm{a}_0$ and the p-wave resonance position $E_r^{\mathrm{avg}} \pm 0.2\,\mathrm{meV}$. When varying the s-wave scattering length and the p-wave resonance position we find that the variation of $a_s^T(0)$ almost completely defines the error bar for the dimer D. However, for the excited dimers the variation of E_r^{avg} becomes more relevant (in fact comparable with the variation of $a_s^T(0)$), which is to be expected since the wavefunctions of the excited dimers extend to smaller internuclear distances where the p-wave contribution increases.

The excited dimers $\mathrm{D}^\star$ and the trimer state (T), which are bound by quantum reflection, were first observed by Bendkowsky *et al.* [33]. The authors of ref. [33] applied a modified effective-range expansion based on [130] modeling the p-wave phase shifts to match their experimental findings. Importantly, in contrast to our method (cf. section 4.4), the modeling in [33] is based on the measured binding energies of $\mathrm{D}^\star$ and T which are partly influenced by s-wave and p-wave scattering.

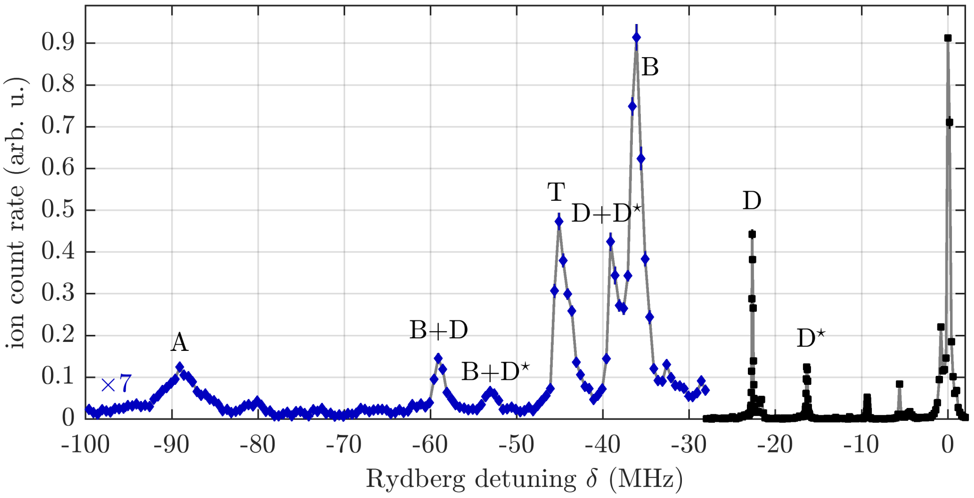

Fig. 4.4: ULRM spectroscopy of the dimer states A, B and D (excited dimer D*). The ion signal is shown as a function of detuning δ from the Rydberg state $\left|35S_{1/2}, m_j = 1/2\right\rangle$. For better visibility, the data for the deeply bound molecular states are enhanced by a factor of 7. For small detuning the spectrum from figure 4.3 is shown. The solid lines connect the data points and serve as a guide to the eye. The identified diatomic (A, B and D) and triatomic (T, dimer+X) molecular bound states are labeled accordingly.

Next, let us turn to the molecular states dominated by p-wave scattering. According to the considerations of the last section, the binding energies of the deeply bound dimer states are strongly influenced by the exact positions of the ^3P_J shape resonances. In particular, the dimer state A is heavily affected, whereas the dimer state B is less strongly influenced since B is located further away from the resonance position. To potentially detect the spin-orbit coupling of the ^3P_J anion state of Rb$^-$, we spectroscopically measure the so-far unobserved deeply bound p-wave dominated dimer states. To this end, ULRM spectroscopy is performed over a large range of principal quantum numbers ($31 \leq n \leq 37$) and the molecular bound states are identified. In figure 4.4 a typical ULRM spectrum is shown for $n = 35$, where the signal for larger red detuning is magnified for better visibility. As before, we identify the dimer state D (excited dimer state D*) for smaller

Rydberg detunings with the assistance of the computed molecular bound states. Furthermore, for larger red detuning we can assign the molecular peaks in the spectrum to the dimer states A and B, as well as triatomic molecules assembled from various combinations of dimer bound states which are labeled accordingly. For example, the trimer T appears for a detuning which is equal to twice the binding energy of the dimer D. Similarly, we can assign the triatomic peak B+D as a combination of the dimer state D and B, et cetera.

In the following, the measured binding energies of the states D, A, and B are compared with the computed bound state energies resulting from PECs which are obtained from Green's function calculus. As mentioned earlier, the calculations are performed using the s- and p-wave phase shifts which were adapted to match the experimental data. As expected (ref. [32]), the s-wave dominated dimer D shows a monotonic decreasing binding energy for increasing n. For the deeply bound states A and B, however, a qualitatively different behavior is observed. Overall, A and B show a similar trend as D but overlaid with a strong alternation of the binding energy with n. Note that the alternation is artificial and results from the way we have defined the dimer states A and B. As a reminder, A and B are associated with the molecular states bound by the innermost two potential wells in front of the steep drop of the PECs (cf. section 4.1). It simply turns out that for the resulting PECs these two wells are significantly deeper for each odd n. From earlier considerations, we recall that the dimer states are more affected by the anion spin-orbit coupling when energetically ($E_{\mathrm{kin}}(R)$) closer to the p-wave shape resonance position. Further, we know that the steep drop of the PEC occurs due to the strongly increasing p-wave scattering, which means, the deeper the potential wells, the more they are influenced by the spin-orbit coupling. Consequently, we expect that for each odd n the observed dimer states A are particularly affected.

In figure 4.5 the experimentally obtained binding energies and the results of the Green's function calculations are presented. The symbols represent the measured molecular lines, while the solid lines connect the computed binding energies. The shaded areas result from the aforementioned variation of the s-wave scattering length and the p-wave shape resonance position. As a reminder, the fine structure of the ^3P_J state is not included in the Green's function calculus. Nonetheless, the calculations match the measured data very well, including the alternating behavior of the p-wave dominated states A and B, verifying our adapted s- and p-wave phase shifts. Importantly, for $n = 31$ we observe a doublet structure which we can associate with the spin-orbit coupling induced splitting of the PECs. The doublet structure can be explained when including the full molecular spin structure in the computations of the PECs. To this end, the phase shift calculations are performed with our obtained model potential parameters (inner hard-wall position for s-wave and p-wave scattering), where we add now the standard LS-coupling term (cf. section 2.2.1) and with that include the fine structure of the ^3P_J anion state. With the J-dependent scattering phase shifts a diagonalization of the Hamilton (cf. equation 2.30) including the generalized form of the Fermi pseudopotential (ref. [75]) yields the PECs (discriminated by the projection of the total angular momentum onto the internuclear axis $|\Omega| = 1/2, 3/2, 5/2$). Before we discuss the case of $n = 31$ in detail, let us first address the fact that for the dimer state A no splitting is observed for $n = 32, \ldots, 37$, not even for the more deeply bound dimer for odd n ($n = 33, 35$, and 37).

From the calculated Born-Oppenheimer potential energy curves for $n = 35$ (cf. figure 4.2 in previous section), we have learned that the potential well, which supports the p-wave dominated dimer A, does not necessarily exist for all three p-wave scattering channels (associated with $a^T_{p,J}$). Explicitly, we found that for $n = 35$ only the PEC for $|\Omega| = 5/2$ exhibits a potential well which can host

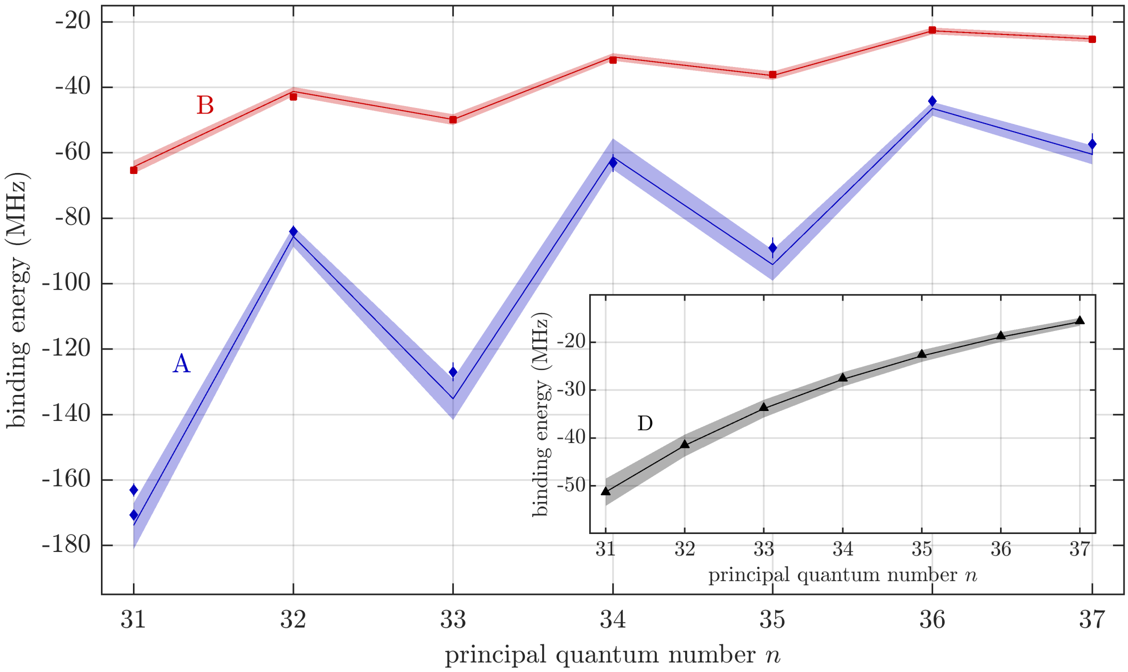

Fig. 4.5: Binding energies of the deeply bound dimer states A (diamonds), and B (squares), as well as the shallow bound state D (inset), as a function of n. The solid lines correspond to the results of the Green's function calculations based on our adapted s- and p-wave scattering phase shifts (see section 4.4). The shaded areas represent the computed binding energies including small variations of the adapted scattering lengths (see text). The error bars of the measured binding energies result from the peak width (fwhm) of the fitted molecular lines, and are usually smaller than the symbol size.

the deeply bound dimer state A. Now, to resolve spectroscopically the spin-orbit coupling induced splitting between the PECs associated with $|\Omega| = (1/2, 3/2, 5/2)$, the potential wells supporting the dimers A have to be close enough to the shape resonance positions (^3P_J), while still forming a deep enough well to potentially bind a ground-state atom. When calculating the PECs for the investigated principal quantum numbers, it turns out that this is only the case for $n = 31$, for which the potential wells are closed for $|\Omega| = (1/2, 3/2, 5/2)$, while the well is located close enough to the resonance positions. In contrast, for $n = 32, \ldots, 37$ either the

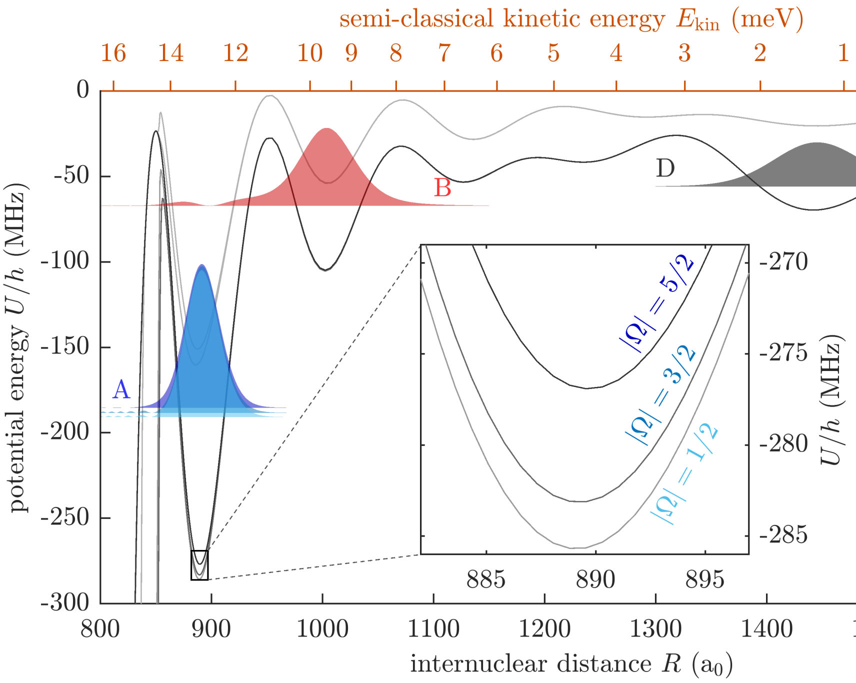

Fig. 4.6: Potential energy curves for zero magnetic field in the vicinity of the $31S$ Rydberg state as a function of internuclear distance R (black line) obtained from the truncated diagonalization method. The zero potential energy is set to the binding energy of the Rydberg electron. The vibrational ground-states of the molecular dimers A (blue), B (red) and D (gray) are represented by shaded areas. The molecular wavefunctions are offset by their binding energies. The zoom-in shows the p-wave dominated potential well which is split due to the spin-orbit coupling of the $\mathrm{Rb}^{-}\ {}^{3}P_J$ state. In gray, the shallow mixed singlet-triplet PEC is shown for the sake of completeness (not accessed in this work).

splitting between the PECs is too small to be resolved spectroscopically ($n = 32, 34$, and 36), or the PECs for $|\Omega| = 1/2$ and $3/2$ are flipped open ($n = 33, 35$, and 37). Consequently, we expect only one molecular line for the dimer states A and B except for $n = 31$, where a substructure should occur for A, which is the case. With this, we fully understand the observed binding energies. The fact that the calculations correctly predict this behavior underlines the precision of our modeling method.

Finally, let us turn to the situation where a doublet structure of the dimer state A is observed ($n = 31$). As mentioned earlier, we now include the LS-coupling in the p-wave scattering phase shift calculations and from them compute the PECs via a truncated diagonalization method. The results are shown in figure 4.6. Each PEC (associated with $|\Omega| = 1/2, 3/2, 5/2$) can support a molecular bound state, which in the case of the potential well associated with the dimer state A are energetically offset to each other due to the slightly different p-wave shape resonance position for the different total angular momenta J. The zoom-in shows the splitting of the PECs for the potential well supporting the dimer A. For completeness, the shallow mixed singlet-triplet PECs (ref. [37]) are shown as well.

We recall that the experiments are performed in a non-zero magnetic field with a spin-polarized ($F = m_F = 2$) sample of Rb atoms and that the laser polarization is set to address the $m_j = +1/2$ Rydberg state. Consequently, we couple into the PEC associated with $\Omega = 5/2$, which gives rise to one peak of the doublet structure. To understand the origin of the second peak, we have to presuppose what is discussed in the following section. For now, let's anticipate that much: For a non-zero LS-coupling the PECs are mixed for angles other than 0 and π between the internuclear axis and the magnetic field axis. As a consequence of this mixing, we expect that not only one but several PECs are addressed in the experiment, potentially leading to a substructure of molecular peak A. In fact, the second peak of the doublet structure mainly originates from an admixture of the uppermost PEC ($\Omega = 5/2$) with the second highest PEC (cf. figure 4.7). From this we conclude that the doublet structure is a direct result of the non-zero LS-coupling and consequently that the experimentally observed doublet directly proves the presence of the fine structure of the ${}^3P_J$ state in Rb$^-$.

4.3 ULRM alignment mediated by spin-orbit coupling in negative ions

In the previous section, the results of an extensive spectroscopic study of ultralong-range Rydberg molecules were presented. The outcome of the experimentally determined molecular binding energies of the dimer states D, A, and B were used to model the s-wave scattering length and the p-wave shape resonance position of the ^3P resonance for electron-Rb scattering, and a remarkable good agreement was found. A detailed description of the fitting procedure is outlined in the following section 4.4. The ULRM spectroscopy (for $n = 31$) allowed us to draw conclusions on the underlying near-threshold anion states. In particular, the observed doublet substructure of the p-wave dominated dimer state A strongly indicates the presence of the fine structure splitting of the ^3P_J state of Rb$^-$.

In this section, we discuss the substructure evident in the spectroscopic data in more detail. In extension to the previous section, high-resolution spectroscopy of the observed doublet structure is performed for different magnetic fields and Rydberg electron spin orientations. In the calculations, we now include the full molecular spin structure, which allows us to analyze the molecular line shape for different angles between the magnetic field axis and the internuclear axis of the molecule. For the phase shift computations, we use the same model potential parameters, in particular the inner hard-wall position, as before which evidently reproduces the measured molecular binding energies of the s-wave (D) and the p-wave (A and B) dominated dimer states (cf. figure 4.5) for various principal quantum numbers ($n = 31, \dots, 37$). To take into account the fine structure of the ^3P_J anion state in the phase shift calculations, we add the standard spin-orbit coupling term to the electron-atom interaction (cf. equation 2.25). As mentioned earlier, the PECs are then obtained from truncated diagonalization calculations, which, in contrast to the Green's function calculus, enable us to include all three p-wave scattering channels ($a^T_{p,J}$) originating from the three p-wave shape resonances associated with the ^3P_J anion states. Importantly, for different angles between the B-field axis and the molecular axis, the resulting PECs exhibit in addition to the spin-orbit interaction induced splitting an angular dependence resulting from an angular-dependent mixing of the p-wave scattering channels [77].

In the following, the resulting potential energy curves are employed to model the molecular line shape of the dimer state A for various magnetic field strengths and different Rydberg electron spin orientations ($m_j = \pm 1/2$). For different B-fields the resulting molecular line shape of A resembles different situations realized in the experiment. For low magnetic fields, the spin-orbit coupling induced (angular-dependent) splitting between the PECs for $|\Omega| = (1/2, 3/2, 5/2)$ is on the order of the Zeeman splitting. As a result, for angles θ other than 0 and π between the field axis and the molecular axis the potentials can cross. Actually, due to the non-zero LS-coupling the PECs exhibit avoided crossings for $0 < \theta < \pi$ [77], mixing the spin character of the PECs associated with Ω for $\theta = 0$. Note that Ω only discriminates the PECs for a B-field parallel to the internuclear axis. As a consequence of the mixing of the different PECs, we couple not only into the uppermost potential (associated with $\Omega = 5/2$) in the experiment, but also address the PECs that lie energetically below, which explains the experimentally observed doublet structure. For stronger magnetic fields, the Zeeman splitting exceeds the LS-coupling induced energy shift, separating the otherwise mixed PECs. In this case, only one of the six PECs ($\Omega = 5/2$) is addressed in the experiment. However, due to the LS-coupling induced θ-dependence, the PEC exhibits a potential minimum when the internuclear axis is perpendicular to the magnetic field axis ($\theta = \pi/2$), which leads to a molecular alignment of the molecules. Further, it turns out that the angular potential well is deep enough to support a series of discrete pendular states.

In figure 4.7 (left) a high-resolution spectrum of the dimer state A is presented for different magnetic field strengths, ranging from the low magnetic field case of $B = 2.2\,\mathrm{G}$ to the strong magnetic field regime $B = 15.4\,\mathrm{G}$. As mentioned above, for low magnetic fields we expect a doublet structure of the molecular line, originating from the mixing of the spin character which is caused by the LS-coupling. In contrast, for higher magnetic fields, the six PECs are untangled by the large Zeeman shift, and only one PEC is addressed which potentially supports several discrete pendular stats. The spectra for low and high magnetic field reflect exactly this behavior (cf. spectra shown on top and bottom in figure 4.7). The spectrum for $B = 5.3\,\mathrm{G}$ resembles the situation of an intermediate regime, in which the PECs are split, but still a mixing of the spin character is present. On the right side of figure 4.7 the θ-dependent potential energy curves $U(\theta)$ at the minimum of the potential well associated with the dimer A ($R \approx 890\,\mathrm{a}_0$) are shown. As a reference, each set of the six PECs is energetically offset by the potential energy of the uppermost PEC ($\Omega = 5/2$). The spin character of the potentials can be calculated by evaluating the projection of m_j and m_F onto the internuclear axis of the molecule. The experimentally accessible spin configuration ($m_j = +1/2$ and $m_F = 2$) is indicated by the coloring of the PECs. Explicitly, the projection of the absolute square of the electronic molecular state onto the $|m_j = 1/2; F = 2, m_F = 2\rangle$ state weighted with the solid angle $\sin(\theta)$ is calculated. When comparing the measured spectra (left in figure 4.7) with the experimentally accessed PECs (right side), we can assign the apparent substructure of the molecular line of the dimer state A with the angular dependent PECs. In excellent agreement with the calculated PECs, the experimental data nicely reflect the predicted transition from a doublet structure ($B = 2.2\,\mathrm{G}$), originating from

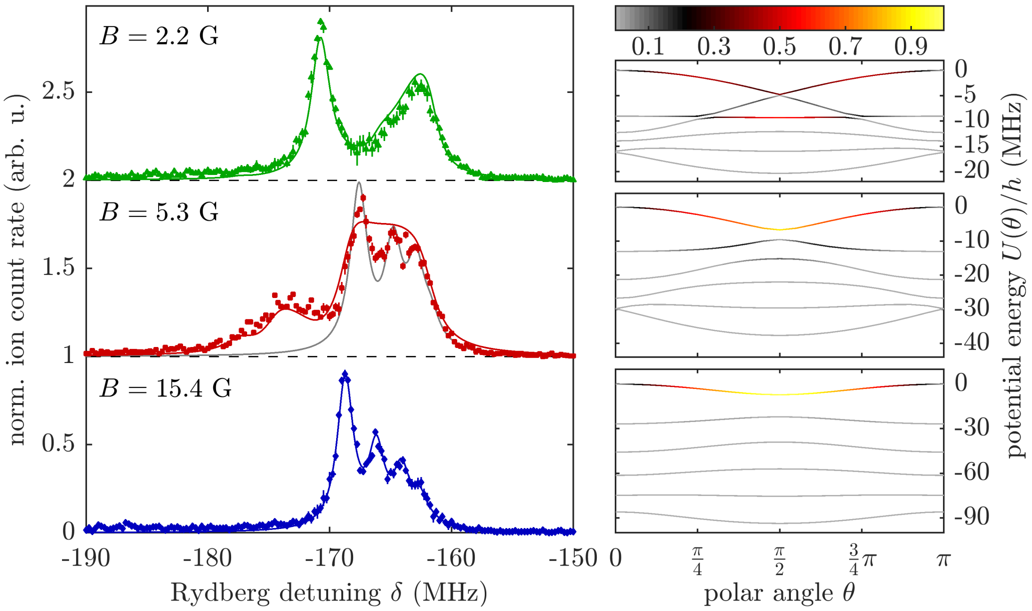

Fig. 4.7: Spin-orbit interaction and molecular alignment for the p-wave dominated dimer A. On the left: High-resolution spectroscopy of the molecular line A for $n = 31$ is shown for various magnetic fields B. $\delta = 0$ corresponds to the atomic resonance of the $\left|31S_{1/2}, m_j = +1/2\right\rangle$ Rydberg state. The solid lines result from simulated line shapes obtained from the θ-dependent PECs (see text). On the right: Angular dependent PECs at the minimum of the potential well associated with the dimer A ($R \approx 890\,\mathrm{a}_0$) for the B-fields indicated on the left (increasing from top to bottom). The energies are referenced to the maximum of the uppermost PEC ($\Omega = 5/2$). The coloring of the PECs represents the spin configuration addressed in the experiment ($m_j = +1/2$ and $m_F = 2$).

coupling to several PECs, to the situation of molecular alignment where we couple only into one PEC ($B = 15.4\,\mathrm{G}$) that exhibits a pendular-state substructure.

For a quantitative comparison between experiment and theory, the θ-dependent PECs $U(\theta)$ are used to model the measured spectral line shapes. Before we discuss how the spectral line shapes are simulated, let us first compare the outcome with the experimental data. The simulated spectral line shapes are compared with the measured spectra in figure 4.7 (gray and colored lines). In the case of unresolved pendular-states ($B = 2.2\,\mathrm{G}$ and $B = 5.3\,\mathrm{G}$) a semiclassical sampling technique is employed (details below), for which the relevant PECs are used as input. For higher magnetic fields ($B = 15.4\,\mathrm{G}$) we apply a rigid-rotor model as individual pendular states are resolved in the experiment. The deviations of the line shape for the intermediate situation ($B = 5.3\,\mathrm{G}$) for detunings $\delta > -170\,\mathrm{MHz}$ occur due to a strong onset of the molecular alignment supported by the uppermost PEC. To validate this, the line shape obtained from the rigid-rotor model using that particular PEC is also shown (gray line), which nicely reproduces the measured spectrum associated with the uppermost potential ($\delta > -170\,\mathrm{MHz}$).

To describe the situation where the spectral line shape resembles a pendular-state substructure, a rigid-rotor model is employed. For the model, we can describe the system with the rotational Hamiltonian

$$H_r = \frac{\hat{N}^2}{2\mu R_0^2} + U(\theta) \tag{4.3}$$

with the rotational angular momentum operator $\hat{N}$ and the diatomic reduced mass μ, where we fix the radial coordinate R to the internuclear distance R_0 for which the potential well associated with A has its minimum. The separation of the angular part from the radial part of the total Hamiltonian is justified by the fact that in our case the energy scale of the radial excitation largely exceeds the energy scale of the angular excitation. Classically speaking, the radial motion is much faster than the angular and because of this, we can use the average radial diatomic distance for calculating the angular part, which in our case coincides with the minimum of the potential well of A. The diagonalization of equation 4.3 in the basis of the Legendre polynomials with $\chi(\theta) = \sum_N c_N P_N(\cos(\theta))$ yields the eigenvalues E_ν and the eigenstates $\chi_\nu(\theta)$. Note that alternatively, one can employ standard methods e.g. finite difference or discrete variable representation. The contribution of each eigenstate to the total line shape is then determined by the Franck-Condon overlap $\Gamma \sim \left|\int d\theta \sin\theta \chi_\nu(\theta) d(R_0, \theta) \chi_i(\theta)\right|^2$, where χ_i represents the initial state, and $d(R_0, \theta)$ the electronic dipole moment. Here, the initial state is assumed to be isotropic, i.e. independent of θ. The dipole moment $d(R_0, \theta)$ is obtained from the projection of the eigenstates $|\Psi_\epsilon(R,\theta)\rangle$ of the electronic Hamiltonian, employed for calculating the PECs (cf. equation 2.30), onto the experimentally addressed states: $|d(R,\theta)|^2 = \left\langle \Psi_\epsilon(R,\theta) \middle| \hat{P} \middle| \Psi_\epsilon(R,\theta) \right\rangle$, with $\hat{P} = |m_j; F, m_F\rangle \langle m_j; F, m_F|$.

While the rigid-rotor model provides a description for the situation for high magnetic fields ($B = 15.4\,\mathrm{G}$ in figure 4.7), where strong angular confinement is evident, for lower magnetic fields, when the PECs mix and as a result a broad spectral line is observed instead of the discrete molecular lines, we need to employ a different modeling technique.

The line shapes for $B = 2.2\,\mathrm{G}$ and $B = 5.3\,\mathrm{G}$ are modeled employing a random sampling technique, which treats the rotational degrees of freedom classically. To this end, we draw a random angle θ from an isotropic distributed gas ($p(\theta) = \sin\theta$), calculate the energy for θ using the PECs $U(\theta)$, which we finally weight with the squared electronic dipole moment $|d(R,\theta)|^2$. This procedure is repeated ten thousand times to obtain enough statistics for the resulting histogram.

At last, to model the experimental line shapes using the above described techniques, we further apply three fit parameters. First, we take into account the finite lifetime of the radial quantum reflection state. For this, the energy of each eigenstate $\chi_\nu(\theta)$, or in the case of the sampling technique the obtained histogram, is convoluted with a Lorentzian line shape reflecting the lifetime of the corresponding radial dimer state. Secondly, we take into account the radial binding energy. For this, the calculated line shape is energetically shifted to fit the molecular line position to the observed binding energies. Finally, we rescale the overall amplitude of the simulated line shape to match the experimental spectra.

Overall, we find that the theoretically obtained line shapes are in excellent agreement with the measured spectra, which validates the extraction of the fine-structure splitting of the ^3P_J anion state from the modeled phase shifts. For the fitted spectral line shapes presented in figure 4.7, we obtain the p-wave resonance positions from the applied phase shifts as: $E_r^{J=(0,1,2)} = (24.4, 25.5, 27.7)\mathrm{meV}$. Apart from the slightly larger value of the measured J-averaged resonance position E_r^{avg} (cf. section 4.2), the acquired fine-structure splitting agrees well with the results of the *ab initio* calculations in ref. [84].

Finally, we investigate the spin character of the spin-orbit coupling influenced potential well of the dimer state A. For this purpose, the excitation laser polarization is changed to address the Rydberg electron spin-down orientation ($m_j = -1/2$), coupling to couple the $\left|31S_{1/2}, m_j = -1/2\right\rangle$ Rydberg state. The resulting spectra for low and high magnetic fields are presented in figure 4.8. The gray data represent the spectra from figure 4.7, where we couple to the spin-up component of the Rydberg state ($m_j = +1/2$). The angular-dependent PECs and the spin character for the experimentally addressed spin configuration ($m_j = -1/2$ and $m_F = 2$) is shown on the right side of figure 4.8. Similar to the above presented situation ($m_j = +1/2$), the angular-dependent spin-orbit coupling mixes the spin character of the PECs in the low-field regime ($B = 2.2\,\mathrm{G}$), while for a high magnetic field ($B = 15.4\,\mathrm{G}$) the Zeeman shift is large enough that the spin mixing is strongly suppressed and as a consequence mainly one PEC ($\Omega = 3/2$) is addressed in the experiment. As a result of the strong spin mixing in the low-field case (cf. spin character of figure 4.7 and 4.8), the spectrum for $m_j = -1/2$ changes only slightly compared to the $m_j = +1/2$ case due to a small shift of the excitation strength to smaller energies. In the high-field case, we again resolve pendular states as a result of the spin-orbit coupling induced angular-dependence of the PECs. In comparison to the spin-up case, the pendular states are mostly Zeeman shifted to smaller energies. However, in contrast to the spin-up case, the molecules are aligned along the internuclear axis. Note that we again find an excellent agreement between the measured spectra and the simulated line shapes. Further note that,

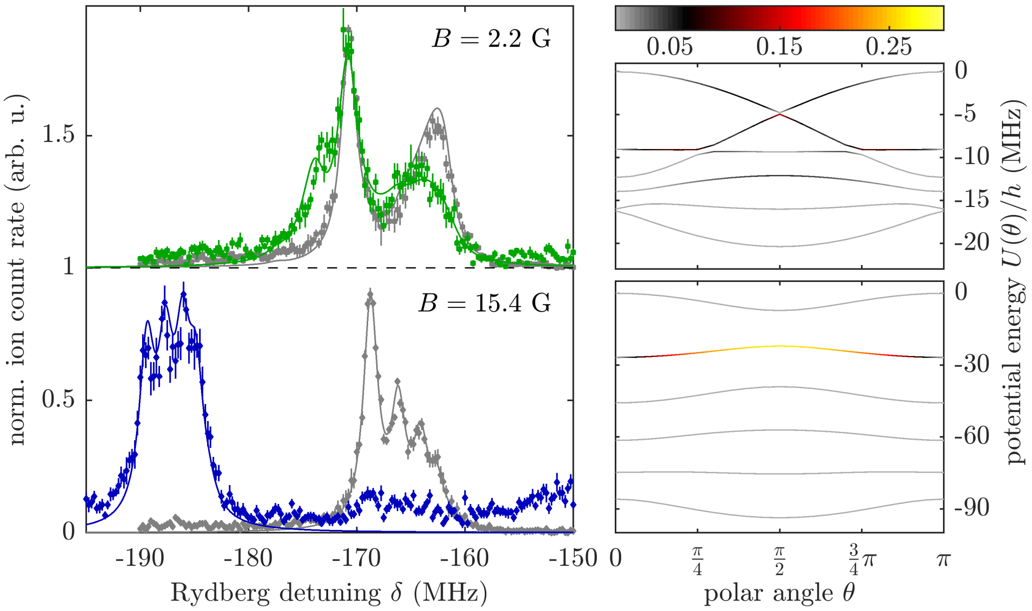

Fig. 4.8: ULRM spectroscopy and spin character mixing due to spin-orbit interactions. On the left: High-resolution spectra of the p-wave dominated dimer A are shown for various magnetic fields B as indicated. The laser polarization is set to address the $m_j = -1/2$ Rydberg state. For comparison, the gray data sets show the resulting spectra for $m_j = +1/2$ reprinted from figure 4.7. $\delta = 0$ corresponds to the atomic resonance of the $\left|31S_{1/2}, m_j = +1/2\right\rangle$ Rydberg state. The colored solid lines result from line shape simulations obtained from the θ-dependent PECs, which are depicted on the right. The projection onto the $m_j = -1/2$ and $m_F = 2$ is represented by the coloring of the curves.

contrary to the simulated line shapes presented in figure 4.7, for the modeling in figure 4.8 the spin-orbit interaction strength is scaled with a factor of 1.05 to fine-tune the modeled line shapes.

4.4 Fitting phase shifts

In the previous two sections, we have discussed the outcome of an extensive experimental and theoretical study of ultralong-range Rydberg molecules that are partly influenced by spin-orbit coupling of the underlying e$^-$-Rb scattering. For the theoretical description of the molecular bound stats and the spectral line shape modeling, own phase shift calculations were performed based on a comparatively simple model potential for the electron-atom interaction (cf. 2.2.1). The model potential has been fine-tuned to match the experimental findings. In this section, we review in more detail, in which way the experimental data was used to adapt the phase shift calculations.

To start with, the model potential has been adjusted to match the experimental findings of section 4.2. In particular, the inner hard-wall position r_0 of the e$^-$-Rb interaction is fine-tuned independently for the s-wave and p-wave scattering, modeling the close range physics. The long-range interaction is included via the polarization potential, using the ground-state polarizability α_{gs} from ref. [113]. Note that the functional k-dependence of the phase shifts is insensitive to the precise value of α_{gs}, i.e. for small variations of α_{gs} a slightly different hard-wall position can be found to reproduce the same phase shifts. For modeling the (triplet) s-wave scattering length $a_s^T(k)$ we can benchmark our bound state calculations using the dimer state D, which importantly is unaffected by p-wave scattering. For the p-wave calculations, we then use the measured binding energies of the dimer states A and B to minimize the deviations between the computed and the measured bound state energies. Note that we use all binding energies for state B, while for state A a subset of states is selected. Specifically, we use the energies obtained for $n = 32, 34$, and 36, for which state A is less deeply bound and consequently less affected by spin-orbit coupling. With this, we can model the measured binding energies using Green's function calculations (see section 2.2.2).

Next, to model the experimental data for the spin-orbit affected dimer state A, the full molecular spin structure is included in the phase shift calculations. For this, we add the standard LS-coupling term to the e$^-$-Rb interaction model potential (cf. equation 2.25 in section 2.2.1), while keeping the prior determined model potential parameters (inner hard-wall position r_0) for s-wave and p-wave scattering. When adding the LS-coupling to the phase shift calculations, three J-dependent scattering channels arise ($a^T_{p,J}$) for p-wave scattering. Note that in this case, the Green's function approach is insufficient to model the experimental data as the method does not include spin-interaction effects. For instance, the hyperfine structure of the ground-state atom, the fine structure of the Rydberg atom, and most importantly their coupling by electron scattering (for more details see supplemental material of ref. [S2]), are not included. Consequently, a truncated diagonalization method is employed instead of the Green's function approach (see section 2.2.2). As mentioned earlier, the quantitative uncertainties of the resulting PECs (arising from the choice of the basis set) can be largely reduced by comparing the results of the truncated diagonalization with the Green's function calculations when switching off the LS-coupling. At this point it is important to note that it is the combination of both methods, the Green's function approach and the truncated diagonalization method, that permits us to draw conclusions from the experimental data, which then allows us to extract the scattering phase shifts from the measured binding energies.

Let us now turn to the results of our extracted phase shift parameters and compare them with previous estimates. First, we recall the s-wave scattering length $a^T_s(0) = -15.2\,\mathrm{a}_0$ and the (J-averaged) p-wave shape resonance position $E^{\mathrm{avg}}_r = 26.6\,\mathrm{meV}$ extracted from the experiment. In comparison to the theoretical estimated resonance position published in ref. [84] where electron correlations are taken into account via a two-active electron model, our extracted value for

E_r^{avg} is about 20% larger. However, a similar discrepancy has been reported for photodetachment experiments in Cs$^-$ [84, 129]. While the extracted resonance position deviates from the theoretical predictions, our obtained value for $a_s^T(0)$ is located between previous estimates ($-13\,\mathrm{a}_0$ [84] and $-16.9\,\mathrm{a}_0$ [79]).

Second, the phase shift calculations including the standard LS interaction result in the following J-dependent shape resonance positions: $E_r^{J=(0,1,2)} = (24.4, 25.5, 27.7)\mathrm{meV}$. As expected for pure Russel-Saunders coupling (LS coupling with L being the total orbital angular momentum and S the total spin, cf. section 2.2.1), the obtained J-dependent resonance positions fulfill the Landé interval rule [84]. Note that the authors in ref. [84] report that their estimated fine structure splitting (associated with the E_r^J splitting) deviates from the Landé interval rule by about 10% for Rb$^-$, indicating the importance of relativistic effects for heavy alkali-metal atoms, which are not included in our applied model potential.

In figure 4.9 the results of our adapted phase shift calculations (solid lines) are presented. The J-averaged p-wave scattering phase shift lies between $^3P_2$ and $^3P_1$ shifts. For comparison, the dotted lines represent the results of the *ab initio* phase shift calculations given in refs. [78, 84]. As mentioned earlier, our extracted J-averaged resonance position occurs for slightly larger scattering kinetic energies, and consequently, compared to the *ab initio* phase shifts, our J-dependent p-wave data are shifted towards higher scattering energies.

As stated before (in section 4.2), the binding energies calculated with the *ab initio* phase shifts showed a rather poor agreement with the experimental data. In conclusion to this chapter, let us substantiate this statement. In figure 4.10, the measured binding energies are compared with the energies calculated using our extracted phase shifts (reprinting the data from figure 4.5) and the *ab initio* phase shifts shown in figure 4.9. For the s-wave dominated dimer state D, the *ab initio* data lead to slightly lower binding energies compared to the experimental data. In

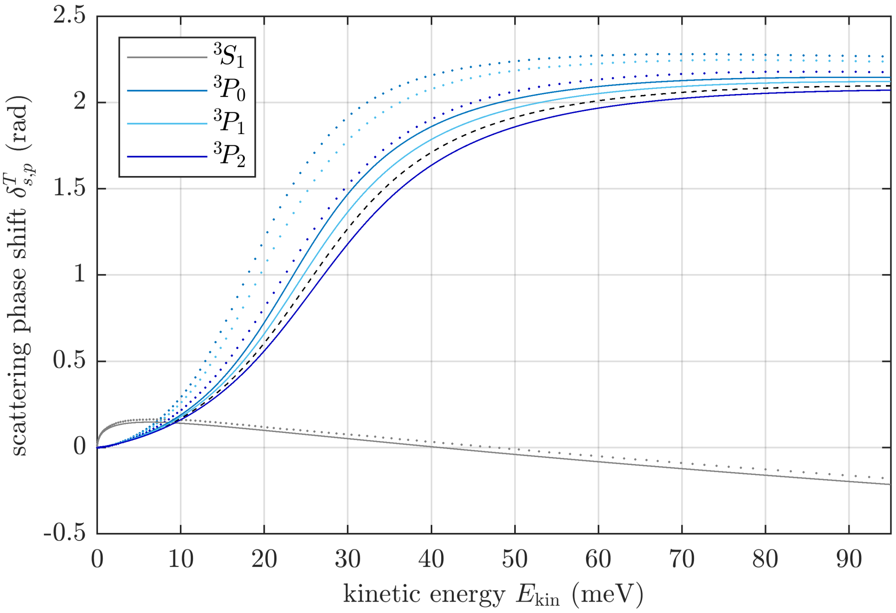

Fig. 4.9: Triplet s- and p-wave scattering phase shifts for e$^-$-Rb scattering. The solid lines represent the adapted shifts δ^T_s and $\delta^T_{p,J}$ as a function of $E_{\text{kin}} = \frac{\hbar^2 k^2}{2m_e}$ obtained from fitting the measured molecular states. The dashed line shows the (J-averaged) p-wave phase shift in absence of spin-orbit coupling applied for Green's function calculations. The dotted lines correspond to the predicted phase shifts reported in refs. [78, 84].

contrast, we observe a larger discrepancy for the p-wave dominated dimer states A and B. It is particularly striking that the zigzag structure is poorly captured by the calculations when using the *ab initio* phase shifts (cf. open and filled symbols in figure 4.10). Typically, the *ab initio* data deviate from the measured binding energies by a few tens of MHz for the dimer states A and B. For example, the calculated binding energy of the dimer state A is off by more than 40 MHz for $n = 37$. Furthermore, at $n = 31$ the calculations predict the doublet structure close to binding energies of -140 MHz, but no molecular lines were found in this region ($\delta = -160 \cdots -120$ MHz) in the experiment. Instead, the experimental data clearly show that the doublet of A occurs for binding energies around -170 MHz. Overall, we find that the calculations based on the *ab initio* phase shifts result

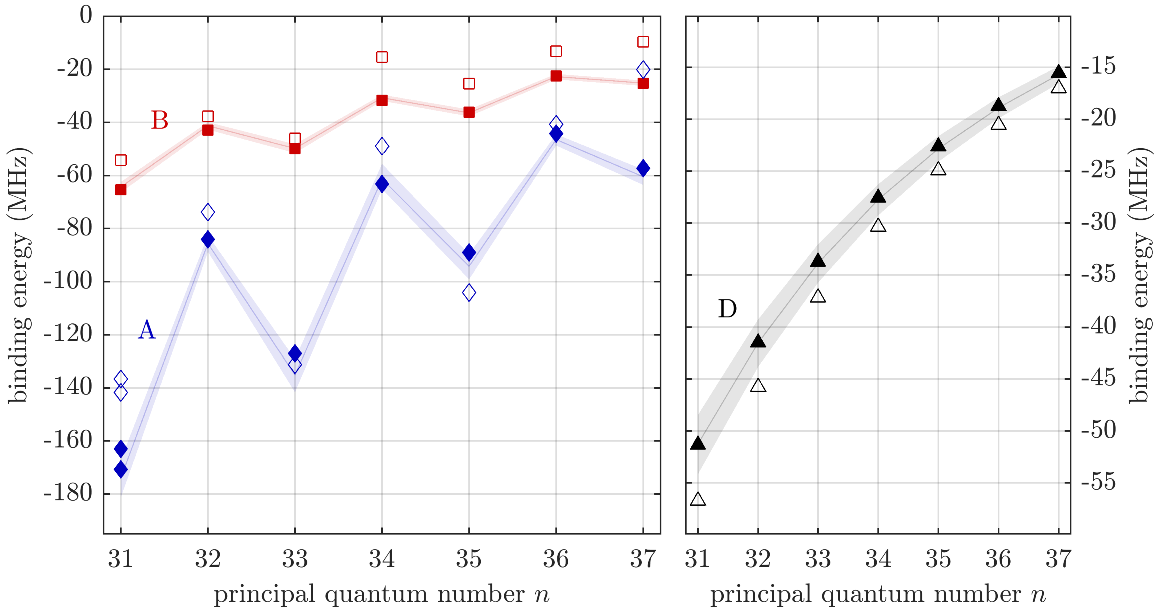

Fig. 4.10: Comparison of the binding energies of the deeply bound dimer stats A and B (on the left), as well as D (on the right). The filled symbols represent the measured molecular lines. The transparent data correspond to the binding energies resulting from our adapted phase shifts, while the open symbols are calculated using the predicted phase shifts from refs. [78, 84] for s- and p-wave scattering.

in binding energies which underestimate the bound state energy of the p-wave dominated dimer A (except for $n = 33$ and 35) and B. For the dimer state D the prediction lies below the experimentally obtained binding energies.

5

Local atom loss in a BEC induced by Rydberg atoms

This chapter reports on the status of an ongoing research on an experimentally and theoretically investigated local atom loss in a Bose-Einstein condensate induced by Rydberg atoms. The following sections show that the observed atom loss is connected to the Rydberg excitation in the BEC. Explicitly, in the region of the Rydberg excitation, a decreasing condensate density is observed. The measured loss feature grows continuously over time, even long after the Rydberg atom is no longer present. The feature is mainly limited to the position of the excited Rydberg atom. The amount of observed loss greatly exceeds previously measured atom loss induced by free-particle and phonon excitations (ref. [46]) in the condensate. The experimentally observed loss feature is compared to numerical simulations, which largely underestimate the amount of condensate density change in the excitation region. Parts of the work presented in the following are prepared to be published in ref. [S3].

5.1 Initial motivation: Imaging an atomic orbital

A central element in the description of quantum mechanics is the wavefunction, which behaves according to the time-dependent Schrödinger equation [131]. It is the Copenhagen interpretation from the 1930s that tells us that from the wavefunction one can obtain the probability of observing the outcome of measurements on a quantum mechanical system [132], for instance, the energy of a state or the momenta or the position of constituents of the system. Essentially, the interpretation allows us to connect microscopic phenomena of quantum mechanical nature, which are described by the wavefunction, with the macroscopic observations in the laboratory, which corresponds to the observation of one of several possible realizations that are permissible for the wavefunction.

In atomic physics, a prime example of such a measurement is the direct imaging of the spatial atom density distribution of a Bose-Einstein condensate (first direct observation of a BEC ref. [133]), which comprises an ultracold and dense atomic ensemble of atoms that is described by a single state of matter, namely the Bose-Einstein condensate wavefunction. The direct optical imaging of a BEC is made possible by two things. First, the typical size of a condensate realized in laboratories is on the micrometer scale and thus large enough to be resolved with light of the visible spectrum, which is also commonly used for preparation and manipulation of the atomic states. Second, the light-matter interaction between the imaging light and the condensed atoms is strong enough to result in a measurable signal using state-of-the-art imaging techniques.

In solid-state physics, the scanning tunneling microscopy (STM) invented in 1982 (ref. [134]) has had outstanding success and turned out to be a powerful tool for visualizing the electronic surface state of conductive material. STM is often used to map out the orbital structures of complex molecules [135], which are placed on a conductive substrate with a thin non-conductive layer, however, strong interactions with the substrate often obscure the resulting image data [136].

Another method for visualizing the orbital density of an electronic wavefunction is the reconstruction from high harmonic generation of intense femtosecond laser pulses. The reconstruction method has been applied to molecules in the solid-state, by means of photoemission spectroscopy [137], and to molecules (ref. [138]) and atoms (ref. [139]) in the gas phase, successfully reconstructing an image of the orbital density of the electronic wavefunction. Another approach has been realized by Stodolna *et al.* (ref. [140]). In their work, the authors were able to directly observe the nodal structure of stark states for hydrogen by photo-ionization and subsequent electron detection. Yet another method for mapping out the electron wavefunction has been realized recently by Waitz *et al.* (ref. [141]). The method combines photoelectron emission measurements with the coincident detection of reaction fragments, allowing the authors to visualize the probability density of the correlated two-electron wavefunction of a hydrogen molecule.

All imaging techniques mentioned above are essentially based on a tomographic reconstruct of the electronic orbitals. In this work, a completely different approach is pursued. The method is based on the electron-atom interaction for a Rydberg atom immersed in a Bose-Einstein condensate (cf. ref. [46]), and was proposed in 2015 by Karpiuk *et al.* [142]. The main idea is to exploit the imprinted phase on the BEC-wavefunction caused by the Rydberg electron-atom interaction. Essentially, the condensate acts as a contrast agent resembling the Rydberg electron density distribution given enough time for the imparted phase to manifest in the condensate density. In contrast to all above-mentioned methods this approach potentially allows the direct optical observation of electron orbitals in a single shot experiment. Recently, the method has been studied theoretically demonstrating the potential use for studying ultracold quantum dynamical processes by tracing Rydberg atoms within a BEC [143].

As part of this work, the experimental apparatus has been extended by an optical dipole trap (cf. section A.2) for preparing a flat pancake-like condensate, which brings the experimental realization of the proposed orbital imaging method within reach. In the following, we briefly discuss a parameter set that should make the observation of an electron wavefunction feasible. A detailed discussion and listing of the relevant parameter range for performing the imaging method is given in the thesis of M. Schlagmüller [95] as well as in the work of Karpiuk *et al.* [142].

A fundamental limit of the imaging technique is the optically achievable resolution. In the experiment, the BEC is imaged in-situ via phase-contrast imaging (for details see [102]), making use of a high-numerical aperture (NA = 0.55) aspheric lens (Asphericon A15-12HPX-U), which sets the lateral imaging resolution just below 1 μm for the used 780 nm light. As a consequence, the radial size of the Rydberg orbit needs to be larger than 1 μm, which places the lower limit of the principal quantum number above $n = 100$ for low-angular momentum states.

An upper limit of n is essentially defined by two factors, these are the interaction strength, given by the Rydberg electron-atom scattering potential $V_{\mathrm{Ryd}}(\vec{r})$ (cf. equation 2.33 in section 2.3), and the interaction time of the Rydberg electron with the condensed atoms of the BEC. Both factors directly determine the amount of the imprinted phase on the BEC-wavefunction [95, 142].

For large principal quantum numbers ($n \sim 100$), the collisional lifetime τ of the initial Rydberg state excited in the BEC is on the order of ten microseconds and increases with n^3 for increasing n [S7]. However, the Rydberg orbit size scales with n^2, meaning that the Rydberg electron engulfs a larger volume and thus exhibits a lower local electron density, which consequently leads to a smaller interaction strength (cf. section 2.1.1 and 2.3). Additionally, the interaction strength is needed to be at least comparable to the chemical potential of the condensate [142],

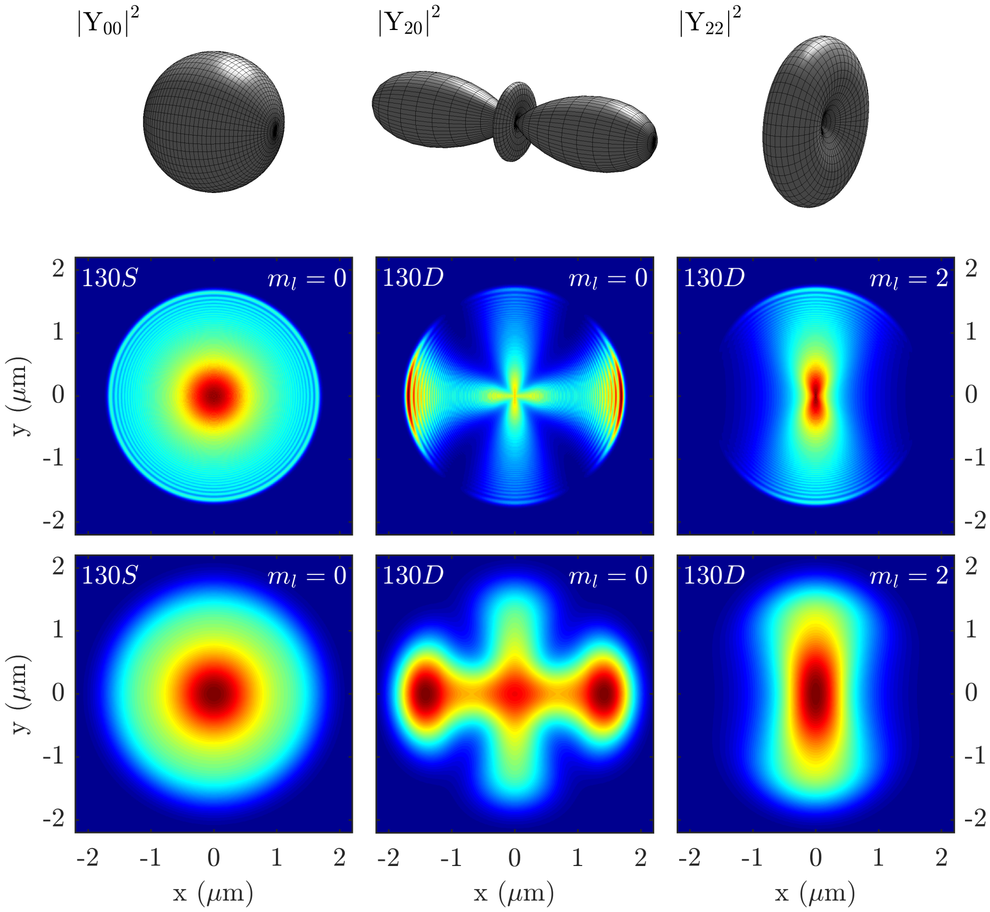

Fig. 5.1: Visualization of the structure of a S-state and D-state orbitals. In the upper section, the spherical harmonics $Y_{lm}(\theta, \phi)$ are shown, representing the spherical shape of an atomic orbital. In the middle and the lower section, the integrated electron density distribution of a $n = 130$ Rydberg state is presented. The lower section includes an imaging resolution of $1\,\mu$m.

which is typically on the order of a few kHz. This sets the upper limit to $n \simeq 200$ for which the depth of the outermost well of V_{Ryd} is on the order of 1 kHz. The depth of the interaction potential scales with n^{-6} (cf. section 2.3), which leads to a combined scaling of $V_{\text{Ryd}} \times \tau \sim n^{-3}$. From this, we can deduce that within the limited range of n ($100 < n < 200$), a lower principal quantum number is more beneficial for imaging the electron orbital.

In figure 5.1 the orbital structure of a S-state and a D-state with $m_l = 0$ and $m_l = 2$ are visualized. The quantization axis is chosen to be along the x-direction. In the top row, the orbitals are represented in a textbook-like manner, showing the isosurface of the corresponding spherical harmonics. On the middle and the bottom row, the integrated electron density distribution is depicted for a $n = 130$ Rydberg state. The angular shape of the electron orbit is modified with the highly oscillating radial structure of the electron distribution. In the bottom row, the density distribution is shown for an imaging resolution achievable in the experiment. The resolution is included by applying a convolution using a 2d Gaussian function with $4\sigma = 1\,\mu$m. As expected, the radial structure is blurred out if the imaging resolution is taken into account.

Besides the Rydberg orbit size and the amount of the imprinted phase on the condensate, the visibility of the imaged electron orbit crucially depends on the integrated atom density along the imaging axis. For a high contrast, it is desirable to minimize the contribution to the integrated density of atoms outside the Rydberg orbit. Therefore, the size of the condensate is ideally on the order of magnitude of the expansion of the Rydberg wavefunction. The condensed atom sample in the newly implemented pancake-like crossed optical trap comprises typically 2×10^5 atoms, and with that exhibits a spatial extension of $d_{xyz} = (21,\, 31,\, 5)\mu$m, fulfilling the aforementioned requirements.

The outcome of a numerical simulation of the Gross-Pitaevskii equation (GPE) is shown in figure 5.2. The time-dependent evolution of the condensate wavefunction is obtained by numerical integration of the GPE using an operator split-step method [144]. At $t = 0$, the electron-atom scattering interaction $V_{\mathrm{Ryd}}(\vec{r})$ ($130D$ Rydberg state with $m_j = 1/2$) is switched on instantaneously and switched off after a phase imprint time of $10\,\mu$s. Due to the imprinted phase gradient, the

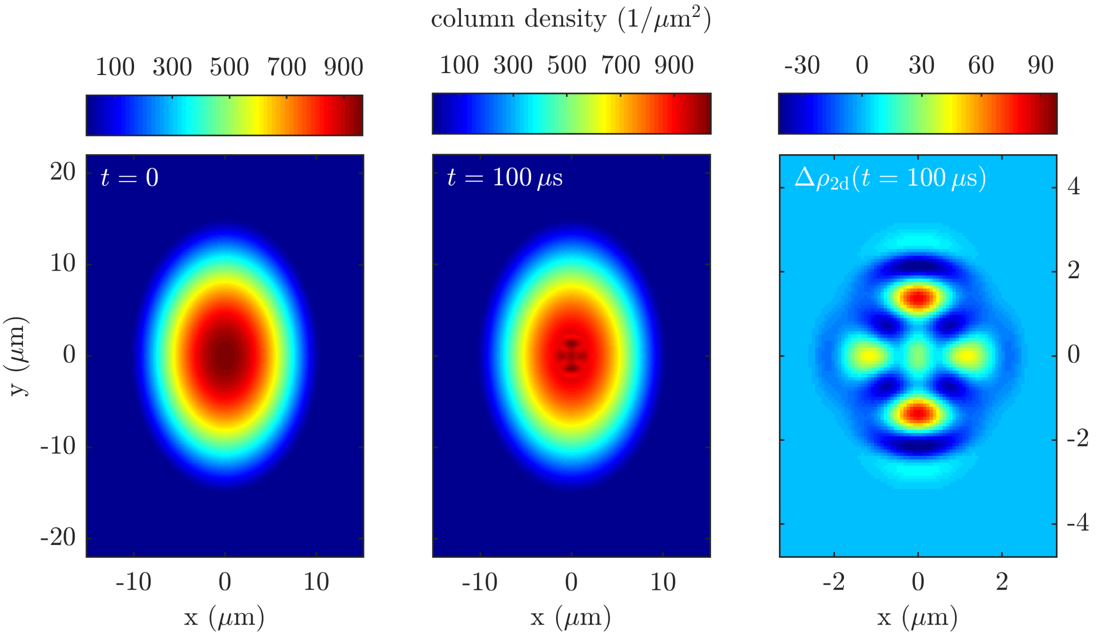

Fig. 5.2: Calculated BEC density distribution for a single Rydberg excitation in the center of the condensate and an imaging resolution of 1 μm. The electron-atom interaction V_{Ryd} is switched on for 10 μs. The density distribution is integrated along the imaging axis (z). The column density $\rho_{2\mathrm{d}}$ is presented in units of the resolution squared ($1\,\mu\mathrm{m}^{-2}$). On the left, the BEC is shown before the phase imprint takes place. The density distribution for an evolution time of 100 μs is depicted in the center. On the right, the column density distribution difference between the condensate with and without Rydberg atom is shown.

atoms of the condensate flow towards the regions of large phase imprint. After an evolution time of about 100 μs the imprinted phase is largely transformed into a local density modulation, which mimics the Rydberg electron orbit. At this point, the condensate exhibits a maximum density increase of about 10% of the original peak density. Overall the density modulation nicely resembles the characteristic shape of the D-orbital (cf. $m_l = 0$ in figure 5.1). For longer evolution times the density modulation abates.

When measuring small atom numbers, one has to take into account the statistical fluctuation (shot-to-shot noise) of the atom number ΔN imaged per resolution unit Δr^2, which possibly diminishes the contrast of the imaged orbit. The statistical fluctuation (ΔN_{r^2}) originates from the measurement of the column density of the condensate, essentially collapsing the BEC-wavefunction onto a state with a defined atom number per resolution unit [145]. In this case, the fluctuation is given by: $\Delta N_{r^2} = \sqrt{N_{r^2}}$.

For the scenario presented in figure 5.2, the column density in units of $\Delta r^2 = 1\,\mu\mathrm{m}^{-2}$ yields an atom number of $N_{r^2} \gtrsim 900$ for the density region that overlaps with the Rydberg atom. The statistical fluctuation in this density region is then given by $\Delta N_{r^2} = 30$, which reaches an amount of about 30% of the maximal expected density enhancement. The expected contrast is lowered by that value. Consequently, the achievable contrast between the background condensate and the imaged club-like shaped orbital is expected to be 7-10% for the case demonstrated in figure 5.2, which makes the experimental observation, in principle, possible.

5.2 Orbital imaging attempt and local atom loss

In the previous section, we discussed a possible set of parameters for experimentally realizing the orbital imaging of a Rydberg electron following the proposal of Karpiuk *et al.* [142]. The outcome of numerical simulations of the Gross-Pitaevskii equation showed that the imaging of an electron orbital in the $130D$ Rydberg state can be achieved with the pancake-like Bose-Einstein condensate prepared with the experimental apparatus. Importantly, the phase which is locally imparted on the BEC as a consequence of the Rydberg electron-neutral interaction, is large enough to result in a considerable density modulation resembling the shape of the Rydberg electron orbit. This density modulation is expected to be well above the estimated shot-to-shot atom number fluctuation.

In this section, the results of time-resolved measurements of the atom density distribution of the condensate wavefunction are presented for a spatially localized Rydberg excitation in the center of the BEC. The atom distribution is obtained from taking in-situ images of the condensate, employing a phase-contrast imaging technique [146]. Each image of the BEC yields an atom number per resolution unit (the atom column density), allowing us to quantify the atomic density distribution. The time evolution of the spatial distribution can be measured by varying the hold time between the Rydberg excitation and the imaging of the condensate.

Exemplarily, the measurement outcome of a single Rydberg excitation is depicted in figure 5.3 for the case calculated in the previous section (cf. figure 5.2). Despite the promising contrast achieved in the simulations, a clear signature fails to appear for the collected data. To improve the signal-to-noise ratio, experiments with multiple subsequent excitations are performed, leading to a measurable local change of the condensate density distribution. Surprisingly, the experimentally obtained atom distributions reveal a decreased atom number in the region of the Rydberg excitation, which further decreases over time even after the Rydberg atom has been extracted. This seemingly contradicts previous theoretical studies [142, 143], which predict an increase in the local density. The experimental results might hint towards a so-far unexplored local atom loss induced by the Rydberg impurity. In order to study the local loss, a series of experimental characterization measurements are performed. The results of these are displayed in figure 5.4. The experimental and theoretical studies outlined in this and the following section are part of an ongoing investigation (ref. [S3]).

First, let us begin with the measurements for the $130D$ Rydberg state. A single Rydberg atom is excited in the center of the BEC, which is held in a crossed optical dipole trap (see section A.2). The condensate typically comprises 2×10^5 ^{87}Rb atoms that are prepared in the spin-polarized $\left|5S_{1/2}, F = 2, m_F = 2\right\rangle$ ground-state. The Rydberg state is addressed via two counter-propagating excitation laser beams (420 nm and 1015 nm) along the z-axis. The two-photon excitation incorporates the intermediate $6P_{3/2}$ state. The intermediate state population is kept low by using a large intermediate detuning of +160 MHz. The excitation of a single atom into the Rydberg state is ensured by the Rydberg-Rydberg excitation blockade [147]. After a successful Rydberg excitation, a strong electric field pulse ionizes the Rydberg atom and guides the generated ion towards a microchannel plate detector. The position of the Rydberg atom is well-localized by the aid of the strongly focused excitation laser beam. The 1015 nm excitation laser is focused through the same high-NA lens that is used for the high-resolution imaging of the atom cloud, yielding a tightly focused laser beam waist of about $w_0 = 1.8\,\mu$m. In addition, the excitation probability in the center of the condensate can be further enhanced by detuning the excitation laser from the atomic resonance by the electron-atom interaction induced density shift (cf. section 2.3).

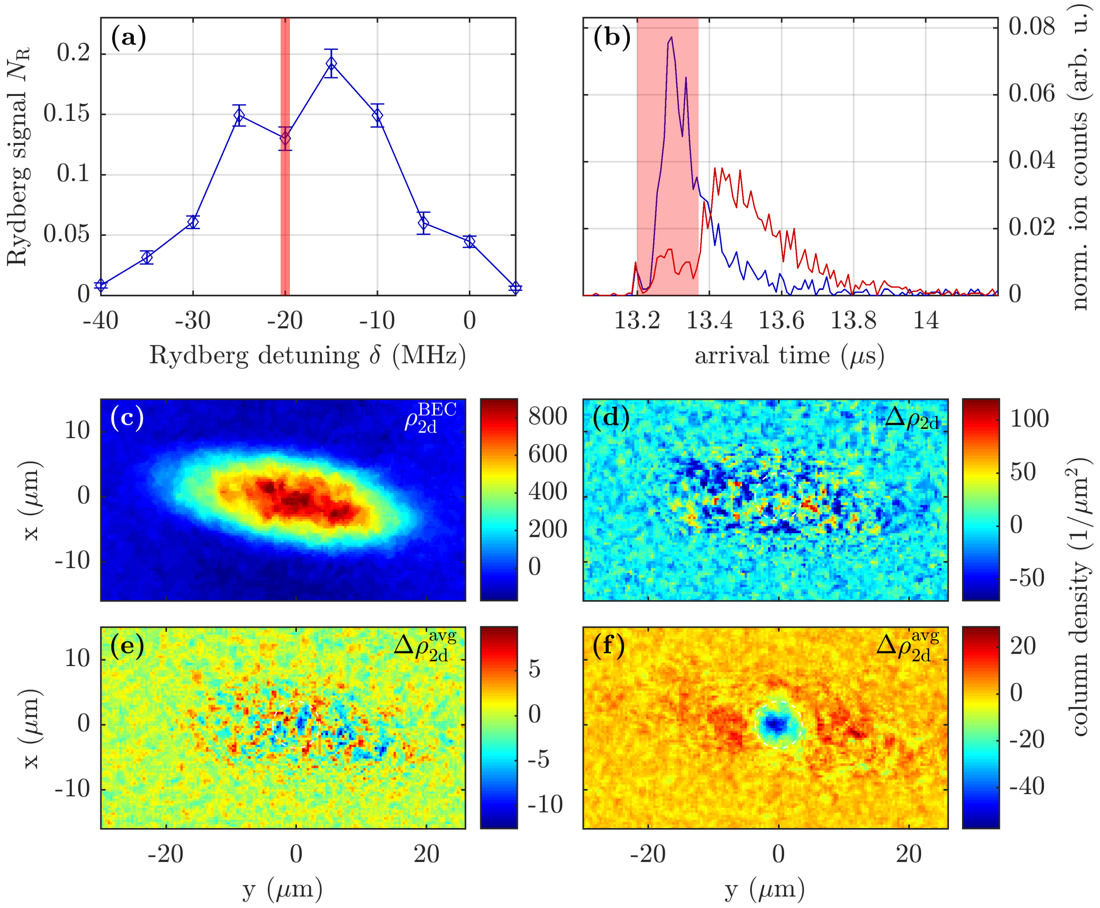

Fig. 5.3: First try of orbital imaging of the $|130D, m_j = 1/2\rangle$ Rydberg state in the optically trapped BEC for an imprint time of $t_d = 10\,\mu$s and an evolution time of $t_{evo} = 100\,\mu$s. (a) Rydberg spectrum taken in the BEC. The atomic resonance of the addressed Rydberg state is set to $\delta = 0\,$MHz. The shaded region indicates the Rydberg excitation detuning ($-20\,$MHz) and bandwidth ($\sim 1\,$MHz) employed for the orbital imaging measurement. (b) Ion arrival time at the detector for a state-selective ionization of the Rydberg atom (see text). The data in blue (red) are taken for an ionization delay of $t_d = 0.3\,\mu$s ($t_d = 10\,\mu$s). The shaded region represents the time window taken for post-selection onto experiments where the Rydberg atom has not undergone a state-changing collision. In (c) - (e) the phase-contrast image of the BEC (c), the difference image of a single experiment (d) as well as the averaged difference image (e) is presented. For comparison, (f) shows the result for multiple subsequent excitations ($N_{pulses} = 30$) for an evolution time of $150\,\mu$s. The column density ρ_{2d} is given in units of the resolution squared ($1\,\mu$m^{-2}).

Figure 5.3(a) shows a Rydberg spectrum for the $|130D, m_j = 1/2\rangle$ Rydberg state excited in the pancake-like condensate. The Rydberg excitation duration is set to $t_{\text{exc}} = 1\,\mu\text{s}$, resulting in an excitation bandwidth of about 1 MHz. The spectrum exhibits a large energy shift and broadening due to the electron-atom interaction between the Rydberg electron and the atoms within its wavefunction. For the orbital imaging measurements, a large red detuning from the atomic resonance is chosen to excite the Rydberg atom primarily in the center of the BEC, at the highest density. The employed Rydberg detuning and the excitation bandwidth is indicated by the shaded region.

To distinguish Rydberg atoms that have undergone a state-changing collision (ref. [S7]) from Rydberg atoms in their initial prepared state, a state-selective electric field ionization is performed. Figure 5.3(b) shows the outcome of such a measurement for a Rydberg excitation in the BEC. The blue data represent a measurement for a short ionization delay time ($t_{\text{d}} = 0.3\,\mu\text{s}$), while the red curve shows the signal obtained for a delay time of $t_{\text{d}} = 10\,\mu\text{s}$. The Rydberg ion count rate is shown as a function of the ion arrival time at the microchannel plate detector. The ionization field is ramped up to 7 V/cm within $3\,\mu\text{s}$. Rydberg atoms that have undergone a l-changing collision ionize diabatically (for $l > 2$) for the applied electric field slew rate and thus exhibit an up to 4 times higher ionization threshold than the initial low-l state that ionizes adiabatically (classical) [S7, 27]. This can be seen in the ion count rate signal as a shift to later ion arrival times. The signal for a short ionization delay (blue) shows a relatively sharp peak around $t = 13.1\,\mu\text{s}$, whereas for a longer interaction time (red) between the Rydberg atom and the many ground-state atoms within its electron orbit, a l-changing collision is more likely, resulting in the above-mentioned signal shift towards later ion arrival times. The separation of the ion signal enables us to distinguish the experimental runs in which the Rydberg atom has undergone a state-changing collision from the events in which the Rydberg atom has not changed its angular momentum state. The shaded region in figure 5.3(b) represents the ion arrival time window that is used for post-selecting the experimental runs of the orbital imaging measurements. Note that it has been experimentally verified that the collisional lifetime in the condensate is similar for the nS and the nD Rydberg state for the investigated principal quantum numbers.

For the orbital imaging measurements, the BEC is imaged after an evolution time of $t_{\mathrm{evo}} = 100\,\mu\mathrm{s}$, where $t_{\mathrm{evo}} = 0$ is set to the beginning of the Rydberg excitation pulse. The imprint duration is defined by the Rydberg ionization delay $t_{\mathrm{d}} = 10\,\mu\mathrm{s}$. Note that the atoms are exposed to the imaging light for $10\,\mu\mathrm{s}$, which is fast compared to the dynamics of the condensate and thus can be neglected to a large extent. By post-selecting for the ion signal, which corresponds to a low-angular momentum state (cf. figure 5.3(b)), we ensure that the Rydberg atom has remained in its initially prepared state. The bottom panel (c-f) in figure 5.3 displays the atom column density $\rho_{2\mathrm{d}}$ and the difference column density $\Delta\rho_{2\mathrm{d}}$ obtained from the orbital imaging measurements. The column density is calculated from the measured phase-contrast image [102]. The difference column density is determined by subtracting a matching reference image. Due to the shot-to-shot fluctuation of the BEC position and phase errors caused by the imperfection of the imaging system, an image recognition algorithm is used to reconstruct a suitable reference image (for details see section C.1). For the difference images shown in (d) and (e), a set of 300 reference BEC images is used. The reference images are recorded in the absence of the Rydberg atom. For this, the same measurement sequence including the Rydberg excitation lasers is employed, but for a different Rydberg detuning (typically $+50\,\mathrm{MHz}$) that prohibits a Rydberg excitation. For reference, (c) depicts the column density obtained from a phase-contrast image of the BEC.

For the measurements presented in figure 5.3(d)-(e), in total over 2300 images were recorded. After post-selection on experiments in which the Rydberg atom stayed in its initial state, 144 images remained. Figure 5.3(d) shows the difference column density for a typical single-shot experiment, while in (e) the averaged difference column density of the post-selected data is depicted. The imprint region is indicated by the dashed white circle, the size of which is estimated as the diameter of the Rydberg orbit and the waist of the excitation beam. Neither the single-shot images nor the averaged difference column densities exhibit a clear signal of the excited $130D$ Rydberg state. Note that the measured standard deviation of $\rho_{2\mathrm{d}}$ for the peak density of the BEC leads to a value of $\Delta N_{r^2} \approx 50$, which is larger than estimated in the previous section ($\Delta N_{r^2}^{\mathrm{tot}} = 30$). The enhanced fluctuation of the column density can be explained by the photon-shot noise of the imaging light $\Delta N_{r^2}^{\mathrm{photon}} \approx 15$, which is obtained from the fluctuations outside of the BEC, and the fluctuating total atom number of the condensate ($\Delta N_{\mathrm{BEC}} \approx 5000\,\mathrm{atoms}$) that leads to an additional fluctuation of $\Delta N_{r^2}^{\mathrm{atom}} \approx 8$.

In order to increase the signal strength of the phase imprint, measurements with multiple subsequent Rydberg excitations are carried out. In the ideal case, the Rydberg atom is continuously re-excited in the center of the condensate [95, 142], leading to a continuous phase imprint of the Rydberg potential V_{Ryd}. To achieve this as seamlessly as possible, the imprint duration and the subsequent Rydberg ionization pulse is kept short. The measurement sequence is structured as follows: The sequence is initiated with the first Rydberg excitation ($t_{\mathrm{exc}} = 1\,\mu\mathrm{s}$) followed by an ionization delay of $t_{\mathrm{d}} = 3\,\mu\mathrm{s}$. To ionize the Rydberg atom an electric field of $E_{\mathrm{ioni}} = 7\,\mathrm{V/cm}$ is applied for $0.5\,\mu\mathrm{s}$ (with a rise/fall time of $10\,\mathrm{ns}$). After the ionization pulse, an additional wait time of $0.3\,\mu\mathrm{s}$ is implemented to allow the electric fields between the electrodes to fall off before the next Rydberg excitation takes place. The whole ionization part takes $t_{\mathrm{ioni}} = 0.8\,\mu\mathrm{s}$. With this, a single pulse sequence out of the total measurement cycle is $4.8\,\mu$s long, which yields a repetition rate of 208 kHz for the imprint sequence. The single pulse sequence is repeated N_{pulses} times. When taking into account the collisional lifetime of $\tau = 10\,\mu$s and the Rydberg excitation duration of $t_{\text{exc}} = 1\,\mu$s, the phase imprint duration per imprint sequence is on average $3\,\mu$s.

The results of the re-excitation measurement for the $|130D, m_j = 1/2\rangle$ Rydberg state is presented in figure 5.3(f). The measurements are carried out for $N_{\text{pulses}} = 30$ subsequent Rydberg excitation pulses and an evolution time of $t_{\text{evo}} = 150\,\mu$s. The difference column density is obtained from 180 condensate images without any post-selection. In contrast to the single-shot experiments, the averaged column density exhibits a significant density change in the imprint region (white circle).

Surprisingly, the atom density decreases despite the fact that the electron-atom interaction V_{Ryd} is mostly attractive. The measured density dip contradicts the outcome of the numerical simulations of the GPE (cf. section 5.3). Summing up $\Delta\rho_{\text{2d}}$ in the area of the reduced density, yields a difference atom number and with that a local atom loss of $\Delta N = -940(90)$ atoms for the multiple excitation measurement. The observed atom loss feature reaches a depth of $\Delta\rho_{\text{2d}} = -60\,\mu\text{m}^{-2}$. In comparison to the single-shot data, the signal depth is similar in amplitude as the observed density fluctuations. However, these fluctuations are largely averaged out for the single excitation experiments, whereas a significant density dip forms for multiple excitations.

In order to investigate the observed local atom loss, a series of characterization measurements are carried out for the $133S$ Rydberg state in the cigar-shaped condensate. In contrast to the above presented D-state measurements, that are performed in a comparatively flat pancake-like condensate (cf. section A.2), the atom loss for the S-state in the cigar-shaped BEC (cf. section A.3), yields a significantly larger signal-to-noise ratio. For the characterization, the same pulse sequence used for the D-state measurements is employed. The results of the 133S-state characterization measurements are presented in the following.

In figure 5.4(a) the atom column density for several excitation pulses ($N_{\text{pulses}} = 10$) and an evolution time of $200\,\mu$s of a single experiment is depicted. The resulting difference column density averaged over 154 experiments is shown in (b). In comparison to the multiple excitation D-state data (figure 5.3(e)), the signal depth of the loss feature is six times greater for a third of the excitation pulses. The obtained local atom loss amounts $\Delta N = -5100(290)$ atoms, which is over five times larger than for the presented D-state measurement. Figure 5.4(c-e) summarizes the characterization measurements for the 133S state. The insets show the resulting difference column density for the measurements as indicated.

Let us first consider the data set for different numbers of excitation pulses (c). The experiments are performed at an evolution time of $200\,\mu$s and a Rydberg detuning of $-50\,$MHz, addressing the center region of the BEC. At first, the observed local atom loss increases linearly with the number of excitation pulses. For a larger number of pulses ($N_{\text{pulses}} > 20$), the Rydberg excitation probability drops as a result of local atom depletion in the excitation region, which is also evident in the recorded ion arrival times. A linear dependence of the atom loss induced by Rydberg excitations within a BEC has been observed previously by Balewski *et al.* [46]. However, the local atom loss observed here is significantly larger. Employing the theoretical description of ref. [46], which includes phonon and free-particle excitations induced by the electron-atom interaction, yields an atom loss per excitation pulse of 40 atoms/pulse, whereas the atom loss presented in figure 5.4(c) yields: $\Delta N/N_{\text{pulses}} = 440$ atoms/pulse, for $0 < \mathrm{N}_{\text{pulses}} < 20$. Note that in contrast to the measurements presented here, the atom loss reported in ref. [46] was determined via absorption imaging of the condensate after a hold time of

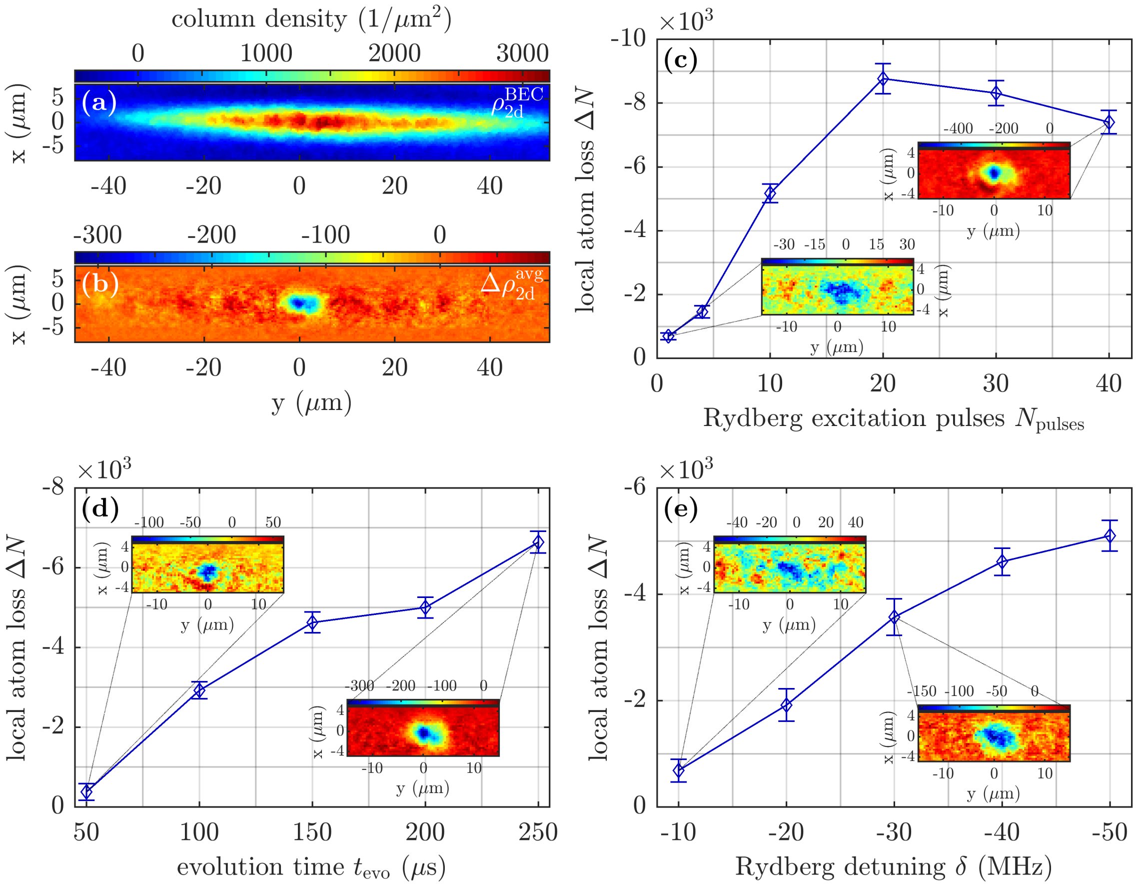

Fig. 5.4: Local atom loss measurements of the $|133S, m_j = 1/2\rangle$ Rydberg state in the magnetically trapped BEC. The Rydberg detuning is set to $\delta = -50\,\mathrm{MHz}$ to address the center of the condensate. (a) Phase-contrast image of the BEC for $N_{\mathrm{pulses}} = 10$ and $t_{\mathrm{evo}} = 200\,\mu\mathrm{s}$. (b) Averaged difference image obtained from (a). (c) Atom loss ΔN as a function of excitation pulses. (d) and (e) Atom loss as a function of t_{evo} and δ, respectively. All error bars indicate one standard deviation. Insets show the column density of the averaged difference images for selected data points.

several milliseconds and a free-flight expansion of 50 ms. At last, note that for a single excitation pulse the determined atom loss with and without post-selection yields: $\Delta N = -652(102)$ and $\Delta N = -694(105)$, respectively, which validates that only a minor fraction of Rydberg atoms has undergone a l-changing collision for the employed Rydberg ionization delay of $3\,\mu\mathrm{s}$.

In figure 5.4(d-e) the local atom loss as a function of evolution time and Rydberg detuning is shown for 10 excitation pulses. For the evolution time measurement, the Rydberg detuning is set to $\delta = -50\,\mathrm{MHz}$, while for the detuning measurement an evolution of $t_{\mathrm{evo}} = 200\,\mu\mathrm{s}$ is used. The local atom loss for both data sets increases approximately linearly with evolution time and Rydberg detuning, respectively. Note that due to the density gradient, the density dip refills with the surrounding condensate atoms as expected for larger evolution times ($t_{\mathrm{evo}} \gtrsim 1\,\mathrm{ms}$, not shown), reflecting the fluid properties of the BEC. From the theory section 2.3 we know that the Rydberg detuning essentially corresponds to the selection of a density region in which the Rydberg atom is excited. For a smaller detuning e.g. $\delta = -10\,\mathrm{MHz}$, the Rydberg atom is preferably excited close to the edge of the condensate, where the atom density is low. When taking into account the tightly focused excitation laser beam, which we recall propagates along the imaging axis, it turns out that Rydberg atoms are preferably excited on the top and the bottom of the condensate. For an intermediate Rydberg detuning e.g. $-30\,\mathrm{MHz}$, the excitation region is closer to the BEC center but moderately suppressed in the middle, where the intensity of the excitation laser is high. As a consequence, the excitation region covers a larger surface area, which is evident in the inset of figure 5.4(e) for $\delta = -30\,\mathrm{MHz}$. The atom loss feature exhibits an increased size.

5.3 Modeling the local atom loss

The previous section presented the result of an experimental study of a Bose-Einstein condensate that interacts with a Rydberg atom impurity. The effects of the impurity on the condensate wavefunction were investigated by probing the local atom density of the BEC after an evolution time of typically 200 microseconds. We recall that the interaction of the impurity atom with the BEC atoms leads to a spatially varying phase imprint on the condensate wavefunction, which reflects the spatial impurity-condensate interaction. Moreover, we recall that over time the imprinted phase evolves into a density modulation of the BEC, which essentially mirrors the phase imprint.

Surprisingly, in the experiment the Rydberg impurity leads to a significant local atom loss, contradicting the outcome of the numerical simulations of the Gross-Pitaevskii equation. To characterize this loss, a series of measurements for several numbers of subsequent Rydberg excitations, different evolution times as well as a series for different Rydberg detunings have been performed. The outcome of these measurements is presented in figure 5.4.

In this section, we discuss the theoretical modeling of the observed local atom loss. In order to better understand the origin of the loss feature, classical and quantum mechanical numerical simulations were performed. By simulating the time evolution of the local atom density distribution, the level of detail of the interactions included can be gradually increased, whereby the origin of the effects caused can be distinguished.

In the following, the outcome of classical trajectory simulations (CT) and the results obtained from solving the Gross-Pitaevskii equation (GPE) numerically are presented. The simulations are carried out applying a simple form of the electron-atom interaction, using s-wave scattering only, and a more detailed form,

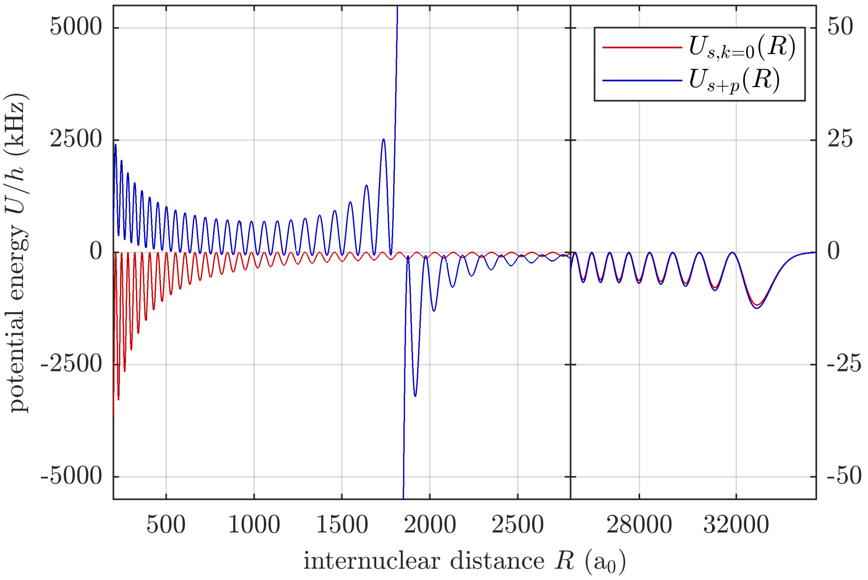

Fig. 5.5: Potential energy curve resulting from e$^-$-Rb scattering for s-wave scattering only (red) and for s- and p-wave scattering (blue) in the vicinity of the $133S_{1/2}$ Rydberg state. The asymptotic zero potential energy is set to the binding energy of the Rydberg electron. The plot range for the internuclear separation is split into two for better visibility. On the left, the inner part of the potential is shown including the avoided crossing between the PEC associated with the $133S$ Rydberg state and the butterfly state resulting from the p-wave shape-resonance (cf. section 2.2). On the right, the PECs are depicted in the vicinity of the outermost potential well.

which additionally includes p-wave scattering. Both the results of CT and GPE simulations reveal a significantly increased atom density at the center position at which the Rydberg atom was placed initially. Therefore, additional calculations including the three-body loss for the rubidium atoms were carried out.

In figure 5.5 the potential energy curve (PEC) for the $133S_{1/2}$ Rydberg state is shown for s-wave scattering only (with the constant triplet scattering length $a_s^T(k=0) = -15.7\,\mathrm{a}_0$) and for s- and p-wave scattering (with the k-dependent triplet scattering length $a_{s/p}^T(k)$, cf. section 2.2). While the potentials are essentially equal at large internuclear distances R between the Rydberg atom and a neutral atom, the interaction energies U differ significantly for smaller separations. At $R \sim 1800\,\mathrm{a}_0$, the calculated PEC including p-wave scattering exhibits an avoided crossing between the potential associated with the $133S$ Rydberg state and the butterfly state, which results from a p-wave scattering shape-resonance. Importantly, the potential energies show a steep drop close to the avoided crossing position and positive energies for smaller distances.

Let us start with the simulations for which only the s-wave scattering of the electron-atom interaction is taken into account. Figure 5.6 shows the outcome of the CT (left) and the GPE (right) calculations for 10 subsequent Rydberg excitations with the same pulse sequence used in the experiment (cf. section 5.2) and an evolution time of $t_{\mathrm{evo}} = (50,\ 100,\ 200)\mu\mathrm{s}$. Note that the ten-pulse sequence ends after $t_{\mathrm{evo}} = 48\,\mu\mathrm{s}$. The bottom row shows the results for many averages (40 for CT calculations and up to 400 for GPE calculations). The Rydberg atom positions are randomly chosen around the origin using a normal distribution with $\sigma_{x,y,z} = (0.4,\ 1.0,\ 0.5)\mu\mathrm{m}$, modeling the spatial excitation probability for the cigar-shaped condensate, including the excitation beam waist ($1.8\,\mu\mathrm{m}$), the atom distribution (see section A.3), and the Rydberg excitation detuning of $\delta = -50\,\mathrm{MHz}$ (cf. section 2.3). Since the Rydberg atom is immersed in an atom sample of approximately homogeneous density and interacts with many atoms at the same time, it is assumed that the Rydberg atom position does not change during the imprint process. For better comparison, the same excitation positions are chosen for the CT and the GPE simulations.

As in the previous sections, the difference column density $\Delta\rho_{2\mathrm{d}}$ of the atoms is shown. The atom density is oversampled by a factor of ten for the non-averaged CT simulations to minimize noise originating from the positional fluctuations of the initially prepared atom sample. The grid size for the GPE simulations is

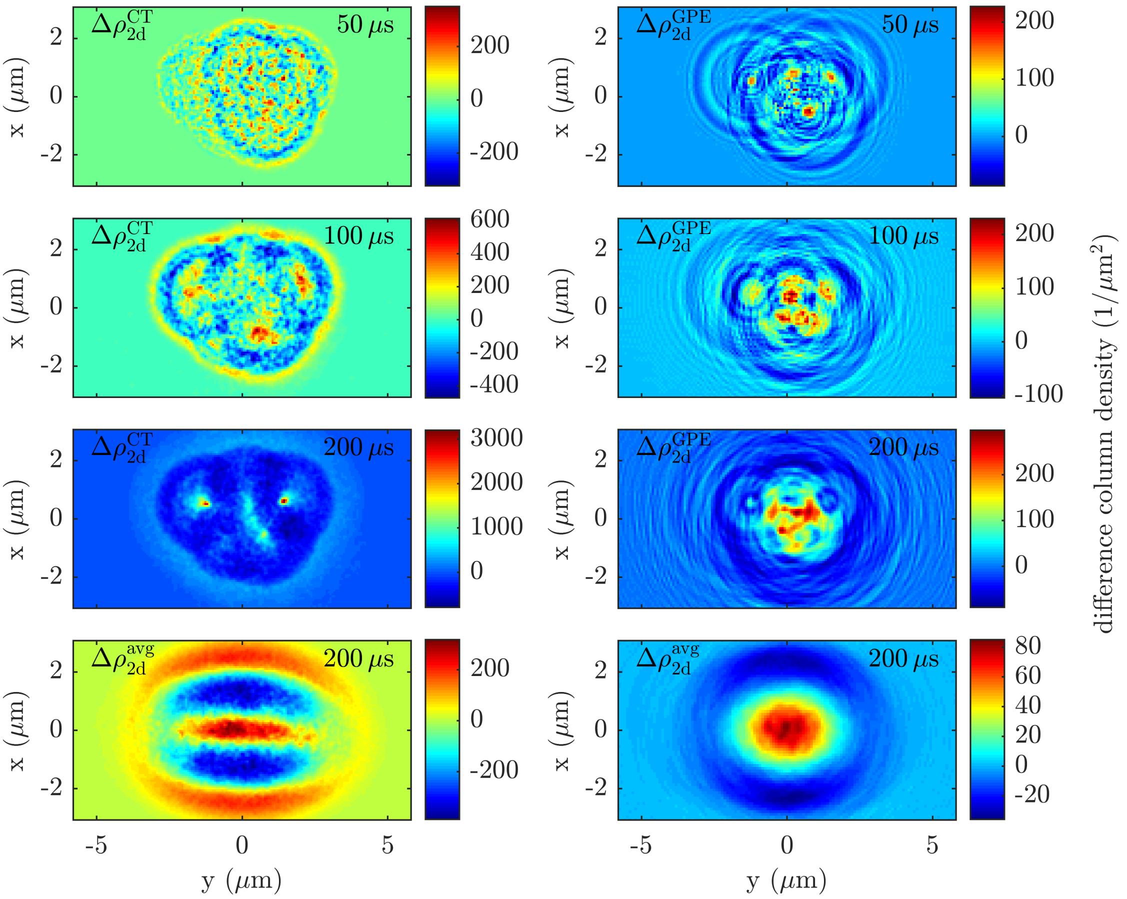

Fig. 5.6: Comparison of classical trajectory simulations (left) and GPE calculations (right) for the $|133S, m_j = 1/2\rangle$ Rydberg state and 10 excitation pulses, applying only s-wave electron-atom interaction. The calculations are performed starting with a constant density of $\rho = 4 \times 10^{14}$ atoms/cm^3. The resulting difference column density $\Delta\rho_{2d}$ is shown for evolution times of 50 μs - 200 μs. The bottom row shows the averaged difference column density of many realizations. The averaged GPE data are kindly provided by [148].

typically just below 100 nm. The electron-atom interaction potential is cutoff for energies $|U| > 1$ MHz for the GPE calculations. The cutoff has been verified by comparing the results with more accurate simulations including a potential cutoff of up to 10 MHz.

The GPE simulations confirm that the imprinted phase on the condensate results in a density enhancement at the center position of the prior present Rydberg atoms on a timescale of several tens of microseconds, even for several subsequent Rydberg excitations. Within the same time, the CT simulations roughly resemble the outline of the different Rydberg excitations, while the atoms inside this region seem to be randomly distributed. The reason for this is the highly oscillating radial structure of the interaction potential. Over the course of the excitation pulses, the atoms experience several momentum-kicks in different directions. On the contrary, in the case of the GPE simulations the radial structure is largely smoothed out over the range of the healing length of the condensate ($\lambda_{\text{healing}} \sim 100\,\text{nm}$). Nonetheless, free-particle excitations are triggered by the oscillating structure which is evident in the simulations for longer evolution times. However, the fraction of free particles moving outwards is low compared to the overall number of atoms affected by the Rydberg excitations. The main difference between the simulation results stems from the fact that in the treatment with GPE on the one hand the interaction between the atoms is included and on the other hand the atomic flow results from the phase gradient of the wavefunction. The increase in density for the GPE simulations is counteracted by atom-atom repulsion, while the CT calculations yield comparatively large densities.

After an evolution time of $200\,\mu$s, the CT simulations reveal significant density peaks at the center of some of the prior present Rydberg atoms. These peaks consist of hundreds of atoms that locally reach densities greater than $1 \times 10^{16}\,\text{atoms/cm}^3$, which is over 20 times the peak density of the BEC. On the contrary, the GPE simulations show a comparatively moderate density increase on the order of the condensate peak density ($\sim 1 \times 10^{14}\,\text{atoms/cm}^3$). In conclusion, the GPE simulations show a smaller density enhancement compared to the CT calculations with an overall larger spatial extension. The same behavior is observed when averaging over many realizations.

Since a local atom loss is observed in the experiment, the question arises what effect leads to an extrusion of atoms in the central region. We recall that the interaction potential including s- and p-wave scattering exhibits a branch of positive interaction energies for small internuclear distances (cf. figure 5.5). In that case, atoms in that inner region are expelled outwards. In order to test the influence of the repulsive interaction, simulations including the interaction potential $U_{s+p}(R)$ were carried out. The results are presented in the following.

Figure 5.7 shows a comparison between the CT simulations and the GPE calculations in a similar fashion as before. Again the calculations for 10 subsequent excitations are shown for different evolution times. Overall, the results of the simulations reveal a similar density distribution compared to the outcomes discussed above. Nonetheless, when taking a closer look at the data, some differences to the previous calculations are visible. In fact, the CT simulations including U_{s+p} show an even further increased density. This can be seen from the simulation for $t_{\mathrm{evo}} = 200\,\mu\mathrm{s}$. The peak density is 25% higher compared to the calculations using $U_{s,k=0}$ (compare left column of figure 5.6 with figure 5.7). This comes with no surprise since the PEC branch for the outer region is gradually bent to lower interaction energies for smaller distances due to the p-wave electron-atom scattering. As a result, the net atom flow towards the central area is larger compared to the case when using only s-wave electron-atom interactions. In contrast, the repulsive branch of the inner part of U_{s+p} leads to a lower density increase for the GPE calculations. The averaged GPE data reveal that, taking into account p-wave scattering for the electron-atom interaction, the peak density is reduced by 50%. Although the overlap between the central region of the Rydberg atom ($R \lesssim 1800\,\mathrm{a}_0$) and the condensate is relatively small compared to the outer area ($R \gtrsim 1800\,\mathrm{a}_0$), the fraction of atoms moving inwards due to the enhanced attractive interaction (when including p-wave scattering) does not outweigh the fraction of

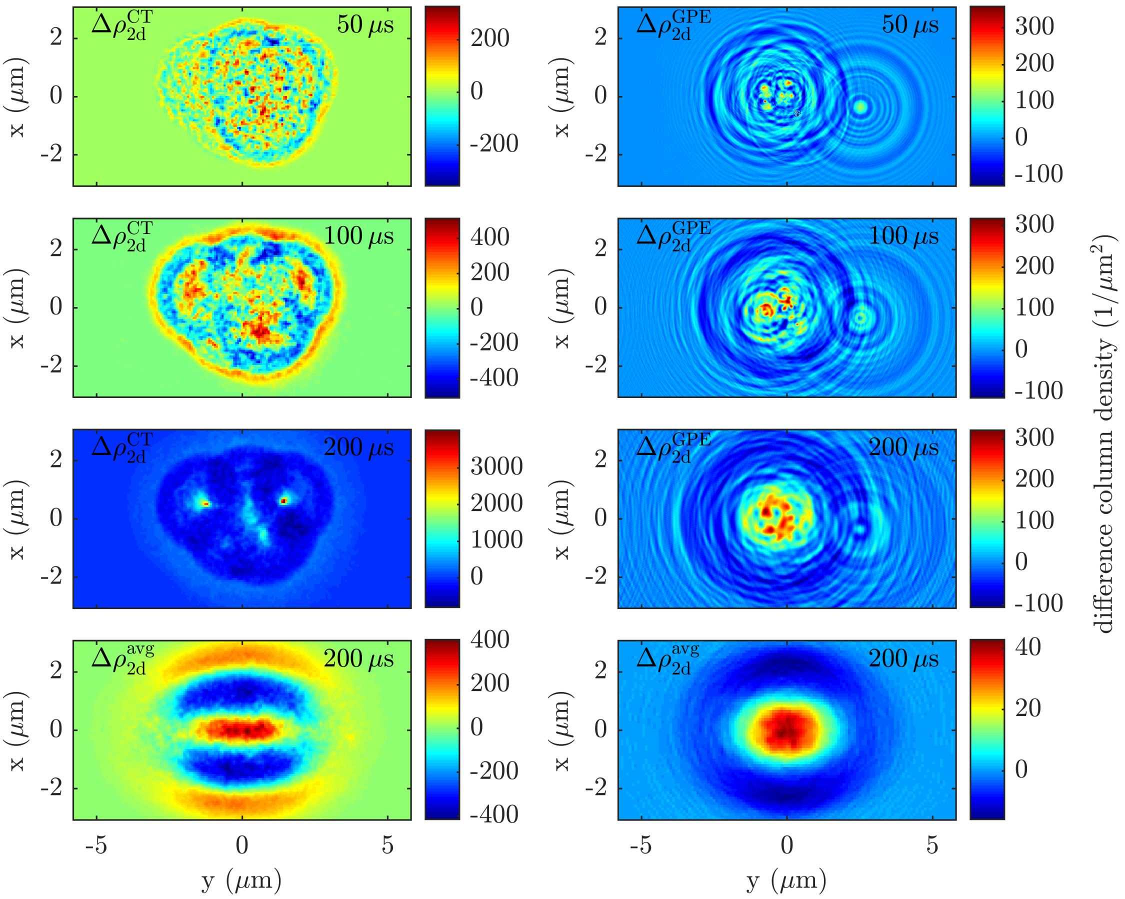

Fig. 5.7: Comparison of classical trajectory simulations (left) and GPE calculations (right) for the $|133S, m_j = 1/2\rangle$ Rydberg state and 10 excitation pulses, for s- and p-wave electron-atom interaction. For the calculations a constant density of $\rho = 4 \times 10^{14}$ atoms/cm^3 is used. The resulting difference column density $\Delta\rho_{2d}$ is depicted for evolution times between 50 μs and 200 μs. On the bottom row, the averaged difference column density of many simulations is shown. The GPE calculations are kindly provided by [148].

atoms that are expelled from the central area. Note that a different set of Rydberg excitation positions was used for the calculations for the non-averaged GPE data.

As mentioned earlier, the classical trajectory simulations revealed relatively large density peaks that occur at the center of the prior present Rydberg atoms. To take into account atom loss due to three-body recombination, simulations including a three-body loss coefficient of $L = 1.8 \times 10^{-29}$ cm^6/s for rubidium (ref. [149]) are

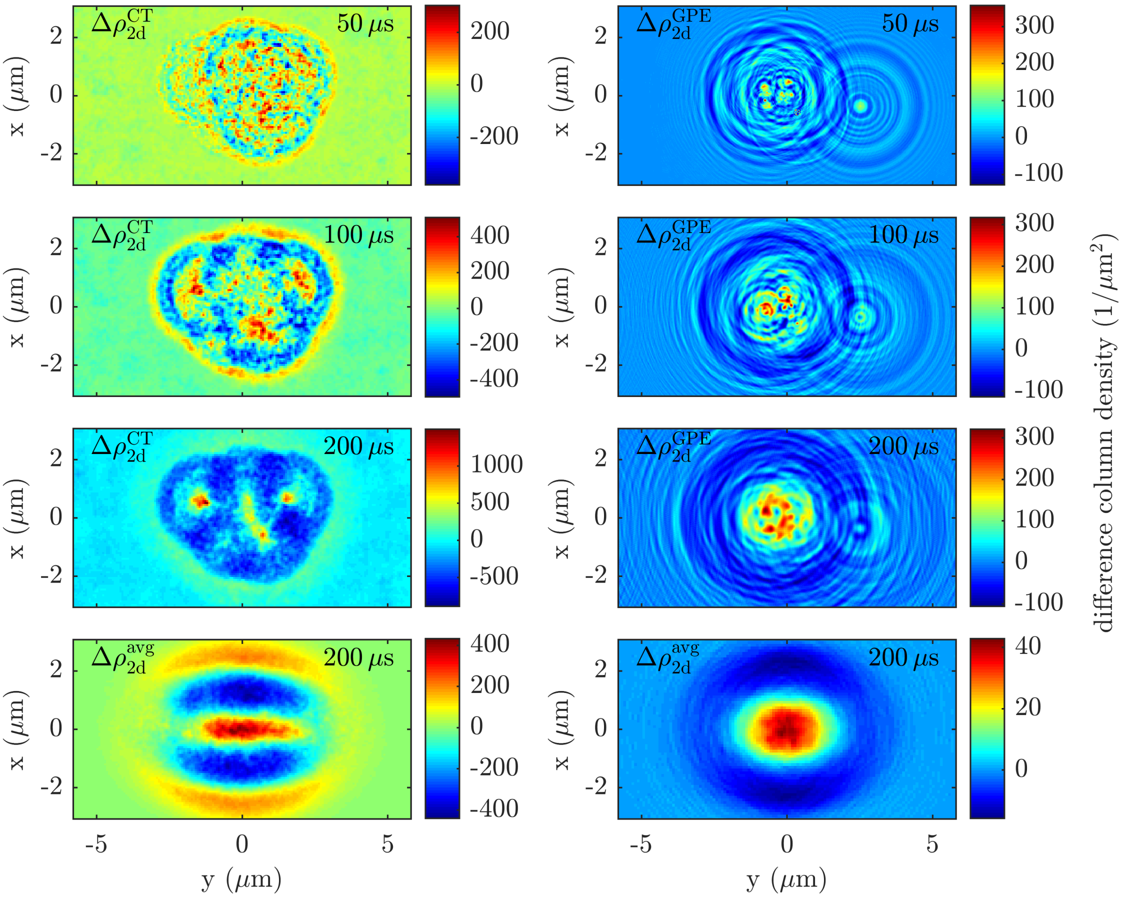

Fig. 5.8: Comparison of classical trajectory simulations (left) and GPE calculations (right) for the $|133S, m_j = 1/2\rangle$ Rydberg state and 10 excitation pulses, including the three-body loss coefficient $L = 1.8 \times 10^{-29}\,\text{cm}^6/\text{s}$ for rubidium (ref. [149]). The calculations are performed starting with a constant density of $\rho = 4 \times 10^{14}\,\text{atoms/cm}^3$. The resulting difference column density $\Delta\rho_{2d}$ is depicted for evolution times of $50\,\mu\text{s}$ - $200\,\mu\text{s}$. The bottom row shows the averaged difference column density of many simulations. The GPE data including three-body decay are kindly provided by [148].

carried out. Again, the results of the GPE and CT simulations for 10 excitation pulses are presented for comparison. Figure 5.8 shows the resulting difference column densities exemplarily for an evolution time of $50\,\mu$s, $100\,\mu$s and $200\,\mu$s for a single excitation sequence (10 pulses) and the average of many realizations for $200\,\mu$s. As a result of the included atom loss mechanism, the apparent density peaks are drastically lowered. In comparison to the data shown in figure 5.7 the density peaks are reduced from a difference column density of $\Delta\rho_{2\mathrm{d}} \approx 4000\,\mu\mathrm{m}^{-2}$ to $1000\,\mu\mathrm{m}^{-2}$, which corresponds to an atom loss of about 100 atoms for a single density peak. However, the resulting averaged density profile shows qualitatively the same features independent of the three-body loss. Since the resulting densities for the GPE simulation remain comparatively moderate, the three-body loss leads to only slight differences.

In addition to the above-presented calculations, simulations employing the truncated Wigner method were performed exemplarily for a single and a 10 excitation pulse sequence, taking into account heating effects on the condensate by incorporating thermal atoms and quantum fluctuations [150], but no significant difference has been found [148].

At last, let us compare the outcome of the simulations with the experimentally observed local atom loss. For this, we extract an atom loss from the numerically obtained column densities. This is achieved by radially integrating outwards from the excitation center ($x = 0$, $y = 0$).

$$\Delta N(R) \equiv \int\limits_0^{2\pi} \int\limits_0^{R} \Delta\rho_{2\mathrm{d}}\, r\, dr d\varphi \tag{5.1}$$

With this, $\Delta N(R)$ yields the atom loss $\Delta N = \Delta N(R_{\mathrm{min}})$, where R_{min} is the global minimum of the function $\Delta N(R)$. Practically, $\Delta\rho_{2\mathrm{d}}$ is summed up to a maximum radius of $R_{\mathrm{max}} = 12\,\mu\mathrm{m}$ and the minimum of $\Delta N(R)$ defines the atom loss ΔN. Note that the asymmetry of the loss feature, which originates from the spatial Rydberg excitation distribution, changes the outcome of ΔN only slightly and can therefore be neglected. Moreover, it has been verified that the experimentally obtained local atom loss yields the same ΔN when applying equation 5.1 within the determined error bars.

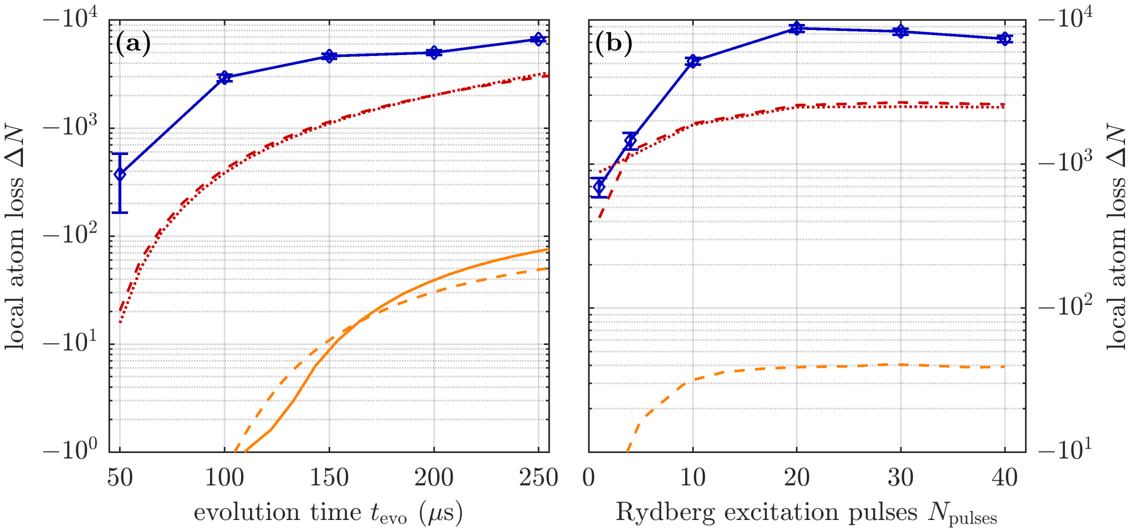

Fig. 5.9: Simulation results and comparison with the experimental data for the $133S$ Rydberg state. The local atom loss ΔN obtained from the GPE (yellow) and the CT (red) calculations are depicted as a function of the evolution time (a) and the number of subsequent Rydberg excitation pulses (b). For comparison the experimental results from figure 5.4 are reprinted in blue (symbols). For the CT data the outcome of the simulations including s- and p-wave electron-atom scattering with (dashed) and without (dotted) three-body loss is shown. For the GPE data the results with (dashed) and without (line) p-wave are depicted. The GPE data are kindly provided by [148].

In figure 5.9 the gathered data from the CT and GPE simulations are shown for the pulse sequence employed in the experiment. The experimental data from figure 5.4(c-d) are reprinted for comparison. While the experimental trend of the data is reproduced by the numerical results, both the CT and the GPE calculations underestimate the experimental data significantly. The fact that the GPE calculations mainly result in an atom increase in the central region of the excitation center leads to a comparatively low atom loss which lies orders of magnitude below the CT calculations. Essentially, the atom loss predicted by the GPE corresponds to the fraction of free-particle excited atoms that are accelerated outwards from the central region. In contrast, the CT calculations reflect the limit of non-interacting free particles only. Interestingly, the results of the CT simulations lie much closer to the experimental findings, but they also underestimate the observed local atom loss.

6

Summary and outlook

This thesis studies interactions of Rydberg atoms with neutral atoms and with single ions. While for the studies of Rydberg atom-neutral interaction the case of one, few, or even many atoms interacting with a single Rydberg electron was investigated, for the ion-Rydberg atom system mostly binary interaction was studied. Beyond that, the level structure of negative ions was explored in the context of ultralong-range Rydberg molecules. The experiments are carried out in a gas made of rubidium-87 atoms at ultracold temperatures, where the motion of atoms is usually frozen out on the time and length scale (micrometer per microsecond) of typical Rydberg experiments.

Ion-induced Rydberg blockade

Over the past decade, ultracold Rydberg atoms have been proven to provide a versatile platform for quantum simulation of long-range interacting many-body systems [10–12], for nonclassical photonic state generation [13, 14], and for quantum information processing [15–17]. A central aspect for many proposals in these fields

[18–20] is the Rydberg blockade phenomenon. The Rydberg blockade results from strong Rydberg-Rydberg interactions that suppress the simultaneous excitation of two or more atoms into Rydberg states within a certain blockade volume. A similar concept applies to hybrid systems that consist of ions and Rydberg atoms. Strong interactions between a single ion and Rydberg atoms lead to charge-induced blockade phenomena mediated over macroscopic distances, which have been proposed as a tool for quantum information transfer between ionic and atomic quantum systems [24]. In traditional hybrid settings, which typically consist of a radio-frequency ion trap and Rydberg states excited in an ensemble of trapped neutral atoms, the ion-trap induced lineshift on the Rydberg states complicates the observation of interaction effects [25].

In the context of this thesis, an alternative approach to the realization of such a hybrid system was demonstrated. A single ion is efficiently created from an ensemble of ultracold rubidium atoms, employing a novel V-type photo-ionization scheme [S1, 92, 93] specifically suited for generating a very low-energy ion. An experimental measurement strategy was presented, including the V-type photo-ionization scheme, a subsequent Rydberg excitation, and a tailored electric field pulse sequence, with which interactions between a single ion and a Rydberg atom were demonstrated by means of an ion-induced Rydberg excitation blockade [S1]; the blockade mechanism was analyzed for a large range of principal quantum numbers.

Furthermore, the ion-induced blockade mechanism was utilized to use the generated single ion as a sensitive probe for small electric fields. The sensitivity of the blockade measurement method was enhanced by increasing the ion-atom interaction strength, which allowed for a stray field compensation down to a level of 100 μV/cm over tens of micrometers, demonstrating a remarkable precise control of electric fields on the micrometer scale.

At last, the efficiency of the V-type photo-ionization scheme was characterized for a single ion generated in a Bose-Einstein condensate. The photo-ionization of the Rydberg atom in the BEC was found to be hampered by dynamics apparent for Rydberg atoms immersed in a condensate. An alternative approach for preparing a single low-energy ion in the BEC was demonstrated and the ion-induced Rydberg blockade mechanism was utilized to trace the ion's motion when pulled through the Bose-Einstein condensate.

The presented technique of creating, controlling, and probing an ion can be further used to study ion-atom collisions and chemistry for an ion immersed in a Bose-Einstein condensate. A faster ionization of the Rydberg atom may lead to an efficient generation of the ion inside the condensate. When applying the photo-ionization scheme, the initial temperature of the created ion can be further reduced by minimizing the ionization excess energy and the photon-recoil transferred on the ion during the photo-ionization protocol. Moreover, the selective photo-association of an ultralong-range Rydberg molecule before the photo-ionization process may provide ideal starting conditions for collision studies, with promising prospects for achieving the ion-atom quantum scattering regime [92].

Precision spectroscopy in ultralong-range Rydberg molecules

Ultralong-range Rydberg molecules have been studied extensively over the past decades. These exotic molecules form when a neutral atom resides within the electron orbit of a Rydberg atom. Large interaction energies arise from low-energy electron-atom scattering between the neutral atom and the Rydberg electron. These interactions potentially lead to molecular bound states for a negative electron-atom s-wave scattering length. In this case, the Rydberg electron binds the neutral atom in a well-confined location, defined by potential minima associated with the oscillating radial Rydberg electron wavefunction. Typically, these types of molecules yield bond lengths of several thousand Bohr radii set by the size of the Rydberg electron orbit.

In the past few years, the interest in this field has shifted from qualitative studies towards a more quantitative and detailed description of the molecular bound states. Recently, a renewed interest in the inclusion of spin effects, in particular the hyperfine interaction in the neutral atom and spin-orbit coupling effects between the neutral and Rydberg atom, has been shown [75–77]. The latter plays an important role in the studies presented in the second part of this thesis, which is based on ref. [S2].

In the presented work, precision spectroscopy has been performed on quasi-bound negative-ion resonances of Rb^-, devising ultralong-range Rydberg molecules (ULRMs) as an ultrasensitive tool. For this purpose, ULRM-spectroscopy was elevated to a so-far unequaled quantitative level of precision, in a combined experimental and theoretical effort. Previously unobserved molecular bound states, that are strongly influenced by resonant electron-atom p-wave scattering, were identified and used to unravel the fine-structure triplet ^3P_J $(J \in \{0, 1, 2\})$ of Rb^-, which by other means is experimentally challenging to resolve. Moreover, careful analysis of the experimentally obtained binding energies allowed the extraction of the s- and p-wave scattering lengths and to pinpoint the p-wave shape resonance position associated with the fine-structure triplet of the Rb^- anion. Furthermore, a molecular alignment of the ULRM mediated by spin-orbit coupling of the underlying electron-atom scattering process has been demonstrated for the first time [S2, 77].

The acquired scattering data may path the way for future experiments on ULRMs that comprise few-body effects [117, 151], molecular dynamics, or even more complex spin couplings [152]. Moreover, the presented scattering data also enable refined predictions for low-energy electron-neutral scattering [78, 80, 84]. Furthermore, the presented technique of utilizing ULRMs to determine the fine details of the underlying electron-atom scattering can be further used to benchmark other atomic systems and potentially may be transferred to molecular systems.

Local atom loss in a BEC induced by Rydberg atoms

The last part of this thesis reports on a local atom loss in a Bose-Einstein condensate induced by a single Rydberg atom. The experiments presented were originally intended to optically image the electron wavefunction of a Rydberg atom. For the wavefunction imaging method, the Rydberg atom is immersed in a Bose-Einstein condensate, where the electron-atom interaction leads to a phase imprint on the condensate wavefunction that is to first order proportional to the absolute square of the electron wavefunction. Due to the gradient of the imprinted phase, the atoms of the condensate flow towards regions of high electron density, which continues even when the Rydberg atom is no longer present.

For experimentally imaging the electron wavefunction, a developed measurement strategy was presented. The strategy includes high spatial resolution imaging and Rydberg atom positioning, post-selection, and image post-processing. Surprisingly, a local density decrease of the condensate was found in the experiment that prevails over the expected density increase in the region where the Rydberg atom was excited. The formation of the observed local atom loss feature in the condensate was characterized for a single Rydberg atom, and several subsequent Rydberg excitations, as well as for different atom densities. Furthermore, the experimentally observed loss feature was compared to numerical simulations, which largely underestimate the amount of condensate density change in the excitation region of the Rydberg atom.

In order to further investigate the local atom loss, measurements can be carried out for different principal quantum numbers, varying the interaction strength between Rydberg and condensate atoms. The outcome of these measurements might provide further insight into the origin of the observed decrease in condensate density. Moreover, a continues re-excitation of a *D*-state Rydberg atom for a higher principal quantum number e.g. $n = 180$ may result in a density feature that resembles the orbital shape of the Rydberg wavefunction.

A

Ion-induced Rydberg blockade

In the main part of this thesis (in chapter 3) we discussed the experimental realization of an ion-induced Rydberg excitation blockade. For the experiments, a single ion was created from an ensemble of ultracold atoms via an all-optical photo-ionization scheme. In this part of the appendix, we review the photo-ionization efficiency and compare the experimental data with the outcome of the simulations for two sets of parameters. Furthermore, the trap geometries of the atomic sample for the blockade measurements in the thermal ensemble and the condensate are presented.

A.1 Photo-ionization efficiency

In section 3.1.2 the measured ionization efficiency of the photo-ionization scheme was presented and compared with the results of a time-dependent four-level system simulation. We found that the simulations match the experimentally obtained efficiencies when taking into account a non-zero detuning from the intermediate $6P_{3/2}$ state for the deexcitation laser pulse. As was already discussed earlier in ref. [99], the high intensities of the photo-ionization and deexcitation lasers

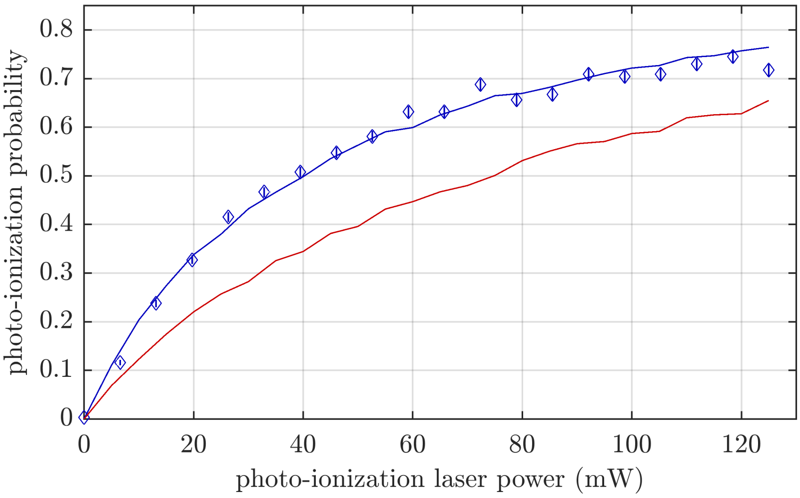

Fig. A.1: Photo-ionization efficiency as a function of the photo-ionization laser power, the experimental data (symbols) are reprinted from figure 3.3. The solid lines correspond to the outcome of a four-level system simulation, including a detuning from the intermediate $6P_{3/2}$ of 35 MHz (blue) and 58 MHz (red).

potentially result in a differential ac stark shift of the intermediate state. In ref. [99] the differential ac stark shift was estimated to be $\Delta_{\mathrm{ac}} = 58\,\mathrm{MHz}$. As stated in section 3.1.2, the four-level system simulations, however, match the experimentally obtained the photo-ionization efficiency when applying an energy shift of $\Delta_{\mathrm{ac}} = 35\,\mathrm{MHz}$, not 58 MHz. To show the difference between the two simulations, we reprint the measured ionization efficiencies in figure A.1 and compare them with the simulated data for $\Delta_{\mathrm{ac}} = 35\,\mathrm{MHz}$ and $\Delta_{\mathrm{ac}} = 58\,\mathrm{MHz}$.

A.2 Crossed optical dipole trap

During this work, the existing experimental setup was expanded by a crossed optical dipole trap with the goal to strongly confine the atomic sample. Details about the existing setup, in particular the experimental control and the atom sample preparation, can be found in earlier works of refs. [95, 102]. The dipole

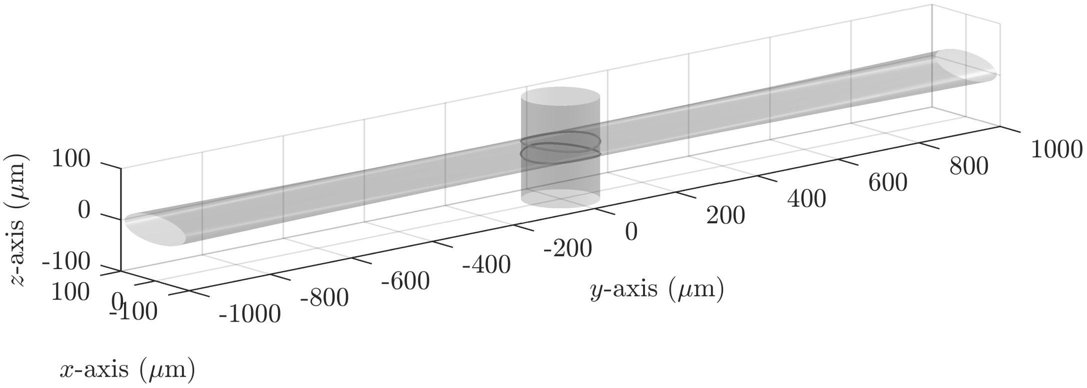

Fig. A.2: Laser beams of the crossed optical dipole trap. The horizontal beam (in xy-plane) is shaped to realize a sheet-like confinement for the atom sample along the z-direction, while the horizontal beam circularly confines the sheet-trap.

trap consists of two laser beams, one of which propagates horizontally and one vertically. For the horizontal beam, a cylindrical lens is used after beam shaping to create a tightly confined sheet-like laser beam propagating along the y-direction. The vertical beam ensures confinement in the xy-plane of the resulting atom trap. Details on optical dipole traps for neutral atoms can be found in ref. [115]. In combination with the tightly focused infrared excitation laser beam (along z-direction), this results in a strongly confined Rydberg excitation volume, which enables us to precisely determine the ion-induced blockade radii presented in section 3.3. Note that, in contrast to the existing Quadrupole-Ioffe configuration trap (QUIC trap), where the offset magnetic field direction is fixed (y-direction), the optical trap allows us to align the magnetic field in an arbitrary spatial direction. Figure A.2 shows the dipole trap laser beams.

Before loading the atoms into the optical dipole trap, the existing QUIC trap (see section A.3) is used to cool the atoms to just below $2\,\mu$K. To transfer the cold atoms from the magnetic trap into the optical trap, the current of the magnetic trap is carefully ramped down (avoiding a zero-magnetic field crossing, which

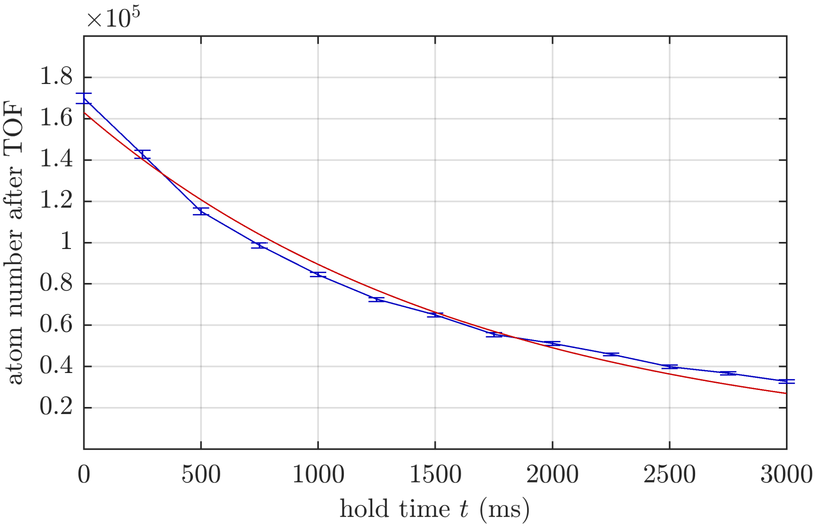

Fig. A.3: Lifetime measurement of the BEC prepared in the crossed optical dipole trap. The atom number (blue) is shown as a function of the hold time after the evaporation. The red curve represents an exponential fit to the experimental data. The atom number is measured in after a time-of-flight of 23 ms.

induces losses due to Majorana spin-flips), while the intensity of the crossed dipole trap is ramped up. The duration of the transfer sequence is mainly given by the time it takes to switch off the QUIC trap in a controlled manner, which typically takes a few hundred milliseconds. After the transfer, the atomic sample can be further confined along the z-direction by increasing the laser intensity (up to a power of 150 mW) of the light sheet beam or the atoms are cooled further down by optical evaporation for which the intensity of the sheet is exponentially reduced.

To reach a Bose-Einstein condensate (BEC), the power of the light sheet is ramped down to 30 mW within 1000 ms. After the evaporation, the condensate comprises typically 2×10^5 atoms. The lifetime of the condensate in this pancake-like atom trap is measured experimentally. In figure A.3 the atom number for different hold times t after the evaporation is shown. The lifetime τ is obtained by an exponential fit to the data, yielding $\tau = 1.7$ s.

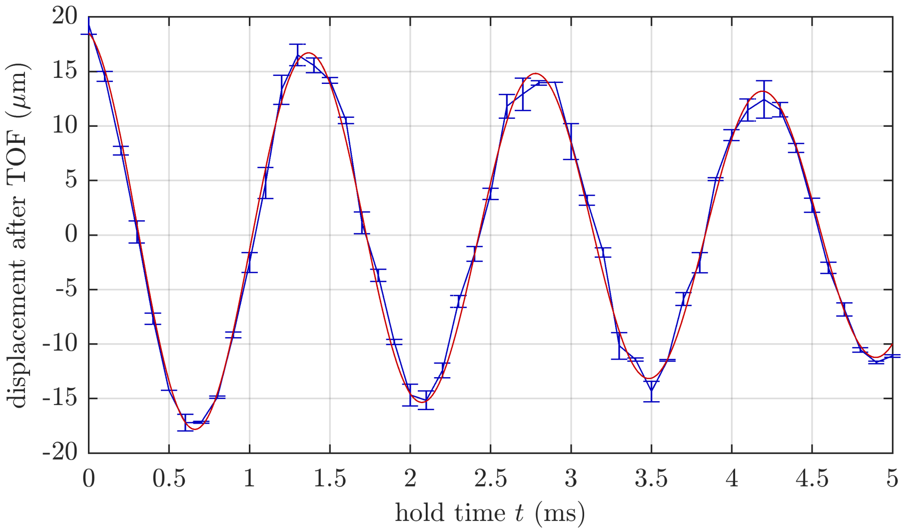

Fig. A.4: Trap frequency measurement for the strong confined z-direction of the crossed optical dipole trap. The atom sample is displaced from its trap minimum by switching off the light sheet for 100 μs. The center of mass motion after a time-of-flight of 23 ms is shown as function of the hold time after the displacement from the rest position.

For the blockade measurements presented in chapter 3, a light sheet power of 150 mW and power of 450 mW for the vertical confinement beam was employed. For these power settings, the atomic ensemble contains typically 1.2×10^5 atoms with a temperature of 1 μK. To determine the sample size, in particular, the confinement along z-direction, trap frequency measurements were performed. The trap frequency can be obtained from the periodicity of the dipole mode of a BEC, which can be excited by displacing the condensate from the potential minimum. For the z-direction, this is achieved by simply switching off the light sheet for a short time in which the atoms fall in the gravitational field. The outcome of the trap frequency measurement for the z-direction is presented in figure A.4. While the trap frequency along the z-direction can be measured directly, for the x- and y-direction the frequencies are obtained from measuring the beam waists in the focal plane with a beam profiler camera. The trap frequencies in x- and y-direction

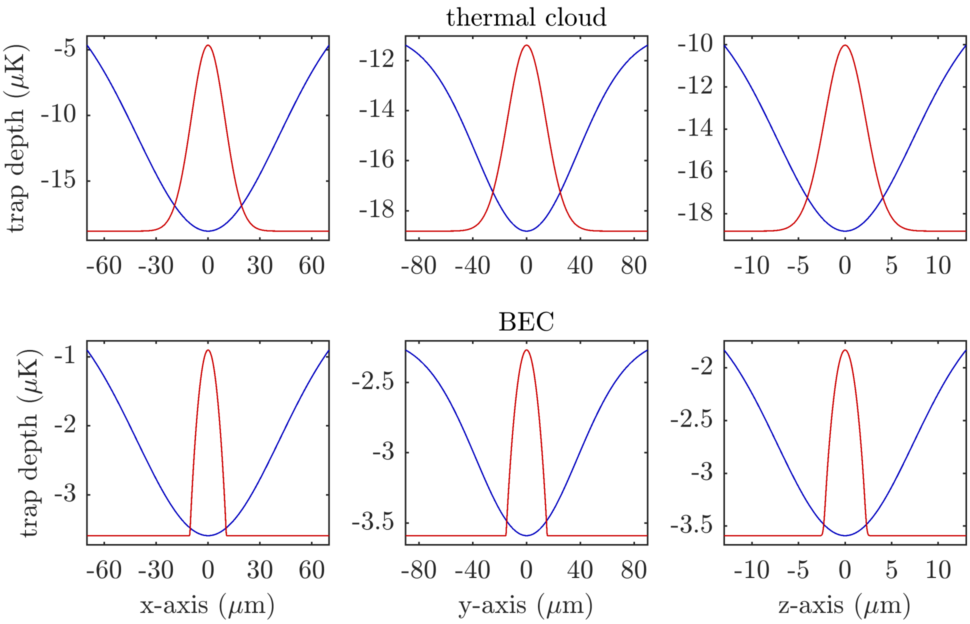

Fig. A.5: Trapping potential and atom sample size of the spin-polarized $\left(\left|5S_{1/2}, F=2, m_F=2\right\rangle\right)$ ^{87}Rb atoms prepared in the crossed optical dipole trap. The top row shows the thermal atom cloud, while the bottom row represents the Bose-Einstein condensate. The trapping frequencies are $\omega_{x,y,z} = 2\pi \times (160, 110, 710)$Hz and $\omega_{x,y,z} = 2\pi \times (70, 50, 320)$Hz for the thermal and the condensate atom sample, respectively. The atom number and ensemble temperature in the thermal cloud are 1.2×10^5 and $1\,\mu$K. For the BEC, the typical atom number of 2×10^5 is used. The resulting peak densities are $2.5 \times 10^{13}\,\text{atoms/cm}^3$ and $3 \times 10^{14}\,\text{atoms/cm}^3$ for the thermal cloud and the condensate, respectively.

are calculated assuming a harmonic trapping potential [115]. The measured waists of the vertical beam and the weak axis of the light sheet are $w_0 = 75(5)\,\mu$m and $w_0 = 90(5)\,\mu$m, respectively. The trapping frequencies of the combined beams are then estimated to $\omega_{x,y,z} = 2\pi \times (160, 110, 710)$Hz. With the beam parameters obtained above, the trap frequencies can also be estimated for the condensed atom sample (BEC) for which we recall the light sheet is ramped down to a power of 30 mW, while the vertical power is typically set to 80 mW. In this case, the trap frequencies are: $\omega_{x,y,z} = 2\pi \times (70, 50, 320)\text{Hz}$. The resulting trapping potential and the corresponding atom sample density profile in the optical trap are shown in figure A.5 for typical atom numbers and temperatures (see above). Note that the density distributions are calculated following standard textbook approaches (for example see [153]) and that the thermal fraction of the condensate, which is very small due to the shallow potential depth, is neglected in figure A.5.

A.3 Magnetic trap

In chapter 3 of the main part of this thesis, the blockade measurement method was employed to trace the ion motion in the Bose-Einstein condensate (cf. section 3.6). Although the optical trap offers several advantages over the magnetic (QUIC) trap, for instance, a freely adjustable magnetic field direction and field strength, a relatively small excitation volume due to the tight confinement along the z-direction, or the vanishingly small thermal fraction of the condensate, the QUIC trap is used for the blockade measurements in the condensate. The reason for this is that we actually utilize the comparatively large thermal fraction (typically 0.2) of the magnetically trapped BEC. Furthermore, the magnetic trap not only provides a larger atom sample, which allows us to repeat the experiments more often with a single atom cloud, but also the trap geometry of the magnetic trap is more advantageous for ion transport measurements. As mentioned earlier, the experimental setup and specifically the atom sample preparation in the magnetic trap is outlined in ref. [102].

In the following, the trapping potential of the magnetic trap and the corresponding atom density profiles are shown in figure A.6. The trap frequencies ($\omega_{x,y,z}$) used for the calculations were measured by displacing the trap minimum in each spatial direction, which is achieved by applying a comparatively fast magnetic

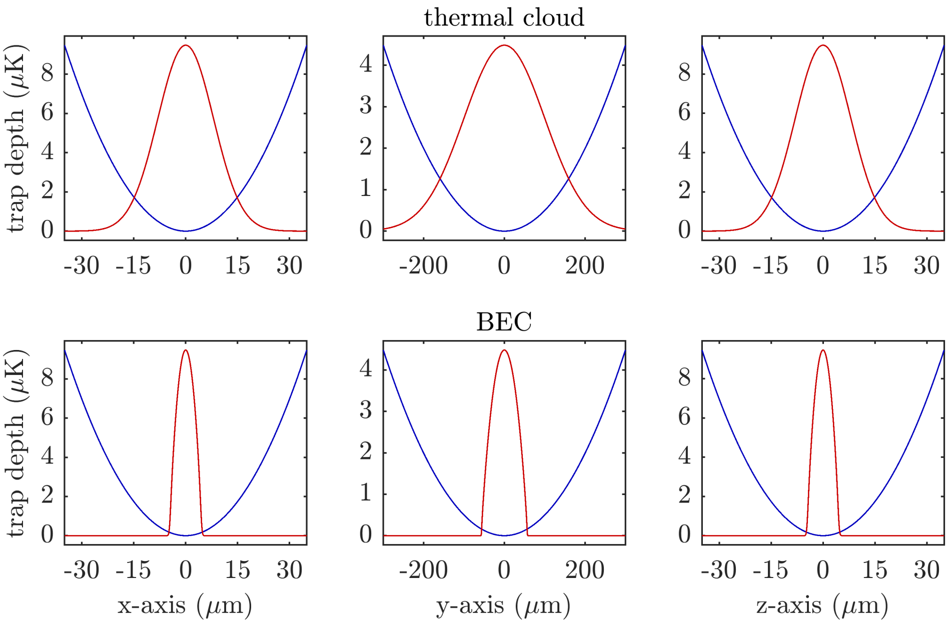

Fig. A.6: Trapping potential and atom sample size of the spin-polarized $\left(\left|5S_{1/2}, F=2, m_F=2\right\rangle\right)$ ^{87}Rb atoms prepared in the magnetic trap. The top row shows the thermal atom cloud, while the bottom row represents the Bose-Einstein condensate. The trapping frequencies $\omega_{x,y,z} = 2\pi \times (194, 16, 194)$Hz are independently obtained by exciting and measuring the dipole mode of the condensate (cf. trap frequency measurement figure A.7). The atom number and ensemble temperature in the thermal cloud are 6×10^6 and $1\,\mu$K. For the BEC, a typical atom number of 1×10^6 is reached. The resulting peak densities are $5.9 \times 10^{13}\,$atoms/cm^3 and $4.5 \times 10^{14}\,$atoms/cm^3 for the thermal cloud and the condensate, respectively.

field ramp (typically 10 ms). For completeness, the results of the trap frequency measurements are shown in figure A.7. Note that the thermal fraction is neglected for the presented density profiles in figure A.6 but plays an important role in the blockade measurements in the condensate. For the blockade measurement simulations presented in section 3.6.3, the total density distribution consisting of the thermal and the condensed distribution is calculated following the approach outlined in ref. [154].

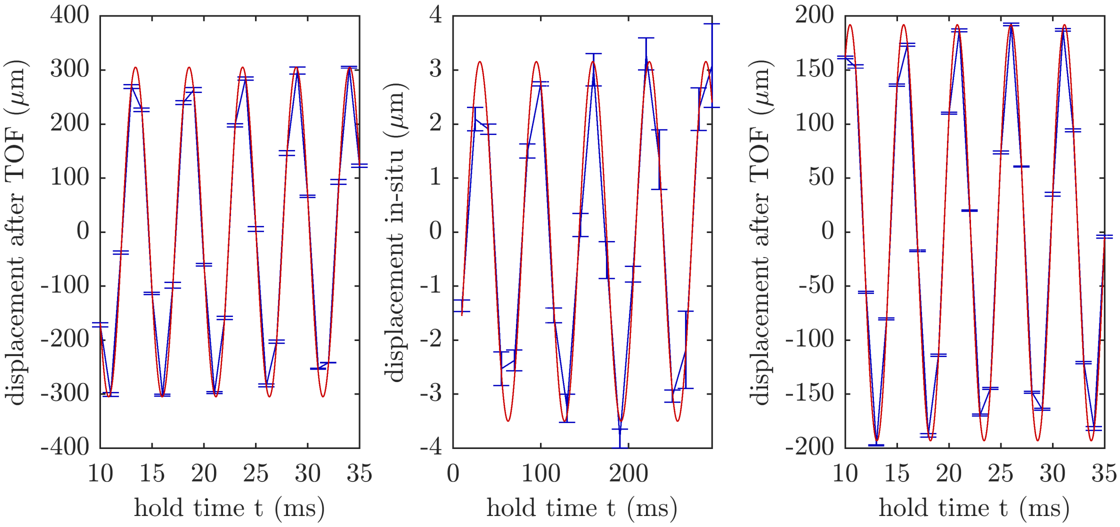

Fig. A.7: Trap frequency measurement of the Quadrupole-Ioffe trap using a Bose-Einstein condensate. The BEC is displaced from its trap minimum by applying a fast magnetic field ramp (10 ms) in each spatial direction (from left to right: x-, y-, and z-direction). The change of the condensate position is measured as a function of the hold time t after the sudden trap minimum displacement. For the x- and z-direction the BEC displacement is measured after a time-of-flight of 23 ms, while for the y-direction the oscillation is recorded in in-situ. The resulting trap frequencies are $\omega_{x,y,z} = 2\pi \times (194, 16, 194)$Hz.

B

Precision spectroscopy in ULRMs

In the context of this thesis (cf. chapter 4), ultralong-range Rydberg molecules were used as an atomic-scale scattering laboratory which allowed us to obtain the fine-structure splitting of the rubidium anion ^3P_J state from the measured binding energies. An essential step for this was the extraction of the s-wave and p-wave scattering parameters from the experimental data. A comparatively simple e$^-$-Rb interaction model potential was used to match the calculated bound state energies of the molecular states D, A, and B (cf. section 4.2) with the measured binding energies. In the following, the applied model potential is used to reproduce the *ab initio* phase shift calculations performed by Fabrikant (ref. [79]) to verify our phase shift calculations. Following this, the spectroscopic data for $n = 31, \dots, 37$ are presented, from which the binding energies of the states D, A, and B were deduced.

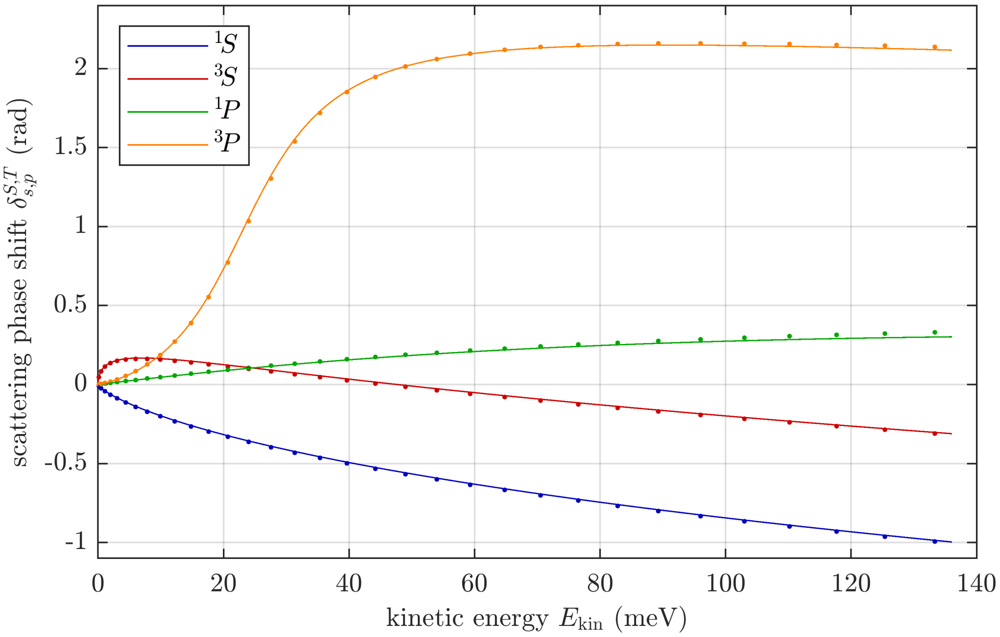

Fig. B.1: Comparison of the s-wave and p-wave phase shifts for singlet and triplet e^--Rb scattering. Data points represent the obtained phase shifts from calculations presented in [79]. The lines correspond to the phase shifts calculated via the model potential equation 2.24 in section 2.2.1.

B.1 Phase shifts

In figure B.1 the phase shifts obtained from the calculations presented by Fabrikant in [79] (data points) are compared with the shifts calculated with the method presented in section 2.2.1 (lines). The inner hard-wall position r_0 is adjusted to match the *ab initio* calculations of each scattering channel (^1S, ^3S, ^1P, ^3P). For this comparison, the LS-coupling term (equation 2.25) was set to zero. As is apparent from figure B.1, the reproduced phase shifts match the *ab initio* calculations.

B.2 Spectra

In this section the spectra used to match the outcome of the bound state calculations with the experimentally obtained binding energies are presented. The measured spectroscopic data for $n = 31, \ldots, 37$ are shown in the following. The used molecular states D, A, and B are assigned to the corresponding molecular line. Additionally, the bound states of the excited dimer states $\mathrm{D}^\star$, the trimer state T as well as various combinations (e.g. B+D) of triatomic states are labeled. Note that the excited dimers are collectively referred to as $\mathrm{D}^\star$ for simplicity. The ion signal is shown as a function of the Rydberg detuning δ and the atomic line of the investigated Rydberg state is set to $\delta = 0$. The gray lines correspond to a fit to the data using a sum of multiple Lorentzians. For better visibility, the data for larger red detuning are magnified as indicated. Note that the excitation strength was set independently for each part of the spectrum.

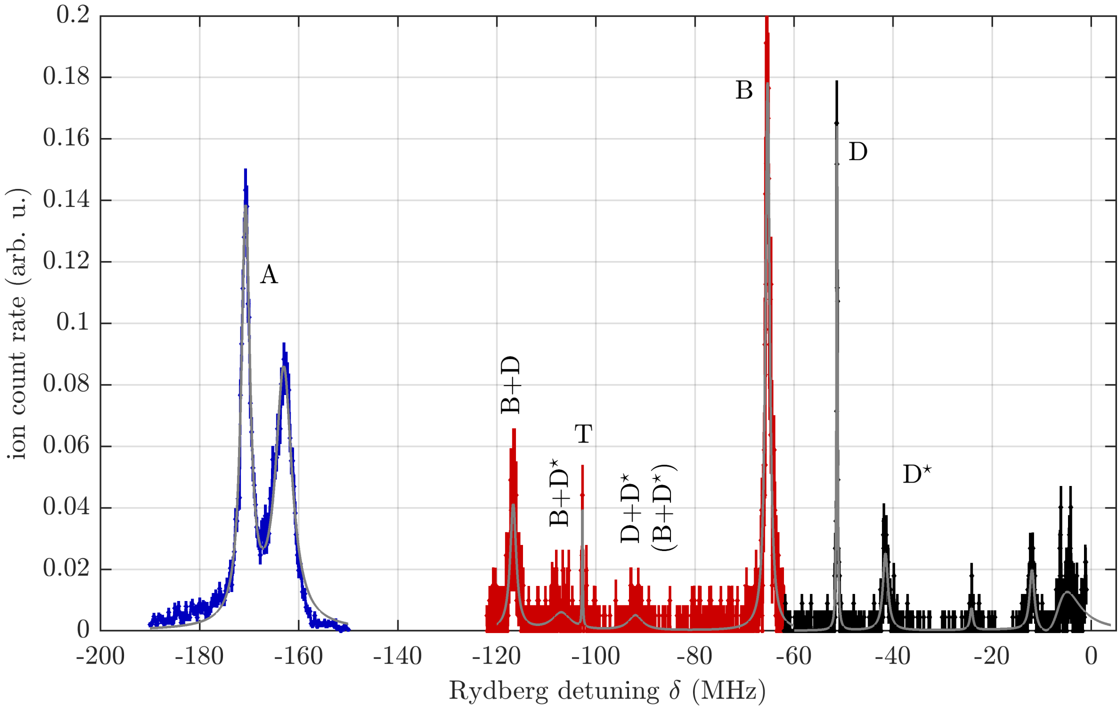

Fig. B.2: ULRM spectroscopy in the vicinity of the $\left|31S_{1/2}, m_j = +1/2\right\rangle$ Rydberg state.

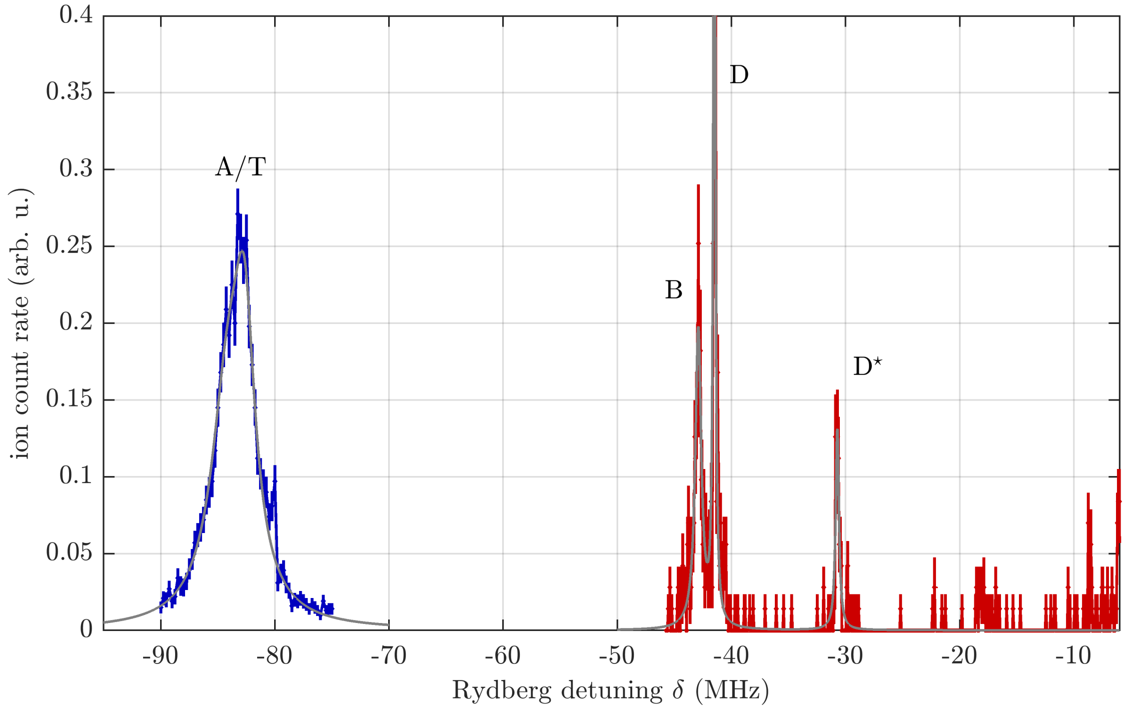

Fig. B.3: ULRM spectroscopy in the vicinity of the $\left|32S_{1/2}, m_j = +1/2\right\rangle$ Rydberg state.

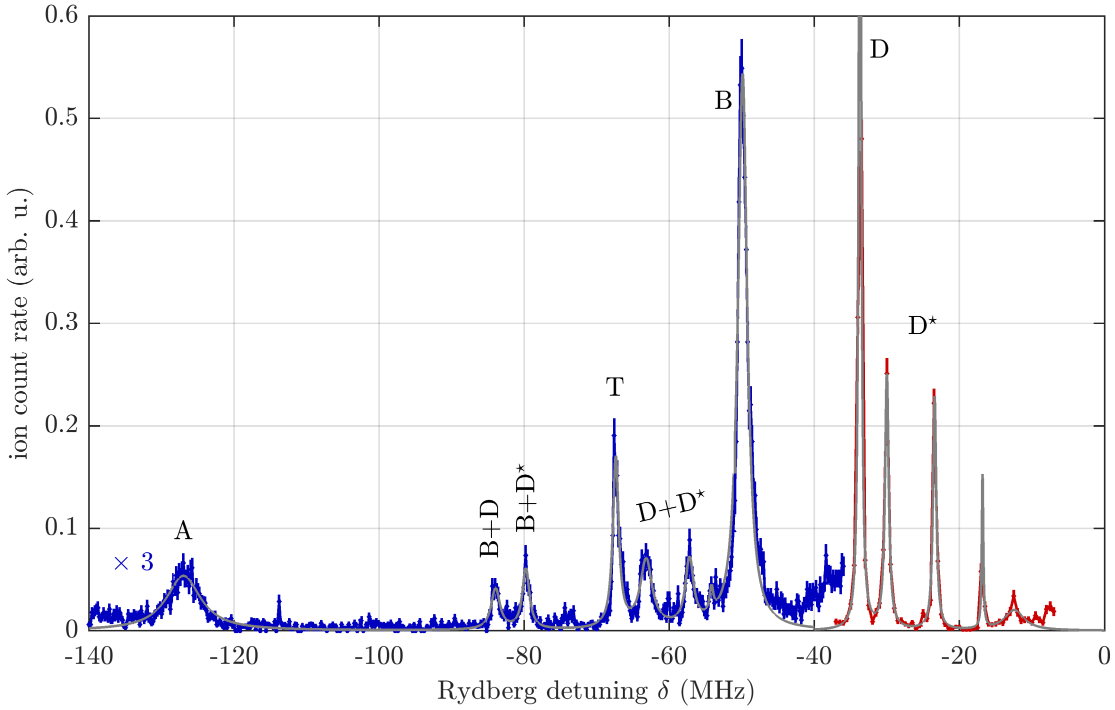

Fig. B.4: ULRM spectroscopy in the vicinity of the $\left|33S_{1/2}, m_j = +1/2\right\rangle$ Rydberg state.

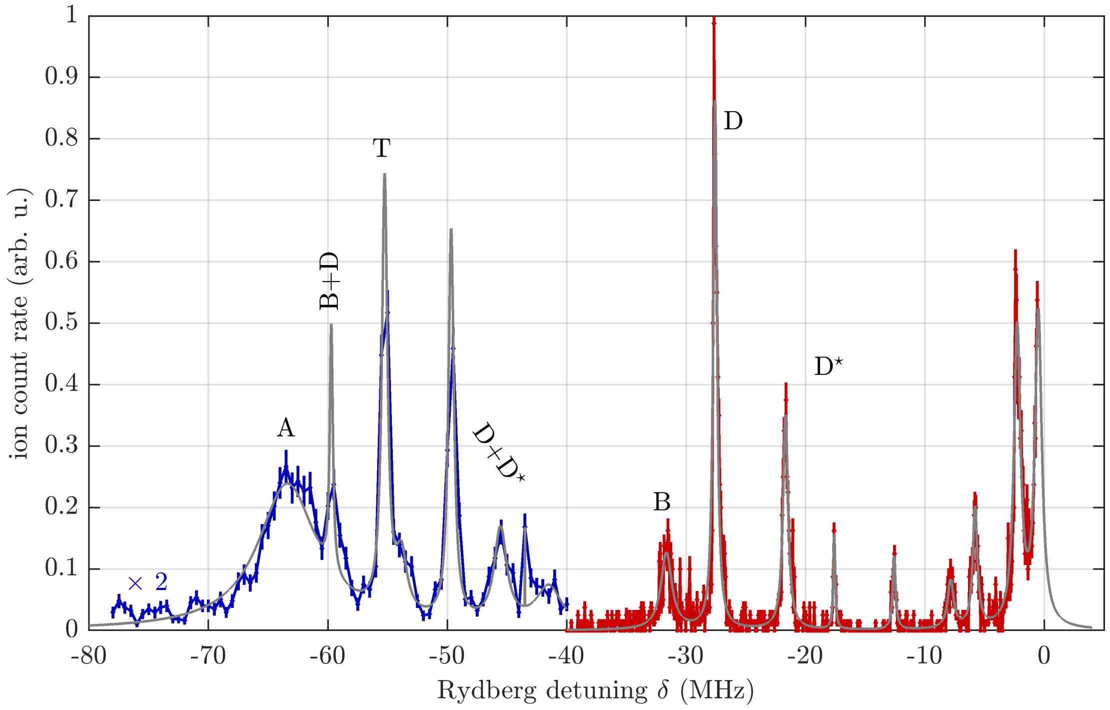

Fig. B.5: ULRM spectroscopy in the vicinity of the $\left|34S_{1/2}, m_j = +1/2\right\rangle$ Rydberg state.

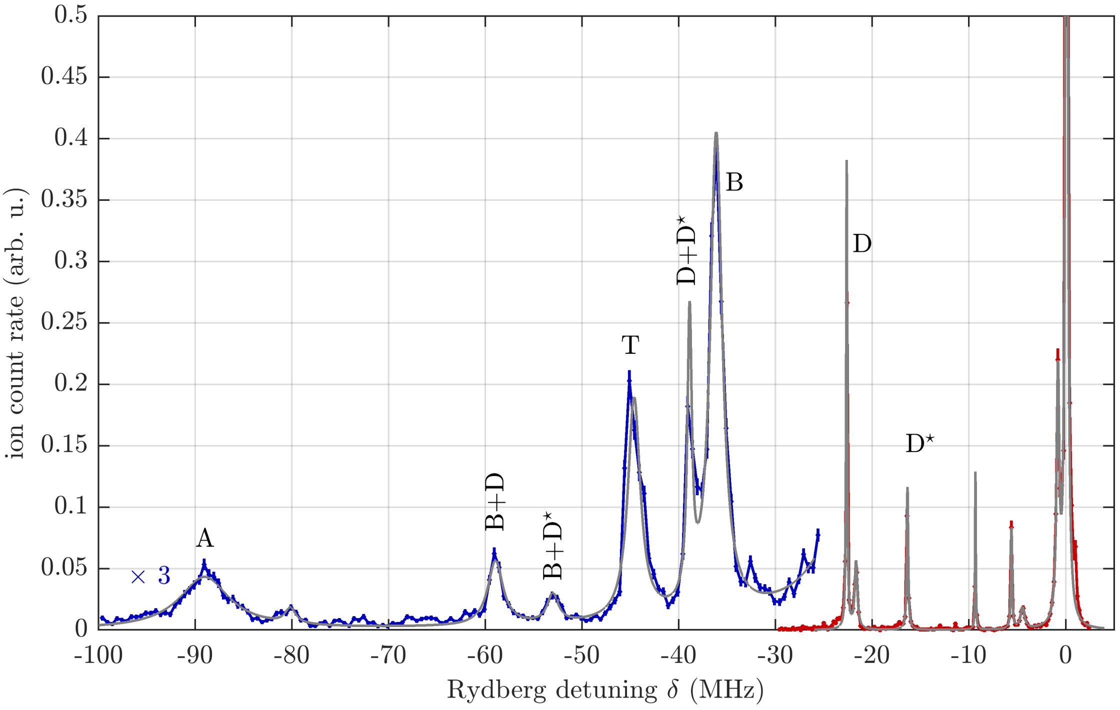

Fig. B.6: ULRM spectroscopy in the vicinity of the $\left|35S_{1/2}, m_j = +1/2\right\rangle$ Rydberg state.

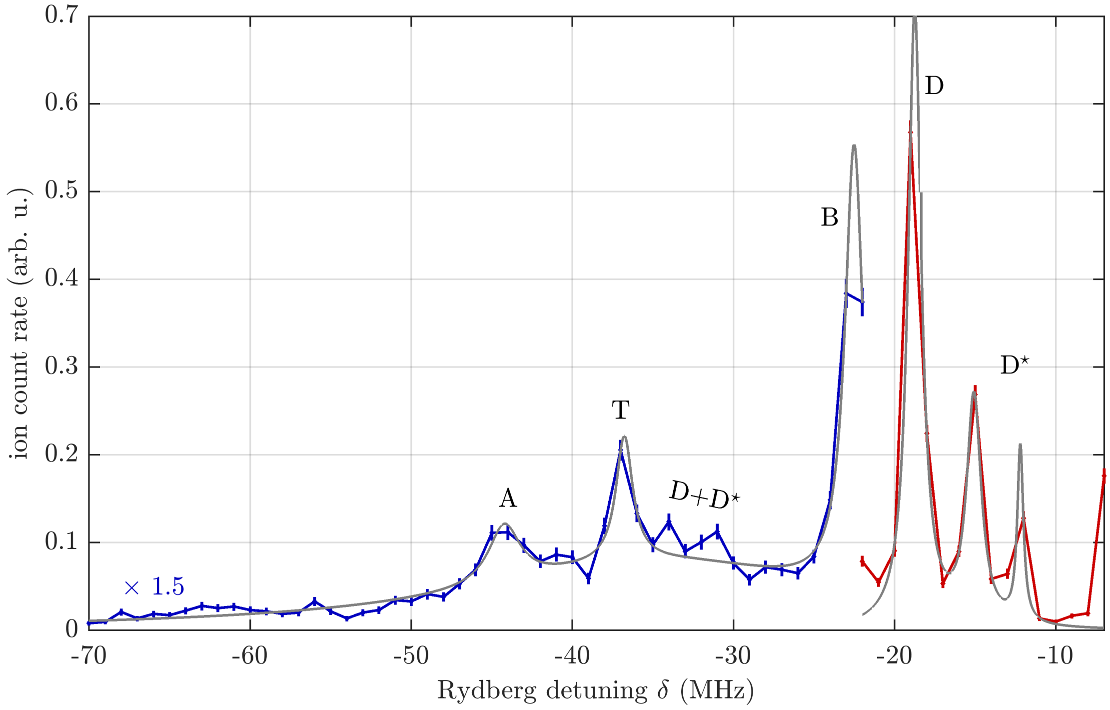

Fig. B.7: ULRM spectroscopy in the vicinity of the $\left|36S_{1/2}, m_j = +1/2\right\rangle$ Rydberg state.

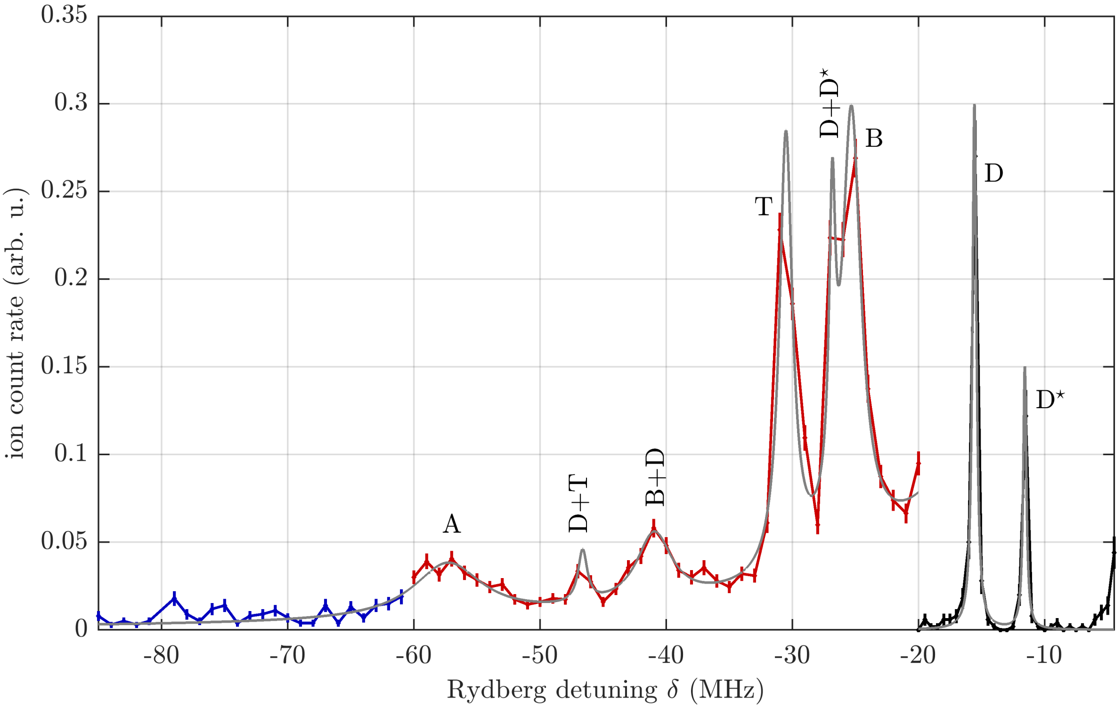

Fig. B.8: ULRM spectroscopy in the vicinity of the $\left|37S_{1/2}, m_j = +1/2\right\rangle$ Rydberg state.

C

Local atom loss in a BEC

In the main part of this thesis measurements of local atom loss in a Bose-Einstein condensate (BEC) induced by Rydberg atoms is presented (cf. chapter 5). The loss feature was observed by imaging the condensate atom distribution in-situ, and was quantified by integrating the column density in the region of the atom loss. For quantifying the atom loss, a reference image was subtracted from imaged condensate, yielding a difference image and with that the difference column density used to determined the atom loss. The reference image for each measurement is generated from a set of images using an image reconstruction algorithm.

C.1 Image reconstruction algorithm

In the experiment, the atom distribution is imaged in-situ using the phase-contrast imaging technique, which relies on the dispersion of the light scattered by the atom cloud. Details about imaging a BEC can be found in ref. [146]. Furthermore, a detailed description of the current imaging setup can be found in ref. [102]. Briefly summarized, a part of the imaging light scatters off the atom cloud, which results in a phase difference between the scattered and unscattered light. The phase imparted on the imaging light is then used to extract the spatial atom column density distribution. For this, a set of three pictures is recorded. The first picture I_{atoms} imparts the information of the atom cloud (atom picture). For the second picture I_{bright} the atom trap is switched off and only the imaging light is recorded (bright picture). For the last picture I_{dark} the imaging light is turned off and an image of the background is taken (dark picture) is taken. Note that the wait time between the images is 1 ms. From the three pictures the phase distribution is then obtained by (ref. [146]):

$$\phi = \left(\frac{\tilde{I}_{\text{atoms}}}{\tilde{I}_{\text{bright}}} - 1 \right) /2, \tag{C.1}$$

where $\tilde{I}_{\text{atoms}}$ and $\tilde{I}_{\text{bright}}$ are obtained by subtracting the background I_{dark} from I_{atoms} and I_{bright}, respectively. The phase ϕ is connected with the atom column density $\rho_{2\text{d}}$ via the imaginary part of the refractive index n^i_{ref} (ref. [146]). In the experiment, linearly polarized light couples the ground-state $\left|5S_{1/2}, F=2, m_F=2\right\rangle$ of the atoms to the $\left|5P_{3/2}, F=2, m_F=2\right\rangle$ state and the $\left|5P_{3/2}, F=3, m_F=2\right\rangle$ state via a π-transition. In this case, both transitions have to be taken into account. By doing so we get the following expression:

$$\begin{aligned}\phi &= \frac{4\pi}{\lambda} n^i_{\text{ref}} \\ &= \frac{4\pi}{\lambda}\rho_{2\text{d}} \left[\frac{d^2_{\text{red}}/6}{\epsilon_0 \hbar \Gamma} \cdot \frac{-\Delta_{F=3}/\left(\Gamma/2\right)}{1+\left(\Delta_{F=3}\right)^2/\left(\Gamma/2\right)^2} + \frac{d^2_{\text{red}}/6}{\epsilon_0 \hbar \Gamma} \cdot \frac{-\Delta_{F=2}/\left(\Gamma/2\right)}{1+\left(\Delta_{F=2}\right)^2/\left(\Gamma/2\right)^2} \right],\end{aligned}$$

where we used the atom polarizability for the addressed imaging transitions [146], with the laser detuning $\Delta_{F=2}$ and $\Delta_{F=3}$ from the excited $6P_{3/2}$ state, the natural linewidth Γ for the transition, and the reduced matrix element $d_{\text{red}} = \langle J=1/2|er|J'=3/2\rangle = 4.227\, ea_0$ multiplied with the corresponding Clebsch-Gordan coefficient $\sqrt{1/6}$ and $-\sqrt{1/6}$ [97].

For the experiments in the magnetic trap, a typical imaging detuning of +500 MHz from the excited $F=3$, $m_F=2$ state is employed. For the imaging of the optically trapped atoms a smaller detuning of +200 MHz can be used. For both atom sample geometries the density dependent phase shift ϕ imparted on the imaging light is in the linear regime for the typical densities reached in the experiments. Note that this has also been verified experimentally.

In section 5, the atom column density obtained from the in-situ images of the atom distribution is used to quantify the observed local atom loss. Typically, the change in column density is on average on the order of a few % of the peak column density of the condensate. The extraction of a reliable atom loss is challenged by the statistical fluctuation ΔN_{r^2} of the local atom number per resolution unit and the atom number fluctuations of the condensate (cf. section 5.1 and 5.2), as well as the photon-shot noise, the fluctuation of the atom trap position, and phase errors imparted on the imaging light by the imperfection of the imaging system.

In order to extract the local atom loss, an image reconstruction algorithm is employed to construct a reference image for each imaged atom distribution from a basis set of condensate images. The algorithm is based on a post-processing imaging cleaning method used for the detection of small atom numbers [155], which was derived from the eigenface method presented in ref. [156]. The algorithm is presented below and demonstrated on a typical image of the atom loss measurements.

In figure C.1(a) the atom column density of a single image of the loss measurements for the $133S$ state is shown. In (b) the column density of the corresponding reconstructed reference image (I_{ref}) is depicted. The reference image is constructed by building a linear combination of 200 basis images.

The coefficients c_i for each basis image $I_{b,i}$ is determined by building the dot product s_i of $I_{b,i}$ with the measured image I.

$$s_i = \sum_{n,m} I(n,m) \cdot I_{b,i}(n,m) \tag{C.2}$$

Here, (n, m) corresponds to the pixel location of the image. The coefficients c_i are then determined by solving the linear system:

$$\mathbf{B} \cdot \mathbf{c} = \mathbf{s}, \tag{C.3}$$

where **B** is the correlation matrix for the used basis, which is constructed of the dot product of the basis images:

$$\mathbf{B}(i,j) = \sum_{n,m} I_{b,i}(n,m) \cdot I_{b,j}(n,m). \tag{C.4}$$

With that the reference image is given by:

$$I_{\text{ref}} = \sum_{i} c_i \cdot I_{b,i}. \tag{C.5}$$

The created reference image in figure C.1(b) nicely reproduces the image shown in (a). In (c) the corresponding difference column density $\Delta\rho_{\text{2d}}$ is depicted, which is obtained by subtracting the measured image from the created image. In (d) the difference column density for a measurement with Rydberg atoms present is shown. Since the atom loss feature is not included in the basis set, the area of the feature is excluded (masked) from the determination of the coefficients c_i in equation C.3, but is included for the construction the reference image from the basis set (equation C.5). The difference column density in (d) reveals a significant dip of the local atom density for a single measurement of the condensate atom distribution.

Note that the effects of the excitation lasers on the atom cloud and drifts of the trap position are included in the used basis set. The basis images are recorded in absence of the Rydberg atom by switching the Rydberg detuning to a positive value (typically $\delta = +50\,\text{MHz}$), for which no excitation takes place. Furthermore, the basis images are taken every second experimental run during a measurement, and with that also include systematic positional drifts of the atom cloud.

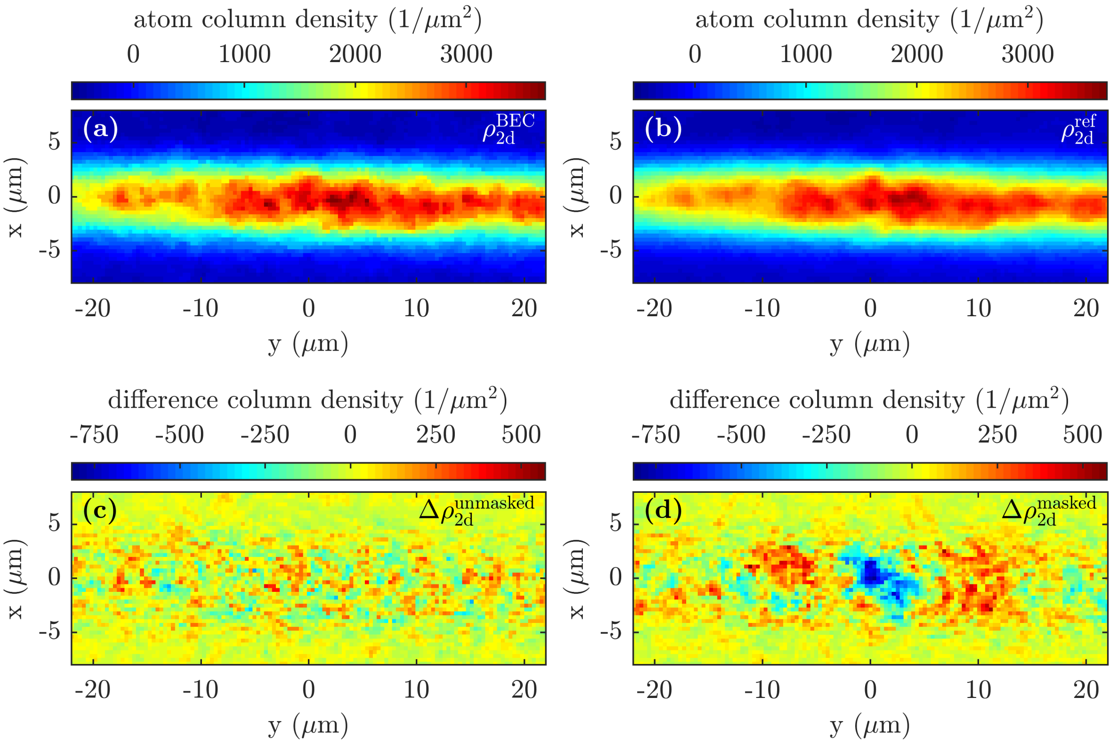

Fig. C.1: Imaging cleaning algorithm employed on single shot images of the 133S state atom loss measurements for an evolution time of 200 μs and 10 excitation pulses. (a) Shows the atom column density obtained from the raw images (see text). The image is taken in absence of the Rydberg atom. In (b) the column density of the corresponding reference image, reconstructed from 200 basis images, is depicted. (c-d) Shows the difference column density for a measurement without (c) and with (d) the Rydberg atom present in the condensate. For (d), the area of the atom loss is masked for the reference image reconstruction (see text). For better comparison, the same color range is used for $\Delta\rho_{2d}$ in (c) and (d).

Bibliography

[S1] F. Engel, T. Dieterle, T. Schmid, C. Tomschitz, C. Veit, N. Zuber, R. Löw, T. Pfau, and F. Meinert. "Observation of Rydberg Blockade Induced by a Single Ion". Physical Review Letters **121** (2018), 193401. arXiv: `1809.00993` (cit. on pp. 10, 16, 56, 180).

[S2] F. Engel, T. Dieterle, F. Hummel, C. Fey, P. Schmelcher, R. Löw, T. Pfau, and F. Meinert. "Precision Spectroscopy of Negative-Ion Resonances in Ultralong-Range Rydberg Molecules". Physical Review Letters **123** (2019), 073003. arXiv: `1904.08372` (cit. on pp. 11, 16, 17, 41, 48, 49, 119, 145, 182).

[S3] F. Engel, T. Dieterle, S. K. Tiwari, S. Wüster, M. Wagner, C. Fey, R. Schmidt, R. Löw, F. Meinert, and T. Pfau. "In preparation". 2020 (cit. on pp. 149, 158).

[S4] K. S. Kleinbach, F. Engel, T. Dieterle, R. Löw, T. Pfau, and F. Meinert. "Ionic Impurity in a Bose-Einstein Condensate at Submicrokelvin Temperatures". Physical Review Letters **120** (2018), 193401. arXiv: `1802.08587` (cit. on pp. 11, 16, 39).

[S5] K. S. Kleinbach, F. Meinert, F. Engel, W. J. Kwon, R. Löw, T. Pfau, and G. Raithel. "Photoassociation of Trilobite Rydberg Molecules via Resonant Spin-Orbit Coupling". Physical Review Letters **118** (2017), 223001. arXiv: `1703.01096` (cit. on pp. 11, 16, 39, 117).

[S6] M. Schlagmüller, T. C. Liebisch, H. Nguyen, G. Lochead, F. Engel, F. Böttcher, K. M. Westphal, K. S. Kleinbach, R. Löw, S. Hofferberth, T. Pfau, J. Pérez-Ríos, and C. H. Greene. "Probing an Electron Scattering Resonance using Rydberg Molecules within a Dense and Ultracold Gas". Physical Review Letters **116** (2016), 53001. arXiv: `1510.07003` (cit. on pp. 11, 16, 39, 52, 53, 103, 117).

[S7] M. Schlagmüller, T. C. Liebisch, F. Engel, K. S. Kleinbach, F. Böttcher, U. Hermann, K. M. Westphal, A. Gaj, R. Löw, S. Hofferberth, T. Pfau, J. Pérez-Ríos, and C. H. Greene. "Ultracold Chemical Reactions of a Single Rydberg Atom in a Dense Gas". Physical Review X **6** (2016), 031020. arXiv: `1605.04883` (cit. on pp. 11, 16, 39, 97, 101, 117, 152, 160).

[S8] T. C. Liebisch et al. "Controlling Rydberg atom excitations in dense background gases". Journal of Physics B: Atomic, Molecular and Optical Physics **49** (2016), 182001. arXiv: `1607.01325` (cit. on pp. 11, 16, 53).

[9] R. P. Feynman, R. B. Leighton, M. Sands, and R. B. Lindsay. "The Feynman Lectures on Physics, Vol. 3: Quantum Mechanics". Physics Today (1966) (cit. on pp. 7, 13).

[10] P. Schauß, M. Cheneau, M. Endres, T. Fukuhara, S. Hild, A. Omran, T. Pohl, C. Gross, S. Kuhr, and I. Bloch. "Observation of spatially ordered structures in a two-dimensional Rydberg gas". Nature **491** (2012), 87. arXiv: `1209.0944` (cit. on pp. 9, 14, 55, 179).

[11] H. Labuhn, D. Barredo, S. Ravets, S. De Léséleuc, T. Macrì, T. Lahaye, and A. Browaeys. "Tunable two-dimensional arrays of single Rydberg atoms for realizing quantum Ising models". Nature **534** (2016), 667. arXiv: `1509.04543` (cit. on pp. 9, 14, 55, 179).

[12] H. Bernien, S. Schwartz, A. Keesling, H. Levine, A. Omran, H. Pichler, S. Choi, A. S. Zibrov, M. Endres, M. Greiner, V. Vuletić, and M. D. Lukin. "Probing many-body dynamics on a 51-atom quantum simulator". Nature **551** (2017), 579. arXiv: `1707.04344` (cit. on pp. 9, 14, 55, 90, 179).

[13] T. Peyronel, O. Firstenberg, Q. Y. Liang, S. Hofferberth, A. V. Gorshkov, T. Pohl, M. D. Lukin, and V. Vuletić. "Quantum nonlinear optics with single photons enabled by strongly interacting atoms". Nature **488** (2012), 57 (cit. on pp. 9, 14, 55, 90, 179).

[14] O. Firstenberg, T. Peyronel, Q. Y. Liang, A. V. Gorshkov, M. D. Lukin, and V. Vuletić. "Attractive photons in a quantum nonlinear medium". Nature **502** (2013), 71 (cit. on pp. 9, 14, 55, 179).

[15] L. Isenhower, E. Urban, X. L. Zhang, A. T. Gill, T. Henage, T. A. Johnson, T. G. Walker, and M. Saffman. "Demonstration of a Neutral Atom Controlled-NOT Quantum Gate". Physical Review Letters **104** (2010), 010503. arXiv: `0907.5552` (cit. on pp. 9, 15, 55, 179).

[16] Y. Y. Jau, A. M. Hankin, T. Keating, I. H. Deutsch, and G. W. Biedermann. "Entangling atomic spins with a Rydberg-dressed spin-flip blockade". Nature Physics **12** (2016), 71 (cit. on pp. 9, 15, 55, 179).

[17] D. Tiarks, S. Schmidt, G. Rempe, and S. Dürr. "Optical π phase shift created with a single-photon pulse". Science Advances **2** (2016). arXiv: `1512.05740` (cit. on pp. 9, 15, 55, 179).

[18] D. Jaksch, J. I. Cirac, P. Zoller, S. L. Rolston, R. Côté, and M. D. Lukin. "Fast Quantum Gates for Neutral Atoms". Physical Review Letters **85** (2000), 2208. arXiv: `0004038 [quant-ph]` (cit. on pp. 9, 15, 55, 90, 180).

[19] M. D. Lukin, M. Fleischhauer, R. Côté, L. M. Duan, D. Jaksch, J. I. Cirac, and P. Zoller. "Dipole Blockade and Quantum Information Processing in Mesoscopic Atomic Ensembles". Physical Review Letters **87** (2001), 37901. arXiv: `0011028 [quant-ph]` (cit. on pp. 9, 15, 55, 56, 90, 180).

[20] M. Saffman. Quantum computing with atomic qubits and Rydberg interactions: progress and challenges. 2016. arXiv: `1605.05207` (cit. on pp. 9, 15, 55, 90, 93, 180).

[21] K. Singer, M. Reetz-Lamour, T. Amthor, L. G. Marcassa, and M. Weidemüller. Suppression of Excitation and Spectral Broadening Induced by Interactions in a Cold Gas of Rydberg Atoms. 2004. arXiv: `0404075 [physics]` (cit. on pp. 9, 15, 55).

[22] D. Tong, S. M. Farooqi, J. Stanojevic, S. Krishnan, Y. P. Zhang, R. Côté, E. E. Eyler, and P. L. Gould. "Local Blockade of Rydberg Excitation in an Ultracold Gas". Physical Review Letters **93** (2004), 063001. arXiv: `0402113 [physics]` (cit. on pp. 9, 15, 55).

[23] E. Urban, T. A. Johnson, T. Henage, L. Isenhower, D. D. Yavuz, T. G. Walker, and M. Saffman. "Observation of Rydberg blockade between two atoms". Nature Physics **5** (2009), 110. arXiv: `0805.0758` (cit. on pp. 9, 15, 55).

[24] T. Secker, R. Gerritsma, A. W. Glaetzle, and A. Negretti. "Controlled long-range interactions between Rydberg atoms and ions". Physical Review A **94** (2016), 013420. arXiv: `1602.04606` (cit. on pp. 9, 15, 55, 90, 93, 180).

[25] S. Haze, J. Wolf, M. Deiß, L. Wang, G. Raithel, and J. H. Denschlag. "Stark spectroscopy of Rydberg atoms in an atom-ion hybrid trap" (2019). arXiv: `1901.11069` (cit. on pp. 9, 15, 56, 180).

[26] N. V. Ewald, T. Feldker, H. Hirzler, H. A. Fürst, and R. Gerritsma. "Observation of Interactions between Trapped Ions and Ultracold Rydberg Atoms". Physical Review Letters **122** (2019), 253401. arXiv: `1809.03987` (cit. on pp. 9, 15, 56).

[27] T. F. Gallagher. Rydberg Atoms. Cambridge: Cambridge University Press, 1994 (cit. on pp. 9, 10, 15, 16, 20, 21, 24, 25, 27, 31, 36, 56, 160).

[28] D. Weller, A. Urvoy, A. Rico, R. Löw, and H. Kübler. "Charge-induced optical bistability in thermal Rydberg vapor". Physical Review A **94** (2016), 063820. arXiv: `1609.02330` (cit. on pp. 9, 15, 56).

[29] G. D. Liveing and J. Dewar. "V. On the spectra of sodium and potassium". Proceedings of the Royal Society of London **29** (1879), 398 (cit. on pp. 10, 16).

[30] E. Amaldi and E. Segré. Effect of Pressure on High Terms of Alkaline Spectra. 1934 (cit. on pp. 10, 16, 50).

[31] E. Fermi. "Sopra lo Spostamento per Pressione delle Righe Elevate delle Serie Spettrali". Il Nuovo Cimento **11** (1934), 157 (cit. on pp. 11, 16, 44, 50).

[32] V. Bendkowsky, B. Butscher, J. Nipper, J. P. Shaffer, R. Löw, and T. Pfau. "Observation of ultralong-range Rydberg molecules". Nature **458** (2009), 1005 (cit. on pp. 11, 16, 39, 117, 120, 131).

[33] V. Bendkowsky, B. Butscher, J. Nipper, J. B. Balewski, J. P. Shaffer, R. Löw, T. Pfau, W. Li, J. Stanojevic, T. Pohl, and J. M. Rost. "Rydberg Trimers and Excited Dimers Bound by Internal Quantum Reflection". Physical Review Letters **105** (2010), 163201 (cit. on pp. 11, 16, 39, 117, 120, 129).

[34] W. Li, T. Pohl, J. M. Rost, S. T. Rittenhouse, H. R. Sadeghpour, J. Nipper, B. Butscher, J. B. Balewski, V. Bendkowsky, R. Löw, and T. Pfau. "A Homonuclear Molecule with a Permanent Electric Dipole Moment". Science **334** (2011), 1110 (cit. on pp. 11, 16, 39, 117).

[35] J. Tallant, S. T. Rittenhouse, D. Booth, H. R. Sadeghpour, and J. P. Shaffer. "Observation of Blueshifted Ultralong-Range Cs_2 Rydberg Molecules". Physical Review Letters **109** (2012), 173202. arXiv: `1205.4974` (cit. on pp. 11, 16, 39).

[36] M. A. Bellos, R. Carollo, J. Banerjee, E. E. Eyler, P. L. Gould, and W. C. Stwalley. "Excitation of Weakly Bound Molecules to Trilobitelike Rydberg States". Physical Review Letters **111** (2013), 053001 (cit. on pp. 11, 16, 39).

[37] D. A. Anderson, S. A. Miller, and G. Raithel. "Angular-momentum couplings in long-range Rb_2 Rydberg molecules". Physical Review A - Atomic, Molecular, and Optical Physics **90** (2014), 062518. arXiv: `1409.2543` (cit. on pp. 11, 16, 39, 47, 118, 135).

[38] A. Gaj, A. T. Krupp, J. B. Balewski, R. Löw, S. Hofferberth, and T. Pfau. "From molecular spectra to a density shift in dense Rydberg gases". Nature Communications **5** (2014), 4546 (cit. on pp. 11, 16, 39, 51, 117).

[39] A. T. Krupp, A. Gaj, J. B. Balewski, P. Ilzhöfer, S. Hofferberth, R. Löw, T. Pfau, M. Kurz, and P. Schmelcher. "Alignment of D-state Rydberg molecules". Physical Review Letters **112** (2014), 143008. arXiv: `1401.4111` (cit. on pp. 11, 16, 39, 117).

[40] D. Booth, S. T. Rittenhouse, J. Yang, H. R. Sadeghpour, and J. P. Shaffer. "Production of trilobite Rydberg molecule dimers with kilo-Debye perma-

nent electric dipole moments". Science **348** (2015), 99. arXiv: `1411.5291` (cit. on pp. 11, 16, 39, 117).

[41] B. J. DeSalvo, J. A. Aman, F. B. Dunning, T. C. Killian, H. R. Sadeghpour, S. Yoshida, and J. Burgdörfer. "Ultra-long-range Rydberg molecules in a divalent atomic system". Physical Review A - Atomic, Molecular, and Optical Physics **92** (2015), 031403 (cit. on pp. 11, 16, 39).

[42] H. Saßmannshausen, F. Merkt, and J. Deiglmayr. "Experimental Characterization of Singlet Scattering Channels in Long-Range Rydberg Molecules". Physical Review Letters **114** (2015), 133201 (cit. on pp. 11, 16, 39).

[43] T. Niederprüm, O. Thomas, T. Manthey, T. M. Weber, and H. Ott. "Giant Cross Section for Molecular Ion Formation in Ultracold Rydberg Gases". Physical Review Letters **115** (2015), 013003 (cit. on pp. 11, 16, 39, 117).

[44] T. Niederprüm, O. Thomas, T. Eichert, C. Lippe, J. Pérez-Ríos, C. H. Greene, and H. Ott. "Observation of pendular butterfly Rydberg molecules". Nature Communications **7** (2016), 1. arXiv: `1602.08400` (cit. on pp. 11, 16, 39, 117).

[45] F. Böttcher, A. Gaj, K. M. Westphal, M. Schlagmüller, K. S. Kleinbach, R. Löw, T. C. Liebisch, T. Pfau, and S. Hofferberth. "Observation of mixed singlet-triplet Rb_2 Rydberg molecules". Physical Review A **93** (2016), 032512. arXiv: `1510.01097` (cit. on pp. 11, 16, 39, 118).

[46] J. B. Balewski, A. T. Krupp, A. Gaj, D. Peter, H. P. Büchler, R. Löw, S. Hofferberth, and T. Pfau. "Coupling a single electron to a Bose-Einstein condensate". Nature **502** (2013), 664. arXiv: `1306.5181` (cit. on pp. 11, 16, 39, 51, 149, 151, 164).

[47] F. Camargo, R. Schmidt, J. D. Whalen, R. Ding, G. Woehl, S. Yoshida, J. Burgdörfer, F. B. Dunning, H. R. Sadeghpour, E. Demler, and T. C. Killian. "Creation of Rydberg Polarons in a Bose Gas". Physical Review Letters **120** (2018), 083401. arXiv: `1706.03717` (cit. on pp. 11, 16, 52).

[48] C. Cohen-Tannoudji, B. Diu, and F. Laloë. Quantum mechanics. Wiley, 1977, 1524 (cit. on pp. 20, 25, 28).

[49] G. Drake. Springer Handbook of Atomic, Molecular, and Optical Physics. Ed. by G. Drake. New York, NY: Springer New York, 2006 (cit. on pp. 20, 28).

[50] F. Schwabl. Quantum Mechanics. Berlin, Heidelberg: Springer Berlin Heidelberg, 2007, 1 (cit. on pp. 20, 28, 29, 33).

[51] J. J. Sakurai and J. Napolitano. Modern Quantum Mechanics. Cambridge University Press, 2017 (cit. on pp. 20, 25, 30).

[52] J. J. Balmer. "Notiz über die Spectrallinien des Wasserstoffs". Annalen der Physik **261** (1885), 80 (cit. on p. 20).

[53] N. Bohr. "XXXVII. On the constitution of atoms and molecules". The London, Edinburgh, and Dublin Philosophical Magazine and Journal of Science **26** (1913), 476 (cit. on p. 21).

[54] A. Sommerfeld. "Zur Quantentheorie der Spektrallinien". Annalen der Physik **356** (1916), 1 (cit. on p. 22).

[55] E. Arimondo, M. Inguscio, and P. Violino. "Experimental determinations of the hyperfine structure in the alkali atoms". Reviews of Modern Physics **49** (1977), 31 (cit. on pp. 23, 26).

[56] R. R. Freeman and D. Kleppner. "Core polarization and quantum defects in high-angular-momentum states of alkali atoms". Physical Review A **14** (1976), 1614 (cit. on pp. 24, 25).

[57] W. Li, I. Mourachko, M. W. Noel, and T. F. Gallagher. "Millimeter-wave spectroscopy of cold Rb Rydberg atoms in a magneto-optical trap: Quantum defects of the ns, np, and nd series". Physical Review A - Atomic, Molecular, and Optical Physics **67** (2003), 7 (cit. on pp. 25, 26).

[58] J. Han, Y. Jamil, D. V. Norum, P. J. Tanner, and T. F. Gallagher. "Rb nf quantum defects from millimeter-wave spectroscopy of cold ^{85}Rb Rydberg atoms". Physical Review A - Atomic, Molecular, and Optical Physics **74** (2006), 054502 (cit. on pp. 25, 26).

[59] M. MacK, F. Karlewski, H. Hattermann, S. Höckh, F. Jessen, D. Cano, and J. Fortágh. "Measurement of absolute transition frequencies of ^{87}Rb to nS and nD Rydberg states by means of electromagnetically induced transparency". Physical Review A - Atomic, Molecular, and Optical Physics **83** (2011), 052515. arXiv: `1103.6221` (cit. on pp. 25, 26, 62).

[60] J. E. Sansonetti. "Wavelengths, transition probabilities, and energy levels for the spectra of rubidium (Rb I through Rb XXXVII)". Journal of Physical and Chemical Reference Data **35** (2006), 301 (cit. on p. 26).

[61] S. Civiš, M. Ferus, P. Kubelík, V. E. Chernov, and E. M. Zanozina. "Fourier transform infrared emission spectra of atomic rubidium: g- and h-states". Journal of Physics B: Atomic, Molecular and Optical Physics **45** (2012), 175002 (cit. on pp. 26, 62).

[62] R. Löw, H. Weimer, J. Nipper, J. B. Balewski, B. Butscher, H. P. Büchler, and T. Pfau. An experimental and theoretical guide to strongly interacting Rydberg gases. 2012. arXiv: `1202.2871` (cit. on pp. 27, 61, 90).

[63] M. D. Gregoire, I. Hromada, W. F. Holmgren, R. Trubko, and A. D. Cronin. "Measurements of the ground-state polarizabilities of Cs, Rb, and K using

atom interferometry". Physical Review A - Atomic, Molecular, and Optical Physics **92** (2015), 052513. arXiv: `1509.07091` (cit. on p. 27).

[64] M. Marinescu, H. R. Sadeghpour, and A. Dalgarno. "Dispersion coefficients for alkali-metal dimers". Physical Review A **49** (1994), 982 (cit. on p. 30).

[65] M. L. Zimmerman, M. G. Littman, M. M. Kash, and D. Kleppner. "Stark structure of the Rydberg states of alkali-metal atoms". Physical Review A **20** (1979), 2251 (cit. on pp. 33, 34).

[66] J. Mitroy, M. S. Safronova, and C. W. Clark. "Theory and applications of atomic and ionic polarizabilities". Journal of Physics B: Atomic, Molecular and Optical Physics **43** (2010), 202001. arXiv: `1004.3567` (cit. on p. 37).

[67] Y. Hahn. "Polarizability of Rydberg atoms and the dominant long-range interactions". Physical Review A - Atomic, Molecular, and Optical Physics **62** (2000), 7 (cit. on p. 37).

[68] C. Boisseau, I. Simbotin, and R. Côté. "Macrodimers: Ultralong Range Rydberg Molecules". Physical Review Letters **88** (2002), 4 (cit. on p. 38).

[69] K. R. Overstreet, A. Schwettmann, J. Tallant, and J. P. Shaffer. "Photoinitiated collisions between cold Cs Rydberg atoms". Physical Review A - Atomic, Molecular, and Optical Physics **76** (2007), 011403 (cit. on p. 38).

[70] H. Saßmannshausen and J. Deiglmayr. "Observation of Rydberg-Atom Macrodimers: Micrometer-Sized Diatomic Molecules". Physical Review Letters **117** (2016), 083401 (cit. on p. 38).

[71] S. Hollerith, J. Zeiher, J. Rui, A. Rubio-Abadal, V. Walther, T. Pohl, D. M. Stamper-Kurn, I. Bloch, and C. Gross. "Quantum gas microscopy of Rydberg macrodimers". Science **364** (2019), 664. arXiv: `1812.07533` (cit. on p. 38).

[72] C. H. Greene, A. S. Dickinson, and H. R. Sadeghpour. "Creation of Polar and Nonpolar Ultra-Long-Range Rydberg Molecules". Physical Review Letters **85** (2000), 2458 (cit. on p. 39).

[73] H. R. Sadeghpour and S. T. Rittenhouse. "How do ultralong-range homonuclear Rydberg molecules get their permanent dipole moments?" Molecular Physics **111** (2013), 1902 (cit. on p. 39).

[74] E. L. Hamilton, C. H. Greene, and H. R. Sadeghpour. "Shape-resonance-induced long-range molecular Rydberg states". Journal of Physics B: Atomic, Molecular and Optical Physics **35** (2002), L199 (cit. on p. 39).

[75] M. T. Eiles and C. H. Greene. "Hamiltonian for the inclusion of spin effects in long-range Rydberg molecules". Physical Review A **95** (2017), 042515. arXiv: `1611.04508` (cit. on pp. 40, 46, 47, 49, 118, 132, 182).

[76] F. Hummel, C. Fey, and P. Schmelcher. "Spin-interaction effects for ultralong-range Rydberg molecules in a magnetic field". Physical Review A **97** (2018), 043422. arXiv: `1711.08748` (cit. on pp. 40, 46, 49, 118, 182).

[77] F. Hummel, C. Fey, and P. Schmelcher. "Alignment of s-state Rydberg molecules in magnetic fields". Physical Review A **99** (2019), 023401 (cit. on pp. 40, 48, 49, 118, 119, 137, 182).

[78] A. A. Khuskivadze, M. I. Chibisov, and I. I. Fabrikant. "Adiabatic energy levels and electric dipole moments of Rydberg states of Rb_2 and Cs_2 dimers". Physical Review A - Atomic, Molecular, and Optical Physics **66** (2002), 15 (cit. on pp. 40–43, 47, 127, 146–148, 183).

[79] I. I. Fabrikant. "Interaction of Rydberg atoms and thermal electrons with K, Rb and Cs atoms". Journal of Physics B: Atomic and Molecular Physics **19** (1986), 1527 (cit. on pp. 41, 42, 52, 146, 195, 196).

[80] C. Bahrim, U. Thumm, and I. I. Fabrikant. "Negative-ion resonances in cross sections for slow-electron–heavy-alkali-metal-atom scattering". Physical Review A - Atomic, Molecular, and Optical Physics **63** (2001), 1 (cit. on pp. 41, 43, 121, 122, 126, 183).

[81] U. Thumm and D. W. Norcross. "Relativistic R-matrix calculations for electron–alkali-metal-atom scattering: Cs as a test case". Physical Review A **45** (1992), 6349 (cit. on p. 41).

[82] U. Thumm and D. W. Norcross. "Evidence for very narrow shape resonances in low-energy electron-Cs scattering". Physical Review Letters **67** (1991), 3495 (cit. on p. 41).

[83] U. Thumm and D. W. Norcross. "Angle-differential and momentum-transfer cross sections for low-energy electron-Cs scattering". Physical Review A **47** (1993), 305 (cit. on p. 41).

[84] C. Bahrim and U. Thumm. "Low-lying $^3P^o$ and $^3S^e$ states of $\mathrm{Rb}^-, \mathrm{Cs}^-$, and Fr^-". Physical Review A - Atomic, Molecular, and Optical Physics **61** (2000), 6 (cit. on pp. 41–43, 48, 118, 121, 122, 126, 127, 142, 145–148, 183).

[85] P. G. Burke. R-Matrix Theory of Atomic Collisions. **61**. Springer Series on Atomic, Optical, and Plasma Physics. Springer Berlin Heidelberg, 2011, 750 (cit. on pp. 41, 43).

[86] F. Hummel and C. Fey. *private communication*. Institut für Laserphysik, Universität Hamburg. 2018 (cit. on p. 42).

[87] D. C. Thompson, E. Kammermayer, B. P. Stoicheff, and E. Weinberger. "Pressure shifts and broadenings of Rb Rydberg states by Ne, Kr, and H_2". Physical Review A **36** (1987), 2134 (cit. on p. 44).

[88] A. Omont. "On the theory of collisions of atoms in rydberg states with neutral particles". Journal de Physique **38** (1977), 1343 (cit. on p. 44).

[89] S. Markson, S. T. Rittenhouse, R. Schmidt, J. P. Shaffer, and H. R. Sadeghpour. “Theory of Ultralong-Range Rydberg Molecule Formation Incorporating Spin-Dependent Relativistic Effects: Cs(6s)-Cs(np) as Case Study”. ChemPhysChem **17** (2016), 3683 (cit. on p. 47).

[90] C. Fey, M. Kurz, P. Schmelcher, S. T. Rittenhouse, and H. R. Sadeghpour. “A comparative analysis of binding in ultralong-range Rydberg molecules”. New Journal of Physics **17** (2015), 055010 (cit. on p. 47).

[91] R. Schmidt, H. R. Sadeghpour, and E. Demler. “Mesoscopic Rydberg Impurity in an Atomic Quantum Gas”. Physical Review Letters **116** (2016), 105302. arXiv: `1510.09183` (cit. on pp. 52, 53).

[92] T. Schmid, C. Veit, N. Zuber, R. Löw, T. Pfau, M. Tarana, and M. Tomza. “Rydberg Molecules for Ion-Atom Scattering in the Ultracold Regime”. Physical Review Letters **120** (2018), 153401. arXiv: `1709.10488` (cit. on pp. 56, 58, 94, 180, 181).

[93] T. Schmid. “Rydberg Molecules for Ultracold Ion-Atom Scattering”. PhD Thesis. Universität Stuttgart, 2019, 216 (cit. on pp. 56, 94, 180).

[94] E. Courtade, M. Anderlini, D. Ciampini, J. H. Müller, O. Morsch, E. Arimondo, M. Aymar, and E. J. Robinson. “Two-photon ionization of cold rubidium atoms with a near resonant intermediate state”. Journal of Physics B: Atomic, Molecular and Optical Physics **37** (2004), 967 (cit. on p. 56).

[95] M. Schlagmüller. “A single Rydberg Atom interacting with a Dense and Ultracold Gas”. PhD thesis. Universität Stuttgart, 2016 (cit. on pp. 59, 152, 162, 186).

[96] M. S. Safronova, C. J. Williams, and C. W. Clark. “Relativistic many-body calculations of electric-dipole matrix elements, lifetimes, and polarizabili-

ties in rubidium". Physical Review A - Atomic, Molecular, and Optical Physics **69** (2004), 8 (cit. on pp. 61, 64).

[97] D. A. Steck. "Rubidium 87 D Line Data". Journal of Geophysical Research (2010) (cit. on pp. 62, 202).

[98] R. V. Ambartzumian, N. P. Furzikov, V. S. Letokhov, and A. A. Puretsky. "Measuring photoionization cross-sections of excited atomic states". Applied Physics **9** (1976), 335 (cit. on p. 64).

[99] C. Tomschitz. "A photoionization scheme to create cold ionic impurities from Rydberg atoms". Master thesis. Universität Stuttgart, 2018, 92 (cit. on pp. 64, 65, 185, 186).

[100] T. Feldker, P. Bachor, M. Stappel, D. Kolbe, R. Gerritsma, J. Walz, and F. Schmidt-Kaler. "Rydberg Excitation of a Single Trapped Ion". Physical Review Letters **115** (2015), 173001. arXiv: `1506.05958` (cit. on p. 66).

[101] A. Osterwalder and F. Merkt. "Using High Rydberg States as Electric Field Sensors". Physical Review Letters **82** (1999), 1831 (cit. on p. 68).

[102] K. Kleinbach. "Ions and Electrons Interacting with Ultracold Atoms - Novel Approaches Based on Rydberg Excitations". PhD thesis. Universität Stuttgart, 2018, 152 (cit. on pp. 69, 74, 152, 161, 186, 191, 201).

[103] U. Hermann. "Analysing and improving high resolution Rydberg field ionization statistics". Master thesis. Universität Stuttgart, 2014 (cit. on p. 74).

[104] J. D. Pritchard, D. Maxwell, A. Gauguet, K. J. Weatherill, M. P. Jones, and C. S. Adams. "Cooperative Atom-Light Interaction in a Blockaded Rydberg Ensemble". Physical Review Letters **105** (2010), 193603. arXiv: `1006.4087` (cit. on p. 90).

[105] H. Weimer, M. Müller, I. Lesanovsky, P. Zoller, and H. P. Büchler. "A Rydberg quantum simulator". Nature Physics **6** (2010), 382. arXiv: `0907.1657` (cit. on p. 90).

[106] S. De Léséleuc, S. Weber, V. Lienhard, D. Barredo, H. P. Büchler, T. Lahaye, and A. Browaeys. "Accurate Mapping of Multilevel Rydberg Atoms on Interacting Spin-1/2 Particles for the Quantum Simulation of Ising Models". Physical Review Letters **120** (2018), 113602. arXiv: `1710.06156` (cit. on p. 90).

[107] K. Singer, J. Stanojevic, M. Weidemüller, and R. Côté. "Long-range interactions between alkali Rydberg atom pairs correlated to the ns-ns, np-np and nd-nd asymptotes". Journal of Physics B: Atomic, Molecular and Optical Physics **38** (2005), S295 (cit. on p. 91).

[108] U. Bissbort, D. Cocks, A. Negretti, Z. Idziaszek, T. Calarco, F. Schmidt-Kaler, W. Hofstetter, and R. Gerritsma. "Emulating Solid-State Physics with a Hybrid System of Ultracold Ions and Atoms". Physical Review Letters **111** (2013), 080501. arXiv: `1304.4972` (cit. on p. 93).

[109] T. Secker, N. Ewald, J. Joger, H. Fürst, T. Feldker, and R. Gerritsma. "Trapped Ions in Rydberg-Dressed Atomic Gases". Physical Review Letters **118** (2017), 263201. arXiv: `1612.07112` (cit. on p. 93).

[110] L. Wang, M. Deiß, G. Raithel, and J. H. Denschlag. "Optical control of atom-ion collisions using a Rydberg state". Journal of Physics B: Atomic, Molecular and Optical Physics **53** (2019), 134005. arXiv: `1901.08781` (cit. on p. 93).

[111] R. Côté. "From Classical Mobility to Hopping Conductivity: Charge Hopping in an Ultracold Gas". Physical Review Letters **85** (2000), 5316 (cit. on pp. 93, 94).

[112] M. Tomza, K. Jachymski, R. Gerritsma, A. Negretti, T. Calarco, Z. Idziaszek, and P. S. Julienne. "Cold hybrid ion-atom systems". Reviews of Modern Physics **91** (2019), 035001. arXiv: `1708.07832` (cit. on p. 94).

[113] W. F. Holmgren, M. C. Revelle, V. P. Lonij, and A. D. Cronin. "Absolute and ratio measurements of the polarizability of Na, K, and Rb with an atom interferometer". Physical Review A - Atomic, Molecular, and Optical Physics **81** (2010), 053607. arXiv: `1001.3888` (cit. on pp. 96, 121, 144).

[114] C. Zipkes, L. Ratschbacher, C. Sias, and M. Kohl. "Kinetics of a single trapped ion in an ultracold buffer gas". New Journal of Physics **13** (2011), 053020. arXiv: `1012.0304` (cit. on pp. 96, 108, 111).

[115] R. Grimm, M. Weidemüller, and Y. B. Ovchinnikov. "Optical Dipole Traps for Neutral Atoms". Advances in Atomic, Molecular and Optical Physics **42** (2000), 95. arXiv: `9902072 [physics]` (cit. on pp. 98, 187, 190).

[116] T. Dieterle, M. Berngruber, C. Hölzl, R. Löw, K. Jachymski, T. Pfau, and F. Meinert. "Transport of a single cold ion immersed in a Bose-Einstein condensate" (2020). arXiv: `2007.00309` (cit. on p. 116).

[117] C. Fey, J. Yang, S. T. Rittenhouse, F. Munkes, M. Baluktsian, P. Schmelcher, H. R. Sadeghpour, and J. P. Shaffer. "Effective Three-Body Interactions in Cs(6s)-Cs(nd) Rydberg Trimers". Physical Review Letters **122** (2019), 103001 (cit. on pp. 117, 182).

[118] T. Andersen. Atomic negative ions: Structure, dynamics and collisions. 2004 (cit. on p. 118).

[119] D. J. Pegg. "Structure and dynamics of negative ions". Reports on Progress in Physics **67** (2004), 857 (cit. on p. 118).

[120] R. C. Bilodeau and H. K. Haugen. "Experimental Studies of Os^-: Observation of a Bound-Bound Electric Dipole Transition in an Atomic Negative Ion". Physical Review Letters **85** (2000), 534 (cit. on p. 118).

[121] U. Warring, M. Amoretti, C. Canali, A. Fischer, R. Heyne, J. O. Meier, C. Morhard, and A. Kellerbauer. "High-Resolution Laser Spectroscopy on the Negative Osmium Ion". Physical Review Letters **102** (2009), 043001 (cit. on p. 118).

[122] C. W. Walter, N. D. Gibson, D. J. Matyas, C. Crocker, K. A. Dungan, B. R. Matola, and J. Rohlén. "Candidate for Laser Cooling of a Negative Ion: Observations of Bound-Bound Transitions in La^-". Physical Review Letters **113** (2014), 063001 (cit. on p. 118).

[123] E. Jordan, G. Cerchiari, S. Fritzsche, and A. Kellerbauer. "High-Resolution Spectroscopy on the Laser-Cooling Candidate La^-". Physical Review Letters **115** (2015), 113001 (cit. on p. 118).

[124] A. Kellerbauer and J. Walz. "A novel cooling scheme for antiprotons". New Journal of Physics **8** (2006), 45 (cit. on p. 118).

[125] L. Pan and D. R. Beck. "Candidates for laser cooling of atomic anions: La^- versus Os^-". Physical Review A - Atomic, Molecular, and Optical Physics **82** (2010), 014501 (cit. on p. 118).

[126] S. J. Buckman and C. W. Clark. "Atomic negative-ion resonances". Reviews of Modern Physics **66** (1994), 539 (cit. on p. 118).

[127] K. Bartschat and H. R. Sadeghpour. Ultralow-energy electron scattering from alkaline-earth atoms: the scattering-length limit. 2003 (cit. on p. 118).

[128] D. H. Lee, W. D. Brandon, D. Hanstorp, and D. J. Pegg. "Resonance states in Li^- and B^-". Physical Review A - Atomic, Molecular, and Optical Physics **53** (1996), R633 (cit. on p. 119).

[129] M. Scheer, J. Thøgersen, R. C. Bilodeau, C. A. Brodie, H. K. Haugen, H. H. Andersen, P. Kristensen, and T. Andersen. "Experimental Evidence that the $6s6p^3P_J$ States of Cs^- Are Shape Resonances". Physical Review Letters **80** (1998), 684 (cit. on pp. 119, 146).

[130] T. F. O'Malley, L. Spruch, and L. Rosenberg. "Modification of effective-range theory in the presence of a long-range (r^{-4}) potential". Journal of Mathematical Physics **2** (1961), 491 (cit. on p. 129).

[131] E. Schrödinger. "An Undulatory Theory of the Mechanics of Atoms and Molecules". Physical Review **28** (1926), 1049 (cit. on p. 150).

[132] H. Wimmel. Quantum Physics and Observed Reality. WORLD SCIENTIFIC, 1992 (cit. on p. 150).

[133] M. R. Andrews, M. O. Mewes, N. J. Van Druten, D. S. Durfee, D. M. Kurn, and W. Ketterle. "Direct, Nondestructive Observation of a Bose Condensate". Science **273** (1996), 84 (cit. on p. 150).

[134] G. Binning, H. Rohrer, C. Gerber, and E. Weibel. "Surface Studies by Scanning Tunneling Microscopy". Physical Review Letters **49** (1982), 57 (cit. on p. 150).

[135] J. Repp, G. Meyer, S. M. Stojković, A. Gourdon, and C. Joachim. "Molecules on Insulating Films: Scanning-Tunneling Microscopy Imaging of Individual Molecular Orbitals". Physical Review Letters **94** (2005), 026803 (cit. on p. 150).

[136] R. Temirov, S. Soubatch, O. Neucheva, A. C. Lassise, and F. S. Tautz. "A novel method achieving ultra-high geometrical resolution in scanning tunnelling microscopy". New Journal of Physics **10** (2008), 53012 (cit. on p. 151).

[137] P. Puschnig, S. Berkebile, A. J. Fleming, G. Koller, K. Emtsev, T. Seyller, J. D. Riley, C. Ambrosch-Draxl, F. P. Netzer, and M. G. Ramsey. "Reconstruction of Molecular Orbital Densities from Photoemission Data". Science **326** (2009), 702 (cit. on p. 151).

[138] J. Itatani, J. Lavesque, D. Zeidler, H. Niikura, H. Pépin, J. C. Kieffer, P. B. Corkum, and D. M. Villeneuve. "Tomographic imaging of molecular orbitals". Nature **432** (2004), 867 (cit. on p. 151).

[139] D. Shafir, Y. Mairesse, D. M. Villeneuve, P. B. Corkum, and N. Dudovich. "Atomic wavefunctions probed through strong-field light-matter interaction". Nature Physics **5** (2009), 412 (cit. on p. 151).

[140] A. S. Stodolna, A. Rouzée, F. Lépine, S. Cohen, F. Robicheaux, A. Gijsbertsen, J. H. Jungmann, C. Bordas, and M. J. Vrakking. "Hydrogen Atoms under Magnification: Direct Observation of the Nodal Structure of Stark States". Physical Review Letters **110** (2013), 213001 (cit. on p. 151).

[141] M. Waitz et al. "Imaging the square of the correlated two-electron wave function of a hydrogen molecule". Nature Communications **8** (2017), 1. arXiv: `1801.03746` (cit. on p. 151).

[142] T. Karpiuk, M. Brewczyk, K. Rzkazewski, A. Gaj, J. B. Balewski, A. T. Krupp, M. Schlagmüller, R. Löw, S. Hofferberth, and T. Pfau. "Imaging single Rydberg electrons in a Bose-Einstein condensate". New Journal of Physics **17** (2015), 53046 (cit. on pp. 151, 152, 157, 158, 162).

[143] S. K. Tiwari and S. Wüster. "Tracking Rydberg atoms with Bose-Einstein condensates". Physical Review A **99** (2019), 043616. arXiv: `1810.03439` (cit. on pp. 151, 158).

[144] J. Javanainen and J. Ruostekoski. “Symbolic calculation in development of algorithms: split-step methods for the Gross–Pitaevskii equation”. Journal of Physics A: Mathematical and General **39** (2006), L179 (cit. on p. 154).

[145] D. A. Dalvit, J. Dziarmaga, and R. Onofrio. “Measurement-induced squeezing of a Bose-Einstein condensate”. Physical Review A - Atomic, Molecular, and Optical Physics **65** (2002), 4 (cit. on p. 156).

[146] W. Ketterle, D. S. Durfee, and D. M. Stamper-Kurn. “Making, probing and understanding Bose-Einstein condensates” (1999). arXiv: `9904034 [cond-mat]` (cit. on pp. 157, 201, 202).

[147] M. Saffman, T. G. Walker, and K. Mølmer. “Quantum information with Rydberg atoms”. Reviews of Modern Physics **82** (2010), 2313. arXiv: `0909.4777` (cit. on p. 158).

[148] S. K. Tiwari. *private communication*. Department of Physics, Indian Institute of Science Education and Research (IISER) Bhopal. 2020 (cit. on pp. 170, 173–176).

[149] J. Söding, D. Guéry-Odelin, P. Desbiolles, F. Chevy, H. Inamori, and J. Dalibard. “Three-body decay of a rubidium Bose-Einstein condensate”. Applied Physics B: Lasers and Optics **69** (1999), 257. arXiv: `9811339 [cond-mat]` (cit. on pp. 173, 174).

[150] P. Kevrekidis, D. Frantzeskakis, and R. Carretero-González. Emergent Nonlinear Phenomena in Bose-Einstein Condensates. Springer Berlin Heidelberg, 2008 (cit. on p. 175).

[151] M. T. Eiles, J. Pérez-Ríos, F. Robicheaux, and C. H. Greene. “Ultracold molecular Rydberg physics in a high density environment”. Journal of Physics B: Atomic, Molecular and Optical Physics **49** (2016), 114005 (cit. on p. 182).

[152] M. Deiß, S. Haze, J. Wolf, L. Wang, F. Meinert, C. Fey, F. Hummel, P. Schmelcher, and J. Hecker Denschlag. "Observation of spin-orbit-dependent electron scattering using long-range Rydberg molecules". Physical Review Research **2** (2020), 013047 (cit. on p. 182).

[153] C. J. Pethick and H. Smith. Bose–Einstein condensation in dilute gases. Cambridge University Press, 2008, 1 (cit. on p. 191).

[154] S. Jochim. "Bose-Einstein Condensation of Molecules". PhD thesis. Leopold-Franzens-Universität Innsbruck, 2004, 180 (cit. on p. 192).

[155] C. F. Ockeloen, A. F. Tauschinsky, R. J. Spreeuw, and S. Whitlock. "Detection of small atom numbers through image processing". Physical Review A - Atomic, Molecular, and Optical Physics **82** (2010), 061606 (cit. on p. 203).

[156] L. Sirovich and M. Kirby. "Low-dimensional procedure for the characterization of human faces". Journal of the Optical Society of America A **4** (1987), 519 (cit. on p. 203).

Danksagung

Zuletzt bedanke ich mich bei all jenen die mich auf meinem Weg begleitet und bei meiner Doktorarbeit tatkräftig unterstützt haben, recht herzlichen dank!

An erster Stelle geht mein Dank an Prof. Dr. Tilman Pfau für die Möglichkeit zur Promotion und die hervorragende Betreuung. In der Zeit die ich am Institut arbeiten durfte, habe ich in unseren zahlreichen und anregenden Diskussionen und Meetings sehr viel gelernt. Hierbei schätze ich am meisten die anschaulichen Erklärungen und die vielzahl an Analogien und Gleichnisse, welche stets das tiefere Verständnis förderten. Die Betreuung war stets zielführend, wobei zugleich immer die Freiheit bestand eigene Ideen einzubringen und umzusetzen. Vielen Dank auch für die stets vorhandene Begeisterung für die Physik, die vielen anregenden Ideen, den breiten Überblick über verschiedene Bereiche der Physik und die Bereitstellung der finanziellen Mitteln, die es mir ermöglicht haben, viele Ideen zu verwirklichen. Darüber hinaus bedanke ich mich bei Prof. Dr. Peter Michler für die Übernahme des Mitberichts und bei Prof. Dr. Maria Daghofer für den Prüfungsvorsitz.

Des Weiteren geht ein großer Dank an Robert, der sich immer die Zeit nimmt Fragen zur Physik zu beantworten und auch immer hilfreich zu Diskussionen beiträgt. Danke auch für die vielen Ideen, die für mich manchmal anfänglich etwas abstrus wirken konnten, aber dennoch stets zum angestrebten Ziel führten.

Dann möchte ich mich noch bei dem Kernteam bedanken. Bei Kathrin, danke dass du mir gleich zu Beginn geholfen hast mich am Experiment einzubringen und

mich in die Experimentbedienung eingearbeitet hast. Danke auch dafür, dass du es auf dich genommen hast den Umbau am Experiment anzuleiten und mit mir umzusetzen. Erst durch diese notwendigen Umbauten waren die späteren Experimente möglich. An dieser Stelle geht auch ein Dankeschön an Woo Jin, der in dieser Phase des Experiments uns tatkräftig unterstüzt hat. Ein Dankeschön geht auch an Florian, der unser Team hervorragend und zielstrebig geführt hat und auch stets für Fragen zur verfügung stand. Danke auch für die vielen hilfreichen Diskussionen. Des Weiteren bedanke ich mich bei Thomas, der sich schnell am Experiment eingearbeitet hat und eine große Hilfe bei den durchgeführten Experimenten war. Danke dir für die Unterstützung! Ein Dank geht auch an Moritz, der während meiner Schreibphase noch die ein oder andere Charakterisierungsmessung für mich durchgeführt hat. Ein weiterer Dank geht an die Masterstudenten Ai'Lan, Marian und Christian die durch ihr weitgehend eigenständiges arbeiten das Team sehr gut ergänzt haben. Danke auch an das Rybli-Team, Thomas S., Christian V., Nico und Christian T., für die vielen Diskussionen, das Interesse an den Experimenten und das zur verfügung gestellte Equipment für die Photoionisationsmessungen. Darüber hinaus geht ein ganz besonderer Dank an Michael der nicht nur vieles am Experiment aufgebaut und mitgeplant hat sondern auch einen großteil meiner Bachelor- und Masterarbeit betreute und mir vieles in Bezug auf Programmierung und Elektronik beigebracht hat, von dem ich vieles in meiner Doktorandenzeit anwenden konnte. Danke an das Team und das gesamte PI5 für das angenehme Arbeitsklima und die tolle Zusammenarbeit!

Ein großer dank geht auch an das Computeradministratoren-Team Harald, Daniel und Nico. Mit der Bereitstellung und Instandhaltung der Netzwerkinfrastruktur nehmt ihr uns unglaublich viel Arbeit ab. Danke auch dafür, dass ihr stets für Fragen zur Verfügung steht falls mal etwas nicht funktioniert, sei es Datenbanken, Backups, Soft- oder Hardware. An dieser Stelle möchte ich auch

der Administration im PI5 recht herzlich danken. Vielen dank Astrid, Karin, Kati, Karin H., Oliver und Nadine. Auch ihr nehmt dem Institut sehr viel Arbeit ab.

Zuletzt gilt mein Dank meiner Familie die mich stets unterstützt und ermutigt hat, vielen dank! Ein ganz großes Dankeschön geht an meine liebe Frau Maria. Seit Beginn meines Studiums standest du immer an meiner Seite und hast mich in jeder Lage unterstützt. Vielen dank, dass du in den letzten Jahren alle Höhen mit mir durchlebt, und alle Tiefen mit mir durchgestanden hast. Ohne dich wäre vieles nicht möglich gewesen!

Over the past decade, ultracold Rydberg atoms have been proven to provide a versatile platform for quantum simulation of long-range interacting many-body systems and quantum information processing. A central aspect for many proposals in these fields is the Rydberg blockade phenomenon, which also applies to hybrid systems that consist of ions and Rydberg atoms. Besides that, ultralong-range Rydberg molecules consisting of a Rydberg atom and a ground-state atom within the Rydberg electron orbit have been studied extensively, yielding insight into electron-atom scattering interactions. This thesis studies interactions of Rydberg atoms with neutral atoms and with single ions. For the studies of Rydberg atom-neutral interaction the case of one, few, or even many atoms interacting with a single Rydberg electron is investigated, while for the ion-Rydberg atom system mostly binary interaction is studied. Beyond that, the level structure of negative ions is explored in the context of ultralong-range Rydberg molecules. The presented experiments are carried out in a gas made of rubidium-87 atoms at ultracold temperatures, where the motion of atoms is usually frozen out on the time and length scale of such typical experiments. The interactions between a single ion and a Rydberg atom are investigated and measurements on an ion-induced Rydberg excitation blockade are presented. For this, a single ion is created from a cloud of rubidium atoms, employing a novel V-type photo-ionization scheme specifically suited for generating a very low-energy ion. In addition to the studies of the blockade phenomenon, ultralong-range Rydberg molecules are utilized to perform precision spectroscopy on quasi-bound negative-ion resonances of the rubidium anion. For this purpose, spectroscopy on these molecules is elevated to an unequaled quantitative level of precision, in a combined experimental and theoretical effort. The outcome of a carefully carried out analysis of the observed molecular bound states, that are strongly influenced by resonant electron-atom scattering, is used to unravel the fine-structure triplet of the rubidium anion, which by other means is experimentally challenging to resolve. The result of this spectroscopic study is further used to extract the scattering lengths and to pinpoint the *p*-wave shape resonance position associated with the fine-structure triplet of the anion.